Non-contact free-form shape measurement for coordinate measuring machines

Yvonne R. Huddart

Submitted for the degree of Engineering Doctorate at Heriot-Watt University, Department of Mechanical Engineering

March 2010

Abstract

Precision measurement of manufactured parts commonly uses contact measurement methods. A Coordinate Measuring Machine (CMM) mounted probe touches the surface of the part, recording the probe's tip position at each contact. Recently, devices have been developed that continuously scan the probe tip across the surface, allowing points to be measured more quickly. Contact measurement is accurate and fast for shapes that are easily parameterized such as a sphere or a plane, but is slow and requires considerable user input for more general objects such as those with free-form surfaces.

Phase stepping fringe projection and photogrammetry are common non-contact shape measurement methods. Photogrammetry builds a 3D model of feature points from images of an object taken from multiple perspectives. In phase stepping fringe projection a series of sinusoidal patterns, with a phase shift between each, is projected towards an object. A camera records a corresponding series of images. The phase of the pattern at each imaged point is calculated and converted to a 3D representation of the object's surface.

Techniques combining phase stepping fringe projection and photogrammetry were developed and are described here. The eventual aim is to develop an optical probe for a CMM to enable non-contact measurement of objects in an industrial setting. For the CMM to accurately report its position the probe must be small, light, and robust. The methods currently used to provide a phase shift require either an accurately calibrated translation stage to move an internal component, or a programmable projector. Neither of these implementations can be practically mounted on a CMM due to size and weight limits or the delicate parts required.

A CMM probe consisting of a single camera and a fringe projector was developed. The fringe projector projects a fixed fringe pattern. Phase steps are created by moving the CMM mounted probe, taking advantage of the geometry of the fringe projection system. New techniques to calculate phase from phase stepped images created by relative motion of probe and object are proposed, mathematically modelled, and tested experimentally. Novel techniques for absolute measurement of surfaces by viewing an object from different perspectives are developed. A prototype probe is used to demonstrate measurements of a variety of objects.

Acknowledgements

I would like to express my sincere appreciation to my supervisors, Professor Andrew Moore and Dr David Mckendrick, for their advice and encouragement throughout this project.

I am deeply grateful to Dr Nick Weston, who has been the driving force behind this project. Without him this thesis would neither have been started nor finished and I have continually relied on his guidance, support, enthusiasm and sanity over the past few years. I must also thank him for offering me the opportunity to undertake the project.

Many thanks are due to Dr Jesus Valera of Heriot-Watt University, for his assistance throughout the project. Thanks also to Chris Mack and John Mason (Mechanical Engineering) for machining parts for the prototype probe and to Mark Leonard (Physics) for use of the Zygo white light interferometer.

Thanks to my present employer Renishaw, and to the many colleagues who have helped with various aspects of the work. Particular thanks go to Ian McLean, Tim Featherstone, Calum McLean, Anastasios Aretos, Dougie Angus, Duncan MacDonald and Edward Rolfe.

Many thanks go to my friends and family for help, company, and proof-reading, particularly Gayle, Sophie, Helen, Dave and Stephen and of course my wonderful parents Alice and Alan.

This project was part-funded by the Engineering and Physical Sciences Research Council [grant number GR/T11289/01].

ACADEMIC REGISTRY

Research Thesis Submission

Name*:*	Yvonne Huddart		
School/PGI:	EPS (Mechanical Engineering)		
Version: *(i.e. First, Resubmission, Final)*	Final	Degree Sought (Award **and** Subject area)	EngD Photonics

Declaration

In accordance with the appropriate regulations I hereby submit my thesis and I declare that:

1) the thesis embodies the results of my own work and has been composed by myself
2) where appropriate, I have made acknowledgement of the work of others and have made reference to work carried out in collaboration with other persons
3) the thesis is the correct version of the thesis for submission and is the same version as any electronic versions submitted*.
4) my thesis for the award referred to, deposited in the Heriot-Watt University Library, should be made available for loan or photocopying and be available via the Institutional Repository, subject to such conditions as the Librarian may require
5) I understand that as a student of the University I am required to abide by the Regulations of the University and to conform to its discipline.

* *Please note that it is the responsibility of the candidate to ensure that the correct version of the thesis is submitted.*

Signature of Candidate*:*		Date:	

Submission

Submitted By *(name in capitals):*	
Signature of Individual Submitting:	
Date Submitted:	

For Completion in Academic Registry

Received in the Academic Registry by *(name in capitals):*			
Method of Submission *(Handed in to Academic Registry; posted through internal/external mail):*			
*E-thesis Submitted (**mandatory for final theses from January 2009**)*			
Signature:		Date:	

Contents

Related publications

N. J. Weston, Y. R. Huddart, A. J. Moore, “Non-contact measurement apparatus and method”, International Patent Application, Publication number WO2009024756 (2009).

N. J. Weston, Y. R. Huddart, A. J. Moore, T. C. Featherstone, “Phase analysis measurement apparatus and method”, International Patent Application, Publication number WO2009024757 (2009).

N. J. Weston, Y. R. Huddart, “Non-contact probe”, International Patent Application, Publication number WO2009024758.

N. J. Weston, Y. R. Huddart, “Non-contact object inspection”, International Patent Application, Application number 0915904 (2009). Not yet published.

Y. R. Huddart, J. D. R. Valera, N. J. Weston, T. Featherstone and A. J. Moore, “Phase-stepping fringe analysis using a single projected pattern”, in preparation for submission to Optics Express.

Y. R. Huddart, J. D. R. Valera, N. J. Weston and A. J. Moore, “Fringe projection using multiple perspectives for automatic non-contact shape measurement”, in preparation for submission to Optics Express.

Y. R. Huddart, J. D. R. Valera, N. J. Weston and A. J. Moore, “Combining novel fringe analysis and photogrammetry for industrial shape measurement”, Fringe 2009: the 6th International Workshop on Advanced Optical Metrology, Nurtingen, Germany, 13-16 September (2009).

Y. R. Huddart, J. D. R. Valera, N. J. Weston and A. J. Moore, “Combining fringe projection and photogrammetry for the non-contact measurement of objects with free-form surfaces”, Photon 08, 25-28 August, Edinburgh, IOP (2008).

Chapter 1 Introduction

1.1 Background

Methods of shape measurement may be split into two categories: contact and non-contact. Traditional coordinate measuring machines (CMMs) use contact measurement techniques to measure manufactured parts. A probe attached to a coordinate measuring machine touches the surface of the part at multiple points, and the probe tip position is sensed and recorded for each touch. Recently, devices have been developed that enable the probe tip to be scanned in a continuous path across the surface, providing for a shorter measurement time. Contact measurement is highly accurate and fast for shapes that are easily parameterized such as a sphere or a plane, but there is an increasing need within industry for measurement of complex manufactured parts with free-form surfaces [1]. It is possible to measure these more complex objects using a CMM by taking multiple touches on the surface, but this is very slow and requires a considerable amount of user input. In order to measure such an object using a scanning probe the scanning path must be automatically adjusted for deviations of actual shape from the nominal shape, and the probe tip must be compensated for in the direction of the normal to the surface at all points. The software is complex, and for a non-trivial part requires considerable input by a skilled user.

A non-contact probe for a CMM can enable more automatic measurement of complex parts. Sections of an object can be measured separately and the measurements stitched together with the aid of the accurate position reporting of the CMM. Sub-sections of the object can then be re-measured with a touch probe to gain higher accuracy if required, using the measurement of the surface found from the optical probe to create a suitable scanning path. For the CMM to accurately report its position the probe must be small and light, and able to withstand high accelerations. This thesis describes techniques that enable a simple probe, containing no delicate or moving parts, to be used for fast, high accuracy non-contact shape measurement.

The Engineering Doctorate for which this thesis is submitted is an alternative to a PhD with a more industrial bias [2]. The research is carried out as a collaboration between industry and academia, and the project is of interest to the sponsoring company. In this case the sponsoring company is Renishaw Plc [3]. One of Renishaw's main product

lines is CMM products such as CMM controllers, heads and probes. The non-contact probe that is the focus of this research is intended to integrate into Renishaw's existing range of touch probes for high-end CMMs for use within high-value manufacturing. The techniques developed are applicable to many other potential products and market sectors, and contribute to the wider academic body of knowledge of fringe projection techniques for shape measurement.

1.2 Organisation of the thesis

In Chapter 2 the literature forming the background to the project is discussed, with the emphasis on existing commercial systems. Some metrology industry standards and terminology are briefly introduced. Both contact and optical shape measurement techniques are discussed, including the advantages and limitations of each. The choice of phase stepping fringe projection and photogrammetry as the main measurement techniques is justified, and the problems to be overcome are described.

The mathematical framework on which the remainder of the thesis is built is laid out in Chapter 3. Photogrammetry theory is reviewed and applied to fringe projection systems with one or more cameras and fringe projectors. Phase step algorithms are discussed. The accuracy of optical triangulation techniques is fundamentally limited by speckle, so the chapter concludes with a discussion of speckle theory.

Chapter 4 describes the experimental systems and software used to develop and test the new techniques. Photogrammetric measurements with an accuracy of 10 μm (around 1 part in 7500 of the field of view) are achieved, compared to measurements using fringe analysis with an accuracy of around 1 in 3300 (again, relative to the field of view). These results are used a baseline with which to compare results achieved from the techniques developed in the later chapters. Different stages of calibration are described, and some error sources are considered. The software used to process recorded images is described and justification given for algorithms chosen within the processing. Fringe projection is also used to provide corresponding points for photogrammetric measurement by locating points with equal projected phase viewed from different perspectives. Measurements with accuracy of 1 part in 2400 of the field of view are demonstrated. A variety of surfaces are measured in order to investigate the effect of speckle noise on phase measurements, the results of which are used in later chapters.

Phase stepping fringe projection systems create a phase shift either by a moving an internal component such as a mirror or grating relative to the light source, or by using a programmable projector. One of the goals of this project is to avoid the use of internal moving parts within the projector or camera. Chapter 5 introduces the idea of creating a phase step by relative motion of the projector and object to be measured [4]. The camera and projector are held in a fixed spatial relationship as if they were part of a single fringe projection probe. The motion of the object with respect to the camera means that the computation of the phase from a series of images is more complicated than in traditional temporal phase stepping. The relative motion must be compensated for so that the phase at the object's surface can be calculated. Possible methods to do so are modelled and tested experimentally. Accuracy of 60 μm is achieved for an object approximately 60 mm across with a depth range of 40 mm (1 part in 1000 of the lateral extent of the object). Error sources applicable to the new techniques are identified and discussed.

Chapter 6 describes novel techniques to resolve the ambiguity due to the periodic nature of the fringe pattern (referred to as 2π ambiguity). For any isolated surface to be measured, the absolute phase or distance between probe and object must be known for at least one point. Photogrammetry techniques can be used to measure corresponding points in images taken from different perspectives. The measurement of a corner or an edge can be used to resolve the 2π ambiguity on the surfaces that it bounds. This idea is experimentally demonstrated with limited success. The technique is limited by the difficulty of confidently finding corresponding points between the different perspectives. A second technique using multiple perspectives to automatically match surface patches and simultaneously resolve 2π ambiguity on the matched patches is described and demonstrated [5]. The initial step of both techniques is to locate edges and segment the phase maps; a novel means to do so is also described in Chapter 6 [6].

The results of Chapters 5 and 6 are demonstrated in combination in Chapter 7. A prototype probe consisting of a camera and simple fringe projector has been created for use on a five-axis CMM [7]. The probe is described and calibrated and measurement results of a number of objects with different surface finishes are presented. The position of a sphere is measured correct to 100 μm with a mean radial error of 22 μm. A number

of error sources are identified and ways to limit their significance and further develop the prototype to achieve better accuracy are suggested.

Chapter 8 concludes the thesis with a summary of findings and a discussion of further avenues for research. Issues that may need to be resolved in order to turn the prototype and current software into a commercial system are highlighted. Potential alternative approaches are discussed. Possible applications of the new techniques, other than for a CMM probe, are briefly indicated.

A number of people have contributed to the work presented here. In particular, Matlab scripts for flood-fill phase unwrapping and phase stepping were inherited from Andrew Moore and Iain Wallace [123,70]. The photogrammetry software suite was put together by Iain Wallace from existing freeware. Matlab scripts to collect fringe data and process for the polynomial phase to height calibration were written by Jesus Valera [31]. Updates to the scripts and the algorithms described in the remainder of thesis were implemented by the author.

Chapter 2 Background

2.1 Introduction

In this chapter, the background to the project is described. The emphasis here is on existing systems used within the metrology industry. Both contact and optical shape measurement systems are described. The reasons for choosing fringe projection and photogrammetry as the main measurement techniques are discussed, before describing the techniques in more detail in Chapter 3.

2.2 Terminology and standards

2.2.1 Measurement accuracy

According to the International Organisation for Standardization [8], the accuracy of a measurement incorporates two terms. The "trueness" expresses the ability of a measurement to give a correct result. It is found by comparing the mean of a large number of repeated measurements to a known reference. The "precision" expresses the closeness of results of repeated measurements. Precision can include repeatability (the closeness of repeated measurement under the same conditions and the same location carried in a relatively short time frame) and reproducibility (the closeness of measurements carried out at different times, in different locations or by a different person) [9]. The reproducibility is generally larger than the repeatability – that is, repeated measurements yield a larger range of results under reproducibility conditions than under repeatability conditions. The uncertainty of a measurement result is the range of possible values of a measurand that could be expected to have resulted in the measurement result [10]. The resolution of a measurement instrument is the finest detail that can be distinguished and is a factor to be taken into account in evaluating the uncertainty.

Uncertainty, repeatability and reproducibility are often expressed in terms of standard deviations. Manufacturers of all but the most established forms of metrology equipment often quote the accuracy of an instrument without clarifying the procedure used to evaluate it. For contact measurement systems such as CMMs, internationally accepted standard procedures for evaluation of measurement uncertainty exist and reference objects are readily available [11]. Standards are also available for the non-contact

measurement of surface characteristics such as texture and roughness [12]. For free-form shape measurement systems the equivalent metrology infrastructure is under development [13] so the accuracies quoted by metrology equipment manufacturers for different instruments are not necessarily strictly comparable. The accuracy given in marketing material will always have been achieved under favourable conditions and may be difficult or impossible to achieve in practice.

2.2.2 Definition of "shape measurement"

An initial consideration is to try to define what it is we mean by shape measurement. Object recognition and classification is a common problem in the fields of robotics and machine vision [14]. A scene is analysed by image processing or other non-contact techniques. The object of interest must be segmented from the background and classified according to the requirements of the application. This could be in terms of shape, location, orientation and could include factors such as colour. Here, we are less interested in classification and recognition of objects and more interested in spatial dimension measurements. In industrial measurement a CAD model describing the object's nominal features is often available, however for full generality no prior knowledge of the object is assumed here. An object is completely described by a point cloud covering all facets of its surface at some nominal spatial resolution. The resolution will depend upon the design of the device. It is assumed that a parameterised description could be created from the point cloud if required. The "shape" of an object, here, is mostly expected to be a macroscopic property and includes information about its dimensions, orientation, and location in some global reference frame [15]. It is assumed that a cloud of surface points is sufficient to extract whatever derived features are required for a particular application. The "shape" could also include microscopic properties such as surface roughness or texture [12]. Much of the subject matter here is applicable to measurement of microscopic properties even though they are not within the focus of this thesis.

An object is sometimes described in terms of features such as surfaces, edges and corners. However, no standard definitions of these exist [16]. Any definition would be likely to be device or application dependent; for example, an edge might be a set of points on the surface on which the curvature is such that the change of surface normal over a spatial region related to the measurement device's resolution is above some

predefined threshold. Within this thesis the terms surface and edge are used somewhat loosely, and more in a 2D sense than a 3D sense. That is, an edge is a line in an image that bounds a continuous surface patch as viewed from a particular perspective.

2.3 Contact measurement systems

The touch trigger probe was invented by David McMurtry in the early 1970s [17]. The probe acts as an electrical switch that is actuated by means of an attached stylus, triggered when the stylus comes into contact with a surface. The mechanical seating for the switch forms part of the electrical circuit and is implemented in such a way as to open the switch when the stylus is disturbed and return the stylus to its rest position in a highly repeatable way when the switch is closed. Shapes are measured by touching the stylus against the surface at different points. The probe may be moved manually by the operator or automatically by a robot or coordinate measuring machine. Scanning probes that keep the stylus in contact with the surface have been developed more recently. They can be either active (using complex control software to stay in contact with the surface) or passive (following a predefined path regardless of the detected surface). A scanning probe is often attached to an indexing or servoing head on a coordinate measuring machine (CMM), allowing 3 or 5 axis motion. Different probes are appropriate for measuring different features, for example a probe with a long stylus is required for measuring a deep borehole, but shorter, more robust probes are preferable for measuring a plane as they make faster measurements, reduce the likelihood of collisions and are intrinsically more accurate. A CMM may have a rack containing a range of automatically interchangeable probes and styli. Each constituent part of the CMM including the probe, head, linear and any rotary axes must be calibrated to achieve accurate measurement. ISO standards describe calibration procedures and verification tests [11].

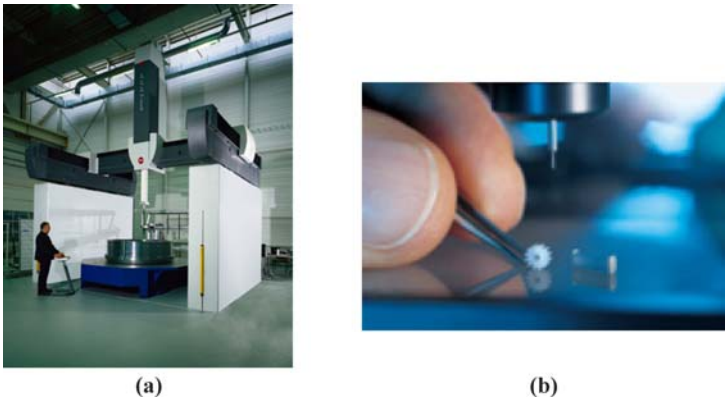

(a) (b)

Figure 1: CMMs of very different sizes - (a) the Letiz PMM-G [18] and (b) the Zeiss F25M [19].

CMMs to measure a wide range of objects from nanometres to metres are available. The Leitz PMM-G is a gantry-style CMM for measuring objects such as aeroplane wings or wind turbine components. It has a measurement volume up to 7 m by 4 m by 3 m with a precision of 3.6 µm [18*]. At the other end of the scale the Zeiss F25 Microsystem CMM [19] has a volume of 0.1 m by 0.1 m by 0.1 m and an uncertainty of 250 nm, and is used, for example, for medical parts. Between these two extremes a huge variety of CMMs exists. The intended application of this research is a typical high end three axis CMM with a two rotary axis servoing head, having a measuring volume at least of the order of 1 m^3 and reporting the position of the tip of a contact probe correct to the order of 1 µm.

2.4 Non-contact measurement techniques

The most common optical measurement methods will now be introduced. The work reported in this thesis has mainly focused on geometric techniques, in particular fringe projection, but the principles of a number of different techniques will be briefly discussed. Accuracies are quoted for some examples of commercially available systems from product marketing material. It should be noted that quoted results will have been determined under favourable measurement conditions which may be difficult or even impossible to achieve in practice.

2.4.1 Time-of-flight

Perhaps the most obvious non-contact measurement technique is time-of-flight. A pulse is emitted towards the object to be measured and the reflected pulse is detected. The distance to the target is calculated from the elapsed time between emission and detection [20]. This is a widely used technique for long-distance measurement in atmospheric studies and astronomy, for example, as well as in more day-to-day applications such as the focussing mechanism of a camera. Photon counting techniques can provide high resolution measurements of targets with non-cooperative surfaces [21]. Time-of-flight techniques are relevant to optical, radio (radar) or sound (sonar), or in fact any form of detectable signal. The speed that the pulse moves at must be known, so in the case of electromagnetic radiation this means the refractive index of the medium

* Marketing literature for commercial systems quoted throughout can be found in Appendix A1.

through which the pulse travels must be known. The accuracy of the distance measurement is dependent on the ability to measure the time delay accurately. For example, to achieve depth resolution of 100 mm a clock cycle of 300 ps (3.33 GHz) is required (for light travelling through air). The accuracies of interest here are of the order of 10 μm and, without oversampling, would need a clock speed of the order of 100 THz! For shape measurement, this is a slow method, as only one point on a surface is measured at once and each of these single point measurements may need to be repeated and averaged to reach the required accuracy.

2.4.2 Interferometric techniques

Interferometric techniques tend to involve splitting a beam from a coherent source into two parts; one follows a known path, the other travels the path to be measured. The two beams interfere on recombination, the pattern of interference depending on the difference in length between the two paths. This kind of technique is useful when very high accuracy is required over a small range, such as for testing optical components. For example, the FizCam range of Fizeau interferometers from 4D Technology [22] offer shape measurement of optical components such as flats, spheres and wedges with an uncalibrated accuracy of up to 30 nm and a repeatability standard deviation of less than 1 nm (although considerable averaging is required to achieve his).

White light interferometry is often used for measurement of surface roughness. For example, the Zygo NewView interferometry series [23] offers measurement of surfaces with a repeatability of 0.01 nm and a vertical resolution of 0.1 nm. The depth range is up to 150 μm. The lateral resolution and field of view depend on the objective lens used but range from 0.35 μm to 9.5 μm resolution over a field of view 0.04 mm by 0.03 mm to 14 mm by 10 mm respectively. A sample can be measured successfully if it is at most within 39º to the horizontal, with different objectives having lower limits. White light interferometry tends to be most successful with smooth, shiny surfaces. Matt, diffuse surfaces can cause problems due to low reflected intensity and because the surface roughness can be outwith the measurement range either in terms of height or angle. The reference path must be kept stable, immune to both temperature variation and vibration.

The limited measurement range means that interferometry is useful for measurement of microscopic shape but has limited usefulness in the macroscopic regime, and this, along with the stability requirements make it an impractical technique for our application.

2.4.3 Geometric techniques

Geometric techniques are the oldest and perhaps the most widely used for non-contact measurement. They are based on the principle of triangulation (Figure 2). By knowing two angles and the length of one side of a triangle, as in Figure 2(a), the other sides and angles may be calculated. In particular, if a laser produces a spot on the surface and a detector a distance b from the laser as depicted in Figure 2(b) detects the spot, then the distance to the surface, z, may be calculated if c and x indicated in the diagram are known. c is the distance from the camera's lens to its pixel array (called the principal distance); x is the position of the image of the spot on the pixel array. The baseline, b is also assumed known. The distance to the surface is given by

$$z = \frac{bc}{x}$$

The accuracy depends on the baseline; if the baseline is increased greater accuracy is possible in principle, but the likelihood of occluded points increases. The accuracy is fundamentally limited by speckle (see section 3.8). This method is relatively slow, as only one point may be measured at a time. By projecting a line (Figure 3) measurements from multiple points may be collected simultaneously.

An extension is to project a two-dimensional pattern on to the surface so that information about a multiple points, lines or an area on the surface may be recorded at one time. Many different forms of pattern projection exist, including single point projection, line stripe projection, fringe projection (see below), Grey code, and random or pseudo-random patterns [24]. Different pattern types have different drawbacks and advantages. Single point or line projection can enable straightforward measurement with little processing, but measuring extended areas is slow. Projecting periodic patterns can speed up the data collection to measure an area of an object but there must be a way to distinguish one period of the pattern from another – this is called the 2π ambiguity problem. The problem can be alleviated to some extent by using colour or more complex patterns, or by projecting different patterns one after another in such a

way as to achieve unambiguous measurement. A discrete pattern such as stripes or spots limits measurement points to the position of the pattern elements.

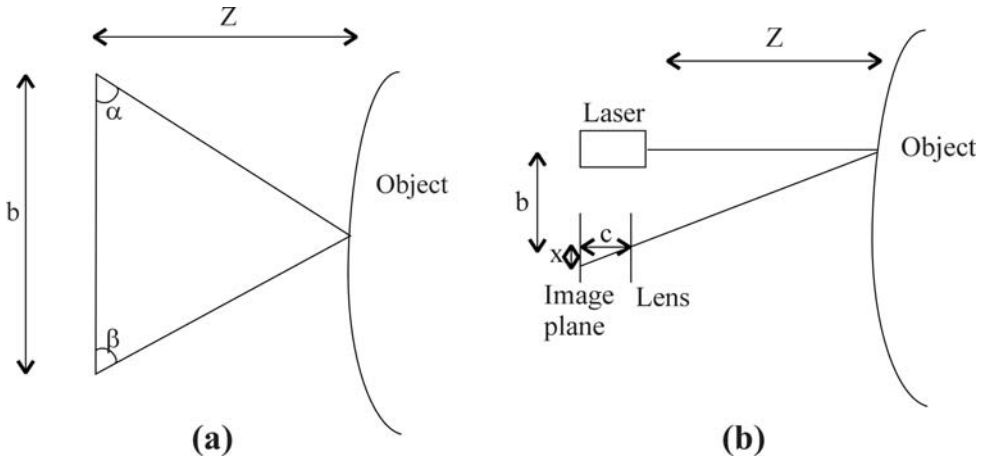

Figure 2: Triangulation.

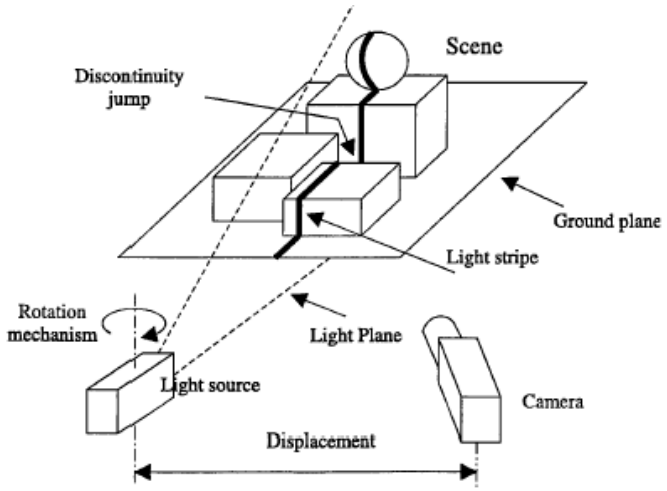

Figure 3: Laser stripe projector [25].

2.4.4 Fringe projection

Projecting a spatially continually varying pattern allows measurement of all points on the object. Measurements based on the intensity of a continually varying pattern are of limited use because of variations in recorded intensity caused by changes in object reflectivity across the surface and the distance to and angle of the surface. Fringe projection uses one or more sinusoidal patterns covering the whole field of view. The phase of the fringe pattern recorded at each pixel encodes the height of the object. The phase can be calculated from the intensity but is independent of the reflection properties and dependent only on the pattern projected, the measurement system itself and the distance to the object. The techniques used to calculate the phase are similar or identical to those used for interferometric techniques and include Fourier [26] and phase

shift techniques [27,28]. Phase shift techniques allow phase to be calculated automatically with no knowledge of the object being measured, whereas Fourier techniques tend to be most useful for smooth objects with limited surface gradients [29]. Phase calculations correct to $\frac{1}{500}$ fringe periods have been reported from digital fringe projection systems using phase stepping [30,31]. The 2π ambiguity problem can be solved, for example, by projecting and recording fringe patterns with varying periods [32]. An example of a fringe projection system available on the market is the Cam3D from 3DShape Gmbh [33]. In the manufacturer's marketing literature it is claimed that measurement with resolution of 100 µm and error up to 30 µm over a measurement volume of 100 mm by 100 mm by 60 mm is achievable. As it is an areal technique fringe analysis is inherently faster than laser point or line triangulation. The accuracies reported over a measurement range of tens of millimetres suggest it is a suitable technique for our application. However the necessity to project multiple patterns to automatically calculate phase and resolve the 2π ambiguity problem for unknown objects are difficulties to be overcome.

2.4.5 Moiré fringes

Moiré fringes provided a way to find object contours prior to the proliferation of digital cameras and the straightforward use of computers for fringe analysis techniques. A Moiré pattern is produced when two identical gratings are viewed with an angle between them or if two gratings have a slightly different period. The period of the fringes is lower than the period of the two gratings, and is related to the difference in periods or the angle between the gratings. For example, Creath and Wyant [34] show the fringes produced by two identical gratings with relative rotation, also two gratings of different period both with the same alignment and with a relative rotation (Figure 4).

In shadow Moiré an object is illuminated and viewed through the same grating. The spacing of the resulting fringes is related to the distance between a reference plane and the object and the viewing and illumination directions. Therefore the shape of the object can be deduced from processing the Moiré fringe images recorded [35]. Projection Moiré, in which two different gratings are used (one for illumination and the other for viewing) can be simpler to implement.

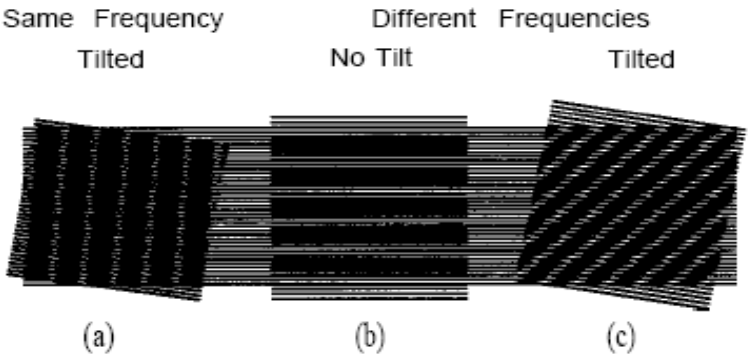

Figure 4: Moiré patterns caused by two straight-line gratings with (a) the same pitch tilted with respect to one another, (b) different frequencies and no tilt, and (c) different frequencies tilted with respect to one another. [34]

In either case, if collimated illumination is used then the fringes produced are contours corresponding to equal object heights and the height of the object is found relative to a reference plane. Phase shifting techniques can be used to calculate the phase, giving height information at each point viewed, although accuracy and spatial resolution is compromised by the requirement to filter out the high frequency carrier. Achievable accuracy is around $\frac{1}{10}$ to $\frac{1}{100}$ of a fringe period [34]. Therefore, as with other fringe analysis techniques the use of the finest resolvable fringes is preferable. Moiré techniques are mostly of historical interest as they were used to calculate contour information prior to digital processing techniques, however some active research is still on-going [36].

2.4.6 Photogrammetry

Photogrammetry is a non-contact technique for shape measurement that uses multiple two-dimensional images to make up a three-dimensional model of an object. If two viewpoints are used this is often known as stereo vision, and is the basis of how we actually see in three dimensions. The technique has been used since the 1850s. It became widely used in World War I for aerial mapping, and has found applications within surveying and civil engineering, as well as archaeology and medical applications. An important point to note is that off-the-shelf equipment may often be used, so this offers an extremely cost-effective measurement technique. Particularly of interest here is close-range photogrammetry – "the extent of the object to be measured is less than about 100 m and cameras are positioned close to it" [37]. Again, photogrammetry uses the principle of triangulation – given the position of points in two or more camera images, the distance to the points may be calculated. One difficulty is ensuring that the

points in the different images correspond – for this reason special targets such as retro-reflectors are often placed on the surface to be measured. This means it is not truly a non-contact measurement technique, and slows the measurement and makes automation difficult. Nevertheless, this is a technique frequently used in industry for high precision industrial inspection. For example, the GOM TRITOP [38] system uses photogrammetry for shape measurement, giving accuracy up to 1 part in 120000 within a measuring volume from 0.1 m by 0.1 m by 0.1 m up to volumes of side lengths of tens of metres. Sub-micron accuracy is attainable with the smaller measuring volume, but as with the structured light systems above the accuracy decreases as the measuring volume increases. Markers must be placed on the surface to give corresponding points in each view. Another commercial example is Geodetic Systems' V-STARS [39], the accuracy of which is 10 μm plus 10 μm per metre standoff distance, and requires retro-reflective markers to be placed on the target.

While photogrammetric systems are capable of extremely high accuracy and can be cost effective as off-the-shelf cameras may be used, they are not without disadvantages. Skilled operation is often required, the surface must contain identifiable features for measurement, and the calibration procedure can be time-consuming and complicated. In addition, the processing of the image information is intensive, and accuracy may have to be sacrificed for an acceptable processing time. Also, specular surfaces present difficulties, as reflections of lights can obscure targets, or appear as surface features. Photogrammetry is normally a passive technique, although structured light has been used to assist in the identification of corresponding points [40]. There is significant research into automatic corresponding point identification, but it remains a difficult and application dependent problem [41].

2.5 Non-contact probes for coordinate measuring machines or robots

The ultimate aim of the project is a non-contact probe for a CMM with a servoing head. There are a few probes for indexing heads and robots on the market, as summarised in Table 1. Again, the accuracies given here are those quoted by the machine manufacturers themselves, and as such have mostly been tested under optimum conditions, and may be difficult to attain in practice. Also the overall accuracy possible will depend on the CMM and head on which the probe is mounted. As previously stated there are currently no national standards for shape metrology from non-contact

measurement systems such as these. The existing standards apply to contact measurement systems only. Therefore, the accuracies given here may not be strictly comparable as they may have been calculated using varying techniques and definitions. Furthermore, different manufacturers quote different details. Any accuracy given should be seen as highly surface dependent. Table 1 summarises some example probe specifications from the manufacturers' product literature. The measurement volume details in the table are for a single measurement position. Measurements from different positions, using the positioning of the CMM or robot on which the device is mounted, are stitched together using either matching or photogrammetric techniques. A photogrammetry probe for a CMM has been considered [42], but to the best of our knowledge none is available to buy.

The Wolf & Beck OTM probe series [43], Figure 5, is an example of a commercial product using laser spot projection. These probes are designed to be attached to a CMM, thus enabling non-contact measurement of parts in the same environment as contact measurements are generally made. The sensor takes the form of a ring around the point of laser projection; each measurement is an average reading from each part of the sensor, thus increasing the accuracy that would otherwise be low due to the small baseline. This design also reduces the risk of occlusion – it is unlikely that the spot could not be viewed from any angle of the sensor array.

The Nikon ModelMaker series [44], Figure 6(a), are examples of laser scanners for robot arms, while the LC [45] series, also from Nikon, are CMM laser stripe probes. Data for a line of points are collected simultaneously so measurement is faster than with spot projection probes, up to 82,000 points per second with the ModelMaker D. To gain full three-dimensional information the surface must be scanned three times with the stripe in a different orientation. The Nikon XC65, Figure 6(b), combines three laser stripe projectors and three sensors at different orientations so that three-dimensional information may be collected in one scan of a surface.

Table 1: Specifications of examples of optical CMM probes.

System	Type	Speed (points per second)	Field of view (mm)	Depth range (mm)	Resolution (μm) (Relative to FOV*)	Repeatability (μm) (Relative to FOV*)	Accuracy (μm) (Relative to FOV*)	Size (mm)	Weight (kg)
Wolf & Beck OTM3-20	Laser spot triangulation	3500	N/A	20	2 (1:10 000)	10 (1:2000)	50 (1:400)	52x52x179	0.35
Nikon MMD50	Laser stripe triangulation	82 000	50	50	50 (1:1000)		8 (1:6000)		0.4
Nikon XC50	Laser stripe triangulation	75 000	65	65	Lateral 65 (1:1000)		15 (1:4000)	155x86x142	0.44
GOM Atos III	Fringe projection	2 000 000	150		70 (1:2000)	4 (1:38 000)		490x300x170	7.4
Breuckmann OptoTopHE	Fringe projection	1 400 000	80	50	Lateral 60 (1:1300) Vertical 2 (1:40 000)	7 (1:11 000)	10 (1:8000)		2.5
Steinbichler Comet 5 4M	Fringe projection	800 000	55	50	25 (1:2200)				

* For the OTM3 laser spot triangulation, resolution, repeatability and accuracy are relative to measurement range.

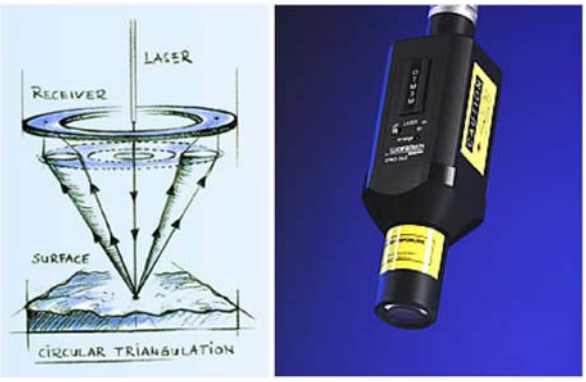

Figure 5: The Wolf & Beck OTM3 [43]

(a) (b)

Figure 6: Laser scanners: (a) the Nikon MMD laser scanner [44] and (b) the Nikon XC50 laser scanner [45]

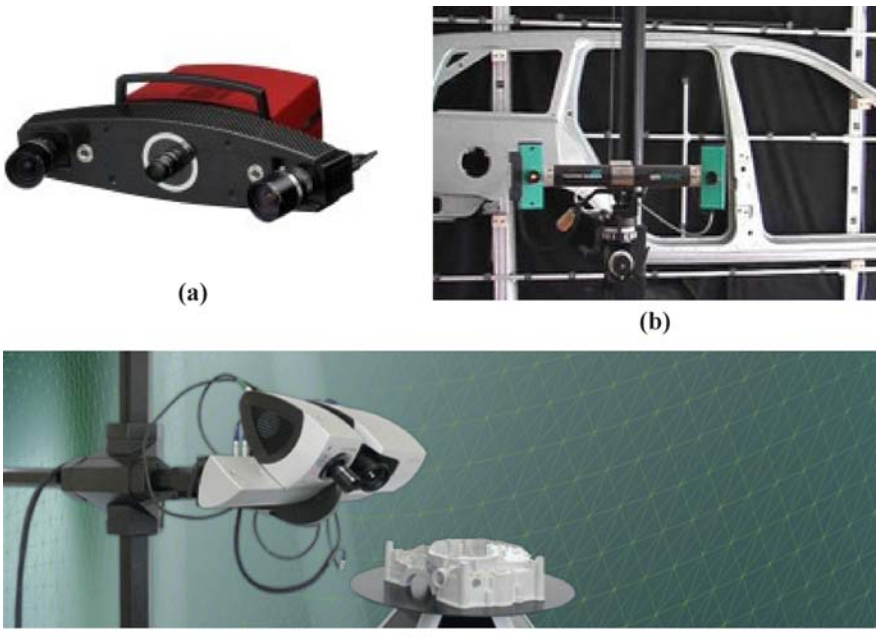

(a) (b) (c)

Figure 7: Fringe projection probes: (a) The GOM ATOS III [46], (b) the Breuckmann OptoTOP-HE [47] and (c) the Steinbichler Comet 5 [48]

Much faster measurement is achievable using fringe projection since data are collected for all pixels viewing the object. The ATOS system by GOM [46] is an example of a fringe projection probe that can be mounted on a robot (Figure 7). A white light projection unit is used to project a series of patterns on to the target surface. Cameras record the resulting images, two being used to lessen occlusion problems. It takes 8 seconds to collect 4 million points in a measuring volume of up to 2 m^3, with a resolution 1 mm and an accuracy of 50 µm. Accuracy of up to 4 µm is possible with a smaller measuring volume. Another example is the Breuckmann OptoTOP-HE [47], which collects 1.4 million points in under a second with an accuracy of between 7µm and 60µm, again depending on the measuring volume used (Figure 7). The maximum measuring volume is around 0.5 m^3. The Steinbichler Comet 5 [48] is a further example of a fringe projection probe (Figure 7). Like the ATOS, the OptoTOP-HE and the Comet 5 can be mounted on a robot.

In order to make a measurement in the coordinate system of the robotic arm, a procedure called a hand/eye calibration must be carried out to find the orientation of the camera with respect to the arm. The hand/eye calibration is generally carried out in one of two ways [49]. The first is to couple the hand/eye calibration with a conventional robotic arm calibration, finding the robotic kinematic parameters simultaneously with the hand/eye parameters [50]. The second option decouples the hand/eye calibration from the arm calibration, so that the robot is calibrated by conventional means, and the hand/eye calibration is carried out separately [51]. The former case involves a global optimisation over a large number of unknowns, and thus requires good initial guesses for successful convergence. In the second case the technique generally involves carrying out multiple camera calibrations at different positions and orientations to find the camera locations with respect to the calibration target, and using the information from this along with the relative positions and orientations used from the robotic arm to solve a matrix equation for the transformation between the camera coordinate system and that of the robot arm.

2.6 Conclusions

The available fringe projection probes are too heavy or large to be used on a five axis CMM. A probe for a servoing head must weigh at most 0.5 kg with maximum dimensions approximately 150 mm^3. The weight should be distributed such that the

probe's centre of gravity is close to the centre of rotation of the head so that the head motors can safely move the probe around without overheating or breaching the current limits. To be automatically changed in a probe change rack it must be robust enough to withstand high acceleration up to around 20 ms^{-2} which means it should contain no delicate or moving parts. Measurement resolution should be around 1 point per 50 µm, with the position of a fitted surface correct to around 30 µm, although the repeatability of individual points can be considerably larger. Measurement should be possible with little user input.

Fringe projection offers the opportunity to measure an imaged area in a small number of images. Assuming a 1000 by 1000 pixel camera, phase shifting and temporal unwrapping of million points requires approximately 30 images (depending on the algorithms used) [52,53]. The same measurement would require 1000 images using a line scan probe. The shorter data collection time is expected to compensate for the more complex processing requirements of fringe projection data. To automatically calculate the phase from fringe images of complex objects phase shifting is the most widely used technique. To get an absolute measurement the 2π ambiguity must also be resolved automatically. The phase shift is provided either by a relative motion of a light source and grating, or using a programmable digital projector. If a grating and light source are relatively moved, a precisely calibrated translation device must be used, which is unlikely to be light-weight or robust enough for the CMM probe. A programmable projector can also be used to project different patterns to resolve the 2π ambiguity. A standard video projector is too large and heavy to be attached to the CMM. Miniature projectors have recently become available [54]. A miniature projector could be within the size and weight, but those currently available do not have the resolution for our requirements and do not provide enough illumination. It will be shown in Chapter 4 that the stability characteristics and warm-up time are not ideal for the application, and furthermore it is not certain that a mini-projector could withstand the accelerations exerted on the probe. A final disadvantage is the cost of the mini-projector.

It is proposed here to create a probe consisting of a camera and very simple fringe projector that projects only a single pattern. The CMM will be used to move the whole probe to provide a phase shift (Chapter 5). The motion of the camera must be compensated for so that the phase recorded can be calculated and transformed to the 3D location of each surface point imaged. The phase shift caused is dependent on the

distance between the object and the probe. Edges, corners, and any other identifiable features can be measured using photogrammetric techniques. The 2π ambiguity is resolved either using these measured features or by measuring surfaces using fringe projection from multiple perspectives, using the CMM to reorient the probe to the required viewpoints (Chapter 6). A prototype probe for a CMM is demonstrated in Chapter 7.

Chapter 3 Mathematical framework

3.1 Introduction

In order to develop the new techniques a mathematical framework is required. In this chapter the theory of photogrammetry will be reviewed and applied to fringe projection systems, leading to a more general model for fringe projection than is normally seen in the standard literature. The phase step algorithms that are used for the later experimental work will be discussed in more detail, and the techniques usually used to resolve 2π ambiguity are described. A number of shape measurement systems making use of more than camera or projector (or both) are described. The chapter concludes with a discussion of speckle theory, which is not normally a consideration for white light projection systems, but is significant for the phase shift techniques developed later.

3.2 Camera model

3.2.1 Central perspective projection

A camera can be modelled using the pinhole or central perspective projection model [37], Figure 8.

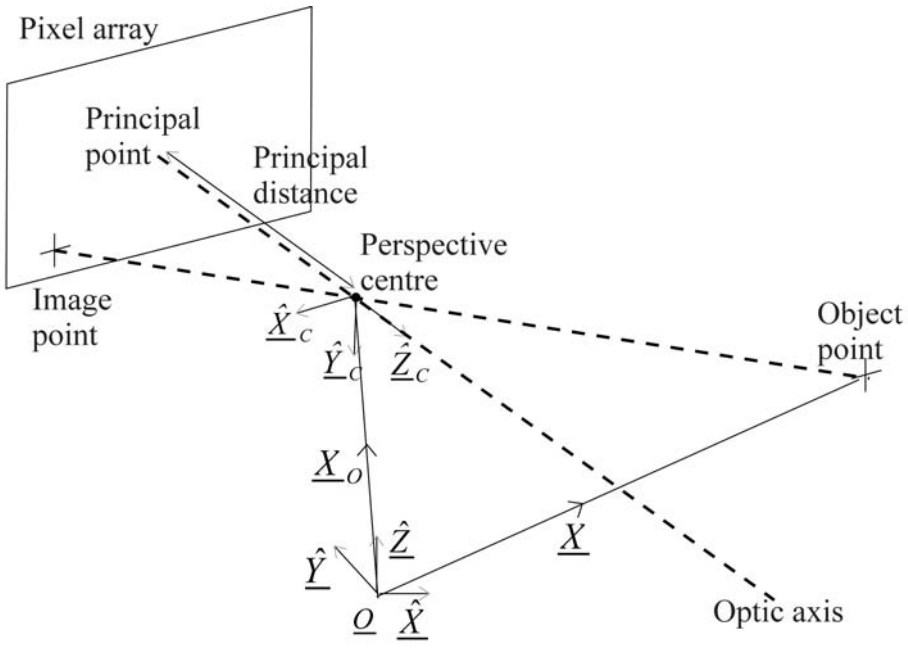

Figure 8: The "pinhole" or central perspective projection model.

The model consists of a bounded plane, the image plane, and a "pinhole" or perspective centre through which light is considered to pass in a straight line. The principal distance is the distance between the perspective centre and the image plane along the optic axis, and the intersection of the optic axis and the image plane defines the principal point. The image plane is normal to the optic axis.

Let $\underline{X} = (X, Y, Z)^T$ be a 3D object point in global coordinates. The camera's perspective centre is at $\underline{X}_O$. Its optic axis and pixel array define a secondary coordinate system denoted $(\hat{\underline{X}}_C, \hat{\underline{Y}}_C, \hat{\underline{Z}}_C)$. A point $\underline{X}$ in the global coordinate system is referred to in camera coordinates as $\underline{X}_C = (X_C, Y_C, Z_C)^T$, where

$$\underline{X}_C = R_C(\underline{X} - \underline{X}_O), \tag{1}$$

and R_C is the matrix representation of the rotation between the global and camera coordinate system. This point is imaged by the camera at

$$\underline{x}_C = \begin{pmatrix} x_C \\ y_C \\ -c \end{pmatrix} = -\frac{c}{Z_C}\underline{X}_C = -\frac{c}{\hat{\underline{Z}}_C.(\underline{X} - \underline{X}_O)} R_C(\underline{X} - \underline{X}_O) \tag{2}$$

in camera coordinates, where c is the camera's principal distance.

3.2.2 Conversion to image plane coordinates

The ideal central perspective model must be extended to take into account the internal parameters of the camera. The image plane of a digital camera is implemented as an array of pixels and the pinhole is normally a simplification of an imaging system comprising a multi-element lens. The internal parameters of the camera include lens distortions and the position, orientation and size of the pixels in the pixel array. In practice, the internal parameters are found by calibration (Chapter 4).

Light is focussed onto the pixel array using a system of lenses, often having a variable focus setting. The lenses are affected by optical aberrations and misalignment errors due to manufacturing procedures [55,56], both of which result in image distortion. A commonly used model splits the image distortion into radial and decentring components [57] as described below. The position of the principal point on the image plane defines the centre of the radial distortion. The distortion coefficients should be found for each

focus setting used, and so a separate calibration is carried out each time the focus setting is changed. The distortion coefficients vary within the depth of field. This is normally neglected but can be relevant for very close range photogrammetry [58]. The variation of lens distortion for the lenses used here is investigated experimentally in section 4.3.2.

Let $\underline{x}_C^{(n)} = \left(x_C^{(n)}, y_C^{(n)}, 1\right)^T$ be the projection of a point in the camera's coordinate system, normalised with respect to the principal distance. From the pinhole model

$$\underline{x}_C^{(n)} = \left(-\frac{x_C}{c}, -\frac{y_C}{c}, 1\right) = \left(\frac{X_C}{Z_C}, \frac{Y_C}{Z_C}, 1\right) \tag{3}$$

Radial lens distortion produces a displacement of the image point of $\underline{\Delta x}_r = \left(\Delta x_r, \Delta y_r\right)^T$, where

$$\Delta x_r = x_C^{(n)}\left(k_1 r^2 + k_2 r^4 + k_3 r^6 + \ldots\right) \tag{4}$$

and

$$\Delta y_r = y_C^{(n)}\left(k_1 r^2 + k_2 r^4 + k_3 r^6 + \ldots\right) \tag{5}$$

where $r^2 = x_C^{(n)2} + y_C^{(n)2}$. Decentring distortion introduces a radial and tangential distortion $\underline{\Delta x}_d = \left(\Delta x_d, \Delta y_d\right)^T$ where

$$\Delta x_d = p_2\left(r^2 + 2x_C^{(n)2}\right) + 2p_1 x_C^{(n)} y_C^{(n)} \tag{6}$$

and

$$\Delta y_d = p_1\left(r^2 + 2y_C^{(n)2}\right) + 2p_2 x_C^{(n)} y_C^{(n)} \tag{7}$$

In these expressions k_1, k_2, k_3, ... and p_1 and p_2 are the coefficients of distortion that must be found by a calibration process.

The distorted image coordinates are defined as $\underline{x}_C^{(d)} = \left(x_C^{(d)}, y_C^{(d)}\right)^T$ where

$$x_C^{(d)} = x_C^{(n)} + \Delta x_r + \Delta x_d \tag{8}$$

and

$$y_C^{(d)} = x_C^{(n)} + \Delta y_r + \Delta y_d \tag{9}$$

The distorted points are converted to image plane coordinates.

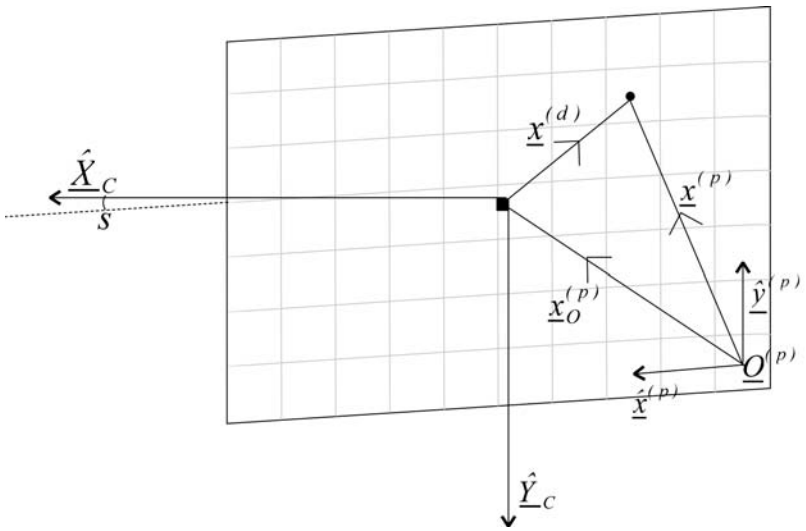

Figure 9: Image plane coordinates.

The image plane of a camera is depicted in Figure 9. The vector $\underline{x}^{(p)} = \left(x^{(p)}, y^{(p)}\right)^T$ is the position of the distorted projection of point $\underline{X}$ in the image coordinate system defined by unit vectors $\left(\hat{\underline{x}}^{(p)}, \hat{\underline{y}}^{(p)}\right)$ and with the origin $\underline{O}^{(p)}$ at the centre of the bottom right pixel as indicated. The pixel dimensions in the horizontal and vertical directions are not necessarily equal. Any non-orthogonality in the pixel axes is represented by angle *s*. The principal point is at $\underline{x}_O^{(p)} = \left(x_O^{(p)}, y_O^{(p)}\right)^T$ in the image coordinate system.

The transformation from the orthogonal camera coordinate system with axes $\left(\hat{\underline{X}}, \hat{\underline{Y}}\right)$ to the non-orthogonal image plane coordinate system is described by the camera matrix *K*, where

$$K = \begin{bmatrix} c_x^{(p)} & sc_x^{(p)} & x_O^{(p)} \\ 0 & -c_y^{(p)} & y_O^{(p)} \\ 0 & 0 & 1 \end{bmatrix} \tag{10}$$

where, $c_x^{(p)}$ and $c_y^{(p)}$ are the principal distance in units of pixel size in the $\hat{\underline{x}}^{(p)}$ and $\hat{\underline{y}}^{(p)}$ directions respectively. The camera matrix is applied to the distorted normalised point as defined above and converts from normalised units (or principal distances) to pixels. The projected point in image coordinates is given by

$$x^{(p)} = c_x^{(p)}\left(x^{(d)} + sy^{(d)}\right) + x_O^{(p)} \tag{11}$$

and

$$y^{(p)} = -c_y^{(p)} y^{(d)} + y_O^{(p)} \tag{12}$$

For many cameras the pixels are square to a high degree of accuracy and array is well-aligned, so the difference in scale and the non-orthogonality may be ignored. Then the camera matrix simplifies to

$$K = \begin{bmatrix} c^{(p)} & 0 & x_O^{(p)} \\ 0 & -c^{(p)} & y_O^{(p)} \\ 0 & 0 & 1 \end{bmatrix} \tag{13}$$

where $c^{(p)}$ is the principal distance in pixels.

3.3 Photogrammetric measurement

If a corresponding point can be identified in the image planes of two or more calibrated cameras, a measurement of the point can be made using an intersection procedure (section 3.3.2), or a more complex process called bundle adjustment (section 3.3.3). Both of these require the positions and orientations of the cameras to be known (at least to a good approximation). The camera positions and orientations are found using resection, which will now be described. These procedures are all well-known within the field of photogrammetry [37].

3.3.1 Resection

Consider an object point $\underline{X}$, known relative to the global origin, imaged by a single camera in an unknown position. Equation (2) can be rewritten for a single camera as

$$\underline{x}_C = \mu^{-1} R_C \left(\underline{X} - \underline{X}_O \right) \tag{14}$$

where $\mu = -\frac{Z}{c} = -\frac{\hat{Z}_C . \left(\underline{X} - \underline{X}_O \right)}{c}$ is the camera magnification (dependent on the distance between the 3D point and camera), and as before R_C is the matrix representation of the camera's orientation to the global coordinate system, $\underline{X}_O$ is its perspective centre and $\underline{X}$ is the object point expressed in global coordinates.

Rearranging equation (14) gives

$$\underline{X} = \underline{X}_O - \mu R^{-1} \underline{x} \tag{15}$$

Equation (15) represents three equations in six unknown variables if the camera's internal parameters are known. Otherwise, as is often the case, the camera is

uncalibrated, the magnification is not known and there are seven unknown variables: three representing the position of the camera; three for its orientation; also the unknown magnification μ. The other internal parameters are neglected.

Three known measurement points results in a system of nine equations in seven unknowns, which can therefore be solved. The equations are non-linear so cannot be solved directly. They are linearised using Taylor's Theorem and solved iteratively in a least squares sense. The magnification μ varies with the camera position and the principal distance so it is recalculated each iteration using the current estimates of the other unknown variables.

The basic resection procedure described above can be extended to use unknown object points to find the position and orientation of the cameras relative to one another. Consider the case of having a set of M unknown 3D points $\underline{X}_j, j = 1,2,...M$ viewed from a set of N calibrated cameras in unknown positions and orientations. The image of each point gives N sets of $2M$ equations, each equivalent to equation (15), with $6N$ unknown parameters. Using one of the N sets to eliminate the unknown positions of the 3D points leaves $2M(N-1)$ equations of the form:

$$\underline{X}_{O1} - \mu_{j1} R_1^{-1} \underline{x}_{j1} = \underline{X}_{Oi} - \mu_{ji} R_i^{-1} \underline{x}_{ji}, i = 2,\ldots N, j = 1,\ldots M \qquad (16)$$

The $6N$ unknown variables representing position and orientation for each camera can clearly be found if $M \geq \frac{3N}{N+1}$. Therefore for two cameras the images of six corresponding points are sufficient to find the camera positions and orientations relative to each other. For a system of three or more cameras three points are sufficient.

3.3.2 Intersection

If two or more cameras are in known positions and orientations (at least relative to each other), and a point can be identified in their image planes as corresponding to the same object point, then the position of the object point can be calculated.

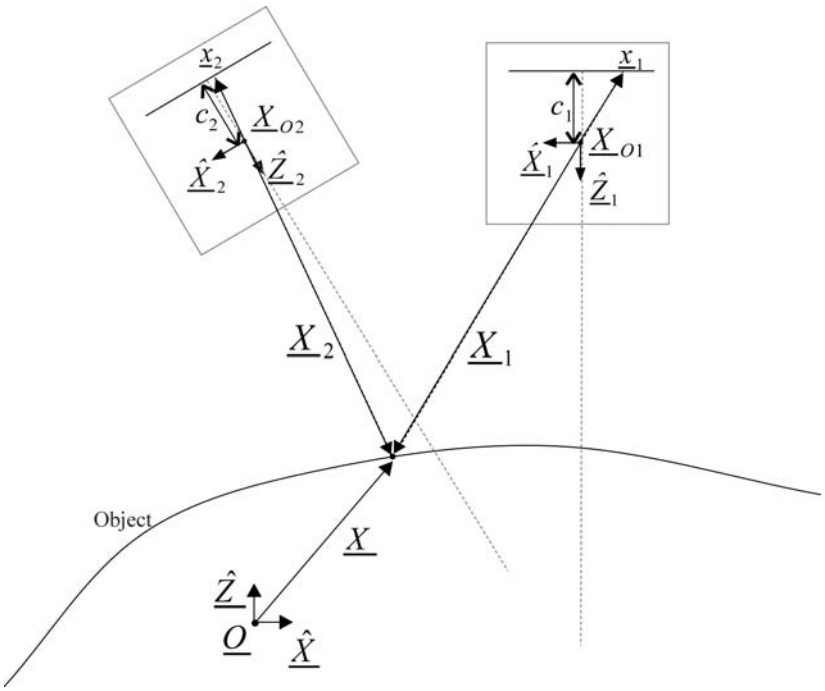

Figure 10: 3D measurement using the pinhole model.

Consider a system of N cameras, where N>1, each modelled using the central perspective projection model, viewing an object. For example, a system with N=2 is shown in Figure 10. Each camera *i* has its perspective centre at $\underline{X}_{Oi}$ relative to the global origin, for *i* = 1,...N. Point $\underline{X}$ is imaged by each camera *i* at $\underline{x}_i$ in the coordinate system of camera *i* (in undistorted image coordinates). The coordinates of $\underline{X}$ can be calculated by finding the intersection of the straight lines through $\underline{x}_i$ and $\underline{X}_{Oi}$ for each camera *i*. Due to noise, digitisation error and any calibration errors the straight lines through $\underline{x}_i$ and $\underline{X}_{Oi}$ may not intersect at a unique point, so an averaging procedure is used in general. Using more cameras gives a greater confidence in the resulting measured point.

Mathematically, intersection is expressed using a set of simultaneous equations. For each camera *i*, the point $\underline{X}$ is imaged at $\underline{x}_i = (x_i, y_i, -c_i)^T$ relative to the perspective centre, where

$$x_i = -c_i \frac{\hat{\underline{X}}_i . (\underline{X} - \underline{X}_{Oi})}{\hat{\underline{Z}}_i . (\underline{X} - \underline{X}_{Oi})} \tag{17}$$

and

$$y_i = -c_i \frac{\hat{\underline{Y}}_i.(\underline{X} - \underline{X}_{Oi})}{\hat{\underline{Z}}_i.(\underline{X} - \underline{X}_{Oi})} \tag{18}$$

Equations (17) and (18) are known as collinearity equations. They are two equations in three unknowns for each camera *i*. Given two or more cameras imaging the same point $\underline{X}$ the set of equations may be solved for $\underline{X}$ in a least squares estimation to give the 3D position of the object point.

3.3.3 Bundle adjustment

A "bundle adjustment" calculates the positions of a set of object points simultaneously. For a set of points identified as corresponding in two or more images, initial estimates of the 3D points are calculated. "Bundles" of light rays from the estimated object points are considered to be projected through the camera perspective centres. The difference between the set of re-projected points and the identified image points defines the re-projection error. The estimated 3D coordinates are simultaneously "adjusted" iteratively such that the re-projection error is minimised in a least squares sense [59].

The collinearity equations (equations (17) and (18) above) have at least one extra degree of freedom – for two cameras viewing a single point they represent four equations with three unknown parameters. More than two cameras or more than one imaged point clearly gives greater redundancy. The extra degrees of freedom are often used in photogrammetry for self-calibrating measurement. Some or all of the camera parameters, both interior and exterior, may be found simultaneously with the 3D coordinates of the object points. It is frequently claimed in the photogrammetry literature [37] that optimising the camera positions and orientations simultaneously with the object points gives higher quality results. However, simultaneous calibration and measurement is not consistent with metrology industry standards [11]. Within the work reported here the bundle adjustment technique has therefore been used to find only the object points.

The advantage (other than the possible refinement of calibration parameters) of using a bundle adjustment over a simple intersection is that there is no requirement to invert the transformation from object to image coordinates. The intersection described in section 3.3.2 relies on being able to transform from image to object coordinates. This inverse transformation is necessarily an approximation, because the form of the lens distortion

model makes the object-to-image transformation non-invertible analytically. The bundle adjustment in theory allows only the forward transformation from object to camera image plane to be used in the calculation. For this reason a bundle adjustment can theoretically give more accurate results. Note, however, that the code used within this project in fact undistorts the images at the outset and then carries out the bundle adjustment using undistorted coordinates, thus losing the advantage. This could be reworked to gain better accuracy in future if required.

3.3.4 Point correspondence

Photogrammetric measurement relies on being able to identify image points corresponding to the same points on an object in multiple images. The commercial systems discussed in section 2.4.6 use uniquely identifiable target features attached to the surface of the object. An alternative is to project a structured light pattern such as an array of dots [40] to identify corresponding points. To find matching features without using cooperative targets is a difficult task, and much research is ongoing. Epipolar matching is one approach that uses the geometry of the system of cameras. As has been shown, the 3D point viewed by a particular image point must lie on the straight line through that point and the camera perspective centre. The projection of that line in a second camera is known as the epipolar line and must contain the image point corresponding to the same 3D point. Therefore the search for a corresponding point is reduced to a search along a line rather than across the whole image plane. If a three perspectives are used, a corresponding point pair in two images can be verified simply by finding the intersection of the epipolar lines corresponding to the point pair in the third image [60]. Due to noise and any errors within the system a corresponding points will never lie exactly on the epipolar line in practice, but rather within some small area close to it. Epipolar matching is combined with many techniques such as least-squares matching [61], statistical techniques [62] and a variety of other sophisticated algorithms [63,64] to find corresponding point sets in the presence of noise and occlusion. Matching algorithms for lines and curves using continuity properties, curvature constraints and correlation techniques have been developed and demonstrated [65,66,67]. Robust, reliable identification of corresponding points remains a difficult task, and the best choice of algorithm is application dependent.

3.4 Fringe projection

The basic fringe projection system consists of one camera and one projector. In the standard fringe analysis literature the system is normally modelled making certain assumptions. The optic axes of camera and projector are normally assumed coplanar, and it is often assumed that the projector is horizontally displaced relative to the camera. Often a large standoff, or telecentric, approximation is used for at least one of the camera or projector. That is, it is often assumed that the camera magnification is constant throughout the measurement volume or that the fringes are collimated. More general models [68,69] or calibration techniques [70] have been considered by a few authors to account for the inaccuracies introduced by such simplifications. Here, a generalised model is developed based on the framework used in photogrammetry described above. Like the camera, the projector is modelled using the central perspective projection model. There are no restrictions on the location of the camera and projector (except that obviously they must have an overlapping field of view). The model can be easily extended to systems consisting of multiple cameras and projectors, or equivalently to a system with a single fringe projection probe that is moved to different positions. A simplified version of the general model, using the coplanar optic axes assumption, is also introduced for convenience later to calculate nominal characteristics of an experimental system.

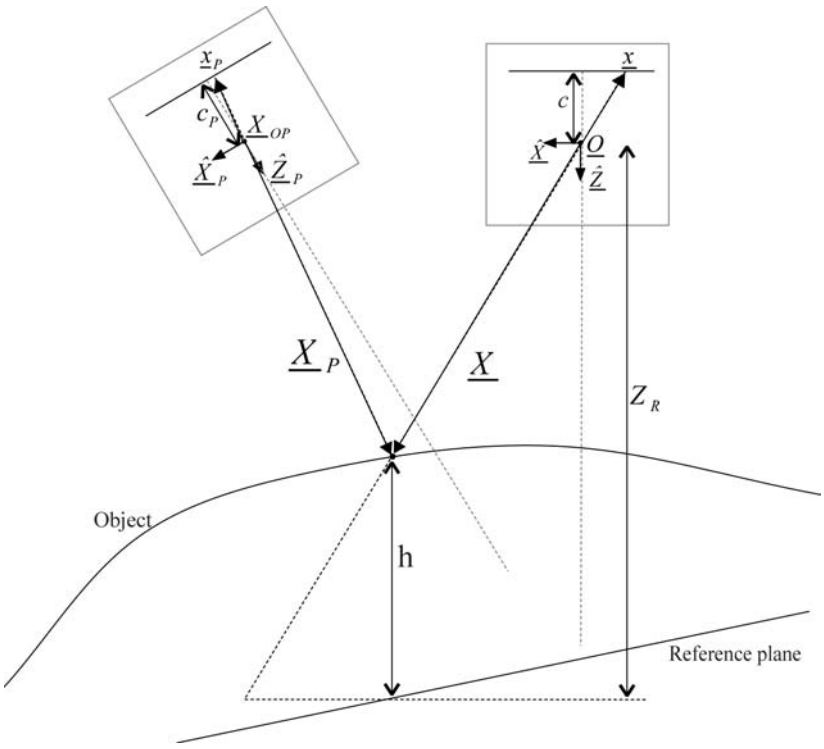

Figure 11: Fringe projection system.

Consider the system depicted in Figure 11, consisting of a camera, a projector and an object. Neglecting lens distortions and air refractive index variations, a light ray travels in a straight line from a point in the projection plane through the projector's perspective centre to a point on the object. A ray of light scattered from that point on the object passes in a straight line through the camera's perspective centre to intersect with the camera image plane. For simplicity the global coordinate system $\left(\underline{\hat{X}}, \underline{\hat{Y}}, \underline{\hat{Z}}\right)$ is defined by the camera axes and the origin is at the camera perspective centre. The projector's perspective centre is at $\underline{X}_{OP} = \left(X_{OP}, Y_{op}, Z_{OP}\right)^T$ relative to the origin, and the projector axes define a secondary coordinate system, called the projector coordinate system and denoted $\left(\underline{\hat{X}}_P, \underline{\hat{Y}}_P, \underline{\hat{Z}}_P\right)$. A point $\underline{X}$ in the global or camera coordinate system is referred to in projector coordinates as $\underline{X}_P$, where $\underline{X} = R\underline{X}_P + \underline{X}_{OP}$, and R is the matrix representation of the rotation between the two sets of axes. In the diagram the camera and projector coordinate systems have parallel $\underline{\hat{Y}}$-axes, however this is not a requirement in practice.

The projection of a point $\underline{X}_P = \left(X_P, Y_P, Z_P\right)^T$ onto the projection plane is $\underline{x}_p$, where

$$\underline{x}_p = -\frac{c_p}{Z_P}\underline{X}_P = \begin{bmatrix} x_P \\ y_P \\ -c_p \end{bmatrix} \tag{19}$$

Without loss of generality, assume that the projector produces fringes extending in the $\underline{\hat{Y}}_P$ direction with period p mm at the projection plane; so the phase at point $\underline{x}_P$ is given by $\frac{2\pi x_P}{p}$. The phase at the point $\underline{X}_P$ due to the projected fringes is

$$\phi\left(\underline{X}_P\right) = -\frac{2\pi c_p}{p}\frac{X_P}{Z_P} \tag{20}$$

and the period of the fringes at this point is $\frac{Z_P p}{c_P}$ mm.

Substituting for X_P and Z_P gives an expression for phase ϕ at any point $\underline{X}$ in the camera coordinate system.

$$\phi(X,Y,Z) = -\frac{2\pi c_p}{p}\frac{\hat{\underline{X}}_P \cdot \left(\underline{X} - \underline{X}_{OP}\right)}{\hat{\underline{Z}}_P \cdot \left(\underline{X} - \underline{X}_{OP}\right)} \tag{21}$$

The point $\underline{X} = (X,Y,Z)^T$ is imaged by the camera at $\underline{x}$, where

$$\underline{x} = -\frac{c}{Z}\underline{X} = \begin{bmatrix} x \\ y \\ -c \end{bmatrix} \tag{22}$$

where, again, c is the camera's principal distance. Substituting into the expression for ϕ gives

$$\phi(\underline{x},Z) = -\frac{2\pi c_p}{p}\frac{\hat{\underline{X}}_P \cdot \left(Z\underline{x} + c\underline{X}_{OP}\right)}{\hat{\underline{Z}}_P \cdot \left(Z\underline{x} + c\underline{X}_{OP}\right)} \tag{23}$$

This is an expression for the phase recorded at a point on the camera image plane expressed in terms of the coordinates of the point and the distance of the corresponding object point from the camera along the camera's optical axis.

In keeping with the standard fringe analysis literature a reference plane is introduced at a distance Z_R from the camera. (Note that the reference plane need not be normal to the optic axis of the camera, and so Z_R may vary for each point in the image plane. In fact, in general, the "plane" can be any known reference surface.) The phase recorded at the camera image plane point viewing an object point with height h above this reference plane is given by

$$\begin{aligned} \phi(\underline{x},h) &= -\frac{2\pi c_p}{p}\frac{\hat{\underline{X}}_P \cdot \left((Z_R - h)\underline{x} + c\underline{X}_{OP}\right)}{\hat{\underline{Z}}_P \cdot \left((Z_R - h)\underline{x} + c\underline{X}_{OP}\right)} \\ &= -\frac{2\pi c_p}{p}\frac{\hat{\underline{X}}_P \cdot \left(Z_R\underline{x} + c\underline{X}_{OP}\right) - \hat{\underline{X}}_P \cdot \underline{x}h}{\hat{\underline{Z}}_P \cdot \left(Z_R\underline{x} + c\underline{X}_{OP}\right) - \hat{\underline{Z}}_P \cdot \underline{x}h} \end{aligned} \tag{24}$$

Therefore, for a given point on the image plane the relationship between the phase recorded and the height of the point viewed may be expressed as

$$\phi(h) = \frac{a + bh}{c + h} \tag{25}$$

where a, b, and c depend upon the image plane coordinate and the system parameters. The parameters may be found for each pixel in the camera image plane via a calibration process. Considering the phase recorded for the same point when the reference plane is in place gives

$$\Phi(h) = \phi(h) - \phi(0) = \frac{a'h}{b'+c'h} \tag{26}$$

where the constants a', b' and c' again depend only upon the system parameters and the image coordinates. Inverting this expression gives the object height in terms of phase of the form

$$h = \frac{A\Phi}{B+\Phi} \tag{27}$$

where A and B depend on the image point $\underline{x}$ and the system parameters Z_R, R, $\underline{X}_{OP}$, p, c and c_P. This expression is of the form found elsewhere in the literature [26, 71].

The above discussion has neglected lens distortions for both the camera and projector. Procedures to explicitly calibrate a fringe projection system are known [72,73]. However an implicit calibration procedure has been shown to be successful [69,70], and is used for phase to height calibration here. The camera is first calibrated. A phase to height calibration is then carried out by measuring a plane at different distances from the camera and a function fitted for each camera pixel relating the recorded phase to the camera-plane distance (relative to the reference plane). In this way, the projector lens distortions and other internal parameters are implicitly accounted for within the phase to height fitted function. This is discussed in more detail with experimental results in section 4.3.8.

3.4.1 Simplified fringe projection system model

In order to aid the physical understanding of the fringe projection systems, and particularly the new phase shift techniques developed in Chapter 5, it can be convenient to consider a simplified system. The simplified model is shown in Figure 12. The camera and projector optic axes are coplanar (as is frequently assumed by other authors). The $\underline{\hat{Y}}$ and $\underline{\hat{Y}}_P$ axes are chosen to be parallel with the fringes extending in this direction. (The camera axis system here is not necessarily identical to the coordinate system defined by the pixels in the image plane in practice; a rotation about the optic axis may be required. For clarity this will be ignored here). This simplifying assumption of coplanar optic axes is likely to be at least nominally true in a practical system due to the requirement for overlapping field of view of camera and projector.

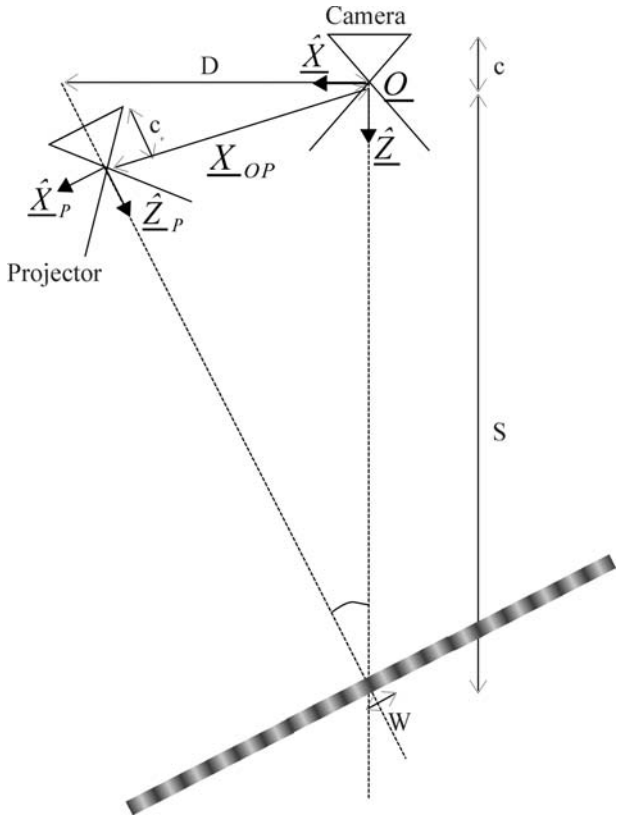

Figure 12: Simplified fringe projection model.

The distance from the camera to the intersection point of the optic axes is defined to be the standoff distance, denoted *S*. The camera $\hat{X}$ axis intersects the projector optic axis (the $\hat{Z}_P$ axis) a distance *D* from the camera pinhole. Then the projector coordinate system is described in camera coordinates by the unit vectors $\hat{X}_P = \frac{(S,0,D)'}{\sqrt{D^2+S^2}}$ and $\hat{Z}_P = \frac{(-D,0,S)'}{\sqrt{D^2+S^2}}$. The fringe pitch at the axis intersection point is

$$W = \frac{p}{c_P}\frac{X_{OP}}{D}\sqrt{S^2+D^2} \tag{28}$$

and the phase at any other point is given by

$$\phi(X,Y,Z) = \frac{2\pi}{W}\frac{X_{OP}}{D}\sqrt{S^2+D^2}\,\frac{S(X-X_{OP})+D(Z-Z_{OP})}{S(Z-Z_{OP})-D(X-X_{OP})} \tag{29}$$

Then the phase recorded at a pixel *x* on the camera image plane is given by

$$\phi(x,Z) = \frac{2\pi}{W}\frac{X_{OP}}{D}\sqrt{S^2+D^2}\,\frac{(Sx+Dc)Z-c(SX_{OP}+DZ_{OP})}{(Sc-Dx)Z+c(DX_{OP}-SZ_{OP})} \tag{30}$$

To help predict the nominal characteristics of the system and limits of the new techniques without specifying the dimensions of the fringe projection system it is convenient to work in normalized units of "standoff distances". Then the phase incident on point $\underline{X} = (X, Y, Z)^T$ may be expressed as

$$\phi(X,Y,Z) = \frac{2\pi}{W}\frac{X_{OP}}{D}\sqrt{1+D^2}\,\frac{X - X_{OP} + D(Z - Z_{OP})}{Z - Z_{OP} - D(X - X_{OP})} \tag{31}$$

where each quantity is expressed as a fraction of the standoff distance *S*.

3.5 Phase calculation

The camera records the intensity of the scattered fringe pattern. The height of an imaged point is related to the phase of the fringe pattern incident on that point. There are a number of ways to calculate the phase from the recorded intensity including Fourier transform [74], wavelet transform [75], Hilbert transform [76], and phase shifting [77] methods. Of particular interest here are phase shift (or phase step) methods as they have been shown to be successful for automatic measurements of objects with edges or isolated surfaces. The other methods listed all suffer from problems with edges and/or high gradients or require careful choice of parameters dependent on the images [78].

There are many different phase step algorithms that can be used, each with different strengths and weaknesses. The best choice of algorithm depends on the experimental system in use and the major error sources affecting the projection and phase step technique. For example, fringes can be created by illuminating a grating or amplitude mask, where the phase shift is created by mounting either the light source or the mask on a translating device such as a piezo-electric translator (PZT). The translator must be very well calibrated, taking hysteresis into account, in order to get sufficiently accurate phase shifts for many of the phase shift algorithms to be successful. Some phase shift algorithms are immune to linear miscalibration effects, but non-linear phase shift error can be a significant source of error [27]. Video projectors provide an alternative method of projecting fringes, and can easily be programmed to project phase shifted patterns. Then the phase shift can be very precisely chosen. However the non-linear response of the LCD or LCOS display can create problems. A gamma calibration must be carried out to account for this [31,79]. The digitisation of the projector may also

cause some error; this can be reduced, at the expense of fringe contrast, by using the projector slightly out of focus.

In Chapter 5, techniques to create phase shifted fringes by moving the fringe projector and the camera relative to the object are investigated. The fringe projector projects only a single pattern and contains no moving parts or complex electronics. The size of the phase shift created by the relative motion is unknown and varies with the object position. Therefore the phase shift algorithm used to calculate the phase must be one that gives accurate results over a range of phase steps. Possible error sources applicable in this case include non-linear phase shift error, change in recorded intensity between phase shifted images, and noise due to surface roughness.

The phase step algorithms used throughout the experimental sections are described in section 3.5.1, below. These algorithms return the phase modulo 2π, referred to as wrapped phase. The phase must be unwrapped to be continuous over each patch corresponding to a continuous surface on the object. Furthermore, the unwrapped phase is correct only up to some unknown additive integer multiple of 2π radians. This is a common problem with fringe projection systems (and other structured light measurement systems in which a repetitive pattern is projected). Many authors consider the phase unwrapping and 2π ambiguity resolution as a single operation, since, if one can find the correct absolute phase for each pixel, the phase map is correctly unwrapped. However for the techniques developed later it is convenient to consider phase unwrapping and 2π ambiguity resolution separately; known techniques are discussed in sections 3.5.2 and 3.5.3, respectively.

3.5.1 Phase step algorithms

The recorded intensity of a camera pixel at $\underline{x} = (x, y)$ in the i^{th} phase stepped image is given by

$$I_i(\underline{x}) = A(\underline{x}) + B(\underline{x}) cos\left(\phi(\underline{x}) + \left(i - \frac{(N+1)}{2} \right) \alpha(\underline{x}) \right), i = 1,..N \qquad (32)$$

where A and B represent background intensity and modulation amplitude of the sinusoid recorded by pixel $\underline{x}$ and α is the phase step between each of the N images. In contrast with most previous work, the variation of phase shift with image coordinate is

explicitly included because in the new phase step techniques described in Chapter 5 the phase shift is unknown and varies throughout the measurement volume.

For the case of a set of N images with a constant phase shift of $\frac{2\pi}{N}$ radians between each, the phase can be calculated from

$$tan\left(\phi(\underline{x})+\frac{\pi}{2}-\frac{N+1}{2}\alpha\right)=\frac{\sum_i I_i(\underline{x})sin\left(i\frac{2\pi}{N}\right)}{\sum_i I_i(\underline{x})cos\left(i\frac{2\pi}{N}\right)} \tag{33}$$

This algorithm was introduced by Bruning et al. [80] and has been used and analysed by many other authors. The minimum number of images is 3. For a set of 4 images the expression reduces to

$$tan\left(\phi(\underline{x})-\frac{3\pi}{4}\right)=\frac{I_4-I_2}{I_1-I_3} \tag{34}$$

It has been shown that using a greater number of images or extending the number of samples beyond a single period can reduce susceptibility to noise, higher harmonics in the projected fringes, linear phase shift errors and non-linear detector errors [81,27]. Many other algorithms also require an arctangent of a fraction of linear combinations of phase shifted images [82]. Note that the form used here is slightly different to that given by most other authors. This form is used so that the phase calculated by this algorithm is exactly equal (apart from noise and error sources) to the phase calculated by other phase shift algorithms described below.

For sets of images with unknown phase shifts (possibly varying with image coordinate) a number of different algorithms exist. Carré's algorithm [83] is a well known algorithm for a set of four images. The phase is calculated from

$$tan\phi=\frac{\sqrt{(a_{14}+a_{23})(3a_{23}-a_{14})}}{b_{23}-b_{14}} \tag{35}$$

where

$$a_{ij}=I_i-I_j \tag{36}$$

and

$$b_{ij} = I_i + I_j \tag{37}$$

The phase shift, α, may be calculated from

$$tan(2\alpha) = \sqrt{\frac{3a_{23} - a_{14}}{a_{23} + a_{14}}} \tag{38}$$

Novak, Novak and Miks [84] give a number of algorithms for calculating phase from phase stepped images with unknown step for sets of 5, 6 and 7 images. For example for a set of 7 images it is possible to calculate the phase shift α from any of the following:

$$cos(2\alpha) = \frac{a_{17} - a_{35}}{2a_{35}} \tag{39}$$

$$cos\,\alpha = \frac{a_{17} + a_{35}}{2a_{26}} \tag{40}$$

$$cos\,\alpha = \frac{b_{35} - b_{17}}{2(b_{26} - 2I_4)} \tag{41}$$

$$cos(2\alpha) = \frac{b_{17} + b_{35} - 2b_{26}}{2(b_{35} - 2I_4)} \tag{42}$$

$$cos\,\alpha = \frac{a_{26}}{2a_{35}} \tag{43}$$

Once the phase shift has been found, the phase can be calculated using any of the following:

$$tan\,\phi = tan\,\alpha\,\frac{2a_{26} - a_{17} - a_{35}}{b_{17} - b_{35} - 2(b_{26} - 2I_4)} \tag{44}$$

$$tan\,\phi = \frac{1}{sin\,\alpha}\,\frac{a_{17} - 3a_{35}}{2(b_{26} - 2I_4)} \tag{45}$$

$$tan\,\phi = \frac{sin\,\alpha}{cos\,\alpha + 1}\,\frac{2a_{26} + a_{17} + a_{35}}{b_{35} - b_{17}} \tag{46}$$

$$tan\,\phi = sin\,\alpha\,\frac{2a_{35}}{2I_4 - b_{26}} \tag{47}$$

$$\tan\phi = \frac{1}{\sin(2\alpha)} \frac{a_{17} + a_{35} - 2a_{26}}{2(b_{35} - 2I_4)} \tag{48}$$

$$\tan\phi = \tan\alpha \frac{a_{17} + a_{35}}{b_{35} - b_{17}} \tag{49}$$

Like the Bruning and Carré algorithms these can all be algebraically derived from equation (32) using trigonometric identities. The different phase shift algorithms respond differently to error sources such as non-linear phase shift error or noise. A stable algorithm will have low error in the calculated phase for a large range of phase shift values. Novak et al. analysed the response of the most stable of these algorithms and compared them to similar five and six frame algorithms as well as Carré's algorithm [84]. They showed that it is generally possible to achieve better accuracy in the presence of noise and other common error sources by using a greater number of frames, although this is not true of all of their derived algorithms. More recently, Magalheas et al. developed a generalised framework for deriving similar algorithms for an arbitrary number of frames and gave specific algorithms up to 15 frames [85]. Again, they showed that it is possible to achieve better results with algorithms using more images. Clearly the processing and memory requirements increase with the number of frames, as does the data collection time. To choose the most appropriate algorithm requires an understanding of the sources of error and the requirements and limitations of the measurement system.

Unfortunately, all of these algorithms have values for which they are either invalid or unstable. This can be due to any of a square root of a negative number, division by a number very close to zero, or an inverse sine or cosine of a number larger than 1, all of which can occur with noisy images or phase shift errors. It is shown in section 4.3.6 that there are advantages to be gained by combining the results from different algorithms.

3.5.2 Phase unwrapping

Phase shifting calculates the phase within a range of 2π radians only, known as wrapped phase. The phase must be unwrapped to remove the discontinuities caused by the limited range of the algorithm calculation. The simplest way to do this is to add an integer multiple of 2π to phase on one side of a discontinuity until the phase is

continuous up to steps of π radians. Different algorithms of varying complexity are available to do this. The simplest techniques simply unwrap along single rows or columns within an image, and stop whenever an invalid phase value is reached. Flood fill algorithms integrate the phase gradient over an area of the image. The integration path is chosen in some predefined manner, such as spiralling out from a set start point. The unwrapping can continue around invalid pixels until the boundaries of the area are reached. If edges or steps exist that have not been detected then the result can be path dependent. Noise can cause errors. Refinements to the technique involve choosing the path according to some measure of confidence (reliability guided unwrapping) [86], or placing unwrapping barriers, known as branch cuts, across noisy or suspect areas so that all allowed unwrapping paths achieve the same result [87]. Alternatives include least-squares or more generally L^P-norm methods [88], often called global techniques, based on minimising a function across the whole phase map [89]. Temporal phase unwrapping [32] has also been used to both unwrap phase and resolve 2π ambiguity (see below) simultaneously, and as no spatial operations are applied is unaffected by steps or discontinuities. However this technique requires the projection of a series of fringe patterns and therefore requires a relatively sophisticated projector and increases the data collection time over spatial unwrapping methods.

A simple flood-fill algorithm was used throughout the work reported here, which is reliant on steps and isolated surfaces on the object being identified. A technique to distinguish between discontinuities in unwrapped phase is described and experimentally demonstrated in Chapter 6, based on processing phase shifted images in different orders and comparing the results. This technique is used throughout the experimental sections of this thesis. Once the edges and steps are located it is straightforward to unwrap the phase on the surfaces bound by the edges using the flood-fill algorithm.

3.5.3 2π ambiguity

The unwrapped phase is correct only up to some unknown additive integer multiple of 2π radians, and the correct phase value must be found for each pixel. In practice this means that either the phase or the height (relative to either a reference plane or the camera), must be known for each isolated surface being measured.

One way to solve the problem is to project a single line or symbol to identify the zero order fringe in a recorded image [70]. This method will fail if the zero order fringe is not projected onto a particular isolated surface being measured. Heterodyne or temporal phase unwrapping solves the problem by projecting a sequence of fringe patterns with different frequencies [90,91]. A sequence of gray-code patterns can also be used to apply a unique code to each imaging pixel [53]. Another option is to project a fringe pattern with known pseudo-random variations allowing the absolute phase to be found [92]. The pseudo-random variations are required to be of the order of the noise in the recorded images.

A number of authors have described systems using multiple cameras and one or more projectors to measure the distance to one or more points on the surface, which then allowed the rest of the surface to be measured unambiguously [93,94,95]. These systems used a projected pattern to identify corresponding points in each of the camera views, and measured the points using photogrammetry. They are discussed in more detail in the following section.

3.6 Multiple cameras and projectors

Thus far, fringe projection systems consisting of only a single fringe projector and camera have been considered. Advantages are to be gained by introducing more than one camera or projector, or by moving the camera and/or projector to multiple positions relative to the object. Measurements can benefit from greater redundancy and full 360° measurements of objects are possible [96]. If each camera/projector (or camera/camera) pair are treated separately it is possible to use stitching or data matching techniques to merge data sets from different pairs [97]. Alternatively if camera positions and orientations are known relatively the data may be automatically created in a global coordinate system [98].

The use of multiple cameras and a single fringe projector can provide a way to resolve the 2π ambiguity problem discussed above or can provide corresponding points on smooth surfaces to be measured using photogrammetry [99,91]. For example, consider the system of two cameras and one projector depicted in Figure 13.

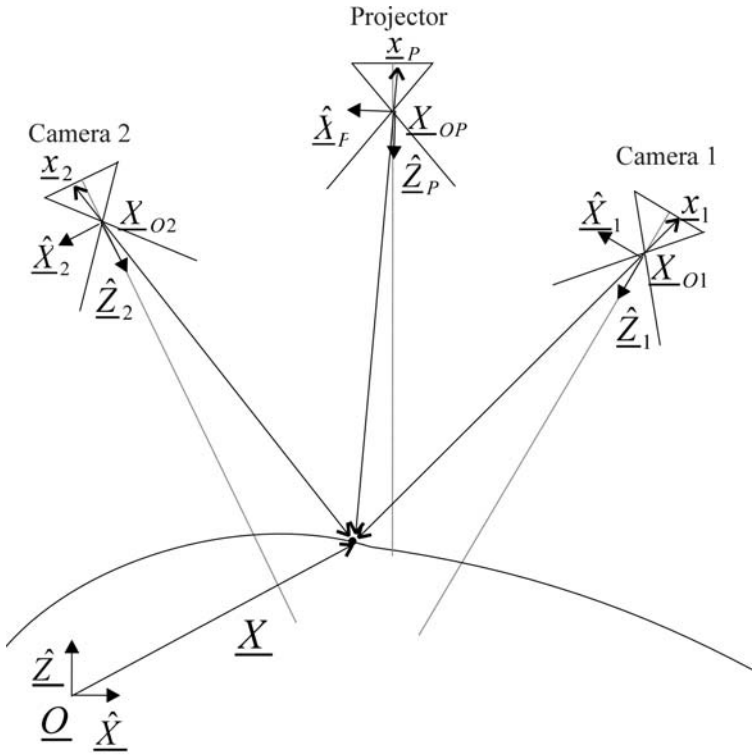

Figure 13: System consisting of two cameras and a single projector.

A point $\underline{X}$ is imaged at $\underline{x}_1$ by a camera 1 with perspective centre $\underline{X}_{O1}$, and at $\underline{x}_2$ by camera 2 with perspective centre $\underline{X}_{O2}$. The projector projects fringes in orthogonal directions in subsequent frames, so that each camera records two phase maps. The wrapped phase values incident on point $\underline{X}$ form a vector $\underline{\phi}_w = (\phi_x, \phi_y) = \frac{2\pi \underline{x}_P}{p}$ due to these orthogonal fringes projected, where the subscript *w* is used to denote that the phase is wrapped, and as before $\underline{x}_p$ is the corresponding point in the projection plane and *p* is the period of the fringes in that plane. The corresponding point in each of the two cameras records the same phase. It has already been shown that for any given image point in a camera image plane, a straight line in 3D space may be constructed, on which the point being imaged must lie. The image of this line in a second camera is known as the epipolar line. The image of the 3D point clearly must lie somewhere on this line. The epipolar line corresponding to any image point $\underline{x}_1$ in camera 1 can be calculated for camera 2 from the coordinates of $\underline{x}_1$ and the (calibrated) geometry of the two cameras. The correct point along the line may be identified using the wrapped phase values. Sub-pixel correspondence can be achieved by interpolating between pixels to find a closer phase match. To find the sub-pixel corresponding point, first the pixel with the closest phase is found in camera 2. A plane is fitted to each phase map on a small set of pixels surrounding this point. The two planes are described by normals

$\underline{n}_1 = (n_{1x}, n_{1y}, n_{1z})$ and $\underline{n}_2 = (n_{2x}, n_{2y}, n_{2z})$ through points $\underline{p}_1 = (p_{1x}, p_{1y}, p_{1z})$ and $\underline{p}_2 = (p_{2x}, p_{2y}, p_{2z})$, respectively. Then the correct subpixel location $\underline{x}_2 = (x_2, y_2)$ satisfies

$$\left((x_2, y_2, \phi_x) - \underline{p}_1\right)\underline{n}_1 = 0 \tag{50}$$

$$\left((x_2, y_2, \phi_y) - \underline{p}_2\right)\underline{n}_2 = 0 \tag{51}$$

Rearranging these equations gives the location of the image point as

$$y_2 = \frac{n_{2x}\underline{p}_1.\underline{n}_1 - n_{2x}un_{1z} - n_{2x}\underline{p}_2.\underline{n}_2 + n_{1x}vn_{2z}}{n_{2x}n_{1y} - n_{1x}n_{2y}} \tag{52}$$

$$x_2 = \frac{\underline{p}_2.\underline{n}_2 - vn_{2z} - y_2 n_{2y}}{n_{2x}} \tag{53}$$

If the phase has been unwrapped, for example using a temporal or heterodyne unwrapping method [91] fewer possible matches are found from the phase. In either case, ambiguities in the matching process can be resolved by either considering neighbouring pixels or probabilistic techniques [94]. Matched points can then be measured using photogrammetry. The fringe projector need not be calibrated as the phase is identical (up to noise) as viewed by each camera. If it is calibrated, however, then any points occluded from one of the cameras but visible from the other can be measured from the phase of one of the imaged fringe patterns, the 2π ambiguity resolved by the photogrammetrically measured points.

An analogous idea is to use one or more cameras and multiple projectors. Phase stepped fringes are combined with Grey code to unambiguously calculate unwrapped phase. By projecting orthogonal fringes from the projectors, each projector encodes the surface with a pair of coordinates, recorded by the camera as phase maps. By using the coordinates from two or more calibrated projectors the surface can be measured photogrammetrically in the same way as if the coordinates were from corresponding points in multiple camera image planes. The point correspondence is trivial in this case as the phase maps are recorded using the same camera. The collinearity equations (equations (17) and (18)) are applied to the phase values rather than the image coordinates and 3D points can be calculated using a bundle adjustment, possibly including simultaneous calculation of projector positions and orientations and

calibration parameters such as lens distortions [98]. The camera is not required to be calibrated, as only projector information is required to calculate the 3D point coordinates.

A second example of measurement requiring multiple projectors requires a minimum of three projectors to encode the surface [100]. Again, gray code and phase shifting is combined to calculate absolute phase. One phase value is provided by each projector. If at least three of the phase values are linearly independent they can be converted to 3D Cartesian coordinates using a predefined calibration. As with the previously described system, the camera is not required to be calibrated.

3.7 Alternative models

Whilst the pinhole model has been used throughout project to model both projector and camera, depending on the hardware used it may not be an appropriate model. In particular if either telecentric or fish-eye lenses are used for either the projector of camera some of the techniques would require adaptation. In systems with a large standoff or telecentric optics the mathematics becomes simpler as the magnification is constant with the distance between perspective centre and the object. This can reduce the calibration requirements. The large standoff approximation is considered briefly in parts of this project, although is not generally used as for the main application, a probe for a CMM, a relatively short stand-off is desirable. Other camera models such as the omni-directional or fish-eye models have not been considered at all as they are not within the focus of this work.

3.8 Speckle

Speckle is a phenomenon caused by a coherent or partially coherent electromagnetic wave scattering from a surface, or transmitted through a diffuser. The microscopic roughness of the surface causes small path differences in the reflected or transmitted wave front, resulting in an interference pattern when the wavefront is imaged. For a given optical system, geometry and surface under inspection the pattern is randomly distributed and related to the properties of the reflective or transmissive surface, the imaging system and the illumination. Speckle fundamentally limits the accuracy of triangulation techniques [101]. While not normally significant for white light projection systems, it is relevant to the phase shifting techniques developed in Chapter 5. A

rigorous treatment of the statistics of speckle patterns is complex and beyond the scope of this work, but some results of previous studies are summarised here.

The contrast C of the speckle pattern is defined as the standard deviation of intensity normalised by the mean intensity:

$$C = \frac{\sqrt{\langle I^2 \rangle}}{\bar{I}} \tag{54}$$

If the light source is temporally coherent with a coherence length long on the scale of the surface roughness the interference pattern imaged through a pinhole has a contrast of 1 for anything but the smoothest surfaces, and is completely dark in some places [102]. A light source that is almost completely temporally incoherent such as a white light source can still result in a speckle pattern if the source exhibits spatial coherence. The contrast is less than 1 and in many cases the intensity variations are not visible to the naked eye and may be indistinguishable from noise from other sources.

Speckle contrast has been shown to vary with surface roughness for polychromatic or white light sources. This has been used to measure surface roughness [103]. For a combined source and detector with narrow Gaussian spectral width* W the speckle contrast can be approximated as

$$C \approx \frac{1}{\sqrt{1+(2W\sigma)^2}} \tag{55}$$

where σ is the RMS surface roughness [104]. Nakagawa and Asakura showed through extensive experimental studies [105,106] that white light speckle contrast has a different dependence on surface roughness. Figure 14(a) plots typical speckle contrasts calculated using equation (55) against surface roughness for an LED and a white light source (spectral widths W=0.6 μm^{-1} and W=6 μm^{-1}, respectively). Figure 14(b), from [106] shows the experimental result from Nakagawa and Asakura.

---

* The intensity recorded at the detector may be expressed in terms of wavenumber $k = \frac{2\pi}{\lambda}$ as $I = \int g(k)I(k)dk$, where $g(k) = \frac{1}{\sqrt{2\pi}W}\exp\left[-\frac{(k-k_0)^2}{2W^2}\right]$ is the normalised spectral density of the combined source and detector and is a Gaussian distribution with width W about mean wavenumber k_0 [104].

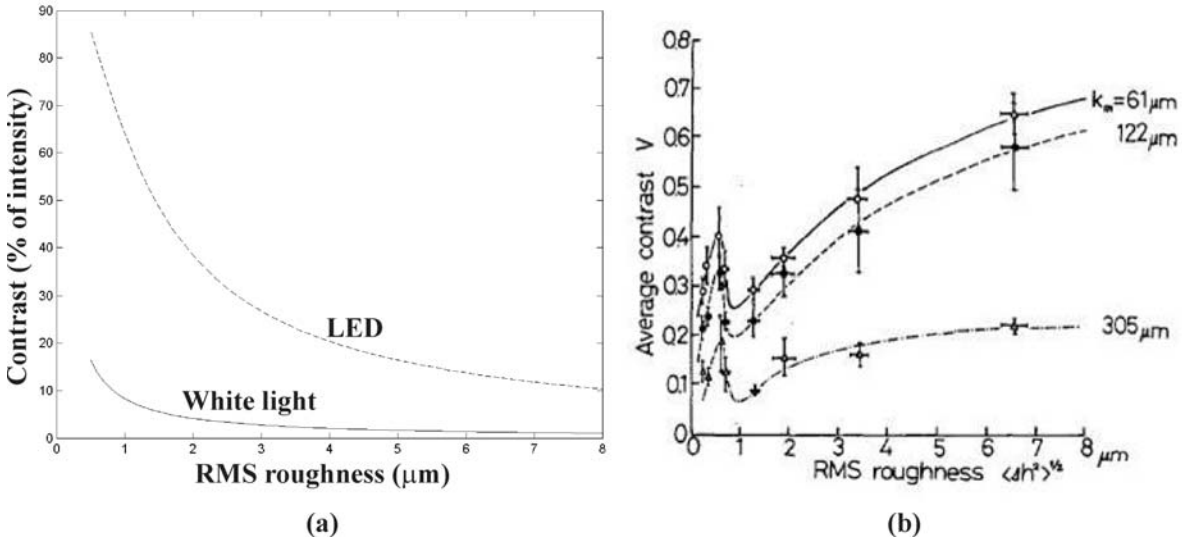

Figure 14: (a) Theoretical relationship [102,104] between speckle contrast and surface roughness for sources with coherence lengths 10μm (LED) and 1μm (white light). (b) Experimentally observed [106] white light speckle contrast variation with surface roughness and aperture diameter.

The variation of speckle contrast with imaging aperture is also shown Figure 14(b), in terms of the point spread (k_m) of the imaging system. The decrease in contrast with decreasing aperture is applicable to polychromatic and monochromatic light as well as white light [107,108] and is due to the point spread for a smaller aperture containing a larger number of uncorrelated speckle patterns than the smaller point spread for a larger aperture. Other ways to reduce contrast include averaging repeated measurements in which something has changed such as the wavelength [109], the polarisation [110], or using a time-varying diffuser [111]. In any of these cases, the speckle contrast is given by

$$C = \frac{1}{\sqrt{N}} \tag{56}$$

where N is the number of uncorrelated speckle patterns observed at a given point in the image plane [102]. Averaging measurements taken using the same setup does not reduce the speckle contrast as the pattern is constant in time. Speckle contrast has also been shown to vary with angle of illumination and observation [112,113]. For example, Figure 15(a) (from Hu [112]) shows the variation of speckle contrast with observation direction for a number of surface roughnesses with the illumination direction parallel to the surface normal. If the observation and illumination directions relative to the surface normal are equal (i.e. observing specular reflection) then the contrast increases slightly with angle (Figure 15 (b)). The variation in terms of angle can be explained by

considering the area of the surface illuminated by a spot of light with finite temporal coherence. The whole illuminated area will contribute to the interference pattern produced at the image plane. However, if the surface is tilted with respect to the source, then the path length to different parts of the illuminated area changes and mutually uncorrelated speckle patterns are created for different regions of the illuminated area. The averaging of uncorrelated speckle patterns leads to a reduction in contrast.

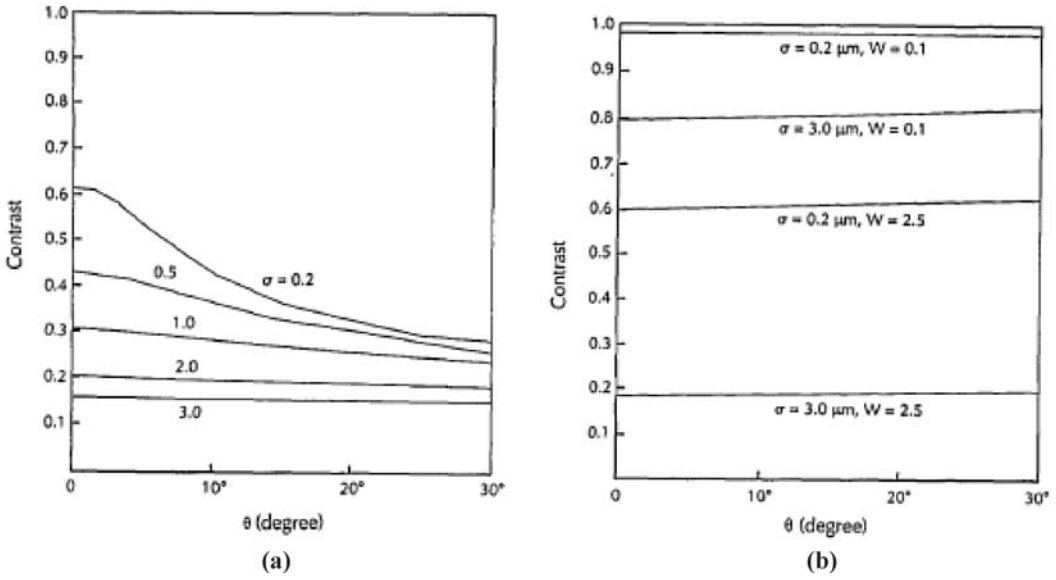

Figure 15: Angular dependence of speckle contrast, from Hu [112]. (a) Contrast against observation direction illumination direction parallel to surface normal. (b) Contrast versus observation angle, for equal illumination and observation angles (relative to surface normal).

Speckle has been shown to be a fundamental accuracy limit of triangulation based measurement techniques [101]. Speckle leads to an uncertainty in the lateral position of a projected spot of δx where

$$\delta x = C \frac{1}{2\pi} \frac{\bar{\lambda}}{\sin u} \tag{57}$$

where C is the speckle contrast, $\bar{\lambda}$ the mean wavelength of the projected light, and u the observation aperture. The lateral uncertainty leads to a height uncertainty of

$$\delta z = C \frac{1}{2\pi} \frac{\bar{\lambda}}{\sin u} \frac{1}{\sin \theta} \tag{58}$$

where θ is the angle between illumination and observation directions.

The effect of speckle on laser-based phase stepping fringe projection systems was investigated by Liu et al. [114] for Bruning's four-step algorithm. They showed that the phase error due to intensity fluctuations at a single pixel is given by

$$\delta\theta = \frac{\int_{-\Delta}^{\Delta}\int_{-\Delta}^{\Delta} sin\left(\frac{2\pi x}{p}\right) S(x,y)dxdy}{\int_{-\Delta}^{\Delta}\int_{-\Delta}^{\Delta} cos\left(\frac{2\pi x}{p}\right) S(x,y)dxdy} \tag{59}$$

where $S(x,y)$ is the speckle intensity distribution and the integration is over the dimensions of the square pixel of side length 2Δ. Here, p is the pitch of the fringes at the image plane, and the fringes run parallel to the image plane y axis. The mean phase error is 0. Furthermore, they show that the maximum phase error occurs if there is approximately one speckle per pixel. Intuitively, for fully resolved speckles covering more than one pixel the variation in intensity across a pixel is smaller leading to lower phase error for larger speckles. For unresolved speckles, averaging of intensity over a pixel leads to a lower error with a larger number of speckles per pixel.

The phase error also increases with decreasing fringe pitch. If a pixel is small in comparison to the fringe pitch ($x << p$), then it be treated as a point detector and the intensity fluctuation is constant and cancels out in the phase calculation algorithm. However, with monochromatic light (and resolved speckles) there will be points in the speckle pattern with zero intensity. The phase of the fringes is obviously unrecoverable at these points. With white (or polychromatic) light the speckle contrast is reduced and no point in the speckle pattern has zero intensity. The phase is recoverable everywhere and without errors from speckle. Errors only occur when the pixel is not of negligible size compared to the fringe pitch at the camera image plane.

3.9 Conclusions

The mathematical theory of photogrammetry has been reviewed, and applied to fringe projection systems. The model can be applied to any number of cameras or fringe projectors, and will be used to develop techniques for a fringe projection probe that can be moved to different positions and orientations. Existing systems consisting of multiple cameras and projectors have been described.

Algorithms for calculating phase from phase shifted fringe images have been reviewed, as have ways to resolve the 2π ambiguity problem inherent to fringe projection. In Chapter 5 phase steps are created by relative motion of the object and fringe projection probe. Speckle is a source of error for this technique, in contrast with traditional temporal phase stepping with stationary object and fringe projection systems. The theoretical and experimental results reviewed above will be used to estimate measurement errors due to speckle with the fringe projection probe. In Chapter 6, the fringe projection probe is moved to different positions and orientations relative to the object being measured to resolve the 2π ambiguity.

Before developing the new techniques, systems were set up implementing existing techniques. The next chapter describes and characterises experimental equipment used to implement photogrammetry and fringe projection separately, and also the combined technique from Reich et al. [91]. Measurements from these techniques are discussed and implementation decisions are justified. The systems were then used for development described in Chapter 5 and Chapter 6.

Chapter 4 Experimental systems and software

4.1 Introduction

This chapter describes the equipment and software used to investigate the new techniques that are the subjects of the following chapters. The aims of work described in this chapter were to provide a base from which to work when developing novel techniques; to characterise the equipment used; and to find the accuracy achievable using known techniques to use later as a benchmark with which to compare the results of the new techniques. Experimental results from measurement using photogrammetry and fringe projection are described. A combination of the two techniques was also implemented, based on previous work from Reich, Ritter and Thesing [91]. The measurement results are followed by a discussion of various aspects of calibration and characterisation of the experimental kit affecting the achieved accuracy. First, the hardware and software used throughout is described.

4.1.1 Equipment

Three monochrome PointGrey FLEA-HIBW [115*] cameras with CCD arrays of 1024 by 768 pixels were purchased for use throughout this project, each with a Computar 8 mm fixed focal length megapixel lens [116]. An Edmund Optics multi-frequency grid distortion target [117] was used for calibration and as a known object to assess measurement accuracy. The calibration artefact had three arrays of dots of different sizes, of which the largest was used. The dots were 1±0.001 mm in diameter and spaced 2±0.001 mm apart. Two digital video projectors were available for use (BenQ MP720p [118] and HP vp6311 [119]). A mini-projector (3M MPro 110 [54]) was also purchased to investigate the possibility of using a small digital projector for a fringe projection CMM probe. The projectors were always allowed to warm up for at least an hour before measurement. The non-linear behaviour of the projectors was corrected for using a lookup table as described by Valera [31]. All three projectors used were DLP (Digital Light Processing) projectors. A projected image is produced by a DMD (digital micro-mirror device) containing an array of micro-mirrors that are flipped between two different angles at high frequency. A bright pixel is in the “on” position more than the “off” position, and for a dark pixel the converse is true.

* Product specifications for the equipment used can be found in Appendix A2.

For initial algorithm development and testing in Chapter 6, a Renishaw PH10 head [120] was made available. The PH10 is a two axis indexing head with 7.5° angular position increments. A static camera and fringe projector viewed an object mounted on the head from a limited number of perspectives. The system is shown in Figure 16. The relative camera perspectives viewing the object attached to the head were found by first calibrating the camera using images of the calibration target mounted on the head. The same head angles were used for measurement as for calibration. The possible angles that could be used were limited by the angles at which successful processing of the calibration target image could be achieved – at too acute an angle the processing fails. The maximum possible head angle was 22.5° from the vertical axis. The limited range of perspectives limits the accuracy achievable with this system.

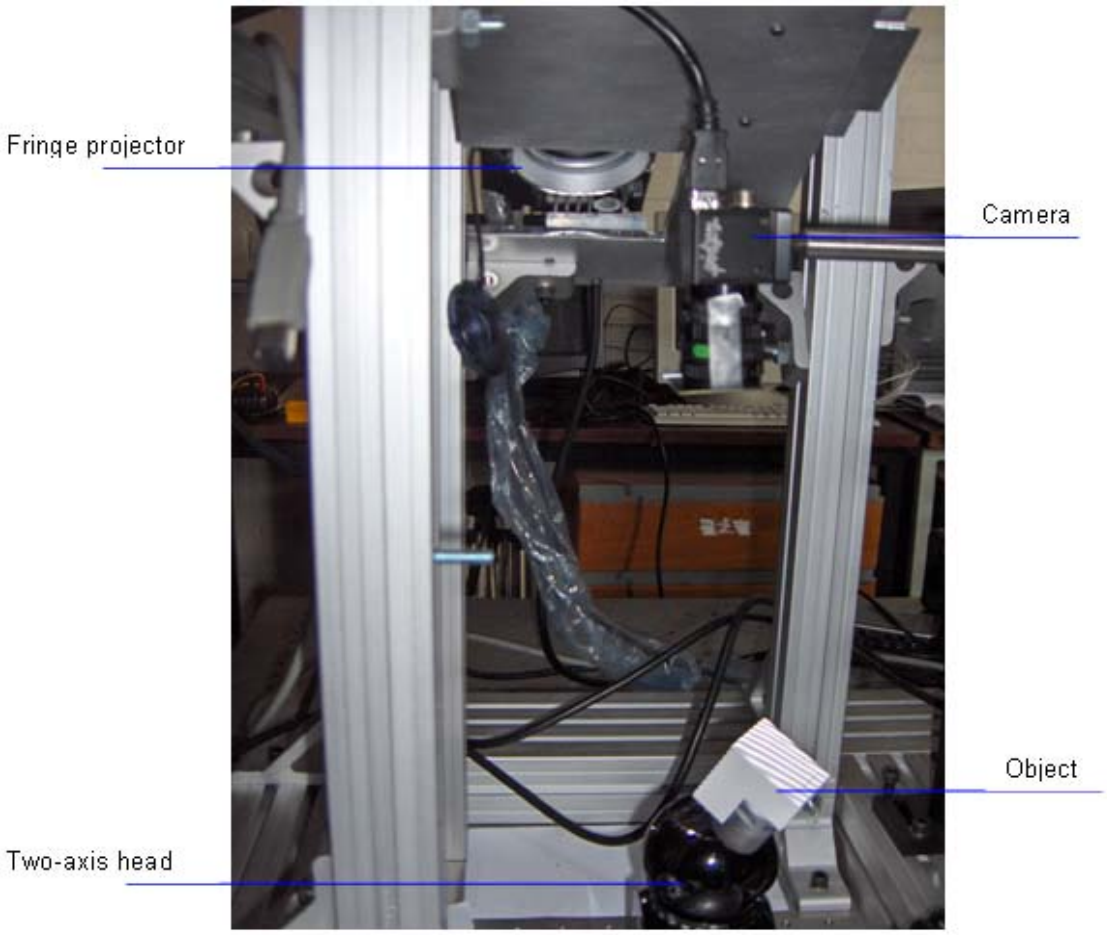

Figure 16: Fringe projection system with measurement object mounted on PH10 (two-axis indexing head).

A CMM was also used for development work, a three-axis Mitutoyo Crysta Apex 9106 CMM with a two-axis Renishaw Revo articulating head. The CMM was driven using a

Renishaw UCC2 controller connected to a Toshiba Portege M300 laptop. Objects mounted on the head were measured using a fixed camera and projector (shown schematically in Figure 17). As described in Chapter 1, a prototype probe was also created to be mounted on the head on this CMM.

The CMM was calibrated using proprietary techniques and software and qualified to ISO 10360 [11]. The calibration procedure has various stages including error mapping of both the linear and angular encoders, finding the parameters describing the mounting of the head on the CMM and the probe on the head, and calibrating the response of the attached probe. Following calibration, the position of the tip of a calibrated touch probe attached to the two-axis head on the three-axis CMM is reported correct to the order of 1 µm.

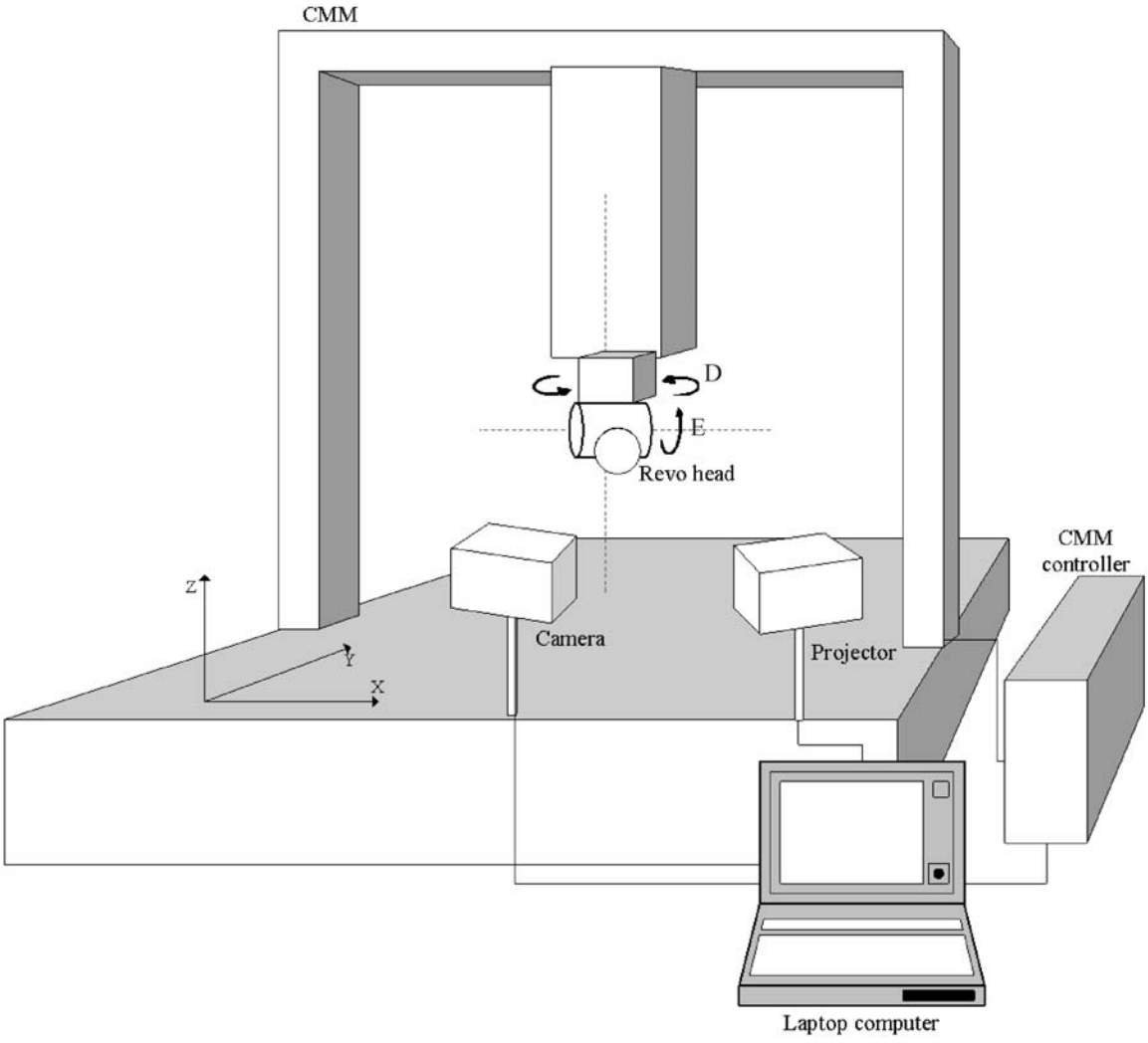

Figure 17: Schematic diagram of CMM with 2-axis articulating head and fixed camera and projector.

The parameters describing the probe-to-head mounting are found by measuring a sphere in a known position using different head angles and calculating the parameters using least-squares fit. A similar technique to the touch probe calibration is used in Chapter 7 to find the parameters describing the mounting of the prototype on the head. For the system using a CMM and a static camera and fringe projector, the position and orientation of the camera with respect to the CMM coordinate system were also found by a least-squares fit procedure. Multiple images of the tip of a touch probe attached to the CMM in different positions were recorded, the centre of the image of the tip found for each one. The different image positions and the known tip positions were used to fit for the 6 unknowns (3 translations and 3 rotations) describing the camera pose. The RMS error from the fit was 0.5 pixels, equivalent to around 25 μm. This could be improved by better lighting conditions or a more accurate image processing technique to find the centre of the probe tip in the images.

The software used throughout the project came from a variety of sources and is described in some detail in the next section.

4.1.2 Software

The software to carry out photogrammetric measurements originated as five separate sets of Matlab scripts, each of which is briefly described below.

- Camera Calibration Toolbox [121] – calibration routines for individual cameras, using the model from [122].
- N camera calibration toolbox [123] - based on a two-camera calibration toolbox from [121], extended to multiple cameras.
- Resection [123] – finds the positions of calibrated cameras with respect to an object.
- Intersection [123] – shape measurement given known positions and orientations of calibrated cameras.
- Bundle Adjustment [124] – shape measurement, camera position and orientation and some calibration parameters given good first estimates of all these parameters.

These software blocks were chosen rather than any commercial photogrammetry software as the availability of the source gives the ability to understand the code and amend it to our particular purposes. Commercial packages may have been more robust but it is unlikely making changes would have been possible. Further advantages were that they were all free and had been used previously by others within the department.

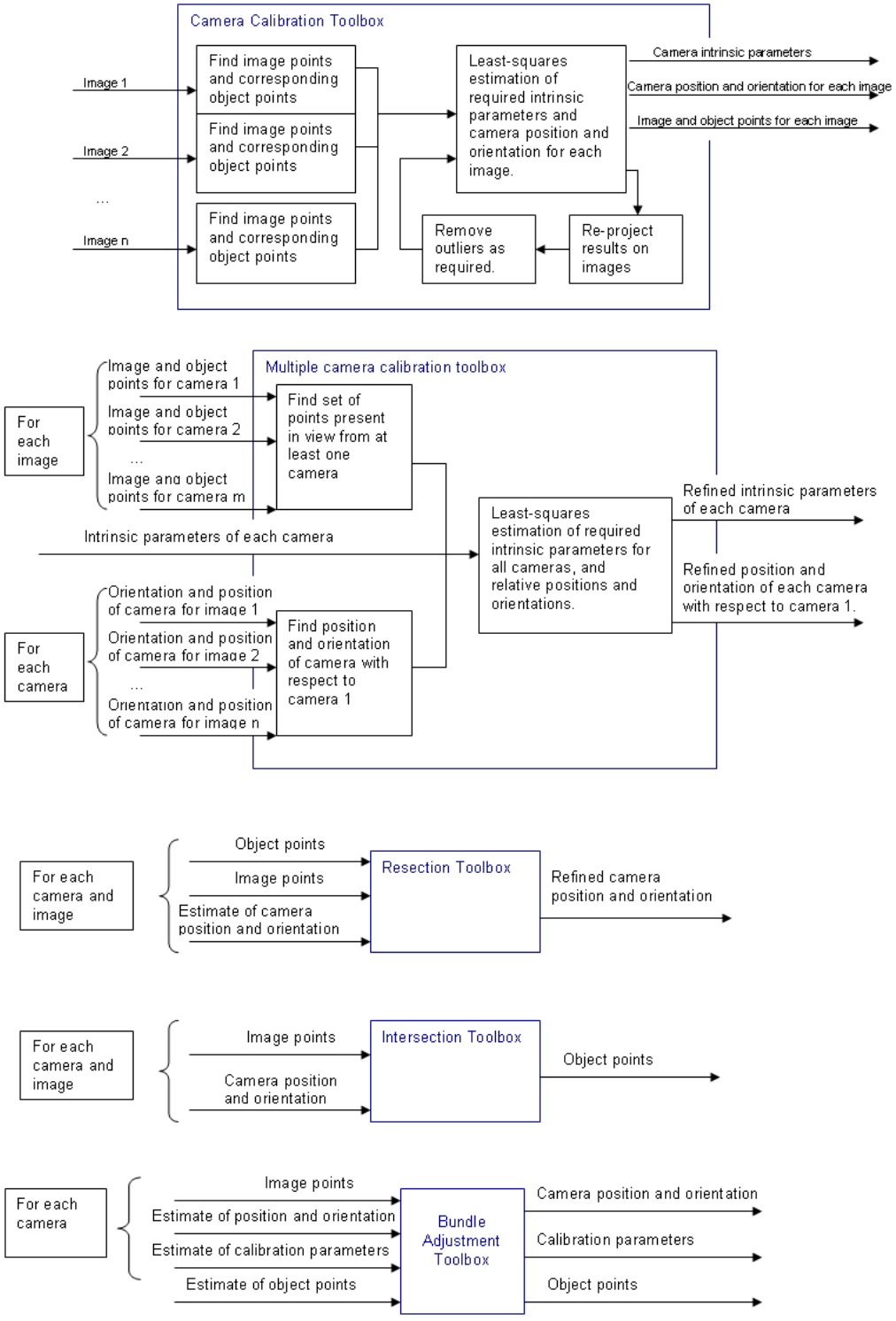

Figure 18: Schematic diagram of photogrammetry software process.

The initial step of the project involved the integration of these five separate software blocks into a form that was more easily usable. Some simple usability improvements were implemented including allowing the user to choose the image files through a GUI rather than having to have the files names in a particular way and a more automatic method to choose the target points within the images. To illustrate the improvement to the selection of target points, a sample image of the calibration is shown in Figure 19. In Figure 19(a) the target area used is highlighted in green. The area was chosen using the original method, in which the user had to manually click on the four corners of the rectangle shown, and also input the dimensions of the rectangle. In Figure 19(b) the possible target points are found automatically and highlighted in pink. The user must then choose only the origin manually, and the axes and actual target points used are found automatically. Not only does this mean that the calibration process is less laborious and sensitive to human error, but it enables more of the calibration target to be used for the process. Fewer images may then be used to attain the same measurement accuracy.

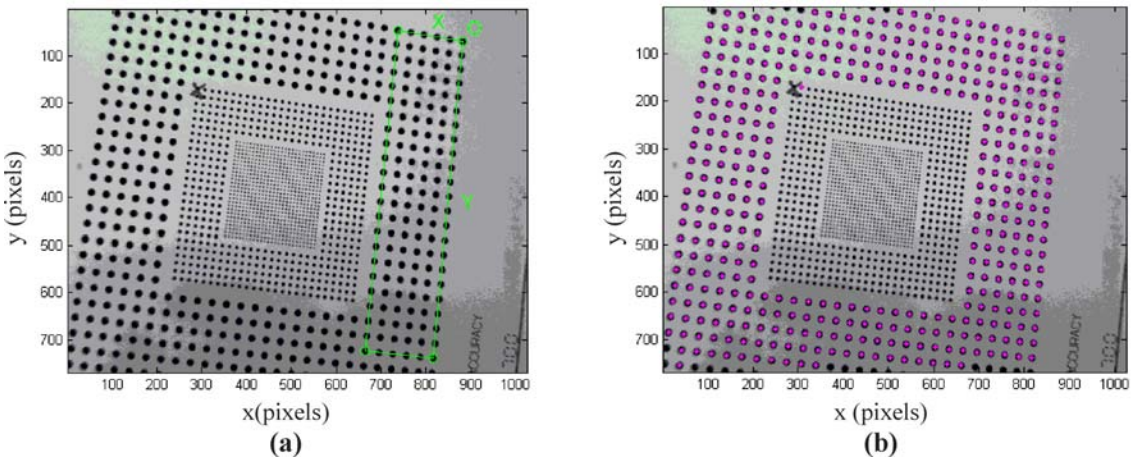

Figure 19: Sample calibration images (a) before and (b) after software updates.

Some other amendments were made to make the different software blocks more compatible. The resection was found to be unnecessary once a stable calibration was available, so it was removed. A GUI similar to that for the calibration software was implemented for intersection and bundle adjustment. The bundle adjustment now runs an intersection automatically so the user need not run it. Functions to choose measurement points and to plot useful results such as re-projection errors were implemented. Also a function allowing the user to remove rogue points and outliers automatically was added. A brief user guide to the software was written. The bundle adjustment software has the facility to run different types of fit as listed below:

1 – fit for motion parameters only

2 – fit for structure parameters only

3 – fit for both structure and motion

4 – fit for camera principal distance only

5 – fit for structure, motion and principal distance

Whilst the photogrammetry literature suggests that a type 5 fit may yield the best results [37], amending calibration parameters during measurement is not compatible with the metrology industry's traceability requirements and best practice guidelines [11]. As discussed in section 3.3.3 an advantage of using a bundle adjustment rather than an intersection is that there is no requirement to invert the transformation from object to image coordinates. Intersection relies on being able to transform from image to object coordinates. This transformation is an approximation, because object-to-image-coordinate transformation is not analytically invertible due to the form of the lens distortions. A bundle adjustment, in theory, allows calculation of object points using only the forward transformation from object to camera image plane. However, the bundle adjustment software used here undistorts the image points using an approximation technique at the start of the process, and then works with the undistorted coordinates, thus losing this potential advantage. It is shown in section 4.3.4 that the measurement results from the type 2 bundle adjustment and the intersection are equivalent.

This software has been used throughout this project, and for two other projects within Heriot-Watt University (one for measurement of hoverfly wings [125], another related to fluid flow [126]), and has also been used by a research group in Cranfield University for the measurement of wings for an MSc project [127].

Further to the photogrammetry software described above, many Matlab scripts to carry out fringe projection and analysis were used. Some of these, in particular the phase unwrapping and some of the phase calculation algorithms, originated within Heriot-Watt University for previous projects [31,128,70]. They have been adapted and developed for use in this project and many more new scripts have been added as the project has developed. Where not otherwise stated below all processing of images and data and all calculations are carried out using Matlab.

4.2 Measurement results

Measurements of known objects were made using the techniques of photogrammetry, fringe analysis, and the combined technique using fringe projection to provide corresponding points for photogrammetric measurement of a smooth surface. The experiments and results are described below. Implementation decisions and error sources affecting the techniques are discussed in section 4.3.

4.2.1 Photogrammetry

Three cameras were calibrated using the Edmund Optics calibration target (Figure 20). The combined field of view was around 75 mm^2, which is approximately the required field of view for the CMM probe.

Figure 20: Experimental setup for fixed camera photogrammetry.

One image of the calibration target (from each camera) was used for measurement and not included the camera calibrations. Figure 21 shows the RMS error from a plane fit to the measured points using different numbers of images for the initial calibration. There was an improvement in the accuracy up to around 12 or 15 images, as seen by the decreasing RMS error. Using more than 15 images resulted in a small improvement to the reliability of the results (smaller error bars) up to approximately 25 images, after which little improvement was seen.

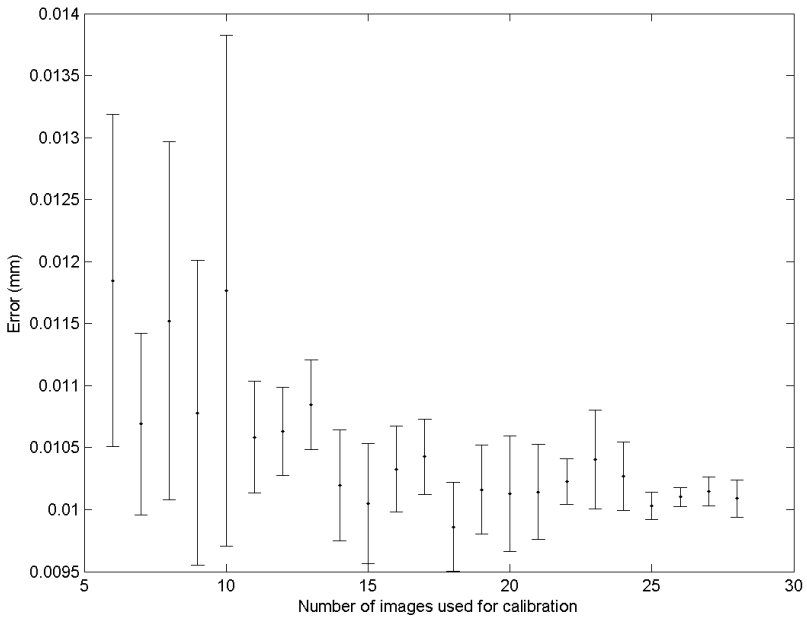

Figure 21: Variation of RMS measurement error with number of images used for camera calibration.

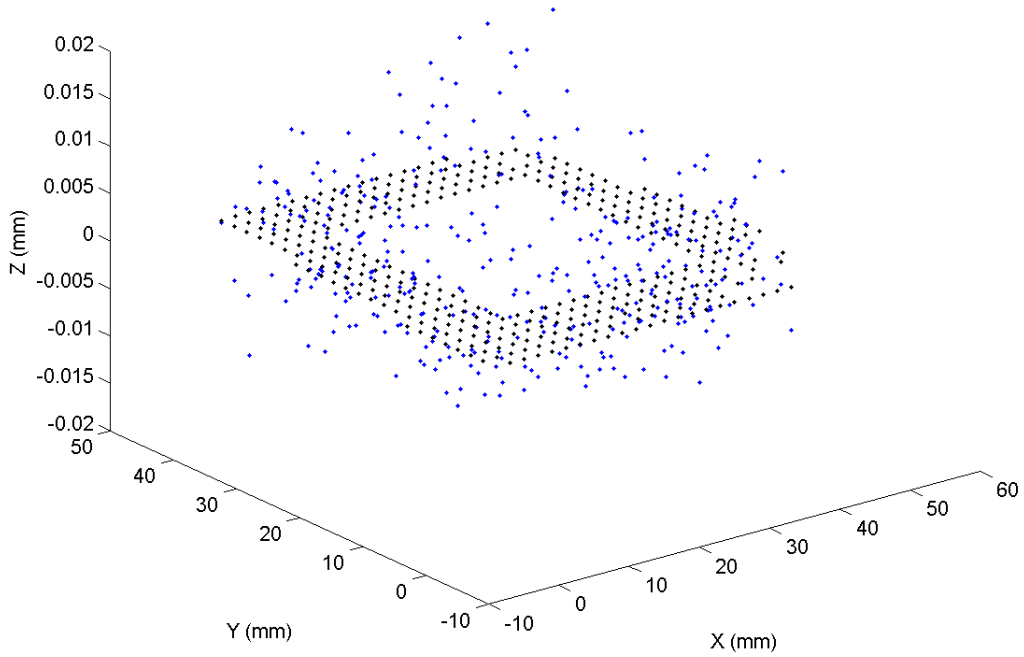

Figure 22: Measured points (blue) and reference points (black).

Figure 22 shows the measured points compared to the known grid points, using 20 calibration images. The RMS error was 10 μm and the maximum error was 26 μm. Figure 23 shows the errors split into in-plane and out-of-plane components against distance from the centre of the image. The in-plane error appears to increase systematically with distance from the image centre. No such systematic error was apparent for the out-of-plane errors (Figure 23(b)). Figure 24 shows the direction of the in-plane errors in the image plane of the camera and further confirms the systematic nature of the error. The systematic error may be due to the assumption that the centre of a target circle projects to the centre of an imaged circle under projective transformation, which, as discussed by Heikkilä [129], is an approximation.

The measurement volume of the three cameras was approximately 75 mm^3, so the RMS error of 10 μm was equivalent to an error of 1 part in 7500. The maximum error observed was equivalent to 1 part in 3000. These errors are approximately an order of magnitude larger than those reported in marketing literature for commercial systems. For example the GOM Tritop has a reported accuracy of 1 part in 120,000 over a measurement volume of 100 mm^3 [38]. Use of higher resolution cameras and more sophisticated measurement algorithms are the most likely reasons for the difference, as well as the likely use of favourable measurement conditions used to get optimum results that may be unattainable in a practical situation.

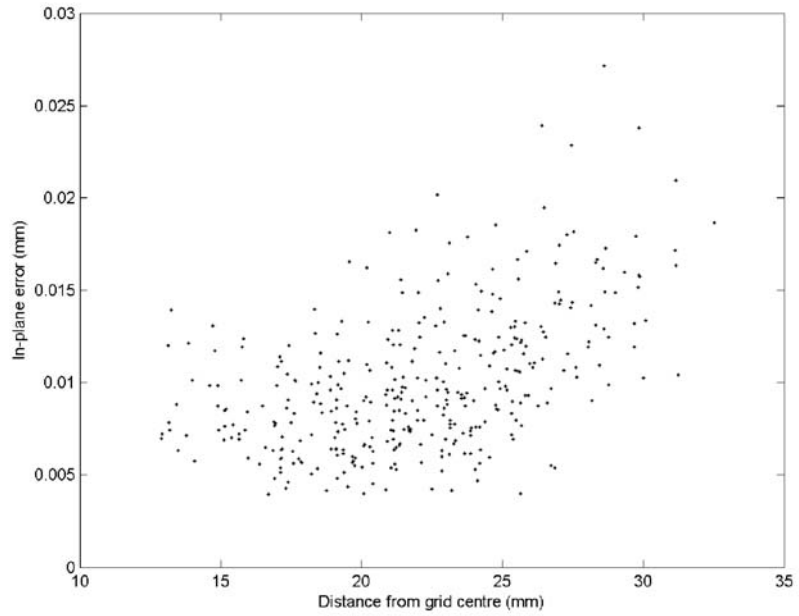

(a)

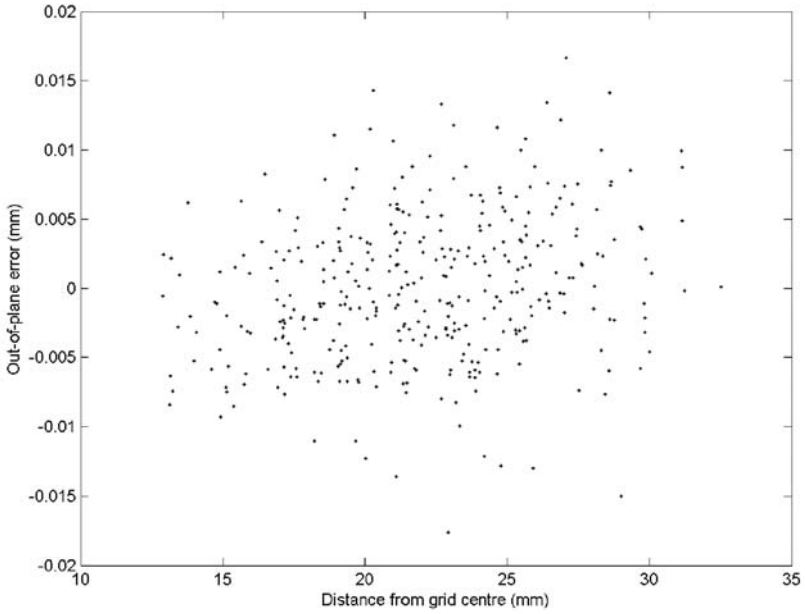

(b)

Figure 23: (a) In-plane and (b) out-of-plane errors against distance from centre of target.

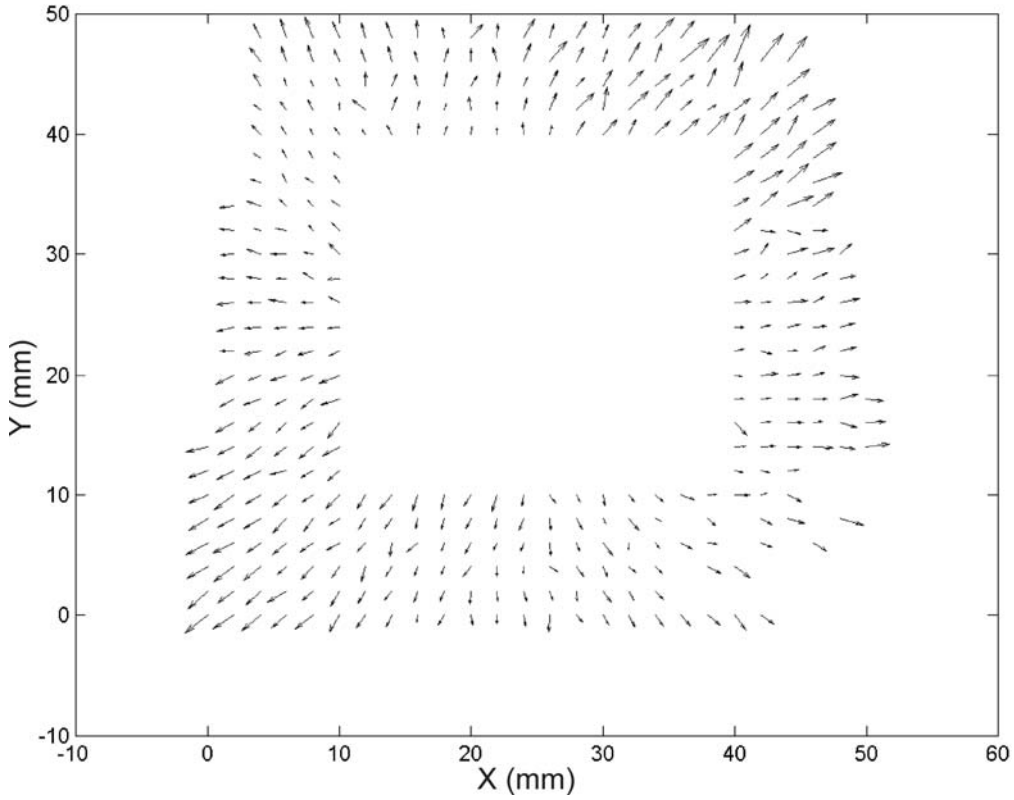

Figure 24: Direction of in-plane measurement errors.

4.2.2 Fringe projection

A planar object was attached to the head on the CMM. Phase shifted fringes were projected towards the object using a programmable projector, and recorded using one of the FLEA cameras. The plane was oriented nominally normally to the camera's optic axis. It was moved to different distances from the camera along the optic axis by moving the CMM linear axes. Two datasets were taken, one with four images per plane position with a $\frac{\pi}{2}$ rad phase step between each, and the second set with five images per position each with a $\frac{2\pi}{5}$ rad phase step. The phase was calculated from each image set using Bruning's algorithm.

As is common for phase to height calibrations one of the plane measurements was chosen as a reference plane. The other plane measurements were used to fit cubic polynomial coefficients for each pixel relating phase to height relative to the reference plane. Relative height errors a plane 50 mm from the reference plane are plotted in Figure 25 for a single line across the image as an example. The mean and RMS errors for the whole plane are listed in Table 11. They were converted to fractions of a fringe

period using the approximate conversion of 1 fringe period to 4 mm corresponding to the nominal fringe period at the intersection point of the camera and projector optic axes.

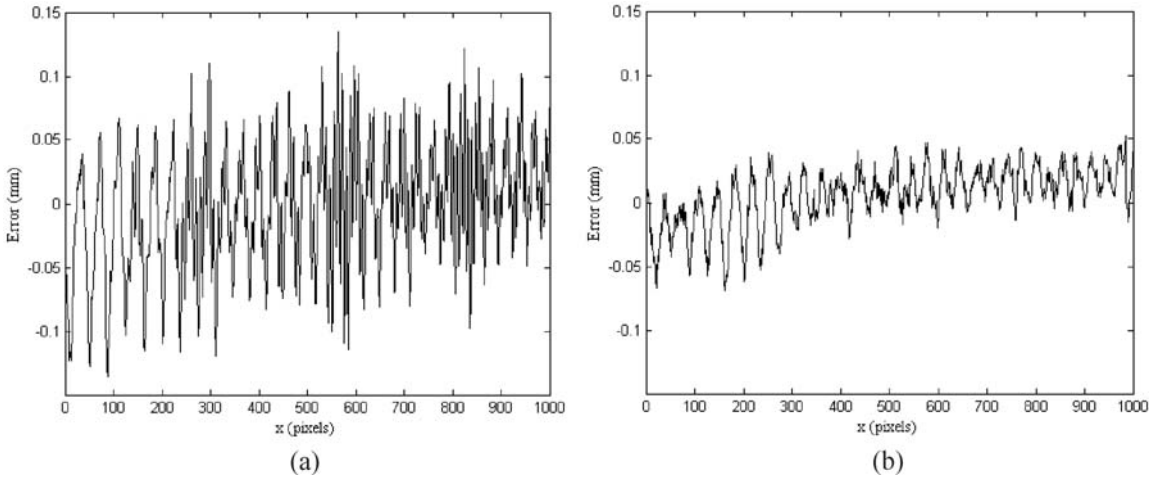

Figure 25: Relative height errors from (a) four frame data and (b) five frame data.

Table 2: Height errors from phase to height calibration data.

Number of frames	Mean error (µm)	RMS error (µm)	Mean error (% of a fringe period)	RMS error (% of a fringe period)
4	-2.5	50.6	-0.06	1.3
5	4.8	23.0	0.12	0.6

The RMS errors were equivalent to approximately 1 part in 1500 of the field of view for the four frame data and 1 part in 3300 for the five frame data. A decrease in error with an increase in the number of frames is typical of phase stepping fringe projection systems, although the decrease observed here is somewhat larger than expected. By using more frames it is likely that the errors would be reduced further. The mean error is small compared to the RMS error, but is a systematic error that can be reduced by fitting a more appropriate function to relate phase to height as discussed in section 4.3.8 below.

4.2.3 Photogrammetry using fringe projection for corresponding point identification

The projection of fringes to provide corresponding points for photogrammetry has been discussed by a number of authors (see section 3.6). Measurements of a plane were carried out using this technique in order to investigate its usefulness and limitations, and to aid our understanding of fringe projection for shape measurement.

The system consisted of a calibrated digital video projector, 3 calibrated cameras and a planar test object. Twelve sets of $\frac{\pi}{6}$ rad phase shifted fringes were projected, recorded by the three cameras, in both horizontal and vertical directions. Bruning's algorithm was used to calculate the phase. With the test plane still in place, the camera calibration target was placed face down on the plane and an image was recorded by each camera. Measurement points were found by locating the grid points on the target, adjusting for refraction at the top surface of the target. This provided two measurements of the calibration target. One, from the location of the grid points in each of the three camera images, was used as a reference measurement. The second measurement was from the location of the grid points in one image and corresponding points in the other two camera image planes found using the calculated phase.

Figure 26 plots the error from a plane fit from both measurements and Table 3 summarises the RMS and maximum errors. The measurement from the points from matching phase showed little obvious systematic error, but considerable noise. The RMS error is equivalent to approximately 1 part in 2400. The errors from the reference measurement were consistent with the measurement made in section 4.2.1 above. The errors from the phase matching technique were approximately three times the reference errors suggesting that there is significant camera-related error in the phase calculation. Errors originating from the fringe projector should affect each camera equally, so any remaining error greater than that for photogrammetry alone must originate from the cameras. Possible examples of camera-related error sources include digitisation and non-linear detector response. Whatever the source of the error, it contributes to the error in any fringe projection measurement.

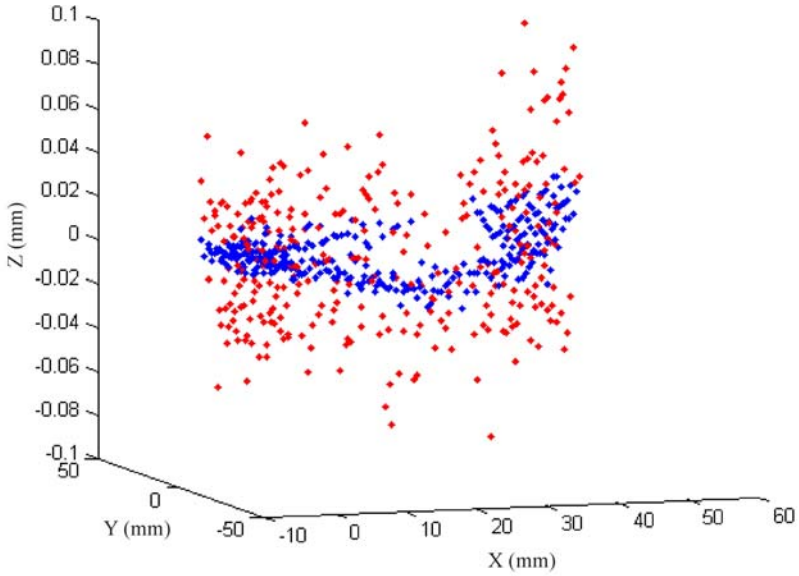

Figure 26: Non-planarity from measurement results from camera calibration target (blue), and points from matching phase (red).

Table 3: Summary of errors from plane measurement.

Corresponding point method	Maximum error (μm)	RMS error (μm)
Calibration target	27	9
Matching phase	96	31

4.3 Discussion of measurement results

A number of different factors that can affect the results of the measurements from these systems are discussed below. Some of these, such as calibration of equipment and algorithms used can be controlled and investigated. Other factors such as noise cannot be controlled but the effect of them can be quantified. Other authors have discussed the effects of gamma calibration of a digital projector [31,79], different camera models [56], image processing algorithms [130,129] and many other aspects of shape measurement using both fringe analysis and photogrammetry. The aims here are to discuss some decisions that have been made that are specific to the equipment in use here and describe the rationale behind those decisions; to discuss some remaining sources of error and potential improvements; and to cover some implementation details that are rarely discussed in the literature.

4.3.1 Camera calibration model

The camera model used in the single and multiple camera calibration toolboxes was based on the central perspective model as described in section 3.2. For each camera there were 16 parameters that could be found: three translations and three rotations, fully specifying the camera's position and orientation in the current coordinate system; the coordinates of the principal point on the camera's image plane; the principal distance; aspect ratio (difference in scale of the pixel axes); skew (non-orthogonality of pixel axes); three radial distortion coefficients; two tangential distortion coefficients. In general, it is known that fitting a model using real data is likely to be more successful if the model only includes parameters with a physical interpretation, and this has been demonstrated for photogrammetry [131]. Some of the internal parameters were not expected to be required for the cameras used. In particular, most modern cameras contain pixels that are square to a high degree of accuracy, so it was expected that aspect ratio and skew would not be necessary. An investigation was carried out into which parameters were required for the Flea cameras and lenses used.

Two separate calibrations were carried out, using the three cameras with positions and settings identical for both calibrations. The two calibrations for each camera should therefore be identical. By using the Calibration Toolbox to fit for different combinations of calibration parameters and comparing the results the set of applicable parameters were chosen. Figures 27 to 29 plot the difference in the fitted parameters between the two calibrations for each of the 13 different calibration types detailed in Table 4. The figures are discussed in more detail below.

Table 4: Calibration types.

Calib-ration type	Aspect ratio	Skew	First radial distortion coefficient	Second radial distortion coefficient	First tangential distortion coefficient	Second tangential distortion coefficient	Third radial distortion coefficient
1	0	0	1	0	0	0	0
2	0	0	1	1	0	0	0
3	0	0	1	1	1	1	0
4	0	0	1	1	1	1	1
5	1	0	1	1	1	1	1
6	1	0	1	1	1	1	0
7	1	1	1	1	1	1	1
8	1	1	1	1	1	1	0
9	0	0	1	1	1	0	0
10	0	0	1	1	0	1	0
11	1	0	1	1	0	0	0
12	0	1	1	1	0	0	0
13	1	1	1	1	0	0	0

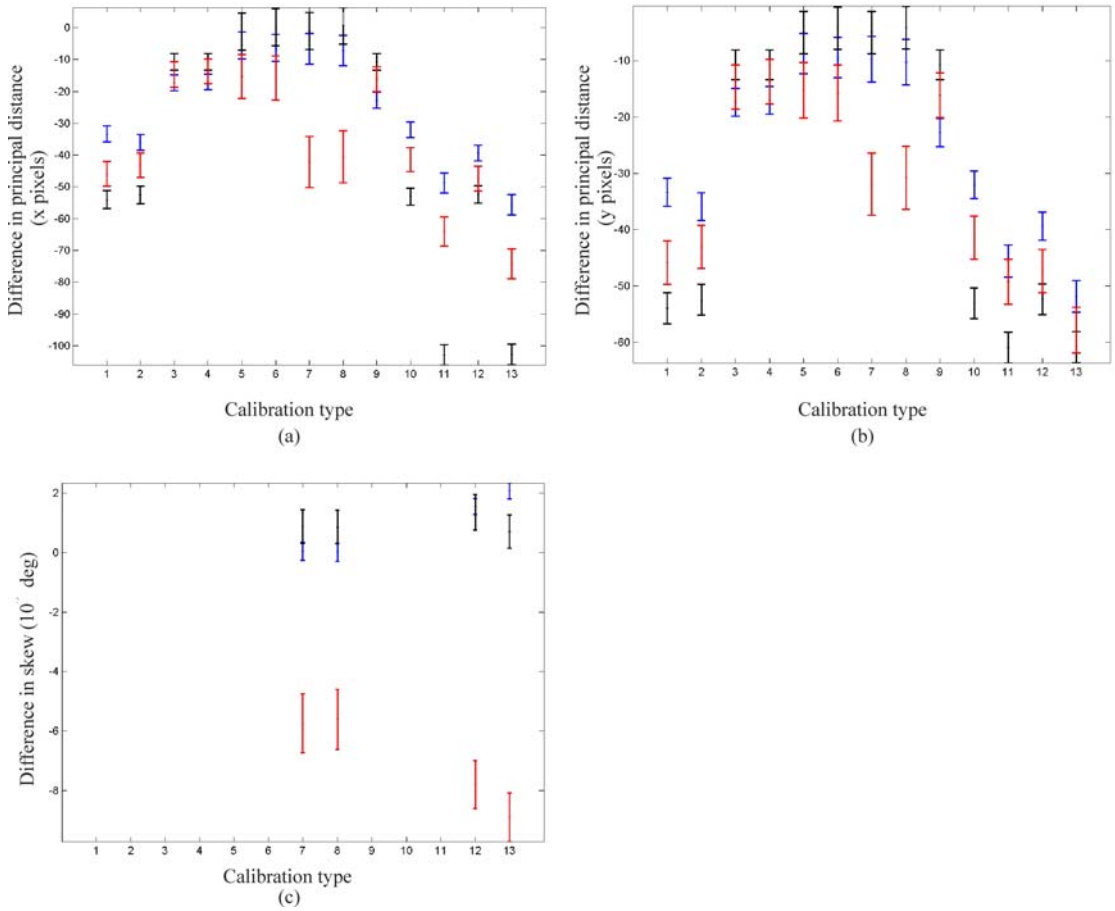

Figure 27: Differences in internal camera parameters describing the pixel array found from repeated calibrations: (a) principal distance in units of x pixels; (b) principal distance in units of y pixels; (c) skew angle. Calibration types are detailed in Table 4. Colours indicate different cameras.

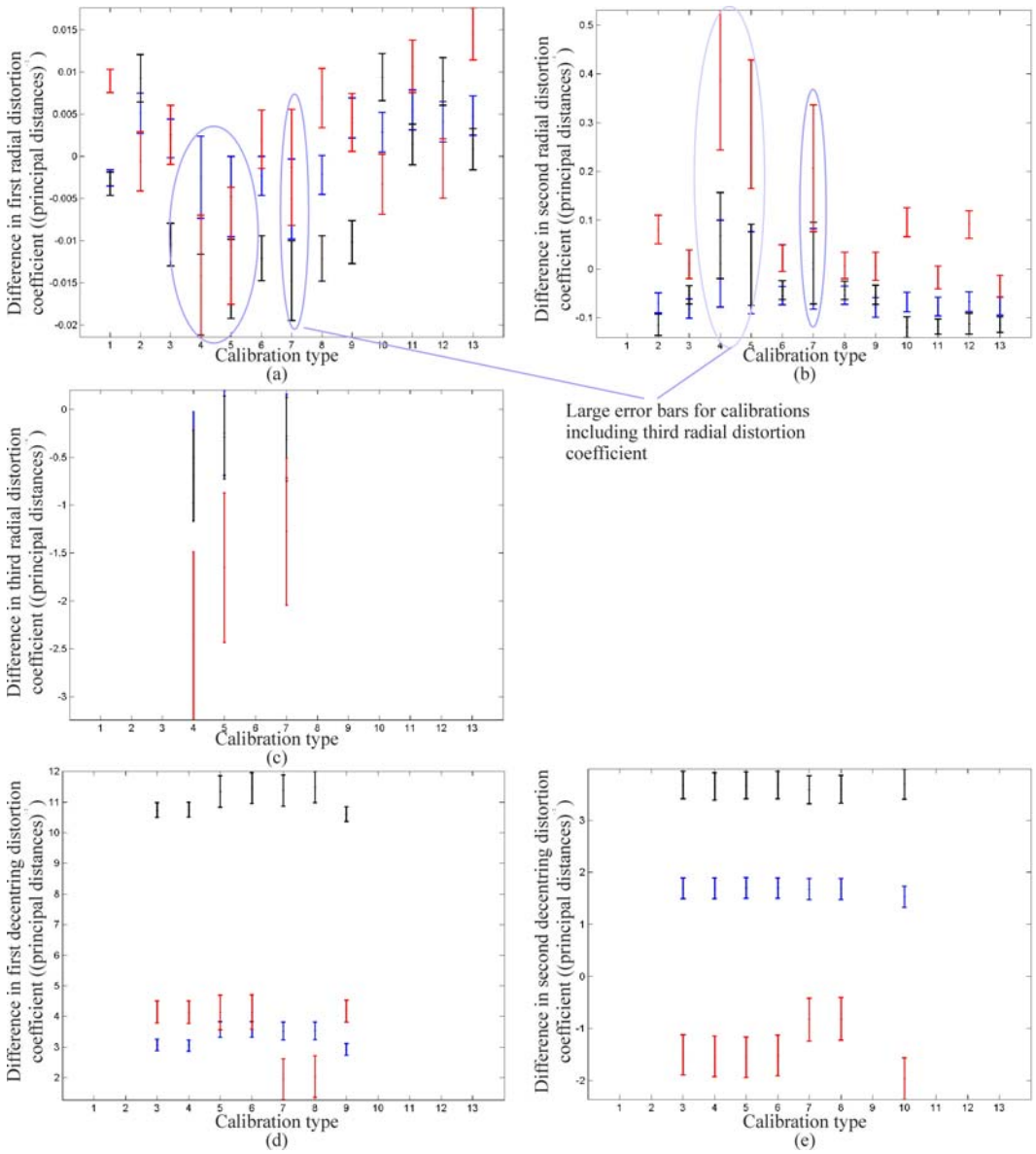

Figure 28: Differences in lens distortion coefficients found from repeated calibrations: (a), (b) and (c) first, second and third radial distortion coefficients; (d) and (e) decentring coefficients. Calibration types are detailed in Table 4. Colours indicate different cameras.

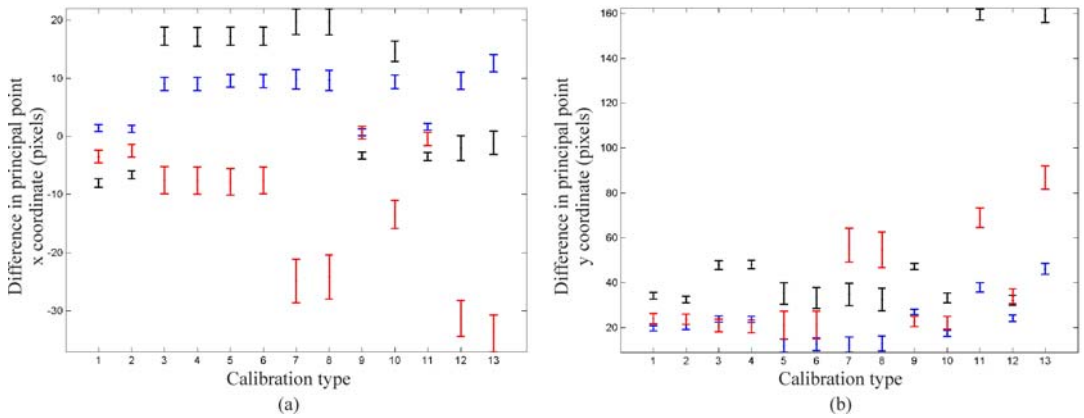

Figure 29: Differences in principal point locations found from repeated calibrations: (a) x coordinate and (b) y coordinate. Calibration types are detailed in Table 4. Colours indicate different cameras.

The results of the experiment were inconclusive. It was hoped that one of the calibration types would consistently have zero difference (up to experimental errors) for each parameter. This was not the case. However, by inspecting the plots in detail some tentative conclusions may be drawn. For example, the smallest differences in principal distances (Figure 27(a) and (b)) were observed for calibration types 3 to 9, indicating that at least the first two radial distortion coefficients and the first decentring coefficient were all required. From Figure 27(c), skew appears to be a required parameter for two cameras but not the third. However the fitted values returned by the calibration were close to zero and so it was assumed that skew was not a required parameter for the FLEA cameras (as expected). From Figure 28(a), (b) and (c), which show the variation in lens distortion coefficients, including the third radial distortion parameter lead to larger uncertainties in the other radial distortion parameters, indicating that it also should be excluded.

The differences in the fitted principal point positions (Figure 29) were of some concern and may indicate that a more sophisticated camera model may be worth implementing. For example a model that separates the principal point from the centre of radial distortions [56], or a model incorporating variations of lens distortions with distance of object from camera (see 4.3.2 below) could be used. Henceforward, a type 3 calibration as listed in Table 4 has been used unless otherwise stated.

The experiment described above is not entirely rigorous. A more complete data collection and statistical analysis might yield stronger conclusions [132], but as the work reported from this point is largely of a comparative nature it is important that the calibration approach is consistent, but not necessarily optimal. The choice of calibration model as indicated by the results here was justified by the fact that the photogrammetric measurement errors above were as low as 10 μm.

4.3.2 Variation of lens distortions with depth

Lens distortions vary with distance of the viewed object from the camera, due to different angles of rays of light passing through the lens. This is normally neglected within photogrammetry as it only becomes a concern for very close range photogrammetry where the standoff and the depth of measurement volume are of

comparable size [57,58]. For the CMM probe the standoff is expected to be around 150 mm and the measurement depth range is up to 80 mm, so the large standoff approximation is not applicable.

To investigate the effect of variations of lens distortion with distance between the camera and object, two calibrations were carried out. For one calibration the target was placed in positions predominantly close to the camera. An example image is shown in Figure 30(a). For the second calibration the target was placed in positions further away from the camera, as in Figure 30 (b). The principal distance and principal point found for each calibration are summarised in Table 5, and the difference in results of lens distortion is depicted in Figure 31. The largest difference is in the upper left where the difference in the lens distortion is 1.2 pixels. These differences in lens distortion, and the other fitted parameters are of some concern, and it suggests that one possible way to improve measurement in future would be to implement a more sophisticated camera model and measurement algorithms capable of including distance dependence.

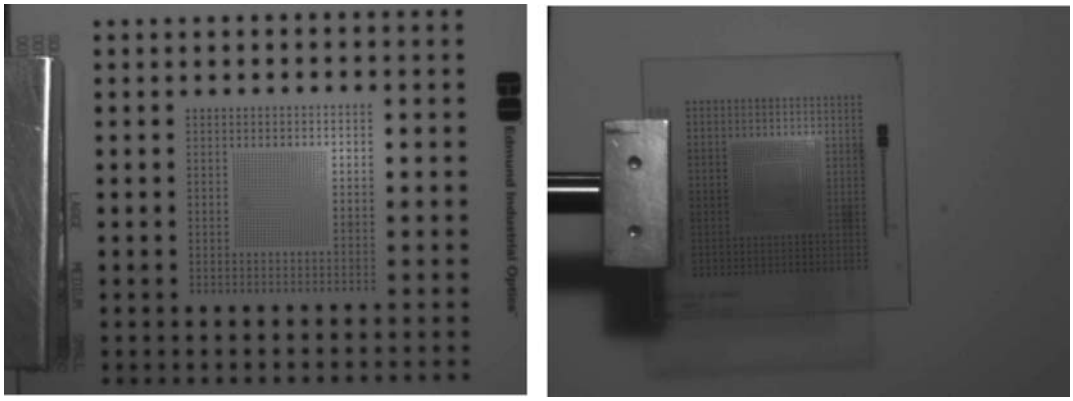

Figure 30: Calibration target image (a) close to and (b) further from the camera.

Table 5: Camera to object distance dependence of internal parameters.

Calibration	Principal distance (pixels)	Principal point x coordinate (pixels)	Principal point y coordinate (pixels)
1 (near)	1787 ± 2	530 ± 1	377 ± 1
2 (far)	1782 ± 7	536 ± 4	383 ± 4

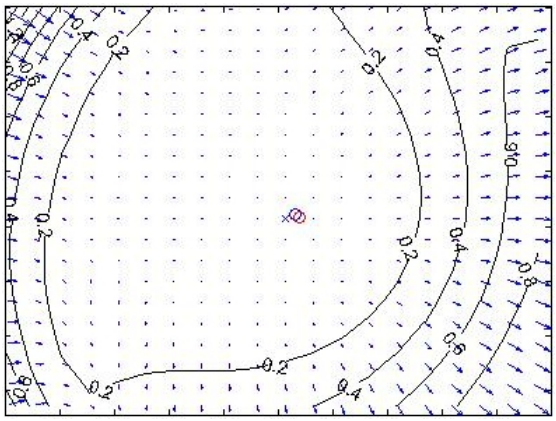

Figure 31: Difference in lens distortions found from the two calibrations.

4.3.3 Inverse of lens distortion

The form of the lens distortion model means that the transformation from camera to image coordinates is not invertible by algebraic means (see section 3.2). Given a point in normalised or ideal pixel coordinates, a line in object space on which the viewed point must lie can be calculated. Specifically, the object point must somewhere on the line through the projected point and the camera perspective centre. The unknown distance along the line is the effect of the projection from 3D to 2D space. However points in a camera image are in distorted image coordinates, and the effect of distortions and any non-ideal internal parameters must be removed prior to the calculation of the straight line.

The removal of the distortion is an approximation, relying on the fact that the distortions are small and slowly varying compared to coordinate in the image plane. The undistorted coordinates can be found by an iterative technique if a small number of points are being considered [122]. If the whole image (or a large portion of it) is to be undistorted then a quicker, non-iterative technique is used. Using the three FLEA cameras, the difference in results from the two techniques was quantified experimentally.

To compare the two algorithms, images were taken of the camera calibration target with three calibrated cameras. Two sets of points were located: one set from the original (distorted) images, which were then undistorted using the iterative algorithm; the second set were found from images undistorted using the whole-image algorithm. Figure 32(a) shows a distorted image with located circle centres, Figure 32(b) shows the equivalent undistorted image, again with the circle centres marked. Figure 33 shows the difference

in the detected circle centres for the two point sets. The maximum distance was less than 0.1 pixels, which is similar to the expected performance of the image processing technique used to find the circle centres.

These differences of up to 0.1 pixels were expected to be insignificant. However, comparing measurements from two sets of points showed that using the whole-image distortion removal method resulted in larger errors than the iterative technique. The measurement errors are shown in Table 6, where it can be seen that the results from the iteratively undistorted image points were more accurate than those found from the faster non-iterative method. Despite this, henceforward images were always undistorted prior to any other processing using the whole-image distortion removal algorithm. To measure many points on smooth surfaces using fringe projection all or most of the image must be undistorted, and to remove the distortion from whole images using the iterative technique currently takes longer than is practical.

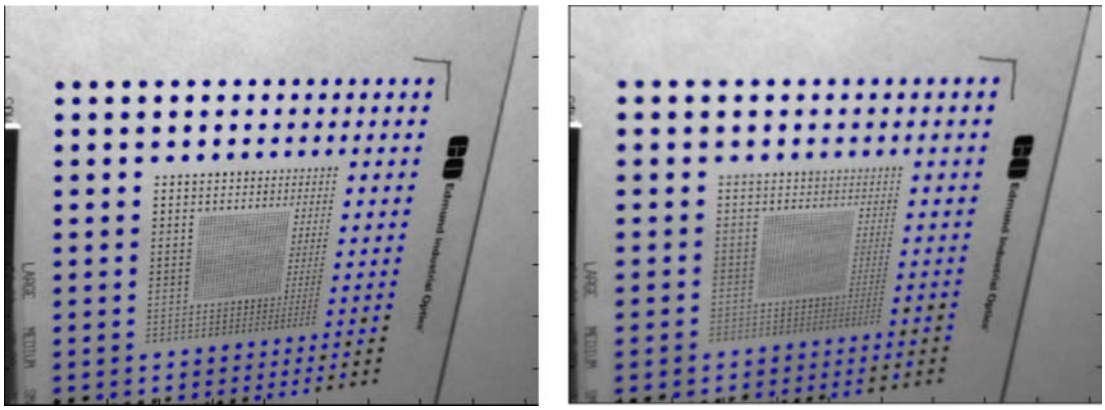

Figure 32: (a) Distorted and (b) undistorted images with located circle centres marked.

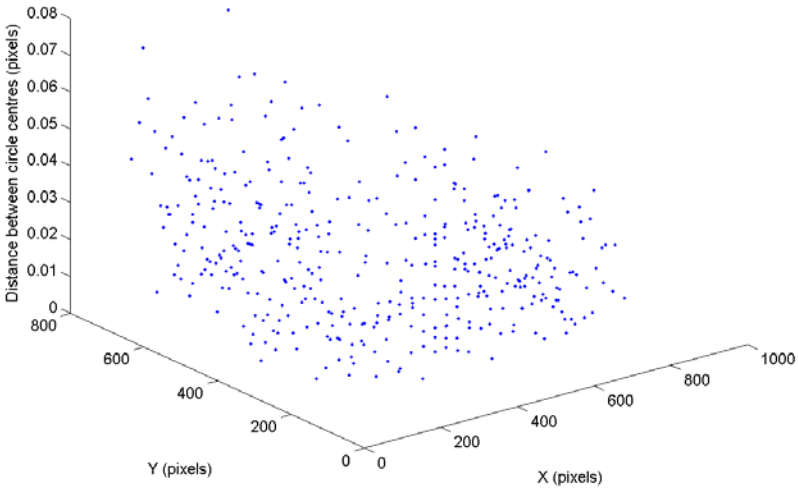

Figure 33: Difference in location of undistorted circle centres, using the two different distortion removal algorithms.

Table 6: Comparison of measurement errors using different techniques to remove lens distortion from image coordinates.

Distortion removal technique	RMS error (μm)	Maximum error (μm)
Iterative	14	46
Non-iterative	23	123

4.3.4 Measurement algorithm (photogrammetry)

As discussed in section 4.1.2 there are two implementations of measurement algorithms available, bundle adjustment and intersection, which are consistent with the metrology industry standards for measurement. The results of the intersection were compared with the bundle adjustment implementation. RMS and maximum errors from both techniques are given in Table 7 and it is clear that the results were almost identical as expected. If the bundle adjustment was re-implemented to only use the forward camera-to-image coordinate transformation a slight improvement would be expected. The measurement results already achieved of approximately 1 part in 7500 are sufficient for the rest of the work reported here.

Table 7: Comparison of measurement errors using intersection and bundle adjustment algorithms.

Measurement algorithm	RMS error (μm)	Maximum error (μm)
Intersection	14	46
Bundle adjustment	15	48

4.3.5 Fringe projector implementation

It was shown by Valera in [31] that the projected intensity from a digital video projector varies significantly until thermal stability is reached, which can take up to an hour. All fringe projection data used here are taken after allowing the projector to warm up for at least an hour. It was suggested that a miniature projector could provide a way to create fringes for a CMM probe. The stability characteristics of the 3M MPro 110 were tested in a similar way to that used by Valera. Figure 34(a) plots the intensities recorded by a selection of pixels over a period of 250 minutes. While some of the camera pixels appear reasonably stable (blue and magenta), the others show different characteristics. Two of the plotted pixels (red and black) seem reasonably stable after approximately an hour, the final one (green) takes around two hours to reach stability. This would clearly be of some concern for any practical system. It might be possible to carry out some kind of thermal calibration for each pixel in order to account for the variations, but it is

preferable to use a system that is inherently more thermally stable. For example, consider Figure 34(b), showing the intensity recorded by a selection of camera pixels viewing an object illuminated by a red LED from switch on for a period of 30 minutes. This is used as the illumination source for the prototype probe in Chapter 7. The plot shows that the intensity variation with time is much lower than that for the mini-projector, and all selected pixels show very little variation other than noise.

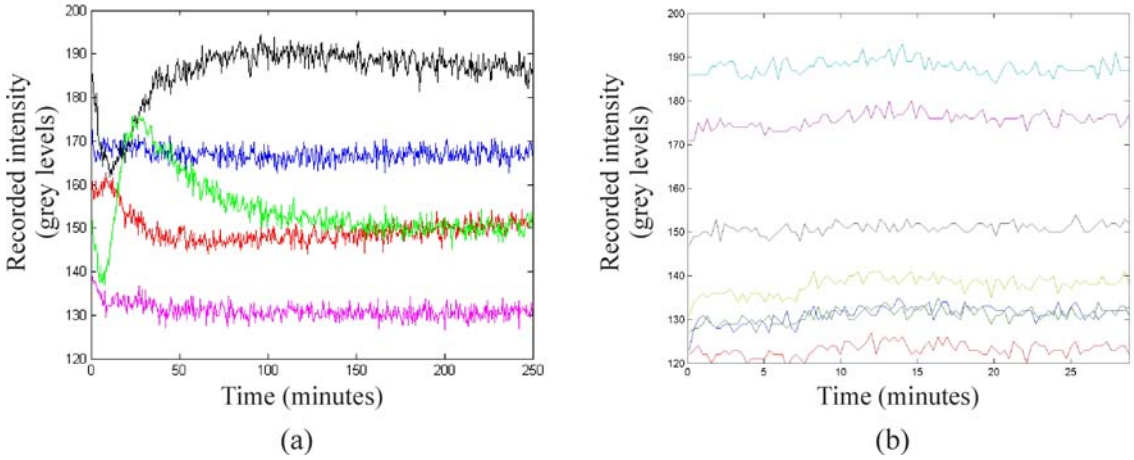

Figure 34: Warm-up characteristics of (a) mini-projector and (b) LED illumination for selected camera pixels.

The lack of thermal stability is not the only disadvantage of the mini-projector compared to the simpler fringe projector using a light source and amplitude mask. Mini-projectors currently available do not have the resolution required for the application. They also do not have strong enough illumination, although using a more powerful light source could remedy this. It is not certain whether a mini-projector could withstand the accelerations exerted on the probe, particularly during automatic probe changes. The switching of the micro-mirrors must be synchronised with the camera shutter to avoid aliasing and noise in the recorded intensity, although this was not done here. Even if all of these problems are overcome with future mini-projectors, they will always be more expensive than the simple light source and mask implementation. From a commercial viewpoint the cheaper option is preferable in order to maximise profit margin whilst maintaining a price point low enough to encourage a reasonable volume of sales.

4.3.6 Phase calculation algorithm

In section 3.5.1 the Novak's 7 frame phase shift algorithms [133] were briefly summarised, and it was noted that in all cases there are points where the algorithms break down, due to noise resulting in a square root of a negative number, the inverse cosine or sine of a number greater than 1, or where the denominator in a fraction equals or is close to zero. Different algorithms show greater noise sensitivity close to different phase or phase shift values.

According to algorithm A7 from Novak the phase ϕ may be expressed as

$$tan\phi = \frac{sin\alpha}{1+cos\alpha}\frac{2a_{26}+a_{35}+a_{17}}{b_{35}-b_{37}} \tag{60}$$

where the phase shift α is found from

$$cos\,\alpha = \frac{a_{26}}{2a_{35}} \tag{61}$$

where $a_{ij} = I_i - I_j$ and $b_{ij} = I_i + I_j$ and the phase shifted intensities in the recorded images are

$$I_i = A + B\,cos\left(\phi + (i-4)\alpha\right), i = 1,\ldots 7 \tag{62}$$

Equations (60) and (61) were used to calculate phase for a plane 8mm above a reference plane. Figure 35(a) shows the unwrapped phase map calculated using this algorithm and, below, the phase step and the unwrapped phase difference for the single line indicated. The "ripple" evident in the phase is an effect noted by other authors and is due to non-perfect sinusoids. The imperfections can be due to many sources (for example digitisation error, noise, higher harmonics in the projected fringes or non-linear detector error). The large spikes in the phase coincide with large spikes in the phase shift and are due to the zero crossings of the denominator in equation (61).

There are a number of possible ways to try to remove the large spikes. One way is to take 8 phase shifted images instead of 7 and, in the calculation of the phase step, α, use whichever set of images provides the larger absolute value in the denominator. The initial set of 7 images could then used to calculate the phase using the resulting phase shift. Figure 35(b) shows the unwrapped phase map calculated using this algorithm, and again, the phase step and the phase difference for a single line are plotted below. It

can clearly be seen that large spikes from the zero crossings of the denominator of the calculated phase step have been removed.

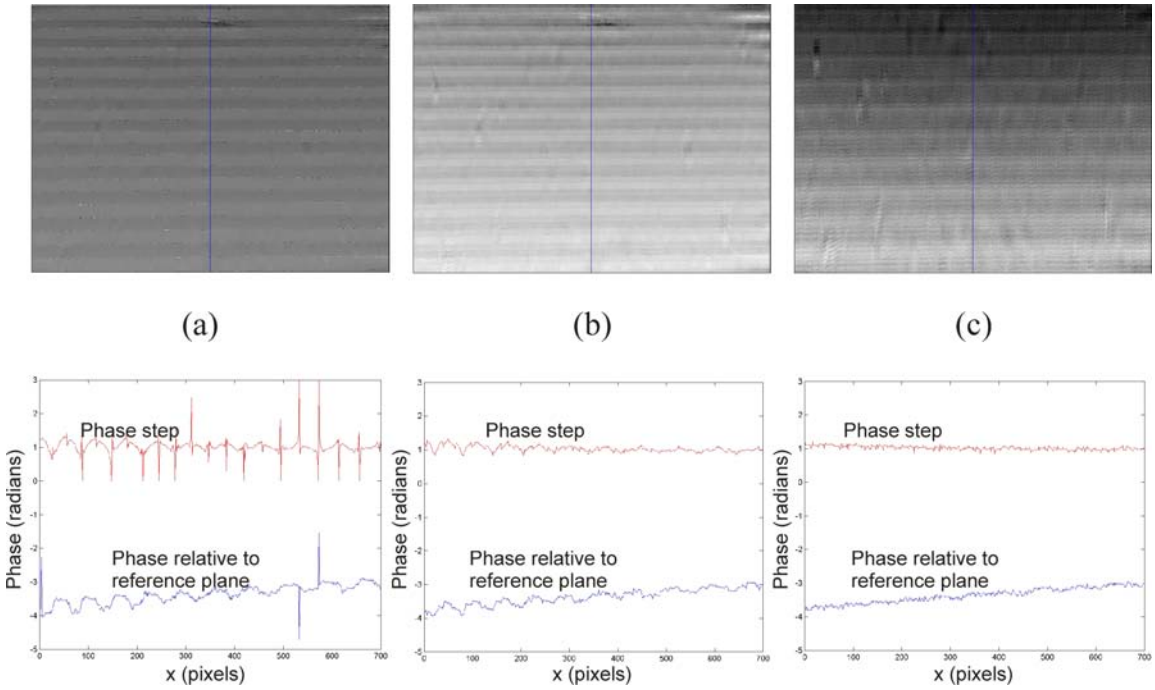

Figure 35: Unwrapped phase maps (top) and phase and phase step along indicated line (bottom) for phase calculated from (a) algorithm A7 from Novak; (b) algorithm A7 choosing best phase step from two sets of 7 images; and (c) mean values from all 7 step algorithms from Novak [133].

There are many other ways phase calculation algorithms could be combined to try to remove susceptibility to other noise sources. One possibility is to use the mean value of a number of different algorithms. First the phase step was calculated using the mean value from the 5 possible methods given by Novak. Then the phase was calculated using the resulting phase step value, again using the mean of all possible values. Any denominator with a less than a pre-defined threshold was marked as invalid and the value was not included in the mean. Any calculation involving an impossible number such as a square root of a negative number or an inverse sine or cosine of a number greater than 1 was also excluded. Eight images were used, and the same algorithm applied to two sets of 7 images, the average of two values giving the final result. The resulting phase map is shown in Figure 35(c), and the phase step and phase for the marked line is again plotted below. It is clear from this that the errors in the phase calculation have been greatly reduced. There is evidently an advantage to be gained in combining algorithms in some way. The use of the averaging, and the threshold for the denominators chosen here was fairly arbitrary. Other possibilities include using the phase and phase shift values from the best available algorithm; to use a weighted mean of values, with weights based on the confidence in a particular algorithm for the

calculated phase and phase shift; or to use a multi-step technique in which one algorithm is used to estimate phase and phase shift, then the algorithm with the most reliable response close to these values used to calculate more accurate values. To find the optimum method would require a more complete modelling of the algorithms, the error sources and an in-depth analysis of the algorithm response, and is beyond the scope of this work.

4.3.7 Phase to height calibration plane

The phase to height calibration plane was custom made in-house. It was a laminate of 1 mm thick carbon fibre reinforced plastic sheets and 12 mm thick aluminium honeycomb bonded with structural epoxy. It was repeatedly lapped flat using carborundum paper on a surface plate, and painted with matt white spray paint, until a uniform white finish was achieved. It was measured using a CMM touch probe taking 100 points in a grid across the plane. The measurement results are shown in Figure 36, and it can be seen that it had a form error of approximately 40 µm. This limits the accuracy with which objects could be measured. It would be possible to correct for the shape of the calibration plane within the phase to height calibration but not enough time was available to implement this. The small error will have an equal effect on all techniques compared. In Chapter 7 a 1 mm thick aluminium oxide plate was used as an alternative phase to height calibration plane. It had a form error of approximately 50 µm, shown in Figure 36(b) and appeared less smooth than the first plane.

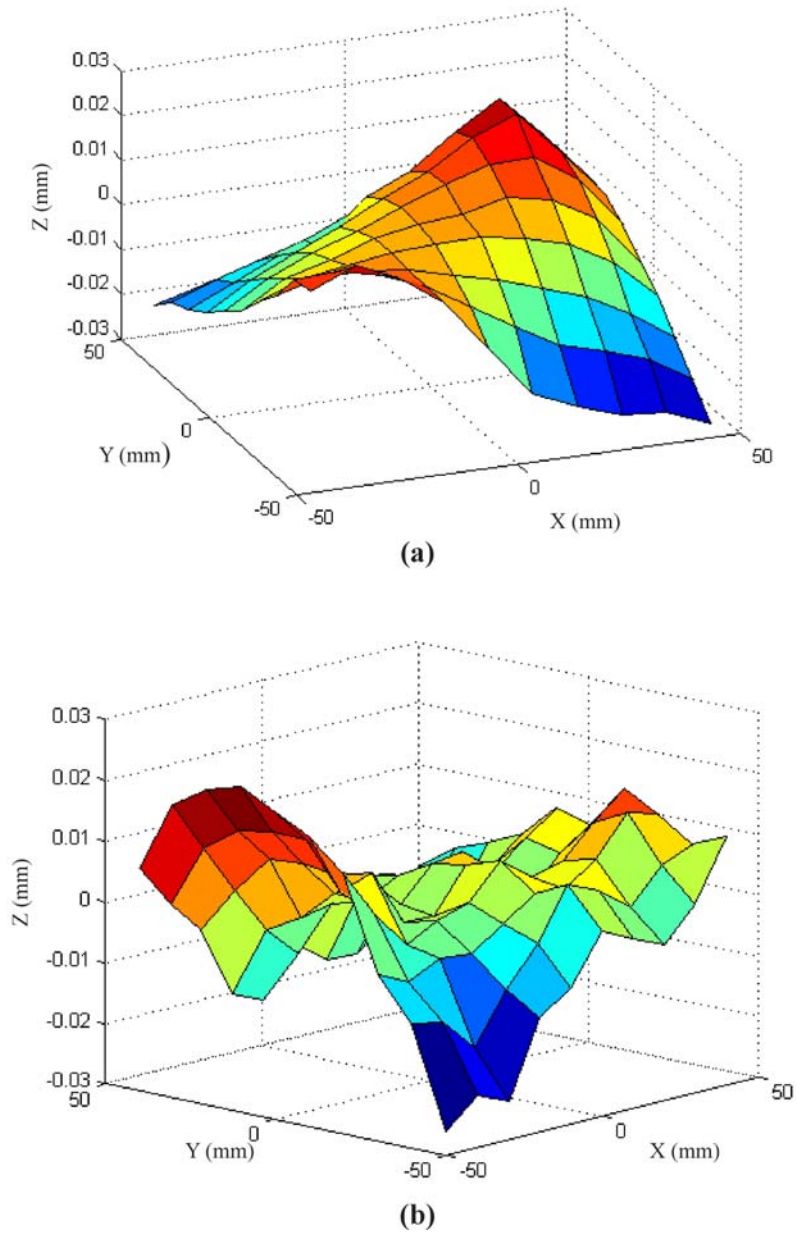

Figure 36: Form of (a) custom made phase to height calibration planes and (b) aluminium oxide plate.

4.3.8 Phase to height calibration model

The calculated phase must be converted to distance from the camera or height above a reference plane. As discussed in section 3.4, some authors calibrate for the system parameters explicitly, but here a simpler calibration process was employed to implicitly calibrate the system instead. The measured phase for each pixel was converted to a height relative to a reference plane and thence to a 3D point. The conversion from phase to height used a pre-calibrated function for each pixel. The phase was recorded for each pixel imaging fringes projected onto a calibration plane placed at a number of different distances from the camera. One of the plane heights was used as the reference plane. A function was then fitted converting phase relative to the reference plane phase to height above the reference plane for each pixel. A quadratic polynomial has been successfully used as the fitted function [31,128,70]. However, it was shown in section 3.4 that the phase relative to the reference plane may be expressed as a function of the form

$$h = \frac{A\phi}{B + \phi} \tag{63}$$

A polynomial can closely approximate this function over a small range, but for a large range of height values fitting directly for A and B can be more appropriate. This was shown experimentally using the prototype system described later in this thesis. Phase was recorded for 12 planes with a spacing of 8mm each. The 8th plane was used as the reference plane. Cubic polynomials were fitted to height and recorded phase for each pixel for different ranges of height values. Also, the constants A and B in equation (63) were fitted for each pixel for the full range. The mean residuals for each fitted function are plotted in Figure 37. Each colour represents a different cubic polynomial fitted to a different range of height values, apart from the green line which is the non-linear function in equation (63). The plot clearly shows that the modelled functional form was the most successful, but that the cubic polynomial was reasonably successful over a reduced range (e.g. yellow, magenta). The calibration procedure fitting for A and B was implemented for use with the prototype in Chapter 7. For the developmental work in Chapter 5 and Chapter 6, and for the fringe projection measurement described above, a cubic polynomial was used.

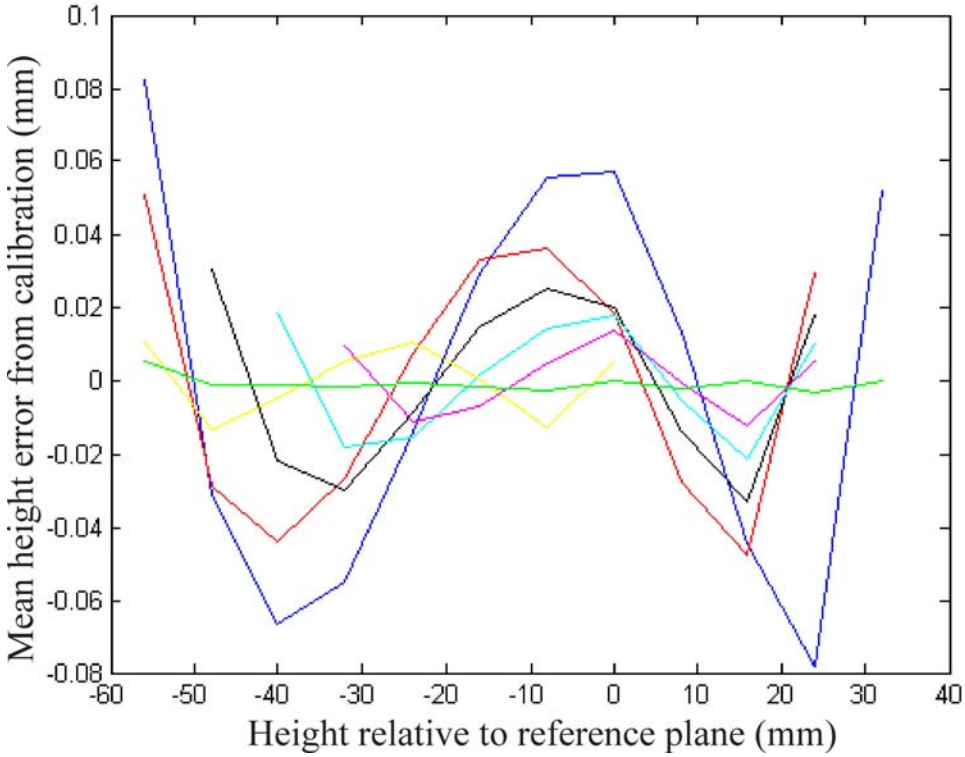

Figure 37: Errors from phase to height calibrations. Green: $h = \frac{A\phi}{B+\phi}$ **Others:** $h = A\phi^3 + B\phi^2 + C\phi + D$ **fitted over different height ranges.**

4.3.9 Noise

There are a number of sources of noise within the measurement system that will ultimately limit the accuracy of any measurement. Noise sources for a DLP projector include the power supply, light source and the electronics controlling the rotation of the micro-mirrors. Camera noise sources include photon noise, circuit noise, dark current, charge transfer noise and quantisation noise. Generally, temporal noise can be minimised by using a low camera gain setting and by averaging repeated measurements, though it cannot be entirely removed. The effect of dark current can be minimised by subtraction of a dark image to remove a fixed pattern. Speckle noise, as discussed in section 3.8, is related to the roughness of the surface, coherence of the light source and the properties of the imaging system, and is spatial rather than temporal. That is, it cannot be reduced by repeated measurements, unless something is changed so that the speckle pattern changes (for example frequency of light source or observation or illumination direction). Speckle noise is not normally significant for white light fringe projection systems; however when phase shifts are created by relative motion of object and fringe projector (Chapter 5) it is a source of error.

The combined effect of the temporal noise sources was quantified by imaging a screen of constant intensity projected onto the phase to height calibration plane. One thousand images were taken in quick succession, and the intensities of a number of pixels were recorded. The projected intensity was varied through a range of values. The standard deviation in the recorded intensities was calculated for each and is plotted against the mean recorded intensity in Figure 38(a). Figure 38(b) shows the standard deviation normalised by the mean intensity. It can clearly be seen that the noise normalised by the mean intensity is approximately constant, although decreases slightly with increasing intensity.

The mean value of the normalised intensity noise is 5.5±0.8 % of recorded intensity. Throughout this thesis, each recorded image is in fact the average of ten images, unless otherwise stated. The averaging reduces the noise level by a factor of $\sqrt{10}$ resulting in temporal noise of 1.7±0.3 % of recorded intensity. A low gain setting is used and the shutter time is always chosen to be a multiple of 0.02 s to average variations in source intensity over the 50 Hz mains electricity cycle frequency.

It has been shown that the uncertainty in phase, σ_ϕ due to intensity noise with standard deviation σ_I can be expressed as

$$\sigma_\phi = \sqrt{\frac{2}{N}}\sigma_I \tag{64}$$

for the N-frame Bruning algorithm [134]. Therefore the phase standard deviation due to recorded temporal noise is expected to be 1.2±0.2 % and 1.1±0.2 % of a fringe period for the four and five frame algorithms used previously. The measurement results from the fringe projection system (errors of 1.3% and 0.6% of a fringe period for the four and five frame algorithms, respectively) are reasonably consistent with this, although the result from the five frame algorithm has a slightly lower error than expected.

It has been shown [134] that the effect of quantisation for Bruning's four-frame algorithm is a phase standard deviation σ_Q varying approximately as

$$\sigma_Q \approx \frac{1}{\sqrt{3}Q} \tag{65}$$

where Q is the number of recorded gray levels. The cameras used here are 8 bit cameras, resulting in a phase standard deviation of approximately 0.2% of a fringe period. For algorithms with lower correlation between frames (such as the 5-frame, 72° phase shift algorithm also used above), the factor $\sqrt{3}$ in equation (65) is increased, resulting in a lower phase error. Therefore it is assumed here that quantisation error is not significant on the scale of the other sources of noise within the system.

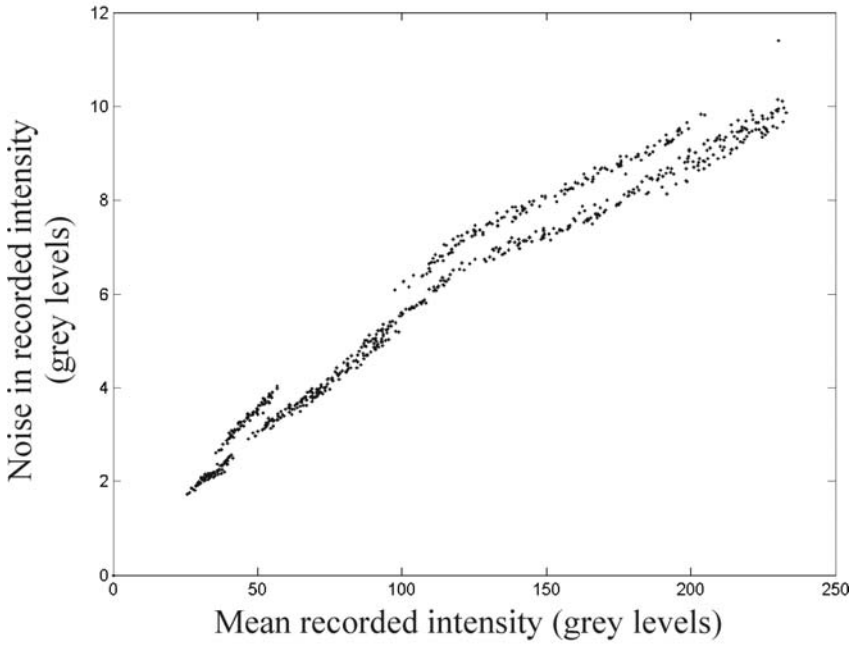

(a)

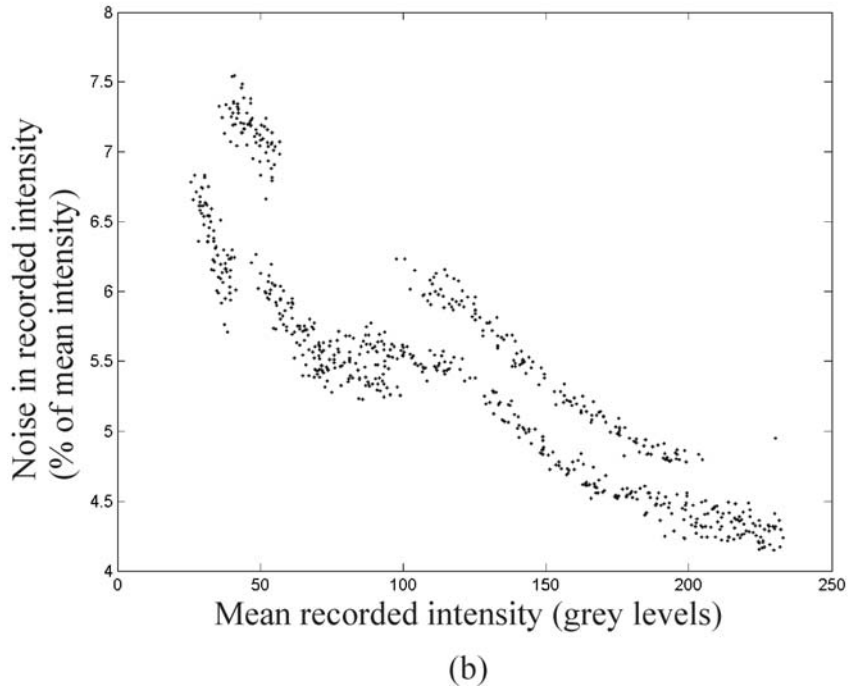

(b)

Figure 38: (a) Intensity noise and (b) normalised intensity noise against mean intensity.

As discussed in section 3.8, speckle noise is not generally a significant source of error for fringe projection systems except those illuminated with a laser. However for the phase shift techniques that are described in the next chapter speckle noise is a limiting factor to the accuracy achievable. Here we attempt to make a quantitative assessment of speckle contrast. The results are later used to estimate the effect of speckle on the new techniques.

Five objects with different surface roughness were chosen as sample objects. The objects are: the phase to height calibration plane described above; the flat piece of aluminium oxide, also used for phase to height calibrations; a block of aluminium with different machined faces; an air bearing housing of machined stainless steel; and a section of a petrol engine timing belt cover of cast aluminium on which two separate areas were used. A photograph of each object may be seen in Figure 39.

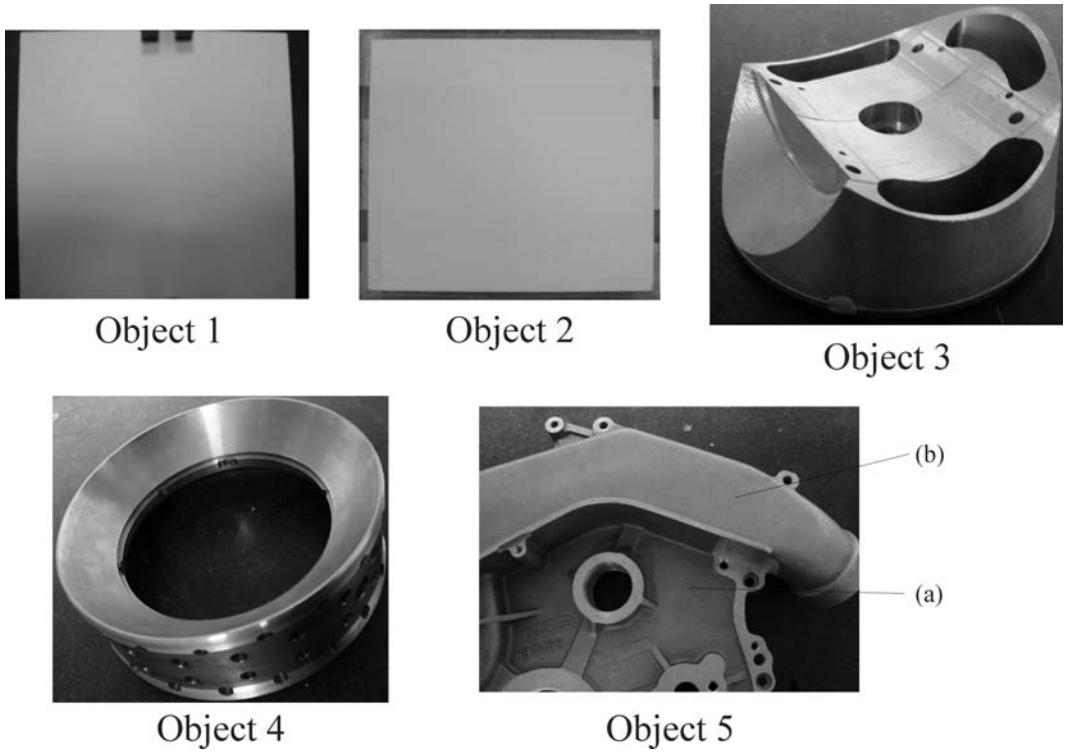

Figure 39: Objects used for measurement: (1) phase to height calibration plane; (2) alumimium oxide plate; (3) machined aluminium block; (4) machined stainless steel ring; (5) cast aluminium block, with two surface areas of different roughness indicated.

First, the surface roughness was measured for each object using a Zygo white light interferometer. The results are summarised in Table 8.

Table 8: Surface roughness.

Object	RMS Roughness (μm)
1	0.65 ± 0.26
2	0.92 ± 0.20
3	0.42 ± 0.10
4	0.62 ± 0.07
5(a)	7.3 ± 1.9
5(b)	5.9 ± 2.1

The speckle contrast was then measured. A constant intensity screen was projected towards each object using a digital projector and recorded with the camera. One thousand images were recorded and averaged to eliminate temporal noise as far as was practical. The contrast was calculated by choosing small areas within the image corresponding to an approximately planar section of the object, fitting a plane to the intensity values and calculating the standard deviation of the errors, normalised by the mean intensity (equation (54)). The plane fit was used to reduce the effect on mean intensity of the angle of the surface, illumination and observation directions.

This was repeated a number of times with different observation apertures. The results are listed in Table 9. It was also repeated, for a single aperture size (1 mm) with a red LED light source, the source used for the prototype probe (Chapter 7).

Table 9: Speckle contrast as % of mean intensity using white light projector.

	F-number				
Object	1.4	2	4	8	16
1	0.67±0.05	0.68±0.11	0.75±0.15	0.95±0.21	0.52±0.19
2	0.57±0.04	0.66±0.05	0.66±0.05	0.41±0.11	0.66±0.17
3	2.4±1.5	5.6±3.0	5.5±3.1	7.1±3.5	3.7±2.1
4	1.8±0.5	3.8±0.9	2.7±0.6	3.2±0.8	1.9±0.5
5(a)	10±1	13±2	10±2	14±2	10±1
5(b)	5.7±1.3	5.7±1.1	6.7±1.1	9.1±0.8	7.1±0.8

Table 10: Speckle contrast as % of mean intensity using red LED with aperture 1mm (F/8).

Object	Contrast (% of mean intensity
1	9.1±0.8
2	1.3±0.3
3	16.7±4.6
4	18.3±7.8
5(a)	16.1±3.0
5(b)	12.4±1.3

The speckle contrast found for an aperture of 1 mm diameter, corresponding to F/8, is plotted in Figure 40 for both the projector and the LED. The speckle contrast was larger for the LED than for the white light projector, as expected from the LED's longer coherence length. (Coherence lengths for the LED and white light were approximately 10μm and 1μm, respectively.) Note the decrease in contrast for both sources between roughness of around 0.5μm and 1μm, with an increase in contrast with roughness above 1μm. This is qualitatively in agreement with the experimental results for white light speckle contrast reported by Nakagawa and Asakura [106], summarised in section 3.8. However more objects with different roughness would help to confirm this. Speckle contrast variation with F-number, plotted for the white light system in Figure 41 does not follow the expected pattern of decreasing contrast with increasing F-number. This may be in part due to the focus setting of the camera, which was constant for each measurement, or due to averaging over a pixel - with a small F-number (large aperture and small point spread) the speckles formed at the image plane may be smaller than a pixel, resulting in a lower averaged speckle contrast than would be recorded on an analogue recording medium. Furthermore, the contrast observed in all cases was lower than that observed by Nakagawa and Asakura. This may be due to the dependence of speckle contrast on angle of observation and illumination. Like most other authors investigating of speckle, Nakagawa and Asakura use a 4f system to make quantitative measurements of diffusing objects and can therefore illuminate and observe a sample normally. However using reflecting objects, as in our case, the angles of illumination and observation have an effect. As previously mentioned the speckle contrast is at a maximum when the observation and illumination angles with respect to the surface normal are equal (i.e. specular reflection), and generally decrease with increasing angle otherwise [112,113]. This can be clearly seen in, for example, Figure 42, which shows the machined stainless steel air bearing. At or close to the specular direction the CCD has been saturated. Close to the saturated area a speckle pattern is observable, and further away the intensity becomes less variable and the contrast is not obvious.

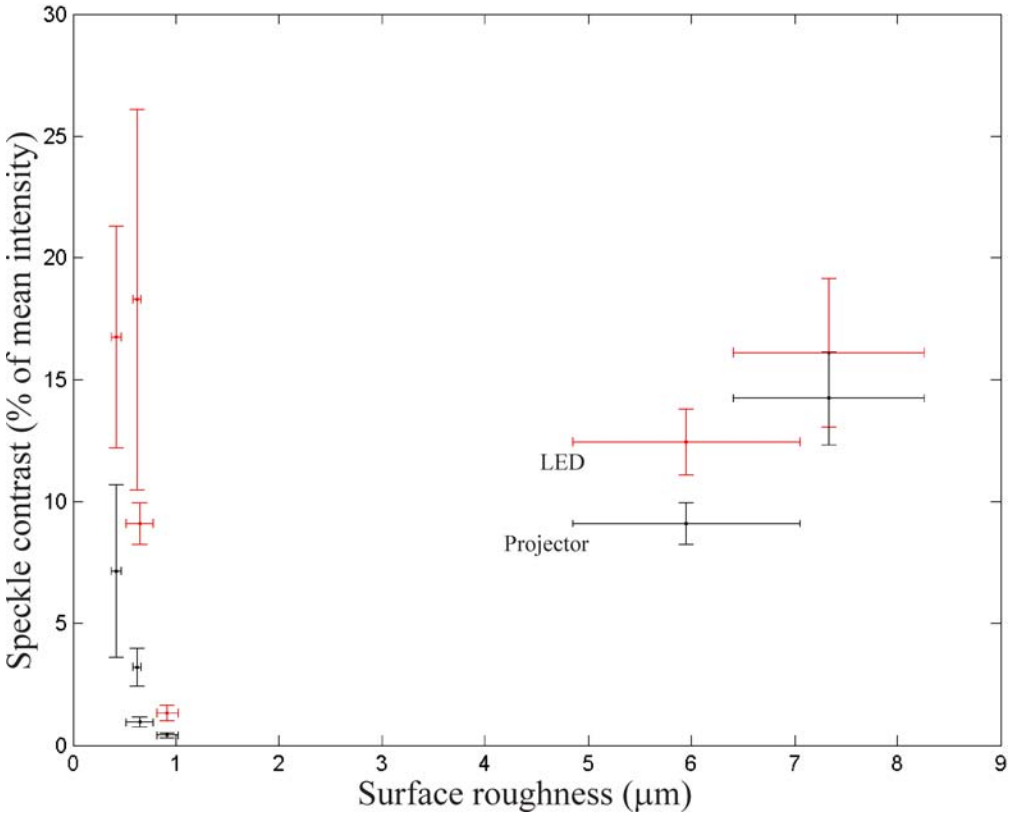

Figure 40: Speckle contrast against RMS surface roughness for 6 different surfaces, with F-number 8, illuminating with a white light projector (black) and and LED (red).

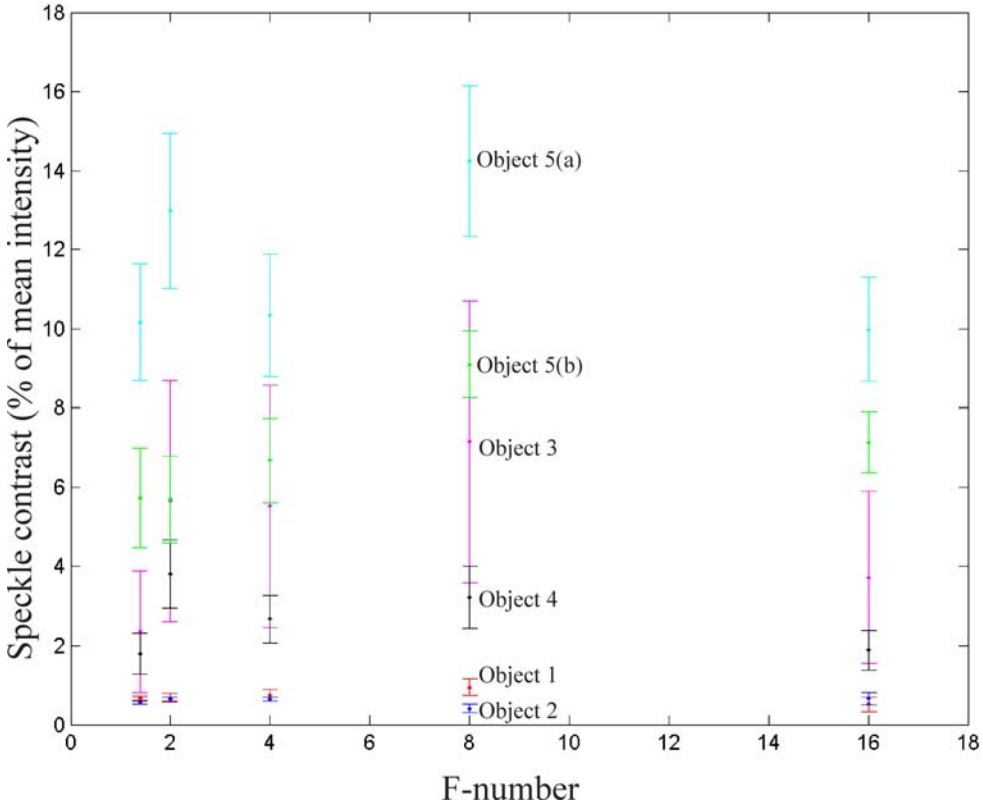

Figure 41: Speckle contrast against aperture diameter for 6 different surfaces illuminated with a white light projector

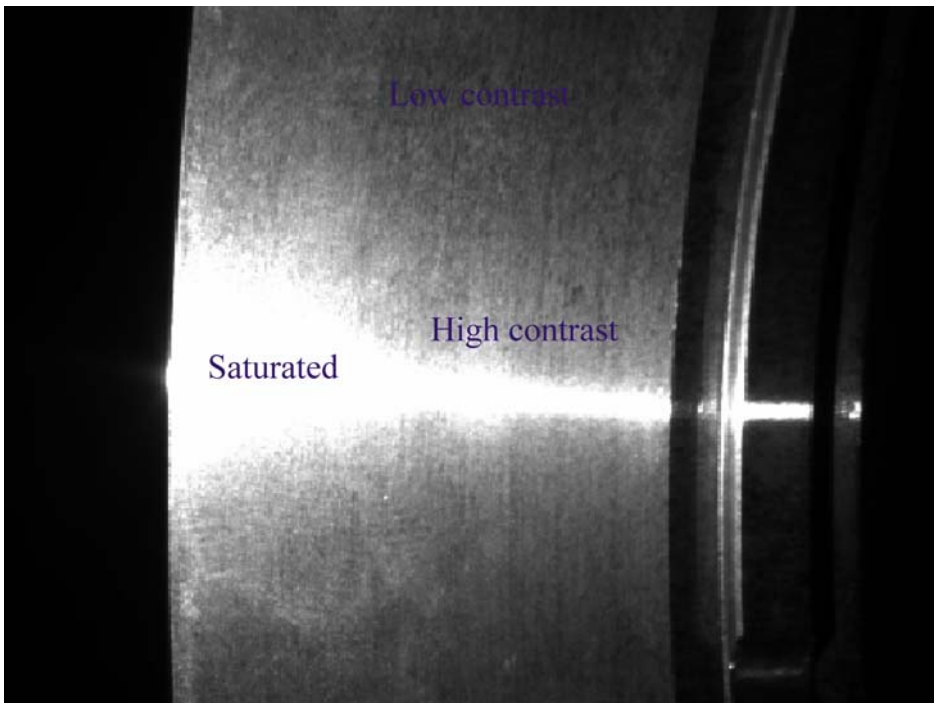

Figure 42: Variation of speckle contrast with angle.

For the measurements of speckle contrast here, the planar or close to planar objects (items 1, 2 and 5) were illuminated approximately normally and observed at an angle of about 30 degrees, corresponding with a typical fringe projection setup. Objects 3 and 4 were non-planar, so the observation and illumination angles both varied across their surfaces. This may have been at least a partial cause of the large error bars in the results for object 3. The small areas chosen to calculate the speckle contrast were chosen to be quite close to, but not within, the saturated areas in order to get the worst case values. The areas were chosen to be small so that the surface shape approximates a plane, as deviation from planarity would result in a higher measured contrast than the true value. The remaining small difference in surface shape between each area could be another cause of the large standard deviation seen in the results, particularly for object 3. Furthermore, in deriving the theoretical relationship between roughness and speckle contrast it is generally assumed that the surface has randomly distributed scattering cells. The objects used here have a systematic component to the surface texture as is usual for manufactured objects. Also, in general, it is not possible to distinguish between intensity variations due to surface texture, but from facets further apart than the coherence length and therefore not contributing to the interference pattern, from those that truly are due to speckle. The results for speckle contrast here should really be viewed as being qualitative and showing the general trend between the different objects rather than a quantitative measurement. Nevertheless they provide an estimate of the speckle contrast that will be used in the later chapters.

4.4 Conclusions

Experimental systems for photogrammetry and fringe analysis have been used to demonstrate photogrammetric measurements with accuracy 1 part in 7500 and fringe analysis measurements with accuracy 1 in 3300. Photogrammetric measurement using measured phase to provide corresponding points yielded an accuracy of 1 in 2400. The software and algorithms used to make these measurements have been discussed in some detail and some causes of error have been highlighted, including noise, the camera model, phase calculation algorithms and the phase to height calibration function.

The next two chapters describe new fringe analysis techniques that have been developed to enable a fringe projection probe to be used on a CMM. The techniques are demonstrated initially using the fixed camera and projector systems characterised above.

Chapter 5 Phase shifting by relative motion of object and projector

5.1 Introduction

In most temporal phase shifting fringe projection systems the phase shift is created either by moving one of the components such as a grating or mirror relative to the light source or by using a programmable projector. In this chapter the creation of a phase shift by relative motion of the object and fringe projector is investigated. The projector need only project a single, fixed fringe pattern to create phase shifted fringe images and can therefore be simply constructed; a digital projector, or moving parts within the projector, is unnecessary. The aim is to develop a CMM-mounted probe consisting of a single camera and fringe projector with a fixed relative spatial relationship. The probe would be moved around with its position accurately reported by the CMM.

Kranz et al. [135] described a system consisting of a camera and fringe projector with an object mounted on a translation stage. The stage was moved parallel to the camera image plane and perpendicular to the projected fringes. The object was moved by a distance equivalent to an integral number of pixels at the camera image plane. Thus, each image could be compensated by translation so that each translated pixel imaged the same point on the object before and after the motion. The phase for each imaged object point was calculated using a phase shift algorithm, and related to the height at each point.

Using the fringe projection model described in Chapter 3, the phase incident on an object point $\underline{X}_p$ (expressed in projector coordinates) was given by equation (20) as

$$\phi\left(\underline{X}_P\right) = -\frac{2\pi c_p}{p}\frac{X_P}{Z_P} \tag{66}$$

Differentiating this with respect to $\underline{X}_P$ gives

$$\underline{\nabla}\phi = -\frac{2\pi c_P}{p}\begin{pmatrix} 1 \\ 0 \\ -\dfrac{X_P}{Z_P} \end{pmatrix}$$

and therefore the change in phase $\delta\phi$ for a general small change in the object position $\underline{\delta X}$ is given by

$$\delta\phi(\underline{X}_P) = -\frac{2\pi c_P}{pZ_P}\left(\hat{\underline{X}}_P - \frac{X_P}{Z_P}\hat{\underline{Z}}_P\right).\underline{\delta X} \tag{67}$$

Assume that the object can be moved relative to the projector parallel to the camera's $\hat{\underline{X}}$ axis, so that the motion can be expressed as $\underline{\delta X} = |\underline{\delta X}|\hat{\underline{X}}$. The phase shift resulting from the motion depends on the distance between object and projector, Z_P, and the relative orientation of the camera and projector. However, since the object has also been moved relative to the camera, in order to calculate the phase at the object's surface the phase shifted images must be compensated for the motion. The shift in the camera image plane equivalent to the motion is given by

$$\underline{\delta x} = \frac{c\underline{\delta X}}{Z} = \frac{c|\underline{\delta X}|\hat{\underline{X}}}{\hat{\underline{Z}}.(\underline{X}_P + \underline{X}_{OP})} \tag{68}$$

So in general the correct image compensation depends on the unknown distance between the camera and the object. That is, the number of pixels equivalent to the object motion varies with distance between the object and camera. If the stand-off distance is large compared to object depth or if a telecentric camera lens is used then the magnification will be approximately constant throughout the measuring volume and Kranz's method may give acceptable results. However if this is not the case and the magnification varies then errors are introduced. In our application we expect to view objects from a relatively short stand-off distance, so that as much of the CMM's measuring volume as possible may be used. A telecentric imaging system is impractical because of the weight and size restrictions of the probe. Therefore we do not expect this method to be successful, and it is mentioned here only as a simple example of calculating phase from phase shifted images created by relative motion of the object and fringe projection probe.

Two different methods are discussed below to create the phase shift used to calculate the phase. In the first method the object and probe are relatively translated as described above, but the object shape provides a phase shift without compensating for the motion. This is referred to as the surface gradient method as the phase shift size depends on the

slope of the surface. The second method, which is called the pinhole or perspective centre rotation method, rotates the probe about the perspective centre of the camera. This motion can be compensated for independently of the distance to the object allowing the phase and therefore the height to be calculated. Experimental results from the two phase step techniques are presented in sections 5.4 and 5.5 below.

5.1.1 Surface gradient method

Like Kranz's method, the surface gradient method also translates the object with respect to the probe. However, rather than compensating for the motion with respect to the camera, the fact that a pixel images different points on the object before and after the motion results in a phase shift. Any change in height between the points imaged before and after the motion will result in a change in the phase recorded. In particular, if the object is translated parallel to the camera image plane and perpendicular to the fringes as in the previous sub-section, then the change in phase experienced by a particular pixel will be only due to the shape of the object. The size of the phase shift is related to the surface gradient and the distance to the object. If the object is planar and parallel to the camera image plane then no phase shift will be observed.

Consider the fringe projection probe and object in Figure 43. The phase incident on the point viewed by pixel $\underline{x}$ in Figure 43(a) was given by equation (24):

$$\phi(\underline{x},h) = -\frac{2\pi c_p}{p}\frac{\hat{\underline{X}}_P \cdot \left(Z_R \underline{x} + c\underline{X}_{OP}\right) - \hat{\underline{X}}_P \cdot \underline{x}h}{\hat{\underline{Z}}_P \cdot \left(Z_R \underline{x} + c\underline{X}_{OP}\right) - \hat{\underline{Z}}_P \cdot \underline{x}h} \tag{69}$$

If the probe is then translated parallel to the camera image plane by some distance δX, then the same pixel $\underline{x}$ will view a different point on the object, see Figure 43(b). The height of this point is $h' = h + \delta h$, and by differentiating equation (24) it can be shown that the change in phase is given by

$$\delta\phi = -\frac{2\pi c_P}{p}\frac{\left[\left(\hat{\underline{Z}}_P \cdot \underline{x}\right)\left(\hat{\underline{X}}_P \cdot \underline{X}_{OP}\right) - \left(\hat{\underline{X}}_P \cdot \underline{x}\right)\left(\hat{\underline{Z}}_P \cdot \underline{X}_{OP}\right)\right]}{\left[\left(Z_R - h\right)\left(\hat{\underline{Z}}_P \cdot \underline{x}\right) + c\left(\hat{\underline{Z}}_P \cdot \underline{X}_{OP}\right)\right]^2}\delta h \tag{70}$$

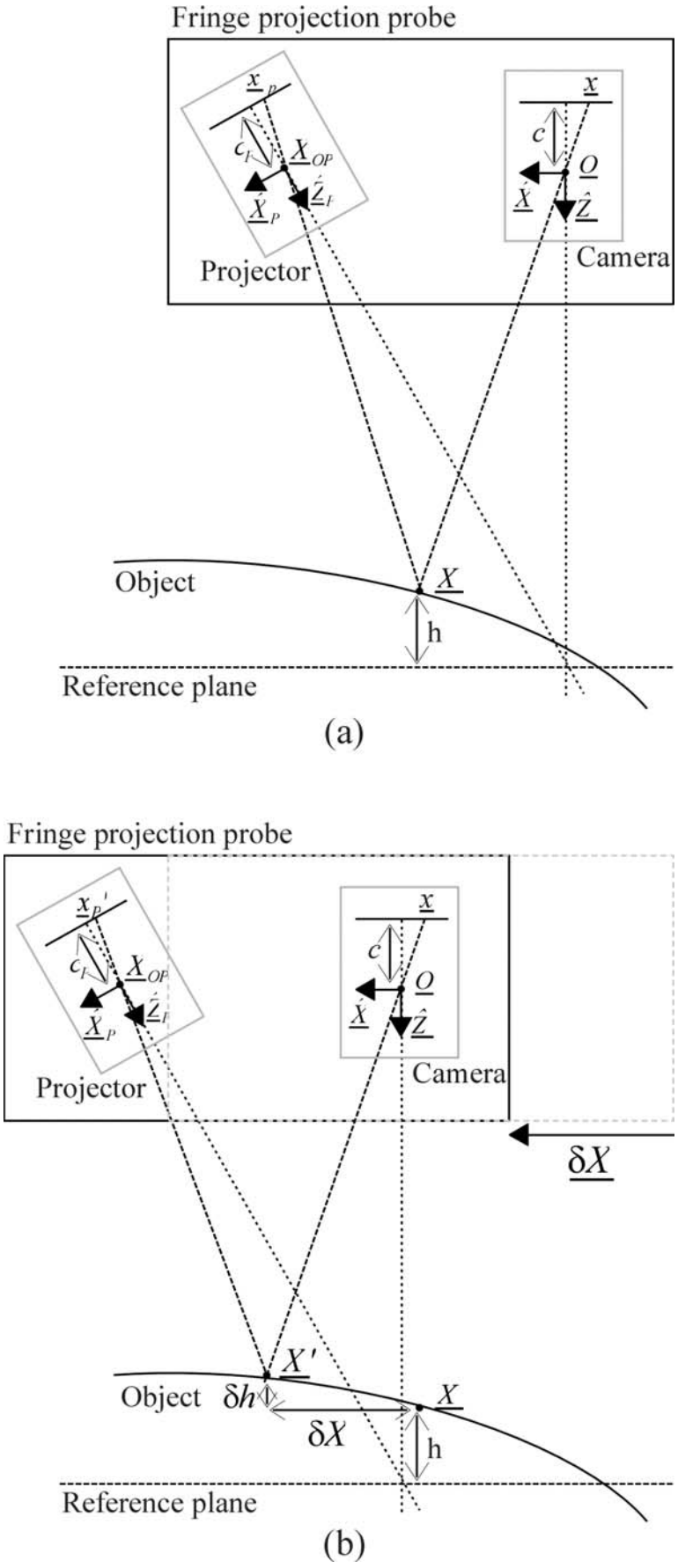

Figure 43: Surface gradient method of phase shifting by relative motion of fringe projector and measurement object.

That is, the change in phase is proportional to the change in height. The factor of proportionality depends on the object shape. The change clearly depends on the shape of the object. For example it can be deduced from Figure 43 that the change in height relative to the reference plane is

$$\delta h = \frac{g\,\delta X}{1 + g\,\frac{x}{z_c}} \tag{71}$$

where g is the average gradient of the object over the distance δX. The limits of this method are the gradient and curvature of the object. If the gradient is too low then little or no phase step is induced. If the is gradient too high then the non-linear relation between phase and height results in non-constant phase steps between successive steps. A curved object may also result in non-constant phase steps. However the distance the probe is shifted can be varied to compensate for these factors, to an extent. If the measured phase shift on some surface area is observed to be too small (or too large) the translation used to create it can be increased (or decreased). In general, however, increasing the translation will increase the likelihood of the surface gradient, height or other surface properties such as reflectivity changing significantly over the scale of the motion, which will cause errors in the calculated phase. The phase step algorithms assume constant phase shift, background illumination and fringe modulation amplitude between frames. Close to edges the algorithm is unlikely to be successful.

5.1.2 Rotation about perspective centre method

Relative translation of object and camera results in a change in perspective, which means that some points on the surface visible before translation may be occluded after it, or vice versa. Relative rotation of object and camera about the camera's perspective centre introduces no perspective change so the same object points are visible before and after the motion (apart from, of course, points close to the edge of the camera's field of view no longer within it after the motion). Furthermore, it is possible to compensate the images for the motion without knowing the distance to the object.

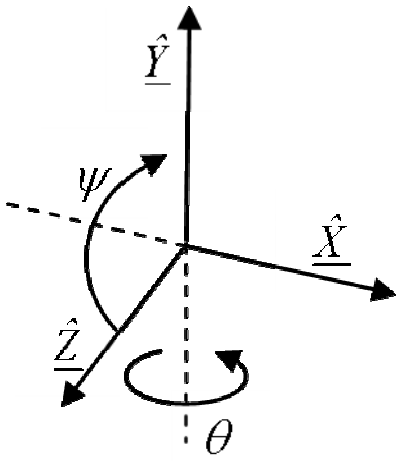

Figure 44: Definition of spherical coordinate system.

Consider a spherical coordinate system (ρ,θ,ψ) with origin coincident with the global origin where θ and ψ are azimuth and zenith angles as indicated in Figure 44, and ρ is the distance from the origin. The directions of the angles are chosen to coincide with the D and E angles, respectively, of an articulating head on a CMM.

A point $\underline{X}$ may be expressed in Cartesian coordinates as

$$\underline{X} = \begin{pmatrix} X \\ Y \\ Z \end{pmatrix} = \begin{pmatrix} \rho \sin\theta \cos\psi \\ \rho \sin\psi \\ \rho \cos\theta \cos\psi \end{pmatrix} \tag{72}$$

According to the pinhole camera model, this point is imaged, in camera coordinates, at $\underline{x} = (x, y, -c)'$ where

$$\frac{x}{-c} = \frac{X}{Z} = \tan\theta \tag{73}$$

and

$$\frac{y}{-c} = \frac{Y}{Z} = \frac{\tan\psi}{\cos\theta} \tag{74}$$

Since these expressions are independent of ρ, the distance between object and camera, then for any pixel imaging an object the pixel corresponding to the same point on the object after rotation about the camera perspective centre can be calculated. This is depicted in Figure 45.

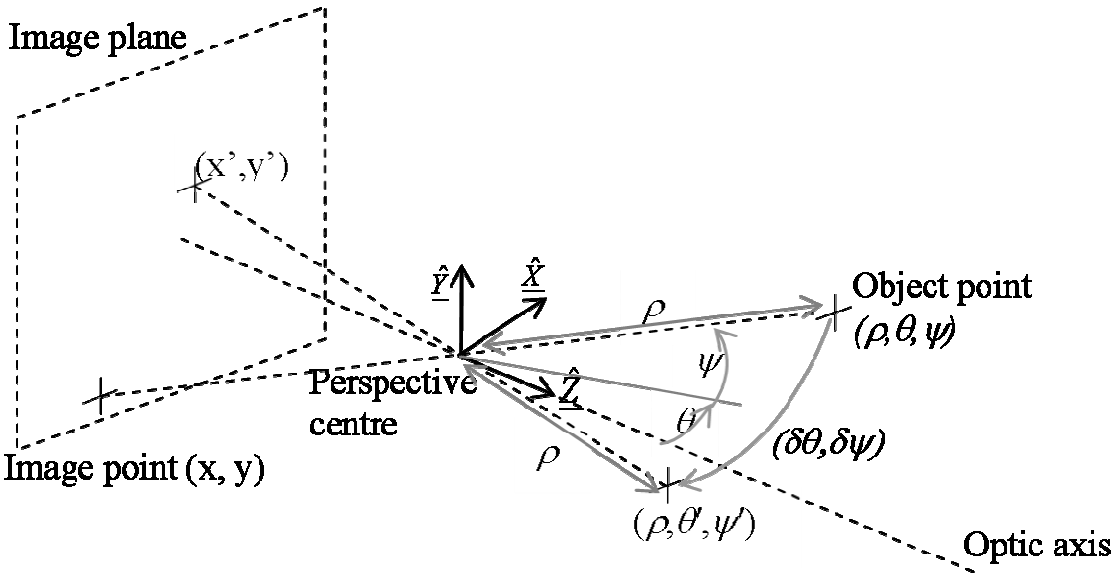

Figure 45: Rotation about perspective centre.

Specifically, if pixel (x, y) images point $\underline{X}$ on an object, and then the object is moved through angles $(\delta\theta, \delta\psi)$, then pixel (x', y') images the same point on the object after the movement where,

$$x' = -c\tan(\theta + \delta\theta) = -c\frac{x + c\tan\delta\theta}{c - x\tan\delta\theta} \tag{75}$$

$$y' = -c\frac{\tan(\psi + \delta\psi)}{\cos(\theta + \delta\theta)} = -c\frac{y + \sqrt{x^2 + c^2}\tan\delta\psi}{\left(x\sin\delta\theta - c\cos\delta\theta\right)\left(\frac{y}{\sqrt{x^2 + c^2}}\tan\delta\psi - 1\right)} \tag{76}$$

These equations can be used to compensate images recorded with relative rotation of object and camera between each image. Then each pixel in a compensated image taken after the motion will view the same point as an image taken prior to the motion. This is verified by experiment in section 5.3.

Because the object has moved relative to the projector, the phase incident on the object point will have changed. Using equation (21), the phase shift may be calculated for a point in 3D space as

$$\Delta\phi = -\frac{2\pi c_P}{p}\left[\frac{\hat{\underline{X}}_P \cdot \left(\underline{X}' - \underline{X}_{OP}\right)}{\hat{\underline{Z}}_P \cdot \left(\underline{X}' - \underline{X}_{OP}\right)} - \frac{\hat{\underline{X}}_P \cdot \left(\underline{X} - \underline{X}_{OP}\right)}{\hat{\underline{Z}}_P \cdot \left(\underline{X} - \underline{X}_{OP}\right)}\right]$$
$$= -\frac{2\pi c_p}{p}\frac{\left(\hat{\underline{X}}_P \cdot \left(\underline{X}' - \underline{X}_{OP}\right)\right)\left(\hat{\underline{Z}}_P \cdot \left(\underline{X} - \underline{X}_{OP}\right)\right) - \left(\hat{\underline{X}}_P \cdot \left(\underline{X} - \underline{X}_{OP}\right)\right)\left(\hat{\underline{Z}}_P \cdot \left(\underline{X}' - \underline{X}_{OP}\right)\right)}{\left(\hat{\underline{Z}}_P \cdot \left(\underline{X}' - \underline{X}_{OP}\right)\right)\left(\hat{\underline{Z}}_P \cdot \left(\underline{X} - \underline{X}_{OP}\right)\right)} \quad (77)$$

By repeating the rotation and compensating the recorded image for the motion each time, a set of phase shifted images is produced which is used to calculate the phase using a phase shift algorithm. The phase shift for each pixel depends on the fringe pattern projected, the relative position and orientation of the projector and camera and the distance to the object, as well as the angles moved through.

The total motion to create a set of images with a satisfactory phase shift is approximately equal to the fringe pitch at the object's surface. The motion and resulting phase shift is discussed below in more detail using a small angle approximation, which is satisfied by having a fringe pitch small compared to the distance between camera and object. This is a desirable condition in general for fringe projection systems as the smaller the fringe pitch the better the height resolution (up to the limits of camera and projector resolution). Using the small angle approximation, a point $\underline{X}$ following the rotation may be expressed relative to the camera perspective centre as

$$\underline{X}' = \underline{X} + |\underline{X}|\omega\hat{\underline{V}} \quad (78)$$

where ω is the small angle moved through and $\hat{\underline{V}}$ is the unit vector in the direction of the motion. To maximise the phase change the direction of the rotation should be perpendicular to the fringes, which again are assumed to extend in the $\hat{\underline{Y}}_P$ direction. In this case unit vector $\hat{\underline{V}}$ is perpendicular to $\hat{\underline{X}}$ and to $\hat{\underline{Y}}_P$ and can be expressed as

$$\hat{\underline{V}} = \frac{\underline{X} \times \hat{\underline{Y}}_P}{\left|\underline{X} \times \hat{\underline{Y}}_P\right|} \quad (79)$$

Using equations (20) and (79), the phase change resulting from the movement described above is

$$\begin{aligned}\Delta\phi &= \frac{-2\pi c_P}{p}\left(\frac{X_P + |\underline{X}|\hat{\underline{X}}_P.\hat{\underline{V}}\omega}{Z_P + |\underline{X}|\hat{\underline{Z}}_P.\hat{\underline{V}}\omega} - \frac{X_P}{Z_P}\right) \\ &= \frac{-2\pi c_P}{p}|\underline{X}|\left(\frac{\hat{\underline{X}}_P.\hat{\underline{V}} - \frac{X_P}{Z_P}\hat{\underline{Z}}_P.\hat{\underline{V}}}{Z_P + |\underline{X}|\hat{\underline{Z}}_P.\hat{\underline{V}}\omega}\omega\right)\end{aligned} \tag{80}$$

To the first order, this gives

$$\Delta\phi \approx -2\pi\frac{c_P}{pZ_P}|\underline{X}|\left(\hat{\underline{X}}_P - \frac{X_P}{Z_P}\hat{\underline{Z}}_P\right).\hat{\underline{V}}\omega,\ |\underline{X}\omega| << Z_P \tag{81}$$

where the linear approximation is valid providing the projector to object distance is large compared to the motion.

Equation (81) separates into a number of factors: $\frac{pZ_P}{c_P}$ represents the period of the fringes at a point some distance Z_P from the projector; $\left(\hat{\underline{X}}_P - \frac{X_P}{Z_P}\hat{\underline{Z}}_P\right).\hat{\underline{V}}$ corresponds to the component of the motion contributing to the phase change; and $|\underline{X}\omega|$ is the magnitude of the motion.

To further aid understanding of the effect of the rotation about perspective centre, consider now the simplified system described in section 3.4.1 and depicted in Figure 12, in which the camera and projector optic axes are coplanar. The direction of the approximate linear motion corresponding to rotation about the camera's $\hat{\underline{Y}}$ axis at the intersection point of the optic axes is $\hat{\underline{V}} = (-1,0,0)'$ (in camera coordinates). The phase change created at this point is

$$\Delta\phi = \frac{2\pi}{W}\frac{S^2}{\sqrt{S^2 + D^2}}\omega \tag{82}$$

where $W = \frac{p}{c_P}\frac{X_{OP}}{D}\sqrt{S^2 + D^2}$ is the fringe pitch at the axis intersection point.

Phase step algorithms tend to have an optimum phase step value, at which their response is insensitive to noise and other error sources. For example, it has been shown that the optimum phase step for Carré's algorithm for noisy images is close to 110°

[136]. Suppose that the phase change at the axis intersection point is chosen to be the optimum phase step value, $\Delta\phi_{opt}$ radians, for whichever phase step algorithm is to be used. Then the required motion is given by

$$\omega = \frac{\Delta\phi_{opt}}{2\pi} W \frac{\sqrt{S^2 + D^2}}{S^2} \tag{83}$$

It is clear that the small angle approximation of ω<<1 is satisfied providing D is at most of the same order as S (i.e. separation of projector and camera is at most comparable to the standoff distance), and the fringe period at the axis intersection point is small compared to the standoff (W<<S).

Any other point $\underline{X} = (X, Y, Z)'$ in this simplified system can be expressed in projector coordinates as

$$\underline{X}_P = \frac{1}{\sqrt{S^2 + D^2}} \begin{pmatrix} S(X - X_{OP}) + D(Z - Z_{OP}) \\ Y \\ S(Z - Z_{OP}) - D(X - X_{OP}) \end{pmatrix} \tag{84}$$

The unit vector direction of the approximate linear motion is

$$\underline{\hat{V}} = \frac{\underline{X} \times \underline{\hat{Y}}}{\left|\underline{X} \times \underline{\hat{Y}}\right|} = \frac{1}{\sqrt{X^2 + Z^2}} \begin{pmatrix} -Z \\ 0 \\ X \end{pmatrix} \tag{85}$$

By substitution into equation (81) it can be shown that the phase change due to the motion is

$$\Delta\phi = \Delta\phi_{opt} \frac{\left(S^2 + D^2\right)^{3/2}}{S^2} \frac{\left|\underline{X}\right|}{\sqrt{X^2 + Z^2}} \frac{XO}{d} \frac{Z(Z - Z_{OP}) + X(X - X_{OP})}{\left(S(Z - Z_{OP}) - D(X - X_{OP})\right)^2} \tag{86}$$

Setting S to 1 to work in units of “standoff distances”, this gives

$$\frac{\Delta\phi}{\Delta\phi_{opt}} = \left(1 + D^2\right)^{3/2} \frac{\left|\underline{X}\right|}{\sqrt{X^2 + Z^2}} \frac{XO}{D} \frac{Z(Z - Z_{OP}) + X(X - X_{OP})}{\left((Z - Z_{OP}) - D(X - X_{OP})\right)^2} \tag{87}$$

This expression allows us to analyse the range of 3D points in space over which a valid result is possible. For instance, for Carré’s algorithm to yield a successful result, a phase step between around $\frac{\pi}{4}$ and $\frac{3\pi}{4}$ is desirable [137,136], so $\Delta\phi$ as modelled above should satisfy $\frac{1}{2} \le \frac{\Delta\phi}{2\pi} \le \frac{3}{2}$.

As an example, consider a system with D=0.5S, giving an angle between the projector and camera axes of approximately 27°, and, furthermore, the projector is at the same height as the camera so that $\underline{X}_{OP} = (D,0,0)'$. Assume the camera has a square pixel array whose width is equal to the principal distance, and is focussed on the intersection point of the axes. By considering the depth of field to be equal to the standoff distance, then the measuring volume is defined by $-0.5 \le X,Y \le 0.5$ and $0.5 \le Z \le 1.5$. Figure 46 shows the calculated phase shifts at different locations throughout the measurement volume. The values are outside the desirable range towards the edge of the measurement volume, indicating that it may be wise to exclude values from the corresponding side of the recording image from the measurement. However most of the measurement volume should yield an acceptable result.

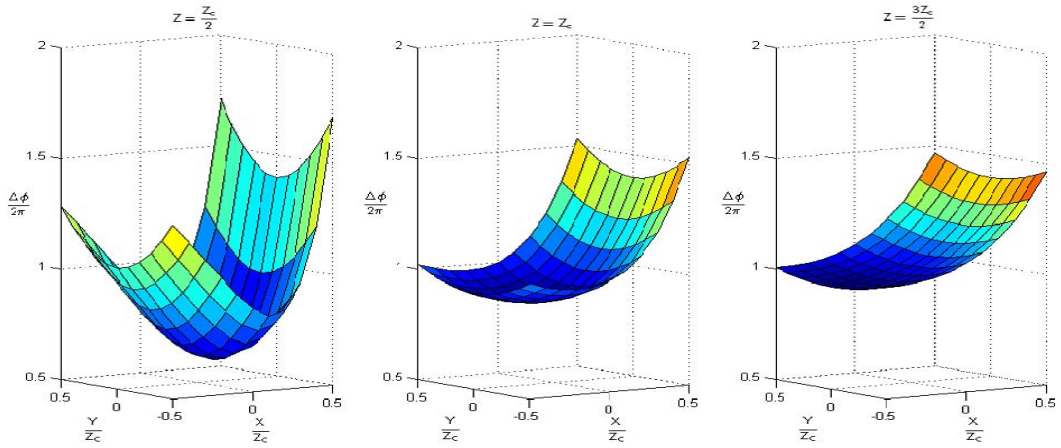

Figure 46: Calculated phase shifts at different places through the measurement volume.

The experimental setup used to investigate both the surface gradient technique and the perspective centre rotation technique will now be described. Results and a discussion of the potential error sources are presented in sections 5.4 to 5.6.

5.2 Experimental setup

The technique was tested using a fixed camera and projector with the object to be measured attached to a five-axis CMM. The equipment used, and the calibration procedures were discussed in more detail in Chapter 4. The approximate fringe projection system dimensions are depicted in Figure 47, using the simplified fringe projection model. Notice that the characteristics of the projector are unknown – that is the position of the pixel array, the lens focal length and the pixel size are unknown, and

therefore so is the position of its perspective centre. The angle between the optic axes was estimated from the relative orientation of the lenses. While the focal length of the projector lens system and the projector's perspective centre could be estimated from its magnification at different image distances this was not necessary. Use of the simplified model introduced earlier allows the system to be analysed in terms of the camera standoff and the width of the fringes at the intersection of the camera and projector axes, and so the parameters relating to the projector are not required to be known.

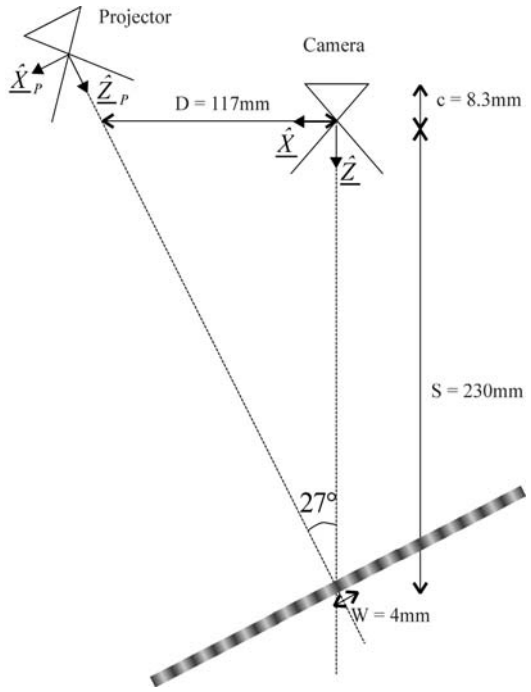

Figure 47: Model of camera and fringe projector used experimentally.

Phase shifts were created using both the surface gradient technique and the rotation about the perspective centre technique described above. The results were compared to standard temporal phase shifting using the programmable digital projector to project multiple phase shifted fringe patterns. For the surface gradient technique, the object was moved nominally in the camera $\hat{X}$ direction. For both techniques sets of both 4 and 5 phase shifted images were collected. The phase was calculated using Carré's algorithm for 4 frame data and algorithm A1 from Novak [138] for the 5 frame data. Phase maps were unwrapped using a standard "flood-fill" algorithm. The zero order fringe from which to start the unwrapping was identified for each phase map from an image of a single projected line.

Section 5.3 validates the compensation of images for rotation about the camera perspective centre. Section 5.4 evaluates phase to height calibrations using the new techniques, and section 5.5 presents some results from measuring a curved object.

5.3 Verification of compensation for rotation about perspective centre

In order to verify equations (75) and (76), a custom made touch probe with a black stylus holder and white spherical tip was attached to the CMM. A photograph was taken of the tip, which was then moved in an arc about the camera's perspective centre, and a second photo taken. This was repeated a number of times, for angles of 1 to 4 degrees at different positions throughout the camera's field of view and at different distances from the camera. A sample image is shown in Figure 48. The centres of the imaged probe tips were found using standard image processing techniques. Equations (75) and (76) were used to predict positions of the tip in the post-rotation images from the centres found in the pre-rotation images. The difference in the calculated positions and the actual positions are shown in Figure 49. The maximum error is 1.1 pixels, and the RMS error is 0.2 pixels which is the estimated uncertainty in the location of the centres of the probe tips in the images.

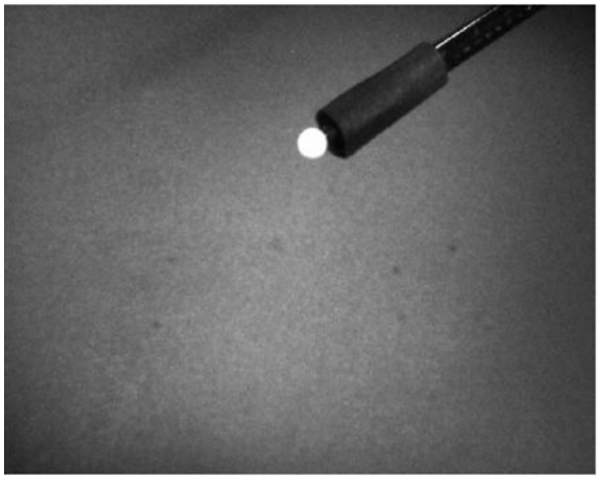

Figure 48: Sample image of tip of custom-made probe for verification of image compensation for rotation about perspective centre.

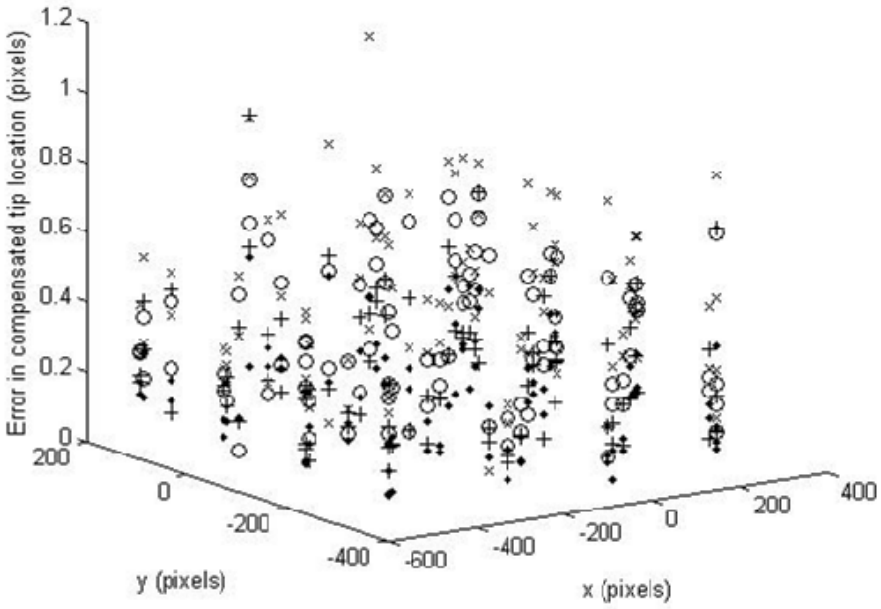

Figure 49: Errors in calculated probe tip positions.

5.4 Phase to height calibration

A phase to height calibration was carried out as described in section 4.2.2, using a planar object attached to the CMM, moved to different heights using the CMM linear axes. The exact mounting of the plane on the head was unknown so an image of the camera calibration target attached to the plane was analysed to find its position and orientation relative to the camera. The plane was nominally normal to the camera optic axis for the perspective centre rotation phase shift technique. With the surface gradient technique no phase step would be observed for a plane in this orientation, so in this case the plane was inclined at a nominal angle of 30° to the camera image plane. For collecting temporal phase shifted data using the programmable projector the plane was nominally parallel to the camera image plane in the usual way. In each case, a set of data with four frames and a set of data with five frames were collected. One of the plane measurements (for each data set) was selected as a reference plane and cubic polynomial coefficients were fitted for each pixel relating phase to height relative to the reference plane measurement.

Relative height errors from the phase to height calibration were calculated for each pixel, for each measured plane. As an example, the errors for a single line across the camera image are plotted for the plane 50 mm from the reference plane in Figure 50.

The mean and RMS errors for the whole plane are listed in Table 11. They were converted to fractions of a fringe period using the approximate conversion of 1 fringe period to 4 mm corresponding to the nominal fringe period at the intersection point of the camera and projector optic axes.

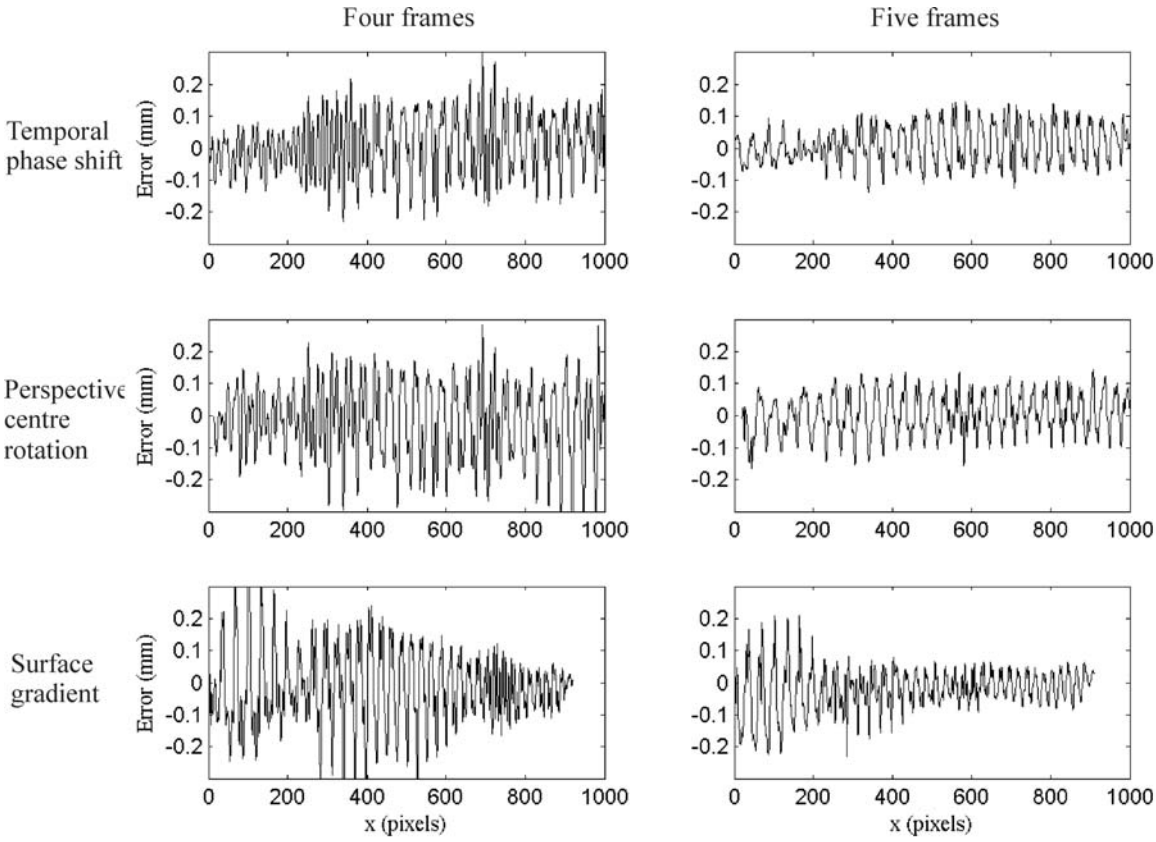

Figure 50: Phase to height calibration errors, relative to the reference plane.

Table 11: Summary of phase to height calibration errors.

Phase shift method	Number of frames	Mean error (μm)	RMS error (μm)	Mean error (% of a fringe period)	RMS error (% of a fringe period)
Temporal (projector) shift	4	7.0	94.6	0.18	2.4
	5	9.6	59.4	0.24	1.5
Surface gradient	4	-15.6	122.9	-0.39	3.1
	5	-20.6	70.0	-0.5	1.8
Perspective centre rotation	4	-1.9	122.0	-0.05	3.1
	5	3.6	65.8	0.09	1.6

The data created with the temporal phase shift were the same data as used in section 4.2.2, but the phase has been calculated using Carré's algorithm, in the case of the four frame algorithm and Novak's algorithm for the five frame data. Comparison of the height errors in Table 11 with those given in Table 2 shows the adverse effect of the unknown phase shift algorithms – the RMS errors here were approximately double

those previously reported. The errors from the new phase shift techniques were comparable to, but slightly larger than, the temporal phase shift data. In each case the RMS error was considerably reduced by using 5 frames rather than 4, as is usual for phase stepping fringe projection. Notice that the improvement for the new phase shift techniques is surprisingly large, around 50%. A reduction in the RMS error of between 10% and 25% would have been expected. Again, the mean errors are characteristic of using the cubic polynomial for the phase to height calibration rather than a more appropriate model. The close agreement in the RMS errors between the new phase shift techniques and the projector shifted data validates both of new techniques as viable approaches to phase stepping.

5.5 Object measurement

Following phase to height calibration an unknown object was measured. A curved object was mounted on the head and measured using the two new methods. Again, a traditional temporal phase shift was also used for comparison. This time, the temporal phase shifted data were processed using Bruning's algorithm to get the best possible measurement with the equipment in use. A sample fringe image of the object is shown in Figure 51, and three phase maps, one from each phase shift technique are shown in Figure 52. Each phase map was unwrapped using a flood-fill algorithm starting from the zero order fringe identified by a single projected line.

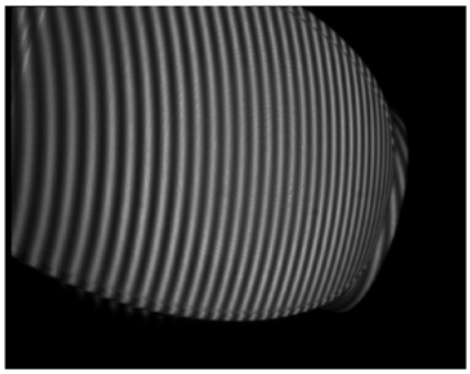

Figure 51: Sample fringe image.

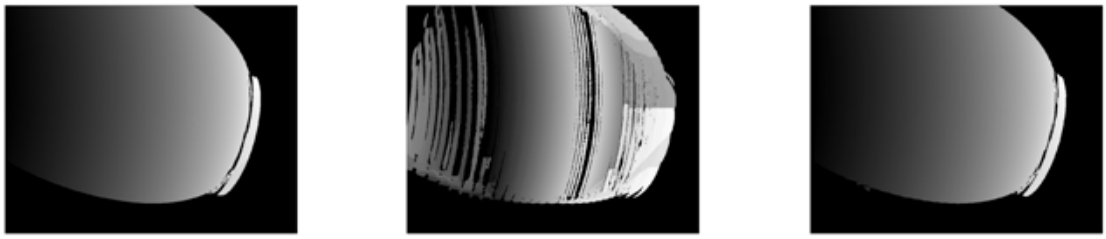

(a) (b) (c)

Figure 52: Phase maps found by (a) temporal (b) surface gradient and (c) perspective centre rotation phase step techniques.

The phase map from the surface gradient method has gaps and the phase unwrapping algorithm has been unsuccessful in some areas. This was expected – as previously noted, the phase shift size is dependent on the gradient of the object. A successful result from the phase shift algorithm can be achieved for a given translation only where the gradient gives a phase shift of a suitable size. To build up a complete phase map the phase shift process could be repeated using different translations until no gaps remain. However, the surface gradient technique was also expected to work only where the surface properties are slowly varying, and therefore was not expected to work on an object with edges. A sample wrapped phase map of a curved object with stepped blocks attached can be seen in Figure 53 to highlight the problem. Blurring is obvious close to the step and also at the edges of the shadows caused by the attached blocks.

Because of these limitations on the surface gradient technique, the remainder of this analysis concentrates only on the perspective centre rotation technique. The phase map using the rotation method (Figure 52(c)) appears qualitatively similar to phase map from the projector shifted data.

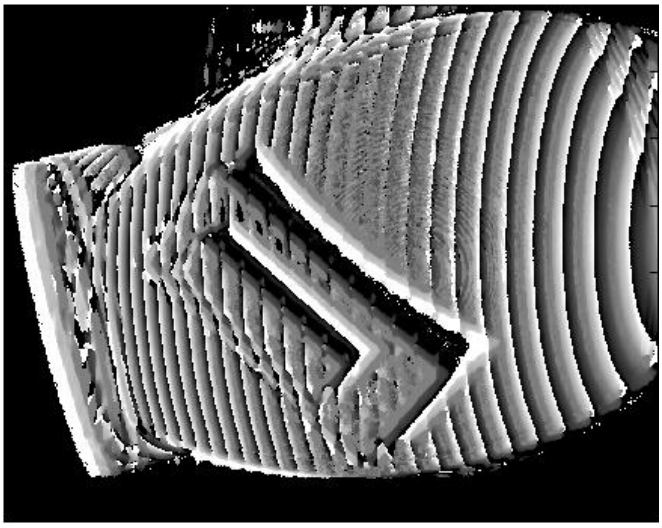

Figure 53: Wrapped phase map created using surface gradient technique, showing problems caused by object edges and shadows.

For a more quantitative comparison, the height of the object relative to the reference plane was calculated using the phase to height calibrations found earlier. The heights for a single line across the phase maps from the 5 frame projector shifted data and the four and five frame perspective centre rotation shifted data are shown in Figure 54. Note that the object depth was around 40 mm. The inset shows a magnified section of the plot where the three sets of data may be seen more clearly over a small range. Also in Figure 54 are the errors for the perspective centre rotation shifted measurements, where the correct measurement is taken to be the 5 frame projector shifted one. The mean and RMS errors are summarised in table Table 12.

Table 12: Object measurement errors from perspective centre rotation method (relative to a measurement from 5-frame projector shifted data).

Number of frames	Mean error (μm)	RMS error (μm)	Mean error (% of a fringe period)	RMS error (% of a fringe period)
4	-29.6	169.7	-0.7	4.2
5	9.7	58.7	0.2	1.5

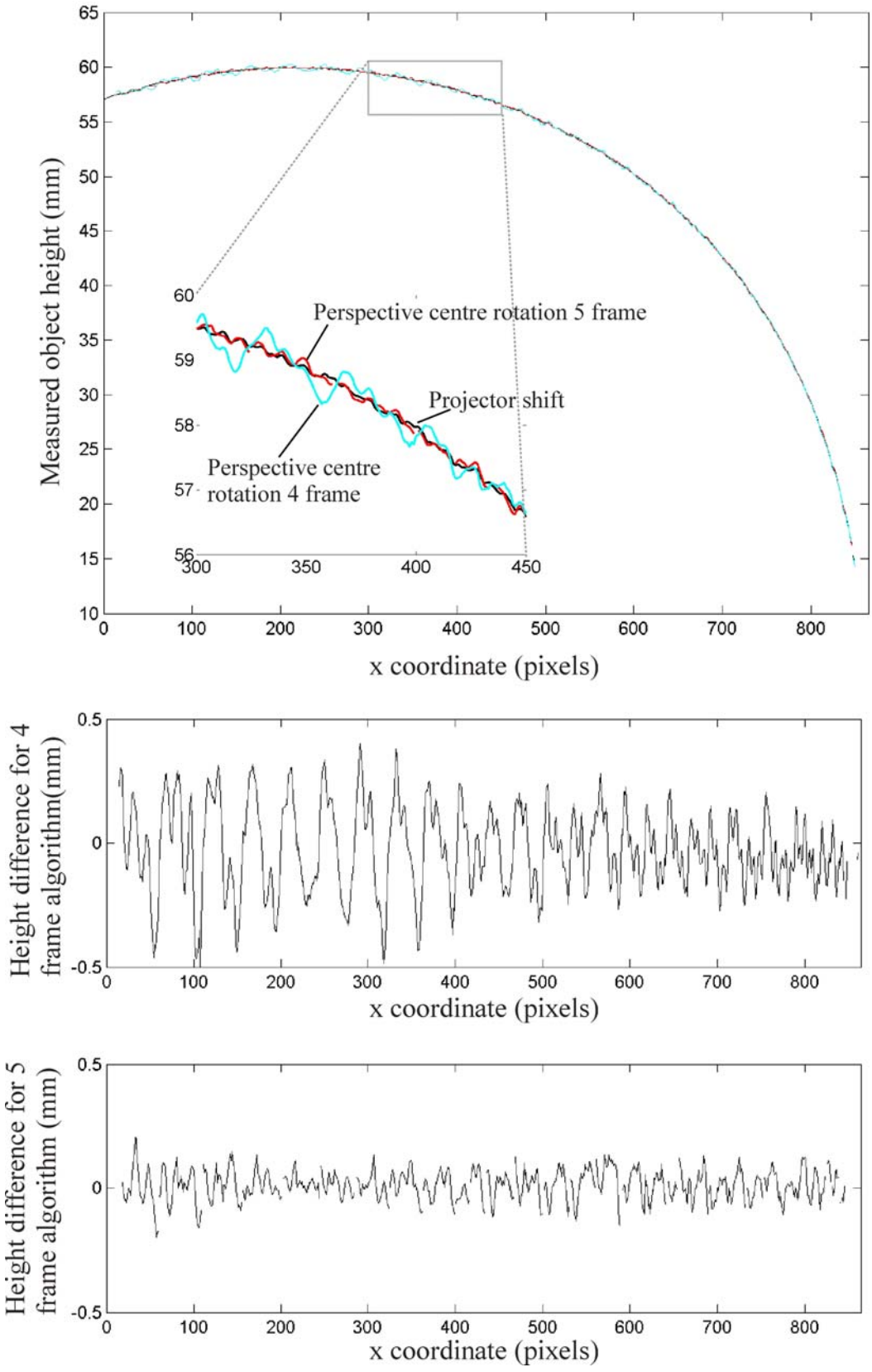

Figure 54: Measured height of object, and errors in perspective centre rotation measurements when compared to projector shifted measurement.

5.6 Discussion

Both of the new techniques have been successfully demonstrated. The calculated phase showed errors comparable to, though slightly larger than, phase calculated from traditional temporal phase shifted fringe images. The surface gradient technique has limited usefulness for objects with edges, and for curved objects requires multiple passes with different translation sizes to build up a complete phase map. Nevertheless, it may be useful as a simple phase step technique for the measurement of smooth objects. The perspective centre rotation technique is more generally useful as was demonstrated by measurement of a curved object. The RMS errors from the measurement were 1.5% of a fringe period, relative to the best available object measurement created using temporal phase stepped data processed using Bruning's algorithm.

The object measured, like the phase to height calibration plane, was a matt white surface. More challenging surfaces such as metallic or non-Lambertian surfaces are expected to result in less accurate measurements from the new techniques compared to temporal phase shifting. Multiplicative noise (speckle), inter-frame intensity variations and non-linear phase shift errors are sources of error that are applicable to the new techniques that are generally insignificant for phase shifting using a programmable projector. The effect of each of these will now be discussed in turn.

5.6.1 Multiplicative noise

Intensity fluctuations due to the roughness of the surface being measured causes multiplicative intensity noise known as speckle noise as discussed in section 3.8. In traditional temporal phase shifting this can reduce the fringe contrast, but affects each recorded image equally and does not cause an error in the calculated phase. However with the phase shift created by relative motion of the object and camera the noise varies from image to image and does not cancel out. The effect of multiplicative noise on the Carré and Novak algorithms was simulated for zero-mean Gaussian distributed noise, and the resulting RMS error for a range of contrast values are shown in Figure 55(a). The RMS value is over one period of phase, and the values have been found by averaging 1000 repetitions of the simulation. The mean phase error is 0.

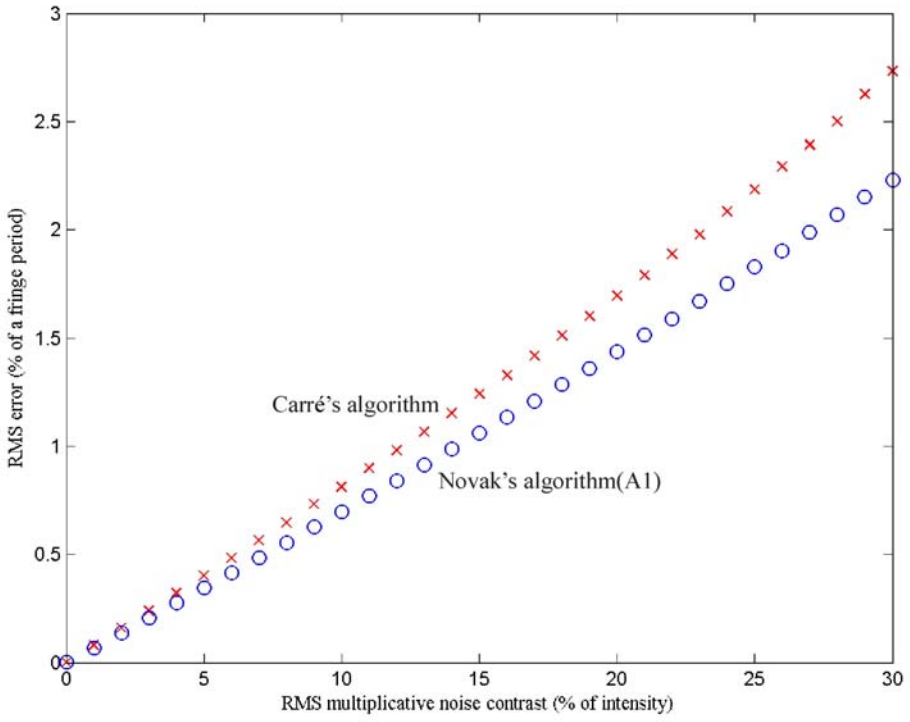

(a)

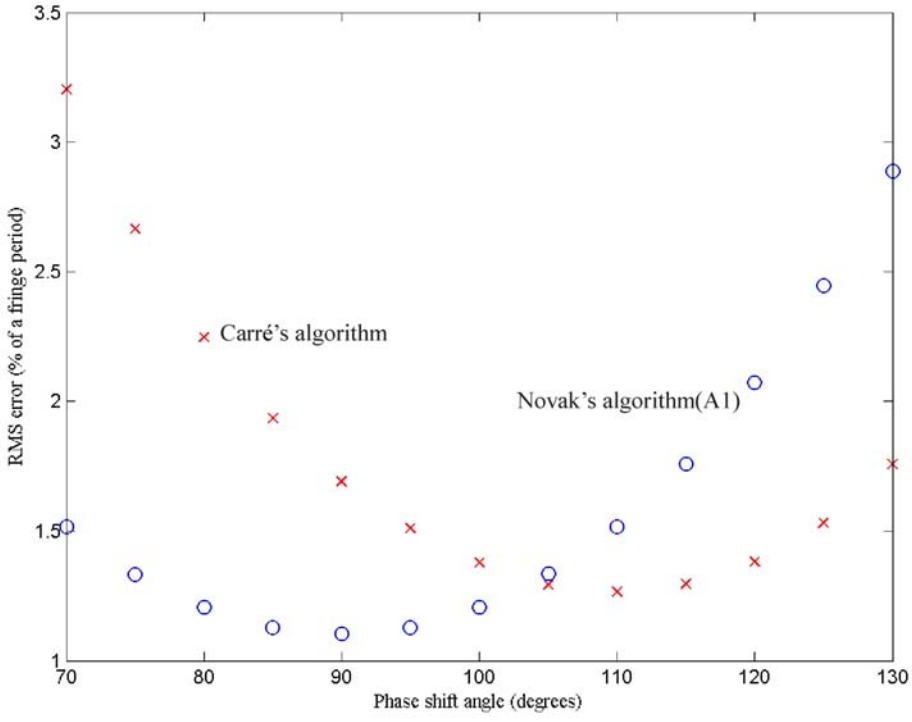

(b)

Figure 55: RMS phase error due to multiplicative (speckle) noise (a) against speckle contrast for phase shift angles of 90° and 110° for Carré's and Novak's algorithms, respectively, and (b) against phase shift angle for a fixed contrast of 20%.

The phase to height calibration plane and the curved object both show a speckle contrast of less than 1% of mean intensity under white light. While speckle noise has had little effect on the measurements presented in this chapter, in Chapter 7 measurements of surfaces with different surface characteristics are demonstrated using a prototype probe with a red LED light source. The surfaces used all have higher speckle contrasts than seen here, and the longer coherence length of the LED compared to white light further increases the speckle contrast. The maximum contrast observed under the red LED is approximately 20% of mean intensity for a smooth machined stainless steel surface. Figure 55(b) shows the simulated variation of RMS phase error against phase shift angle for this maximum typical contrast of 20%. It is clear from this graph that the error from multiplicative noise is minimised for a phase shift of around 110º for Carré's algorithm and 90º from Novak's algorithm.

5.6.2 Inter-frame intensity variation

Because the object is moved relative to the camera and projector to create a phase shift, the mean intensity and amplitude of a recorded fringe may change due to a change in the distance in the path of the light travelling from projector to object to camera. By taking total distance from projector to object point to be approximately equal to the standoff distance S, which is also the distance from camera to object, it can easily be shown that the expected fractional change in intensity is at most of the order of $\frac{W}{4S^2}$. If, for example, the fringe width at the axis intersection point is 0.1S then the intensity change at worst 2.5% of the initial intensity recorded. In general it is to be expected that the fringe width would be considerably smaller than this, therefore the intensity variation is expected to be smaller. For the system used here the fringe width was nominally 4 mm at the standoff distance of 230 mm, giving an estimated intensity variation of less than 0.01% between frames. The resulting phase error is expected to be negligible.

A further source of inter-frame intensity variation is the change in viewing and illumination angle. The variation in reflectance of a surface with viewing and illumination angles depends on the microscopic surface properties [139,140]. For non-Lambertian objects with a specular component to the reflectance, the reflectance changes rapidly with illumination and observation angles close to the specular direction, but more slowly for other angles. For surfaces with a large specular component it is

expected that phase measurement will be less successful close to the specular direction. However for diffusely reflecting regions away from the specular direction it is expected that the reflectance will not change significantly with the small angular change required for the phase shift. The objects measured here were diffuse objects with no obvious specular component, so this was not a significant problem. However in Chapter 7 objects with different characteristics, including non-Lambertian properties, are measured. The response of Carré's algorithm and Novak's algorithm to a linear variation in background intensity and fringe amplitude across a set of phase shifted images was simulated. The mean and RMS errors over one fringe period are shown in Figure 56(a) and (b), respectively. For traditional phase stepping fringe projection systems a mean offset to the calculated phase is constant across the phase map and results in no overall error. Here, however, the mean phase error due to the surface properties can vary across the phase map and cause errors in the shape measurement.

A calibration technique could be developed if these errors are found to be significant. However a more straightforward way to remove much of the intensity variation may be to normalise a set of phase shifted images. For the probe envisaged here, a simpler technique still would be to use the CMM to move the probe to a perspective not close to the specular direction for the surface patch under inspection.

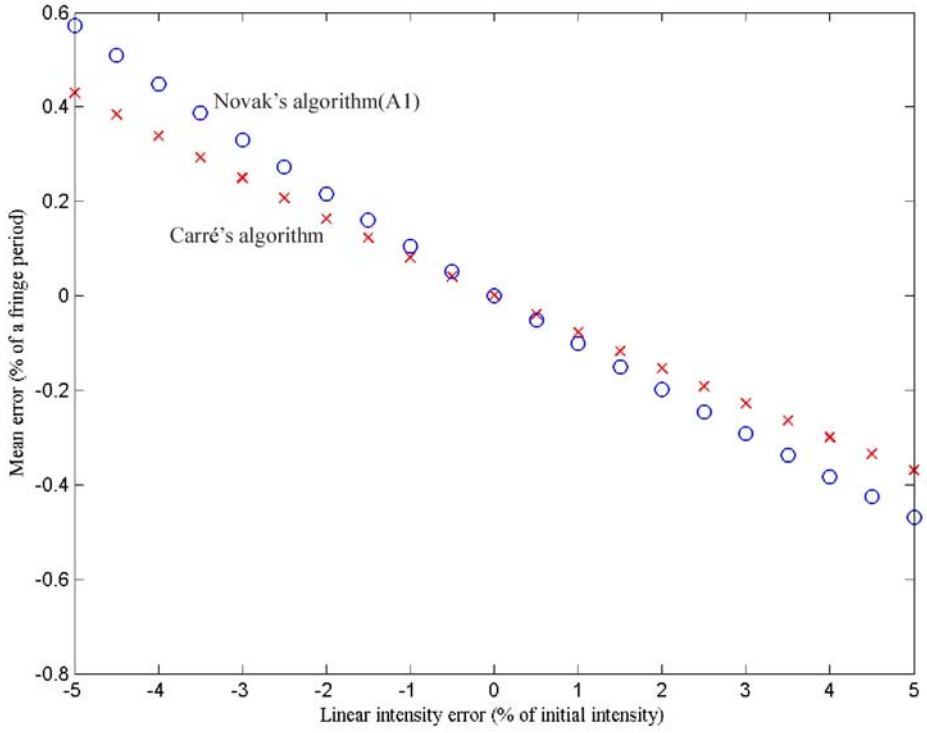

(a)

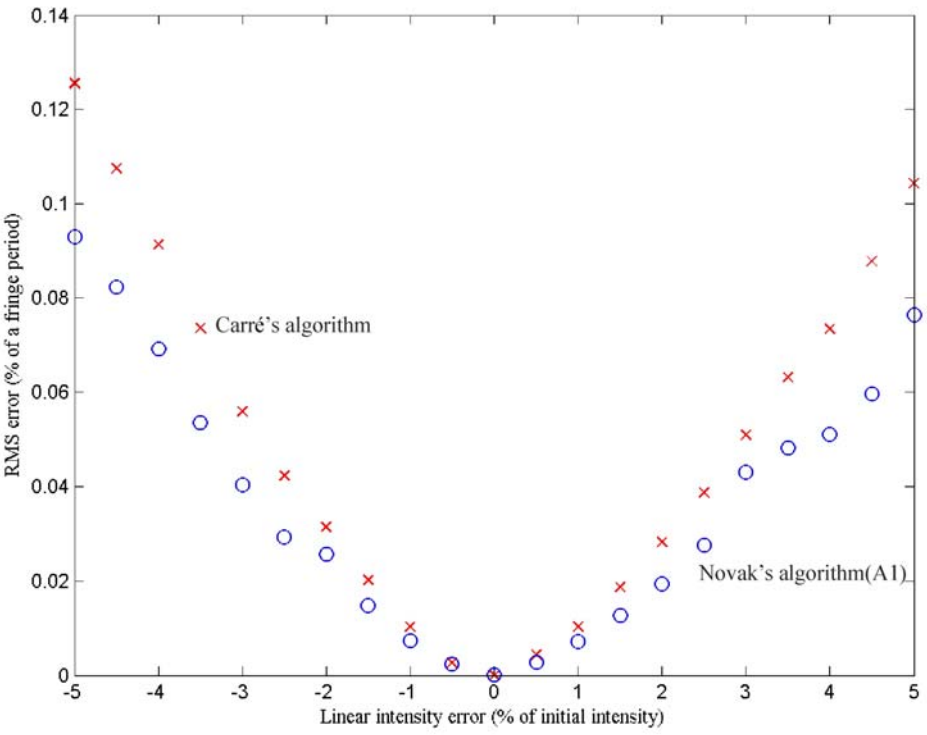

(b)

Figure 56: (a) Mean and (b) RMS phase error due to linear variation in intensity.

5.6.3 Non-linear phase shift error

The algorithms used to calculate phase from the phase shifted images only produce an accurate result if the phase steps are equal. Any non-linearity in the phase shift will result in an error in the calculated phase. By considering the second order approximation of equation (80) the non-linearity resulting from the rotation about the perspective centre phase shift method can be estimated. The second order approximation gives

$$\Delta\phi' = -\frac{2\pi c_P}{p}\left|\underline{X}\right|\frac{\left(\hat{\underline{X}}_P - \frac{X_P}{Z_P}\hat{\underline{Z}}_P\right).\hat{\underline{V}}}{Z_P}\omega\left(1+\frac{\left|\underline{X}\right|\hat{\underline{Z}}_P.\hat{\underline{V}}}{Z_P}\omega\right) \tag{88}$$

Expressing this as $\Delta\phi' = \Delta\phi(1+\varepsilon\Delta\phi)$ after Creath [27] gives the factor of non-linearity as

$$\varepsilon = -\frac{p}{2\pi c_P}\frac{\hat{\underline{Z}}_P.\hat{\underline{V}}}{\left(\hat{\underline{X}}_P - \frac{X_P}{Z_P}\hat{\underline{Z}}_P\right).\hat{\underline{V}}} \tag{89}$$

Using the simplified model introduced in section 3.4.1 with parallel $\hat{\underline{Y}}$ and $\hat{\underline{Y}}_P$ axes and using units of standoff distances it can be shown that

$$\varepsilon = \frac{D}{X_{OP}}\frac{DZ+X}{\left(1+D^2\right)^{3/2}}\frac{\left(Z-Z_{OP}\right)-D\left(X-X_{OP}\right)}{X\left(X-X_{OP}\right)+Z\left(Z-Z_{OP}\right)}\frac{W}{2\pi} \tag{90}$$

This shows that the non-linearity is proportional to the fringe width at the intersection point of the camera and projector axes. The factor of proportionality is at most of order 1 for a practical system and varies with position within the measurement volume. For the system in use here the non-linear phase shift error is less than 1%. As with the other errors, the response of both Carré's algorithm and Novak's algorithm to different amounts of non-linearity was simulated. The mean and RMS errors over 1 period are shown in Figure 57(a) and (b), respectively. As with the inter-frame intensity variation, the mean error may vary across the phase map, and therefore may be significant with the new phase shift techniques, in contrast with traditional temporal phase shifting.

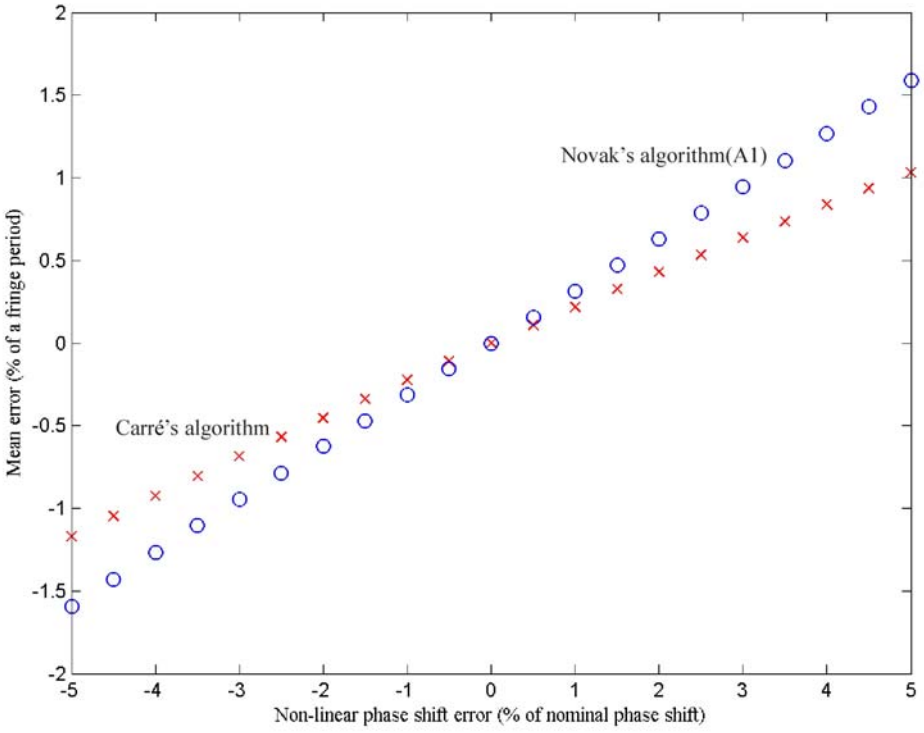

(a)

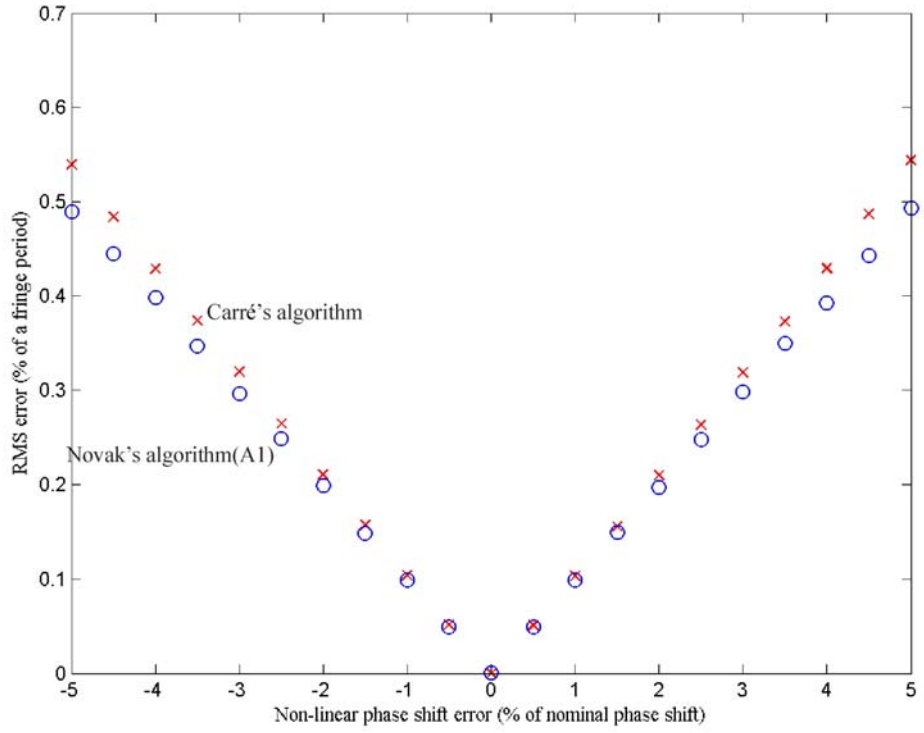

(b)

Figure 57: (a) Mean and (b) RMS phase error due to non-linear phase shift error.

A further calibration procedure could be used to reduce the effect of the non-linear phase shift error if required. An alternative is to choose a phase shift algorithm less sensitive to the error. A third possibility would be to approximately measure the non-linear phase shift error present during measurement by taking an extra frame for each set of phase shifted images and calculating the change in phase shift across the set of frames. None of these ideas have been implemented because the estimated non-linearity for the phase shift created by the rotation about the perspective centre technique is expected to be insignificant in comparison to the other error sources. For the surface gradient phase shift technique, on the other hand, non-linear phase shift error would be expected to increase with the curvature of the object, and may be a significant source of error.

5.7 Conclusions

Two new methods to calculate phase from phase shifted images have been described, both using relative motion of the object and fringe projection system to create the phase shift. The first, called the surface gradient method, relies on the gradient of the object to create a phase shift. This technique was shown to be useful for objects of relatively constant gradient. The second technique, called the perspective centre rotation technique, uses relative rotation of the object and fringe projection system about the camera pinhole. The resulting image movement is independent of the unknown distance to the object, and so can be compensated for, allowing phase to be calculated for the viewed object points.

Both methods show similar errors (for a flat object) to temporally phase shifted fringe data. The surface gradient method fails close to edges or changes in surface reflectivity. The perspective centre rotation method has been used to demonstrate measurement of a curved object correct to 60 μm over a 40 mm depth and a field of view approximately 80 mm (1 part in 1250).

Error sources affecting the techniques that do not affect temporal phase shift techniques have been discussed. Speckle noise was not a significant source of error for the objects measured here, but is expected to affect both new phase shift methods for objects showing a higher speckle contrast. Inter-frame intensity variation is expected to affect measurements of objects with a specular reflectance close to the specular direction.

Non-linear phase shift error can be a significant error source for the surface gradient technique. It is an error source for the perspective centre rotation technique but is not expected to be significant for most practical systems when compared to the other error sources.

The failure of the surface gradient technique close to edges, combined with the dependence of phase shift size on gradient, means that its usefulness is limited to smooth objects with a slowly varying gradient. It will not be considered further.

The perspective centre rotation technique, on the other hand, was used to calculate phase for the prototype probe described in Chapter 7. The technique allows phase shifting without requiring moving parts or complex optics within the probe. A drawback of the technique is that the phase shift varies and depends on the position of the object. This means that an algorithm not assuming a particular phase shift must be used to calculate phase from the phase shifted images. These algorithms are more sensitive to noise and other error sources than the more commonly used phase step algorithms such as Bruning's algorithm. More phase steps may be used to increase measurement accuracy if required, at the expense of data collection and processing time.

The 2π ambiguity inherent in phase calculation techniques was resolved in this chapter by marking the zero order fringe using an image of a single projected stripe. For measurement of more complex objects this is not a practical method of 2π ambiguity resolution. In the next chapter techniques using multiple perspectives to automatically resolve the 2π ambiguity automatically are introduced, and investigated using a phase shifting fringe projector. In Chapter 7 the prototype device is used to demonstrate shape measurement using a single projected pattern via the combined use of the perspective centre rotation phase shift technique with the use of multiple perspective techniques to resolve 2π ambiguity.

Chapter 6 Fringe projection using multiple perspectives for automatic non-contact shape measurement

6.1 Introduction

Fringe projection systems suffer from ambiguity due to the periodicity of the projected pattern. There must be some absolute reference available to ascertain which point of the pattern is under consideration. Either the height or the absolute phase of at least one point must be known for each isolated surface being measured. This is a well known issue dealt with in various ways within the fringe projection literature as summarised in section 3.5.3.

Ways to resolve the 2π ambiguity problem generally require either a number of different patterns to be projected or require the use of multiple cameras or projectors. In temporal, or heterodyne, techniques multiple fringe patterns with different frequencies are projected. Lower frequencies resolve 2π ambiguity, while higher frequencies give the required height resolution. Temporal techniques clearly require either multiple fringe patterns or a programmable projector, and so are difficult to implement with a simple projector without moving parts as required here. Techniques to resolve 2π ambiguity using only a single pattern include marking one or more different parts of the projected pattern in some way, for example marking the zero order fringe. This is likely to only work for fairly simple objects, as for objects with isolated surfaces and steps it is difficult to guarantee that the zero order fringe will coincide with each surface. Another example requiring only a single pattern is described by Fitts [92]. Pseudo-random perturbations, on the scale of the noise in the system, are embedded in the projected fringe pattern. The distribution of the perturbations varies across the projected pattern, so statistical analysis of the noise in the recorded images enables determination of which fringe is which in the recorded images. The disadvantage of this is that the noise in the recorded images depends on the surface being measured.

A number of authors report techniques to resolve 2π ambiguity by projecting a pattern onto an object viewed from a number of different perspectives [95,141]. Phase (wrapped or unwrapped) enables corresponding points to be identified in multiple camera images. The corresponding points can then be measured using photogrammetry.

The remaining points on the surfaces may be measured from the phase maps, using the photogrammetrically measured points to resolve the 2π ambiguity. This technique requires either multiple cameras or for the camera and projector to be able to move independently of each other. The CMM probe envisaged here is limited in weight and size, so it is preferable to use only a single camera and projector. The camera and projector would be in a fixed relative spatial relationship. The whole probe can be easily moved using the CMM on which the probe is mounted. This ability to easily move the probe, combined with the accurate position reporting of the CMM, is exploited to resolve the 2π ambiguity.

Two different methods to resolve the 2π ambiguity are described and tested in this chapter. An object is considered to consist of smooth faces or surfaces. A surface may be bounded by zero or more edges. A point where two or more edges meet is a corner. If corners and edges can be detected in images and measured in 3D space then this is sufficient to localise the position in space of the surfaces they bound. By measuring at least one point on the boundary of each smooth surface using photogrammetry the correct phase across the rest of the surface may be found. This technique is investigated experimentally in section 6.3 below. As it will be seen, the practical difficulties with the method include finding point correspondences confidently enough for accurate measurement and the difficulty of specifying exactly what constitutes an edge and its location.

The second method uses different viewpoints of the same smooth surface section to resolve 2π ambiguity. Given the phase map of a single isolated surface, there are only a limited number of possible 3D positions of the surface, where the total number is governed by the number of fringes projected and the measurement volume of the fringe projection probe. By creating phase maps corresponding to the same surface patch from multiple perspectives it is possible to ascertain which of the possible positions is correct, and simultaneously, which part of different phase maps correspond to the same surface of the object. This idea is demonstrated experimentally in section 6.4.

The first step of either technique will clearly be to identify corners and edges and segment the phase maps into sections corresponding to different surfaces on the object. This is commonly done using image processing techniques such as Canny edge detection [142]. Here we present a novel but simple processing technique to process the

same recorded fringe images that are used for phase calculation to partially segment the phase maps [6]. Section 6.2 below describes the edge detection method and presents some simple experimental results. This technique is also used in the later chapters of the thesis.

6.2 Image segmentation

As has already been discussed, wrapped phase maps are created from a collection of images of projected fringes with a phase step between each. Wrapped phase is limited to a range of 2π radians as a result of the arctangent operation in the calculation of phase from recorded intensity. The discontinuities due to the wrapping must be removed (i.e. the phase must be unwrapped). Edges, and 2π discontinuities, may be identified by thresholding on the gradient of the wrapped phase. Some edges will not be identified because any step within the threshold of an integer multiple of 2π will appear to have continuous phase. Real edges that have been identified must be distinguished from phase wrap discontinuities.

To distinguish between real discontinuities and phase wrap discontinuities, a phase map is recalculated a number of times, each time using the recorded images in a different order. For example, using Bruning's 4-frame algorithm (equation (33)), four different phase maps can be calculated from

$$tan(\phi_1) = \frac{I_4 - I_2}{I_1 - I_3} \tag{91}$$

$$tan(\phi_2) = \frac{I_1 - I_3}{I_2 - I_4} \tag{92}$$

$$tan(\phi_3) = \frac{I_2 - I_4}{I_3 - I_1} \tag{93}$$

$$tan(\phi_4) = \frac{I_3 - I_1}{I_4 - I_2} \tag{94}$$

In each case, the phase wrap discontinuities occur in a different place in the phase map. The real discontinuities due to the object remain stationary. In this way real discontinuities in phase can be distinguished from phase-wrapping discontinuities.

For an example see Figure 58. Figure 58 (a) shows four phase maps constructed from the same images processed in different orders. The difference in phase between neighbouring pixels was found and discontinuities (pixels with an absolute difference greater than a pre-determined threshold - here, $\frac{\pi}{12}$ radians) are marked in red. Figure 58 (b) shows the first phase map with only those discontinuities that appeared in a constant location in all images marked. It can be seen that the remaining discontinuities correspond to real discontinuities on the object and the discontinuities from the phase wrapping have been removed.

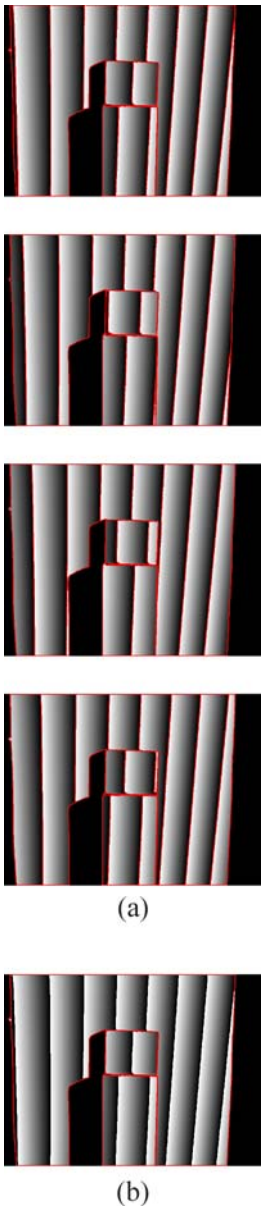

Figure 58: Calculated wrapped phase and discontinuities (a) using images in different orders and (b) real discontinuities appearing in the same location in each case.

This is a simple method to identify edges and steps, requiring no complex processing. An advantage of this method over the more usual image processing edge detectors is that because phase is used rather than intensity the threshold is independent of the reflectivity properties of the object. A single threshold may be used for a collection of phase maps created from different perspectives. The level of the threshold is related to the fringe pitch and the expected maximum gradient of the object with respect to the camera. A real object step that causes a phase discontinuity within the threshold of a multiple of 2π radians will not be detected. Different perspectives may be used to find edges that have not been identified, and to measure faces of the object steeper than the threshold when viewed from the initial perspective.

This technique has been used for initial image segmentation throughout the remainder of this thesis.

6.3 Edge measurement

Once edges and corners have been detected in phase maps from all perspectives, they can be measured in 3D using photogrammetric techniques. A system was set up to demonstrate this experimentally. A fixed camera and projector were used, with multiple perspectives of an object created by mounting the object on a PH10 indexing head. This system has already been described (section 4.1.1), and is shown in Figure 16. The object used for measurement was a flat board with two steps. Sample phase maps created can be seen above in Figure 58.

Edges were identified using the segmentation technique described in section 6.2. Which edge points correspond between different images must be determined. Identifying corresponding points is non-trivial, and much on-going research is dedicated to this problem (see section 3.3.4). Here, the relative position and orientation of the cameras were known, so epipolar matching was an obvious technique with which to ascertain matches. A straightforward epipolar matching method was implemented to find corresponding points. The points were measured using the photogrammetry software described in section 4.1.2.

Once edges were measured, they gave the required absolute measurement to resolve the 2π ambiguity on the smooth surfaces which they bound. A model of the object was

built up, shown in Figure 60, using the projected phase on the smooth surfaces, (unambiguous due to the measured edges) combined with a "wire-frame" model from the edge measurements. Different colours in the diagram are used to identify data originating from different perspectives (in the case of the surfaces), or different combinations of perspectives (in the case of the edges). A number of different surface areas and features have been identified and measured separately, and appear, at least qualitatively, to represent the object.

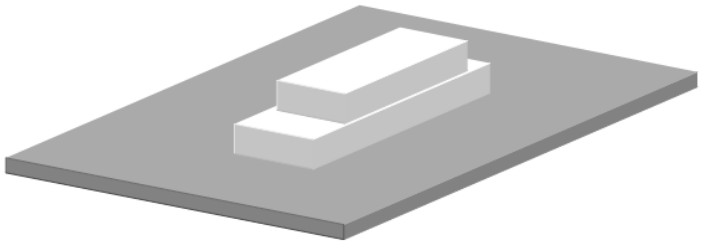

Figure 59: Object used for measurement (two blocks mounted on flat board).

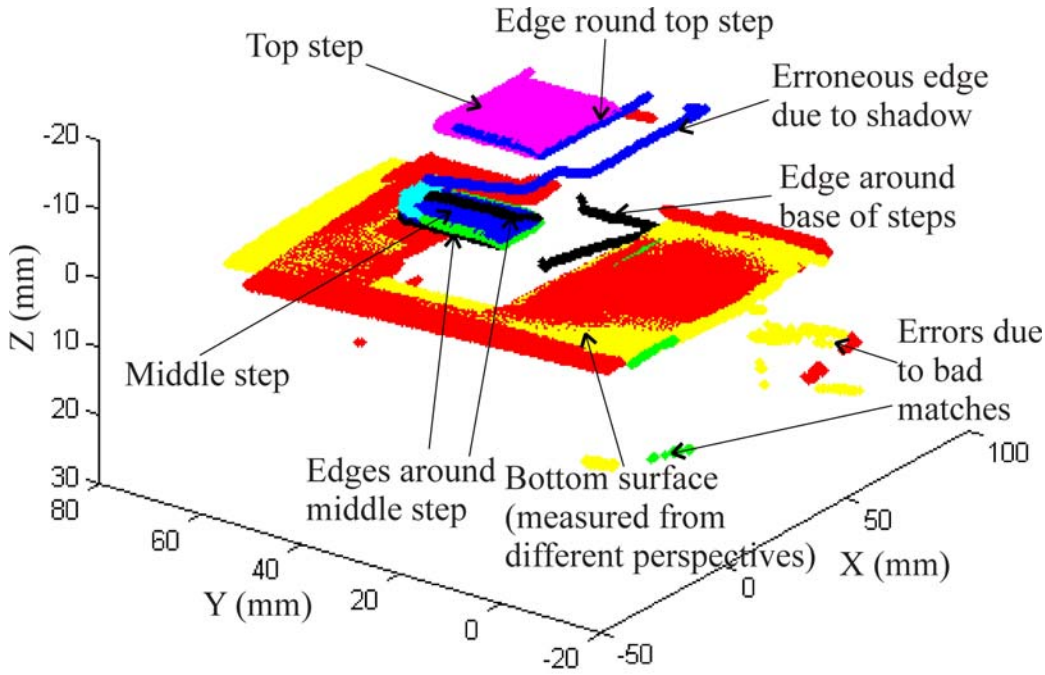

Figure 60: Measurement of object.

There are a number of errors in the model. An edge and some surface areas appear disconnected from the rest of the object. More post-processing could easily remove the disconnected edges and points. Relative camera positions and orientations (with respect to the object) can only be found for head angles up to 22.5° from the vertical axis,

limiting the accuracy achievable. The uncertainty in the relative camera positions is clearly evident in the two measurements of the bottom surface (red and yellow) that are inclined with respect to each other. The side surfaces of the object could not be measured with the limited usable head angles and fixed fringe projector and camera.

A further issue with the technique is related to the edge identification. As has already been discussed, exactly what constitutes an edge is a difficult thing to define. In general terms, a definition of an edge might be a small area over which the curvature of the surface is greater than a given threshold. But here, neither the curvature nor the gradient of the surface are directly measured and phase noise makes them difficult to quantify. Points on the object identified as an edge in one image can easily be further round the object's surface than the points identified as an edge in another image. This difficulty can be minimised, by using a large number of perspectives, but not removed.

In the section 6.4 an alternative approach to resolving 2π ambiguity by considering surface patches is described and demonstrated. This new approach allows direct measurements of edges to be avoided.

6.4 Surface measurement

The measurement approach described in this section in some ways inverts the approach used in the previous section. Smooth surface patches are first identified and measured, to create a point cloud describing the object's surface. It is assumed that any derived features such as edges and corners can be extracted from a point cloud. An advantage to this approach over the previous one is that the description of an object in terms of surfaces and edges is more of an intuitive description rather than a concrete definition. By building the model of the object from surfaces, edges can be identified from the surface areas where the rate of change of gradient is greater than some value, where the threshold is defined according to the application and measurement device [143].

6.4.1 Theory

It was shown in section 3.4 that the phase recorded by a camera pixel viewing an object point can be expressed as a function of the pixel coordinates and the distance to the object point (equation (23)), or height above a reference plane (equation (24)). The form of the function being used for the purposes of this section is unimportant, but it

must be known and must have a known inverse. That is, a function f and its inverse must exist and be known for each pixel (x, y) such that

$$Z = f(x, y, \phi) \tag{95}$$

and

$$\phi = f^{-1}(x, y, Z) \tag{96}$$

where Z distance to the object point and ϕ is the phase recorded by that pixel. Note that if a reference plane is used, then both ϕ and Z will be relative to the reference plane. In practice, it may be convenient to use a lookup table to convert between height and phase rather than a function, in which case the inverse relationship must be available.

The phase above is the unwrapped, unambiguous phase. The phase calculated by the phase step algorithm is wrapped phase. This wrapped phase must be unwrapped to obtain an absolute phase not limited to 2π radians. The unwrapping procedure removes spatial discontinuities in phase by adding or subtracting multiples of 2π rad until the resulting phase map is smooth. The wrapped phase of a set of pixels can be unwrapped from an arbitrary start point using a standard spatial unwrapping algorithm so that each pixel in the set has an unwrapped phase φ_u, which is related to the correct phase by

$$\varphi(x, y) = \varphi_u(x, y) + 2m\pi \tag{97}$$

for some unknown integer m. If the set of pixels corresponds to a continuous surface then m is constant for the whole set. There are a finite number of possible values of m. The limits are defined by the experimental setup used – the depth of the measurement volume of the fringe projection system and the period of the fringes. Consider a point (x_1, y_1) in the image plane of camera 1 (or a camera in position 1). The pixel has k possible values of m, denoted $m_1^{(j)}, j = 1,...k$. Therefore there are k possible Z coordinates corresponding to the imaged 3D point given by

$$Z_1^{(j)}(x_1, y_1) = f\left(x_1, y_1, \phi_{u1}(x_1, y_1) + 2m_1^{(j)}\pi\right), j = 1,..k \tag{98}$$

where f is the function relating phase to height for the pixel in question as described earlier and $\phi_{u1}(x_1, y_1)$ is the unwrapped phase recorded by camera 1 at that image point.

From each of the $\left(x_1, y_1, Z_1^{(j)}\right)$ triplets a point $\underline{X}_1^{(j)} = \left(X_1^{(j)}, Y_1^{(j)}, Z_1^{(j)}\right)$ in camera 1 coordinates can be calculated using the pinhole camera model (equation (2)). The *k* 3D points can be transformed into the coordinate system of a second fringe projection probe. They can then be re-projected onto the camera image plane of probe 2 giving a set of pixel coordinates, each with an associated unwrapped phase $\phi_{u2}^{(j)}$, where, as in the first image, the unwrapped phase for each pixel is related to the correct phase by some unknown integer multiple of 2π radians, denoted m_2. From the re-projected pixel coordinates and the *Z* coordinate of each candidate 3D point an expected phase $\phi_{e2}^{(j)}$ is calculated using the known inverse of the phase to height relationship. Finding the difference $\phi_{diff2}^{(j)} = \phi_{e,2}^{(j)} - \phi_{u,2}^{(j)}$ for each point identifies the real match to the original pixel in the first camera image. In a perfect system with no noise and no other error sources the correct match will be such that $\frac{\phi_{diff,2}^{(j)}}{2\pi}$ is an integer. If more than one re-projected pixel in the phase map of perspective 2 satisfies this condition then the ambiguity may be resolved by using an extra perspective or by considering neighbouring points.

In practice, however, single pixel matching as described above does not work because of the noise, digitisation and the lack of one-to-one correspondence between pixels in image planes from different perspectives. Consider instead a set of *N* pixels from the first image, all viewing the same continuous surface so that the integer *m* is constant for all N pixels. Each possible $m_1^{(j)}$ value leads to a different set of points in 3D space, which in turn leads to a set of phase difference values, $\underline{\phi}_{diff,2}^{(j)}$ for each point set re-projected into the second camera image plane. The standard deviation in the phase difference for such a set of points is

$$\sigma_j = \sqrt{\frac{\Sigma\left(\underline{\phi}_{diff,2}^{(j)} - \overline{\underline{\phi}_{diff,2}^{(j)}}\right)^2}{N}} \tag{99}$$

where $\overline{\underline{a}}$ denotes the mean of vector $\underline{a}$. Then the correct set of points has the lowest standard deviation, and the integer multiple of 2π for the corresponding points in camera 2 is given by

$$m^{(2)} = round\left(\frac{\overline{\underline{\varphi}_{diff,j}^{(2)}}}{2\pi}\right)$$

where $round(a)$ is a function returning the closest integer to *a*.

The uncertainty in the standard deviation of phase difference can be used to check for ambiguity in the result. In such a complex system there are many sources of error, some of which are estimated in the discussion below. However, the main sources of uncertainty in the measurement are the errors and noise in the projected fringes, and the position and orientation of the probe. The combined uncertainty in $\underline{\varphi}_{diff}$ is denoted ε. It can be shown that the uncertainty in standard deviation ε is approximately $\frac{\varepsilon}{\sqrt{N}}$ for a set of *N* points (for large *N*), which is used as the measure of uncertainty to check for ambiguity in the choice of *m*. To resolve ambiguity a third perspective may be introduced, and in general using more perspectives gives a more confident measurement result.

6.4.2 Experimental setup and technique

The equipment used to test the technique was the same as that used in Chapter 5, and depicted in Figure 17, consisting of a five axis CMM and a fixed camera and digital projector. The position and orientation of the camera were found by a least-squares fit procedure based on images of a touch probe tip moved to different known positions using the CMM. An object to be measured was then attached to the head. The CMM was used to move the object to different positions and orientations relative to the fixed camera and projector, the CMM positions and head orientations used to calculate relative camera positions and orientations with respect to the object. Phase shifted fringes were created using the technique of rotation about the camera's perspective centre as described in Chapter 5. Five frames were collected for each perspective and algorithm A1 from Novak [138] was used to calculate the wrapped phase. Carré's algorithm was used wherever Novak's algorithm breaks down similarly to the method described in section 4.3.6. The phase to height relationship used was a cubic polynomial converting between phase and height relative to a reference plane. The cubic polynomial was found for each pixel by measuring a plane attached to the head and nominally perpendicular to the camera optic axis. The plane was moved to 13 different positions along the camera's optic axis, with 10 mm between each. The RMS error from the phase to height calibration was 70 μm, corresponding to an approximate standard error in the phase 0.09 radians. A 70 μm height error from one perspective can

lead to around 1.5 pixel error when projected into the second perspective, which, for the approximate fringe pitch of 30 pixels at the camera image plane can lead to a phase error of 0.3 radians. Combining this with the phase standard error for a second perspective leads to an estimate of the uncertainty, ε, in the phase difference of approximately 0.4 radians. To decrease the likelihood of errors three standard deviations are used, so in the following discussion ε is set to 1.2 radians.

6.4.3 Surface measurement

An object consisting of two oblong blocks on a curved surface (Figure 61) was mounted on the head.

Figure 61: Curved object with steps used for measurement.

Wrapped phase maps were created from 6 different perspectives. The phase maps were initially segmented using the technique described in section 6.2 above. Each segmented area was treated as a separate surface to be measured. The phase for each segmented area was unwrapped from an arbitrary start point using a standard spatial unwrapping algorithm.

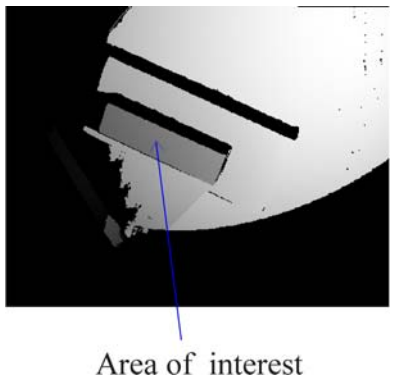

Figure 62: Unwrapped phase from perspective 1.

A phase map taken from a particular perspective, perspective 1, is shown in Figure 62. A segmented area is indicated. The area was from a planar surface measuring 30mm by 10mm. The phase within this area was unwrapped from an arbitrary point so was correct only up to an unknown integer multiple of 2π, $m^{(1)}$. Because the surface was continuous, the value of $m^{(1)}$ is equal for each pixel within the area. There are a finite number of possible values of $m^{(1)}$, where the number of possibilities was limited by depth of the measurement volume of the fringe projection system (in this case 130mm or 160 radians). Possible heights (relative to the reference plane) for each pixel within the segmented area were calculated for each pixel from the recorded phase. The heights, the camera model and the pixel coordinates were used to construct possible 3D point sets corresponding to the surface, each set from a different value of $m^{(1)}$. Some of the possible point sets are shown in Figure 63, in the global coordinate system. The adjustment in radians added to the unwrapped phase for each set is indicated.

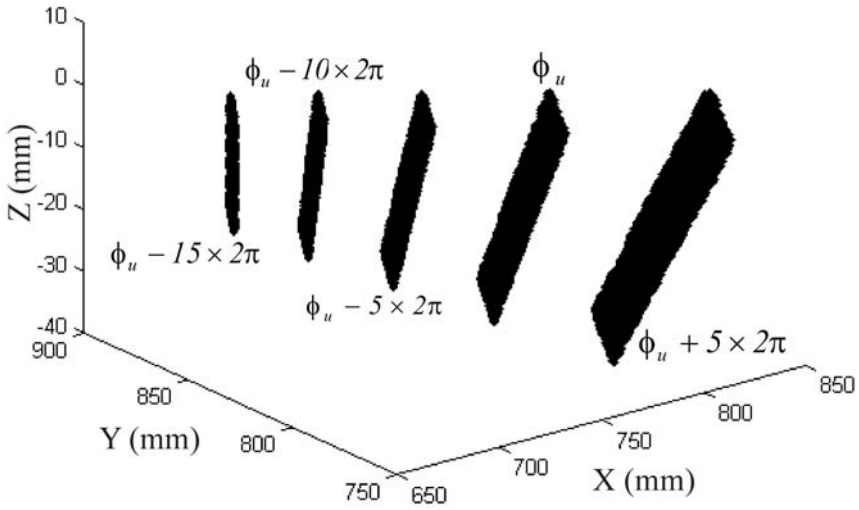

Figure 63: Possible 3D point sets from chosen area from first perspective.

A second phase map, from a second probe position called perspective 2, is shown in Figure 64. The 3D point sets constructed from perspective 1 were re-projected onto this second phase map using the pinhole camera model. Some of the re-projected point sets are shown in Figure 65.

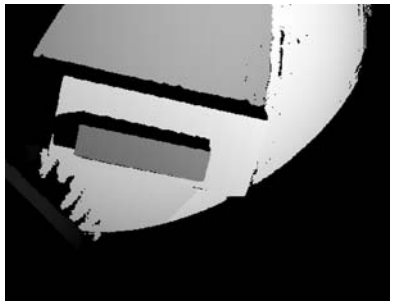

Figure 64: Unwrapped phase from perspective 2.

Any re-projected point set lying over more than one segmented area in the second phase map (up to a tolerance based on the estimated error from the camera calibrations) was discarded. This left, in this particular case, only one possible point set, corresponding to a phase adjustment of -10*2π radians. The 3D point set corresponding to this phase adjustment gave the required surface measurement.

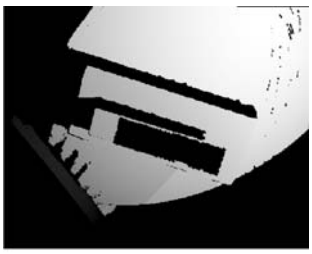

$\phi_u - 15 \times 2\pi$

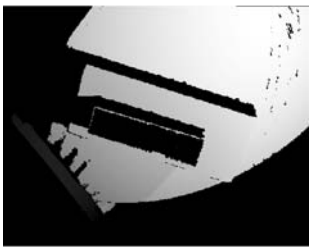

$\phi_u - 10 \times 2\pi$

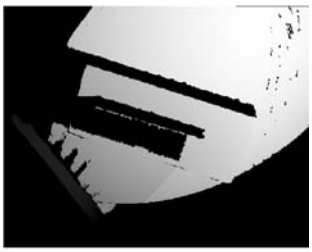

$\phi_u - 5 \times 2\pi$

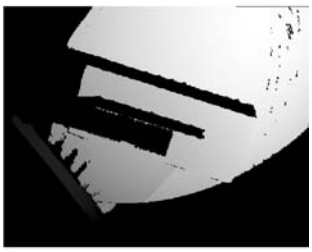

ϕ_u

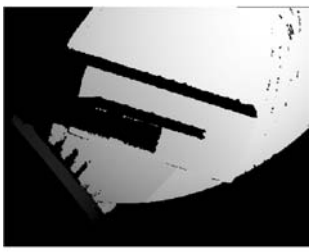

$\phi_u + 5 \times 2\pi$

Figure 65: Candidate point sets constructed from perspective 1, re-projected onto phase map from perspective 2.

The re-projected points can be used to determine the phase adjustment for the area projected onto in the second camera. The expected phase $\underline{\varphi}_e^{(2)}$ was calculated from the 3D points and their re-projected pixel coordinates in the second camera's image plane. The difference between expected and recorded (unwrapped) phase is $\underline{\varphi}_{diff}^{(2)} = \underline{\varphi}_e^{(2)} - \underline{\varphi}_u^{(2)}$.

The mean difference gives the integer multiple of 2π that was the phase adjustment for this set of points

$$m^{(2)} = round\left(\frac{\overline{\underline{\phi}_{diff}^{(2)}}}{2\pi}\right)$$

The value of the standard deviation of $\underline{\varphi}_{diff}^{(2)}$ was checked against a pre-set maximum value to ensure the validity of the result. The threshold was based on the noise and other sources of error in the system. In this particular case the experimental data gave a standard deviation in the phase difference of 0.151 ± 0.002 radians (i.e. less than $\frac{\pi}{20}$ radians), which was well below the estimated maximum value of 0.3 radians (3 times the RMS error of 0.09 radians found for the phase to height calibration, rounded up). If the standard deviation was too large it would have been assumed that either an anomaly such as an undetected edge lay in the area chosen initially, or that the surface was occluded in the second image.

The final step was to produce the 3D point cloud corresponding to the object's surface. Either the original set of points from perspective 1 may be used, or the set from perspective 2, or some combination of the two sets.

The technique to find an absolute measurement has been demonstrated above for a simple case; however there are various complications that frequently occur with real data. Below, some examples of complications and how the technique can handle them are discussed. In particular, situations where the segmentation has failed are considered – that is, where the separate surfaces of the object have not been correctly identified and segmented. Spatial unwrapping algorithms work only on continuous surfaces, and where the surfaces are not correctly segmented the unwrapped phase map may be left with erroneous, path-dependent 2π discontinuities. The discussion is split into two categories; the first where the segmentation has failed in the projected-onto phase map; and the second where the segmentation has failed in the originating phase map, from which the candidate 3D point sets are constructed.

6.4.4 Failure of segmentation in projected-onto perspective

As an initial example consider the phase map from perspective 3 shown in Figure 66. In this phase map the edges of the top surface were not identified by the segmentation technique. The step height was close to a multiple of 2π radians from this perspective, thus the segmentation of the top surface was successful.

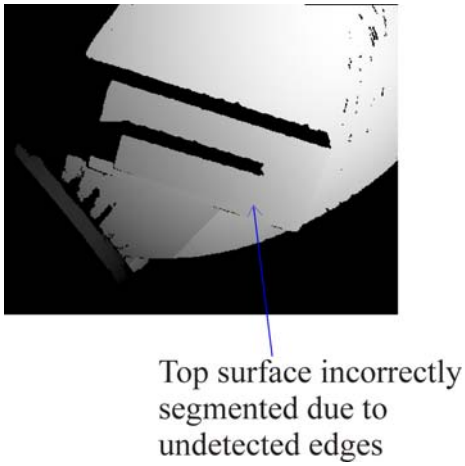

Figure 66: Unwrapped phase from perspective 3. The top surface has not been successfully segmented.

In this case there were a number of adjusted point sets that satisfied the condition of only one segmented area in the re-projection. The standard deviation in the difference between the recorded phase and the expected phase was calculated for each set of pixels and can be seen in Figure 67.

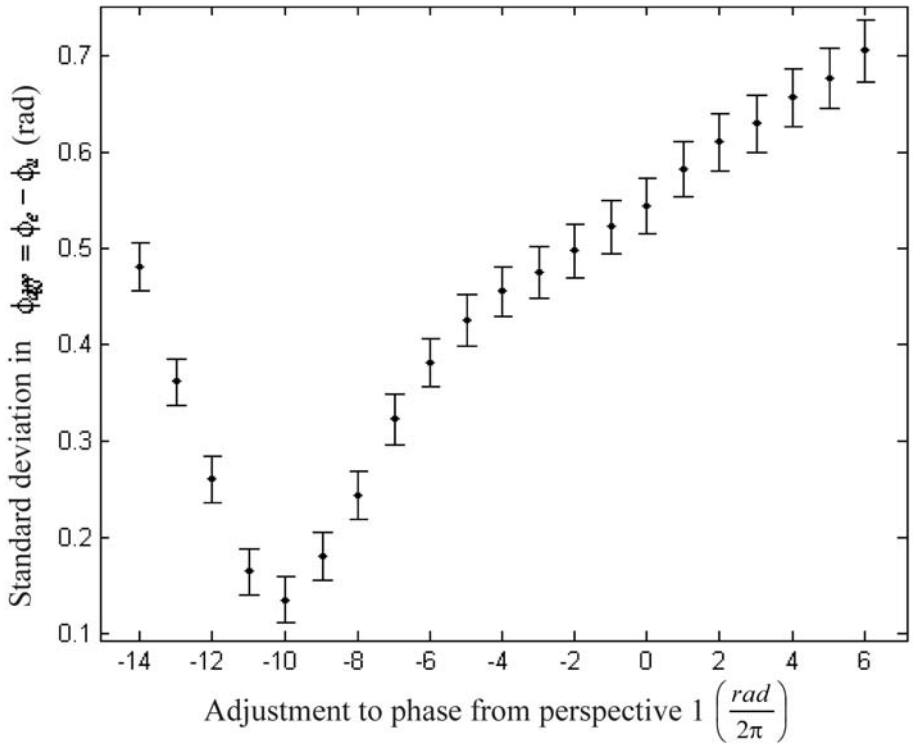

Figure 67: Standard deviation in phase differences for re-projected point sets. Error bars are $\frac{\varepsilon}{\sqrt{N}}$ where ε is estimated uncertainty in phase difference and N is the number of points contributing to the calculation.

The point set with the lowest standard deviation was from the point set adjusted by -10*2π radians. There were two other possibilities within the bounds of the experimental error, indicating that another perspective should be used to confirm the phase adjustment to the point set from perspective 1. For example perspective 2 confirmed the results as shown in section 6.4.3.

In the phase map shown in Figure 68, not only was the segmentation not successful, but so was the phase unwrapping – there were 2π discontinuities remaining in the unwrapped phase, one of which is highlighted. The discontinuities were path-dependent and did not correspond to a real edge of the object. This is indicative of the failure of the edge detection and segmentation. Again, the 3D point sets from the first perspective were re-projected onto the image plane corresponding to this probe position.

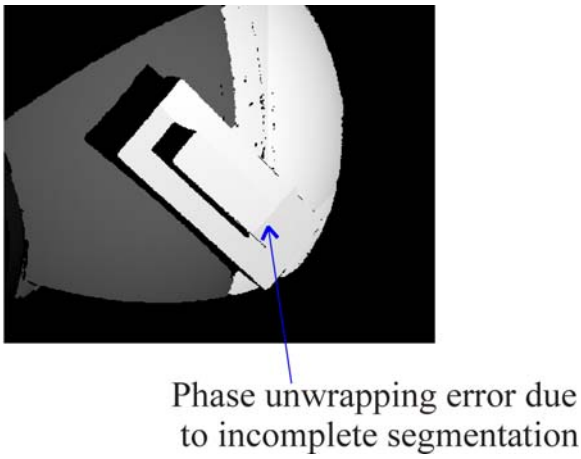

Figure 68: Phase map from perspective 4, with false phase discontinuity indicated.

In this case, again, there were multiple sets satisfying the condition of being re-projected onto a single segmented area. The standard deviation in phase difference was calculated as described above, but with one small difference. Any area covered by re-projected points that contained a discontinuity in the unwrapped phase was unwrapped again, within the region covered by the re-projected points only. If there was a 2π discontinuity remaining within the area after the re-unwrapping it was assumed that an undetected edge lay somewhere within that area, and therefore it could not correspond to the area selected in the initial perspective. If, on the other hand the phase did not

contain a 2π discontinuity then it was a possible match, to be compared to the others in terms of the standard deviation in phase difference.

The standard deviations for the remaining possible matches after unwrapping are plotted in Figure 69.

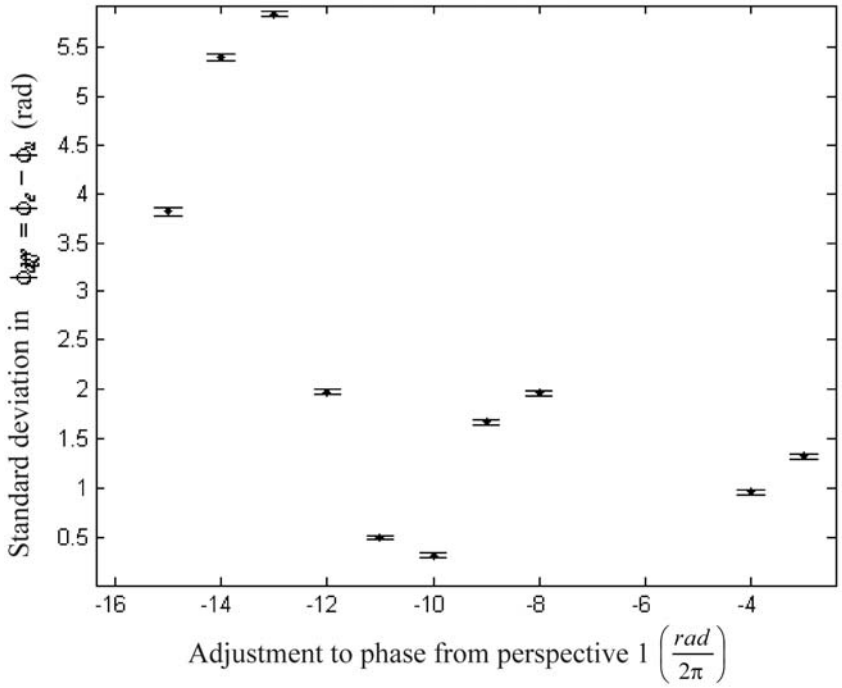

Figure 69: Standard deviation in phase differences for re-projected point sets. Error bars are $\frac{\varepsilon}{\sqrt{N}}$ where ε is estimated uncertainty in phase difference and *N* is the number of points contributing to the calculation.

Again the adjustment -10*2π radians had the lowest error and no other option was within the estimated error of this value. This is in agreement with the two previous examples.

6.4.5 Failure of segmentation in originating perspective

In each of the above examples the chosen pixels from perspective 1 correspond to a single continuous surface. The area of the phase map imaging the surface was successfully segmented and unwrapped. Where the segmentation of the first perspective fails the technique is still useful, as will now be demonstrated by considering different areas from the same phase map, as indicated in Figure 70.

There are four regions of interest shown. One is simply an area of the curved surface. The second is an area of the curved surface but it contains a 2π discontinuity, similar to

that considered previously, that is not real and is a path-dependent failure of the unwrapping algorithm resulting from unwrapping over a non-continuous surface. The third region of interest contains a step on the object that has not been detected. That is, the step, as viewed from this perspective, is of a size close to a multiple of 2π, and thus the wrapped phase is continuous across the step. The fourth is a small region, chosen to demonstrate the effect of an area being too small to achieve unambiguous measurement.

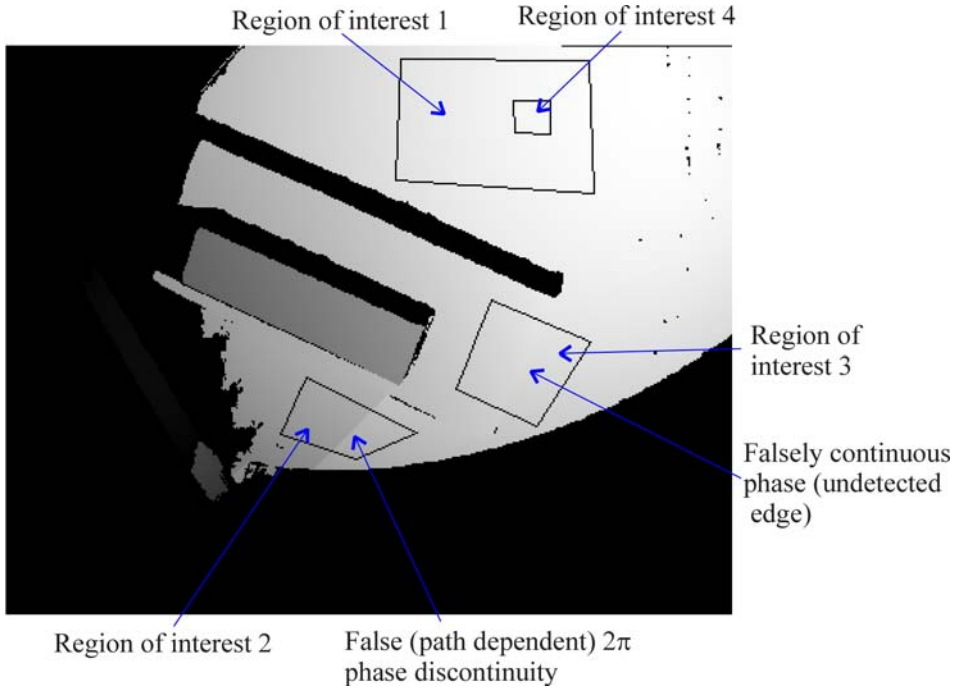

Figure 70: Phase map from perspective 1 with regions of interest with different features indicated.

For each region indicated the candidate 3D point sets were calculated from each possible multiple of 2π that could be added to the phase as before. In the case of region 2 the phase was unwrapped again so that the phase within the region was continuous. If a 2π discontinuity had still existed within the region following the re-unwrapping then it would have been assumed that an undetected step existed somewhere within the region. There were no discontinuities following the re-unwrapping of region 2, so instead it was assumed to be a possibly continuous surface patch.

From the adjusted phase the possible 3D point sets were calculated for each region. They were re-projected onto the image planes corresponding to the three other perspectives previously used. For each set of re-projected pixels the phase was re-unwrapped if it was not already continuous. The expected phase φ_e for each pixel from

the re-projected 3D points was calculated. The difference $\underline{\varphi}_{diff}$ between recorded and expected phase was calculated for all pixels and the standard deviation was found.

The standard deviation values for regions 1, 2 and 3 can be seen in Figure 71. For regions 1 and 2 the standard deviations showed an unambiguous choice of phase adjustment to the region in perspective 1. The lowest standard deviations in phase differences were consistent between all three perspectives. For region 3 this was not the case – while the individual minima appeared conclusive from their error bars, each perspective gave a different result. Each of the minima was greater than the maximum acceptable value of 0.3 radians. Both of these factors indicate that there is an anomaly such as an undetected step somewhere within the region. This could be taken as an indication that another phase map should be constructed from another perspective. Alternatively to try to locate the edge the region could be subdivided and the procedure repeated on the sub-regions. The limit is the minimum size of area that can be unambiguously matched, which depends on the experimental system and the number of perspectives used.

For an example of measurement of a small region, consider Figure 72(a) showing the standard deviations for region 4. In this case the minimum for each region was ambiguous, indicating that the area was simply too small to measure reliably. The combined standard deviations for region 4 are shown in Figure 72(b). There were three possible point sets within experimental error of the minimum value when considering the combined standard deviation. By including yet another perspective it may be possible to resolve this ambiguity. Ideally, the surface would be viewed more closely so that it covers a greater number of pixels in the image giving a confident result. Alternatively, the surface patch may simply be too small for the fringe projection system that was used. Lower uncertainty in the phase measurement or the probe position might allow such a small area to be measured successfully. The uncertainty in the phase measurement could be reduced by using more phase shifted images to calculate the phase. The uncertainty in the probe positions could be reduced by improving upon the calibration technique by using a more cooperative calibration target than the spherical probe tip used for the experiments carried out here.

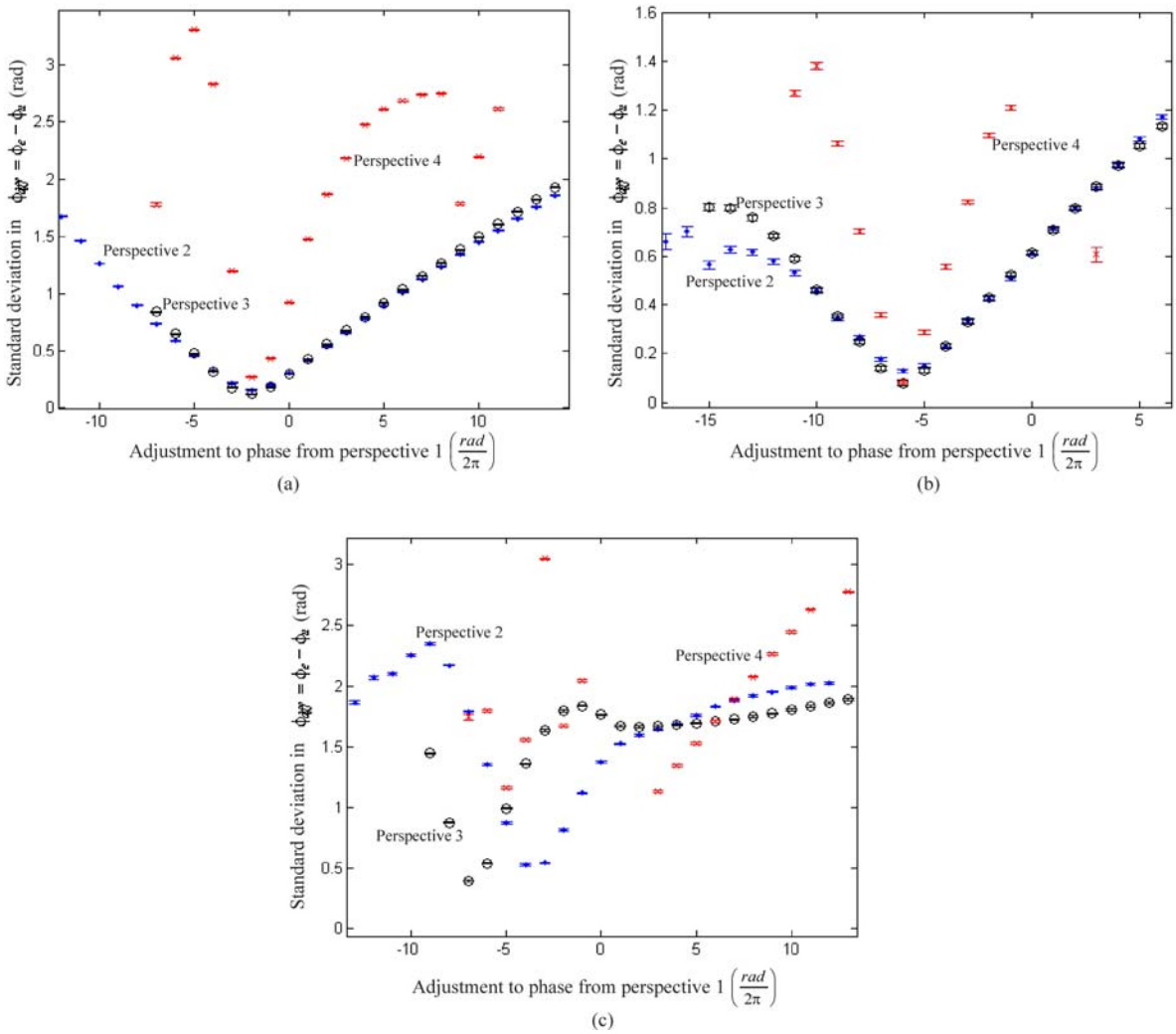

Figure 71: Standard deviation in phase difference for (a) region 1, (b) region 2 and (c) region 3. Error bars are $\frac{\varepsilon}{\sqrt{N}}$ where ε is estimated uncertainty in phase difference and *N* is the number of points contributing to the calculation.

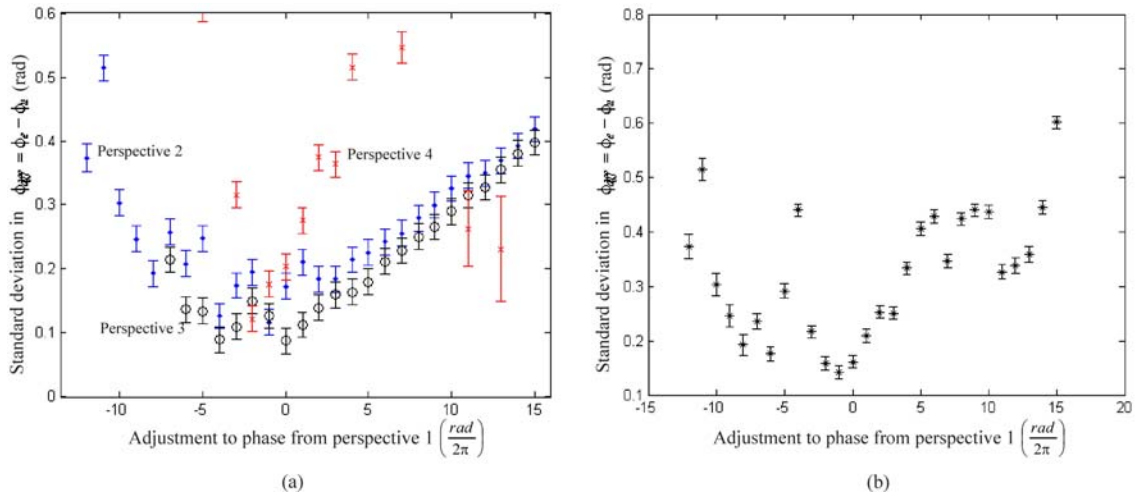

Figure 72: (a) Standard deviation in phase difference for region 4 for each of three perspectives and (b) combined standard deviation from all three perspectives. Error bars are $\frac{\varepsilon}{\sqrt{N}}$ where ε is estimated uncertainty in phase difference and *N* is the number of points contributing to the calculation.

Finally, a more complete model of the object was built up by incorporating images showing surfaces of the object that were occluded for the previous perspectives. Two more phase maps including previously occluded surfaces are shown in Figure 73. The full 3D model from the 6 perspectives considered is shown in Figure 74. This model was built without user intervention (other than choosing the perspectives) using the techniques described in this chapter, implemented in Matlab. More perspectives could be used to fill in the surface areas still missing. The point clouds could be used to fit surfaces and locate edges and corners as required.

Figure 73: Phase maps of the same object from perspectives showing previously occluded surfaces.

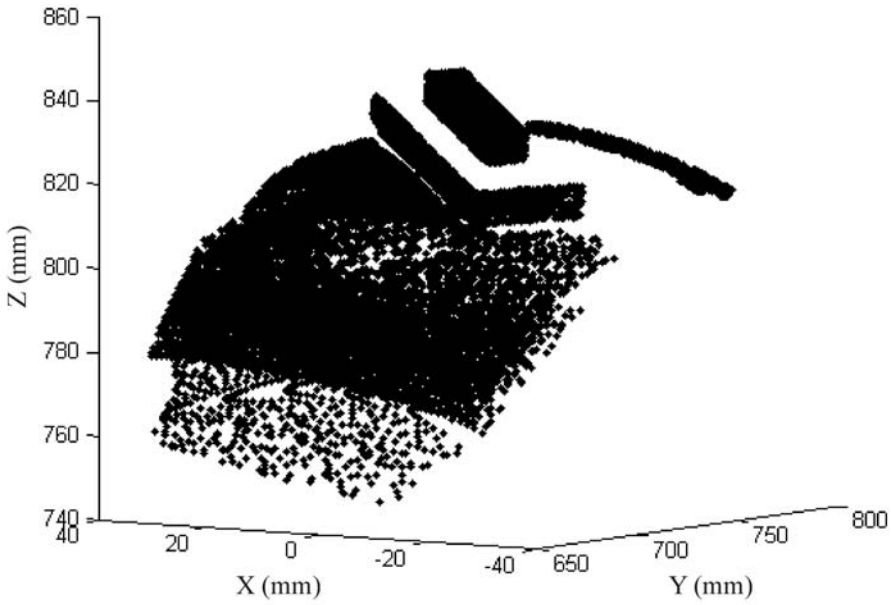

Figure 74: Model of object built from 6 perspectives.

6.5 Conclusions

A simple but novel technique to identify edges on an object by processing fringe images in different orders has been successfully demonstrated. The advantage of this technique over traditional image processing is that the phase variations are used to detect edges, rather than recorded illumination, so performance is independent of background illumination variations and reflectivity properties of the object.

Points identified as edge and corner points in multiple images were measured using photogrammetry, the measured points used to resolve 2π ambiguity from fringe projection on smooth surfaces between the edges. A model of a stepped object was demonstrated, where the model was a combination of surface measurement using fringe projection and a wire-frame model from photogrammetry on edge points. The main problem is the difficulty of identifying corresponding feature points within multiple images.

An alternative way of resolving 2π ambiguity by viewing smooth surface patches from multiple perspectives was also demonstrated. Corresponding areas within different images were identified and measured, simultaneously resolving 2π ambiguity, by analysing the phase recorded from different viewpoints. In contrast with most previous 2π ambiguity resolution techniques, automatic measurement can be achieved using a single camera and projector, fixed relative to each other, projecting a single fringe pattern. It was also shown that the technique can aid further image segmentation by identifying areas within which edges or steps exist but have not already been identified. The technique was demonstrated by building a model of an object consisting of two blocks mounted on a curved surface from six perspectives. The data analysis could be completely automated. The measurements above were created with no user input other than choosing a segmented area from which to start the procedure. Five images were taken for each perspective, so for a single surface patch a minimum of ten images would be required. Two to three perspectives would be required for most surface patches, giving a total of 15 images for around a million measured points (assuming a megapixel camera). For the same number of points to be measured with a line stripe probe around 1000 images would be required (assuming 1000 points per stripe image). The reduced data collection time in comparison to a line stripe probe is of course partially offset by the more complex processing requirements. To build the object model from six perspectives in Figure 74 took around half an hour on a Compaq Evo 310M PC with a

2GHz Pentium 4 processor and 1 GB RAM. The processing was implemented in Matlab. An implementation in C/C++ would be considerably faster. Much of the processing is easily parallelisable and could be implemented on a graphics card to achieve real-time processing. These optimisations discussed in more detail in Chapter 8.

In combination with the phase step technique discussed in Chapter 5 the techniques demonstrated here enable the use of a fringe projection probe for a CMM that projects only a single pattern of illumination. Both the phase shift and the multiple perspectives are provided by moving the whole probe using the CMM. A prototype CMM probe will now be described, and measurements of different objects created using the probe will be presented.

Chapter 7 Prototype demonstration

7.1 Introduction

A prototype fringe projection probe was created to test the subject matter of the previous two chapters in combination and to provide a proof-of-principle for the use of such a probe on a coordinate measuring machine. The probe is described in section 7.2, and its calibration and results of some repeatability tests are described in sections 7.3 to 7.5. Measurement results of a variety of objects are outlined section 7.6. Objects with different surface properties are used to demonstrate the general applicability and limits of the techniques. The object used in Chapter 6, consisting of a curved surface with steps, is measured to demonstrate automatic measurement of a complex object by moving the probe to multiple perspectives. A calibrated sphere and gauge block are also measured to find the achievable accuracy of the probe.

7.2 Probe design

The probe is shown in Figure 75. It consists of a simple fringe projector and a camera. The camera sensor is a Micron ½-inch megapixel CMOS sensor. The sensor, together with the electronics to control it and the interface to the head, constitutes a camera probe, designed and built within Renishaw for other projects. The fringe projector was custom-designed and built specifically for this project. Optical and mechanical designs were created in Renishaw by David McKendrick and Anastasios Aretos, respectively.

The fringe projector contains a red LED source and a condensing lens, illuminating a slide with a 3 period per mm sinusoidal pattern. An 8 mm fixed focal length lens (identical to the camera lenses used earlier) was used to project the pattern onto the object. The aperture of the lens was set to the largest setting (F1.4) so that as much light as possible was available. Therefore the depth of focus was small, and where the fringes are out of focus the contrast is reduced from the optimum, which can limit the possible height resolution. The focussing of the camera is more important. The camera lens used was identical to the projector lens. The aperture was set to a small setting (F8) giving a large depth of field while still allowing sufficient light to reach the detector within a reasonable exposure time for most objects. Each image taken is automatically adjusted for fixed pattern noise by subtraction of a dark image. The projector and camera were attached to each other using custom made brackets (made by John Mason

in Heriot-Watt University), with a hinged joint between them. The LED was powered via an external power supply. The prototype weighed 0.7 kg, and required 0.2 kg counterweights to enable safe movement by the head to which it is attached, bringing the total weight to 0.9 kg. The CMM used was the same one used in Chapters 5 and 6, consisting of a Crysta Apex three-axis CMM with a Renishaw Revo 2-axis head and a Renishaw UCC controller, and controlled using a standard PC running Matlab.

Figure 76 depicts the approximate dimensions of the probe as described by the simplified fringe projection model introduced in section 3.4.1. The angle between the optic axes of the camera and projector was 25°, and the standoff (defined here as the distance between the camera perspective centre and the intersection of the axes) was 175 mm. The period of the projected fringes at this point was 7 mm.

The coherence length of the LED source was approximately 10 μm, compared to around 1 μm for the white light fringe projector. Therefore more speckle noise was expected than was previously seen (see section 4.3.9). The 3D measurement results were also expected to have lower resolution due to the larger fringe period. The purpose of the prototype is to demonstrate that the use of such a probe for 3D measurements is feasible rather than to attain the highest achievable accuracy. Ways to improve the accuracy are highlighted and discussed in more detail in section 8.2.

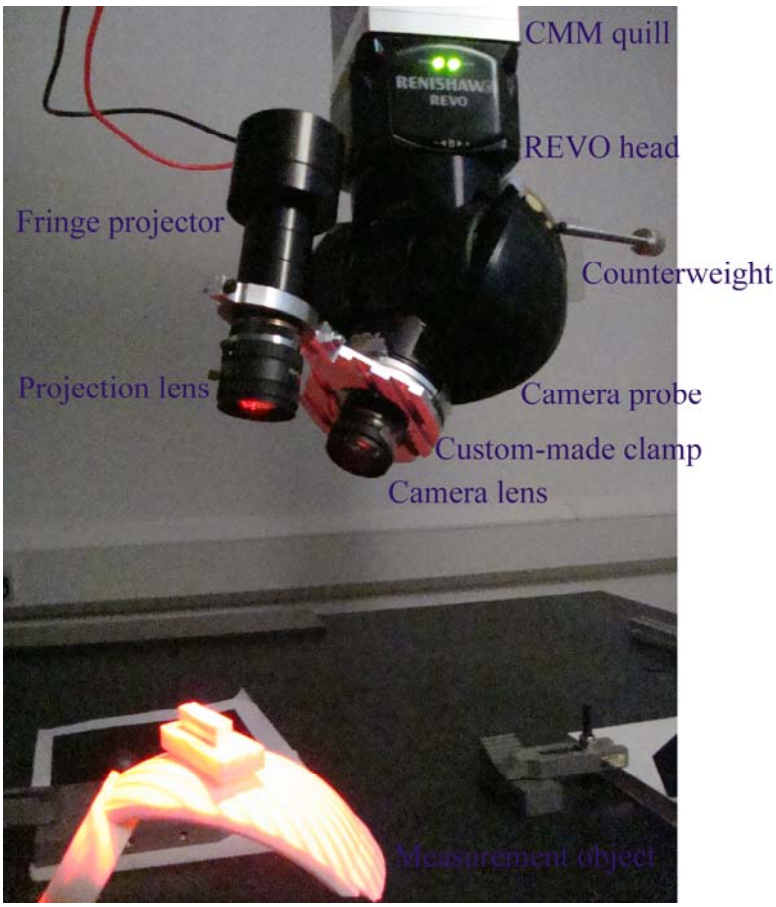

Figure 75: Prototype fringe projection probe.

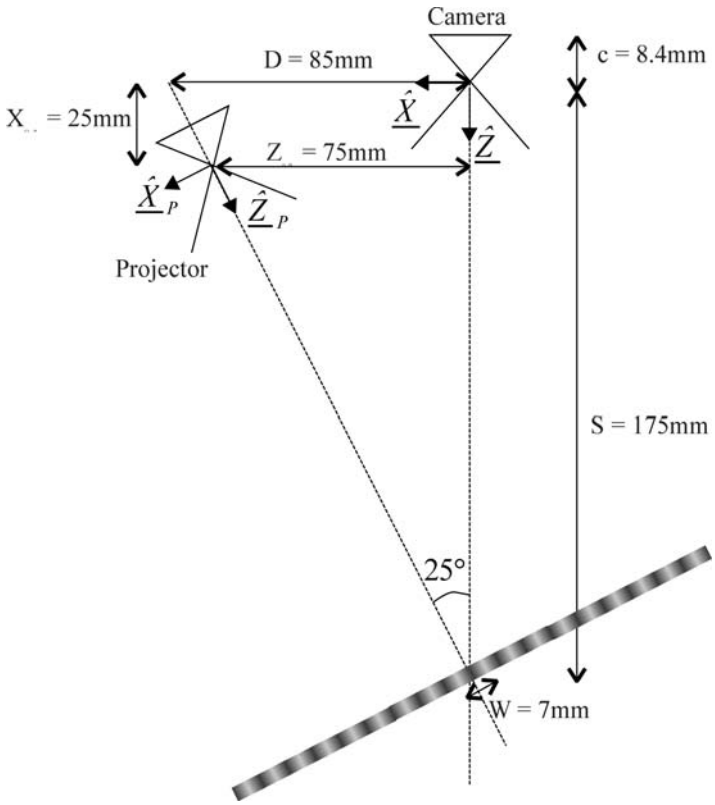

Figure 76: Prototype probe dimensions.

7.3 Camera calibration

In the systems reported in previous chapters each camera was calibrated using the adapted camera calibration toolbox described in section 4.1.2. Multiple images of a grid target were taken at different orientations, and the internal camera parameters, as well as the position and orientation with respect to the target, were found simultaneously. In a multiple camera system the positions and orientations of the cameras were then found with respect to each other by using images of the target in the same position for each camera. Measurements were made relative to one of the cameras. In Chapters 5 and 6 a single camera was fixed to the CMM table and the objects to be measured were mounted to the REVO head on the CMM. The camera position and orientation with respect to the CMM were found from photographs of the tip of a touch probe attached to the CMM.

In this chapter a prototype probe is attached to the CMM. The camera internal parameters must be known and can be found using the calibration target. Also the mounting of the camera on the head must be known so that the position and orientation of the camera is known for any head angle and CMM position. In the case of a touch probe the calibration is carried by measuring a sphere using different head angles and fitting for the parameters describing the mounting of the probe on the head. A similar technique was carried out using a camera. To develop the camera calibration, a probe consisting of a camera only was attached to the head, without the fringe projector. The reduced weight means that the effect of gravity on the probe is negligible. (The effect of gravity on the probe, including the fringe projector, is investigated in section 7.5.) A camera calibration was initially carried out using the grid target to find the camera's internal parameters. Images were then taken of a white sphere, the location of which had been found using a touch probe, from number of different perspectives. A sample image is shown in Figure 77. The centre of the imaged sphere acts as a corresponding point viewed from multiple images, and therefore sphere position can be found in 3D using intersection (section 3.3.2), if the camera positions and orientations are known. Nominal estimates of the parameters describing the mounting of the camera on the head were used to calculate the sphere's position in 3D. The differences between the true and the calculated sphere positions were minimised in a least squares sense, iteratively updating the mounting parameters. To verify the technique a second sphere was measured with the calibrated camera. The centre of the second sphere was found correct to 150 μm. Whilst a number of factors could contribute to the error it was

suspected that the main factor was the lighting causing shadows and variable reflected intensity around the sphere, which results in errors in the located circle centres. A shadow is clearly visible in Figure 77. This can be improved by using a circle as the target rather than a sphere.

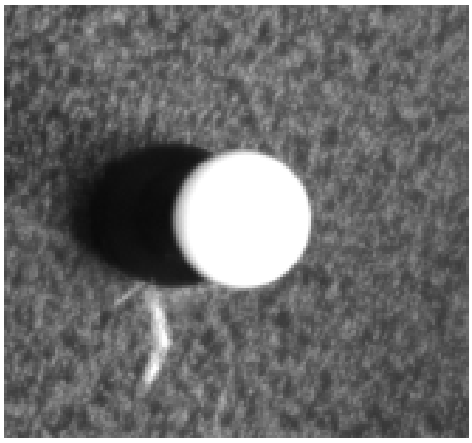

Figure 77: Image of white sphere used for calibration.

Renishaw employee Tim Featherstone has developed a technique to carry out the two step camera calibration in a single step using a custom-made white cylinder as the calibration artefact. A sample image is shown in Figure 78. Its position is easy to measure in the CMM space using a touch probe. The CMM is used to move the camera to different positions, keeping the head orientation constant, and an image is taken at each position. The data are used to find the internal parameters and the camera mounting on the CMM simultaneously.

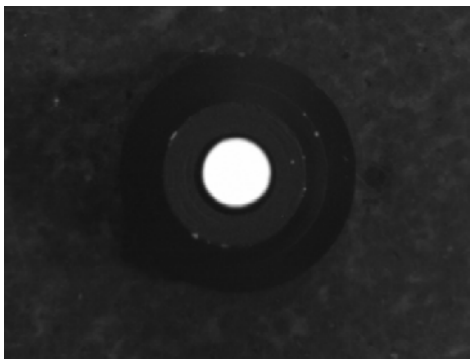

Figure 78: Sample image of white cylinder top.

Two consecutive calibrations were carried out in order to verify that the internal calibration using the new technique was equivalent to the original method. One calibration used the original method with images of the Edmund Optics calibration target; the second used images of the white stick artefact. The internal camera

parameters from each method were compared. Table 13 summarises the internal parameters found from each and Figure 79 shows a schematic diagram of the camera image plane showing the principal points and the difference in the pixel coordinates from the two different calibration methods. The largest difference in image coordinate due to the small differences in the calibrations is 0.38 pixels at one of the image corners. For most of the image the differences are up to 0.1 pixels, equivalent to the expected error in the locations of the circle centres in the images. The principal points found are not within the calculated experimental error from the fit, but are within the variations observed experimentally earlier for repeated identical calibrations (section 4.3.1). The two techniques are therefore taken to be equivalent. The white stick artefact was used to calibrate the prototype probe hereafter.

Table 13: Comparison of internal camera parameters from two calibration techniques.

Calibration method	Principal distance (pixels)	Principal point x coordinate (pixels)	Principal point y coordinate (pixels)	First radial distortion coefficient	Second radial distortion coefficient
Grid target, stationary camera	1613.5±0.7	644.2±0.5	490.3±0.6	-0.136±0.004	0.17±0.02
Single spot target, moving camera	1598.5±0.6	644.7±0.2	490.8±0.2	-0.134±0.001	0.177±0.003

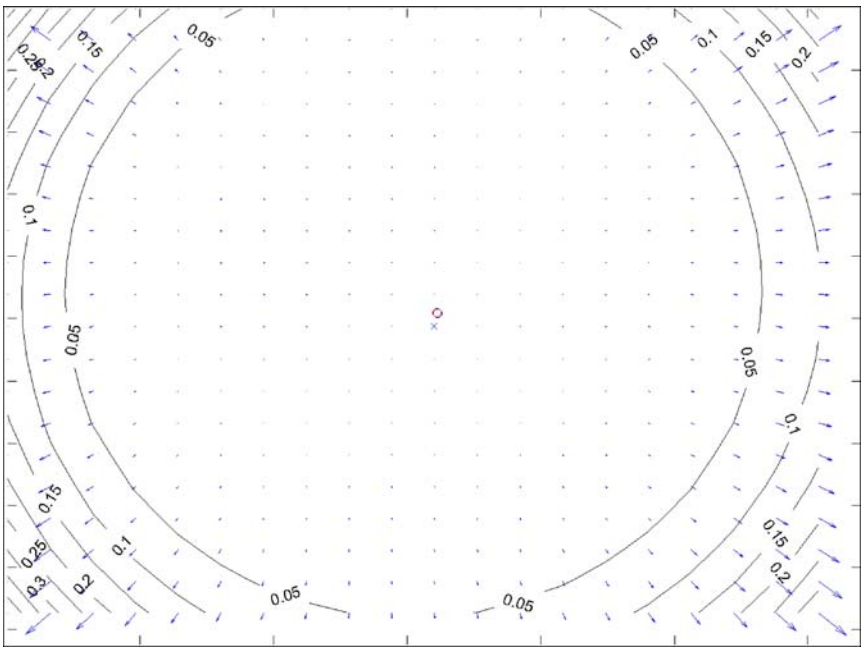

Figure 79: Differences in pixel coordinates from two calibration methods.

7.4 Phase to height calibration

A calibration plane was fixed to the deck of the CMM and measured with a touch probe. The prototype probe was then attached to the head. The plane was measured by the prototype probe at 12 different distances, each separated by 8 mm. The speckle noise for this plane was measured to be 10% of mean intensity under the LED, compared to 1% with the white light fringe projector seen previously. The increase in speckle noise would be expected to double the uncertainty in phase due to speckle, if all other parameters were equal. It was decided to try to compensate for the increase in speckle contrast by increasing the number of phase steps. A combination of 7-frame phase step algorithms as described in 4.3.6 was used to calculate the phase. The zero order fringe from which to unwrap the phase was specified by hand. Phase to height calibration parameters A and B from equation (27) were fitted for each pixel rather than polynomial coefficients, as described in 4.3.8.

Figure 80 shows the error in the fitted height for a single line of one of the planes used in the phase to height calibration. The mean error for the plane is 2.1 μm and the RMS error is 96.3 μm. This is the equivalent of approximately 1.4% of a fringe period, using the nominal conversion of 7 mm per fringe from the simplified model dimensions. Compare this to the 5-frame phase shifted data from the white light system used in Chapter 5 (Table 11), in which an RMS error of approximately 1.6% was observed. The similarity in the magnitude of the errors suggests that the extra speckle noise due to the longer coherence length of the LED source has been almost totally cancelled out by using more phase steps.

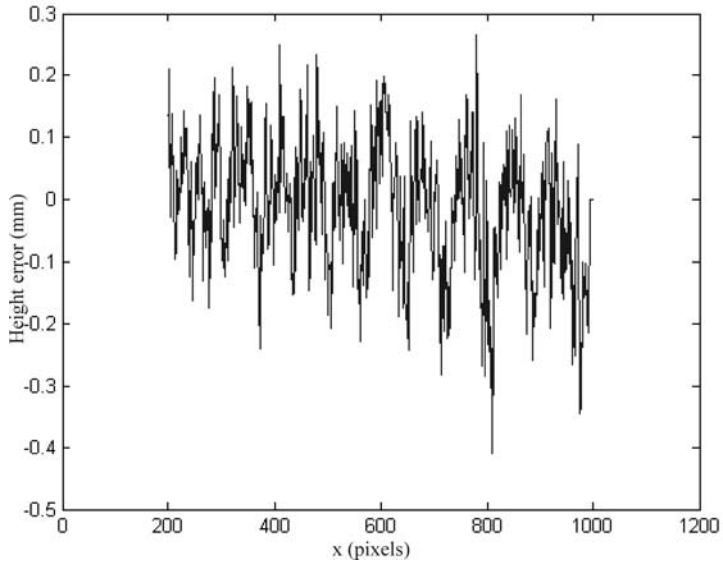

Figure 80: Phase to height calibration error for single line of a sample plane.

7.5 Phase measurement repeatability

The effect on measurement of using the probe at different E angles, and of removing the probe from the head and replacing it was investigated. Two planes were fixed in the CMM measurement volume, one approximately horizontal, and the other nominally at 40° to the horizontal. The two planes were measured using a touch probe. The touch probe was then replaced by the prototype probe, and oriented such that the camera optic axis coincided with the normal of the nominally horizontal plane. Phase was repeatedly measured for the plane to give a baseline repeatability measurement. Figure 81 shows the difference in phase between two consecutive measurements for a single line across the phase map. For speed, the phase calculation algorithm used was the basic 7-step algorithm from Novak rather than a combined algorithm. Large noise spikes are observable in the calculated phase at the zero crossings of the denominator in the formula used to calculate the phase. These result in large standard deviations in the relative phase but do not significantly affect the mean values. This was repeated three times. The mean difference between the repeated plane measurements is 4.2±1.9mrad, equivalent to 4.7±2.1μm using the nominal conversion of 7 mm per fringe period from the simplified model above. Notice that the standard deviation is calculated from the repeated measurements of mean difference and is not necessarily related to the phase noise.

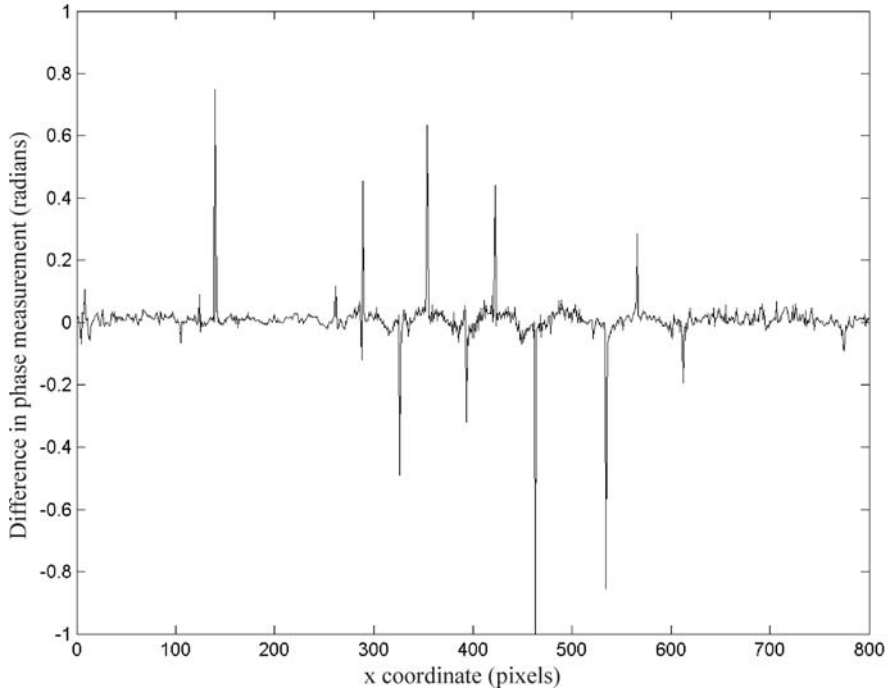

Figure 81: Phase measurement repeatability - difference in phase from two consecutive plane measurements.

The probe was then moved using the CMM to the angle corresponding to the second plane's normal, and used to measure the second plane. Following this it was returned to the original orientation and used to re-measure the first plane. Finally, the probe was removed from the head, replaced, re-oriented to the original angle and again used to measure the first plane. Plots of phase difference (to the original plane measurement) for each measurement are shown in Figure 82 and the mean values from repeated experiments are summarised in Table 14.

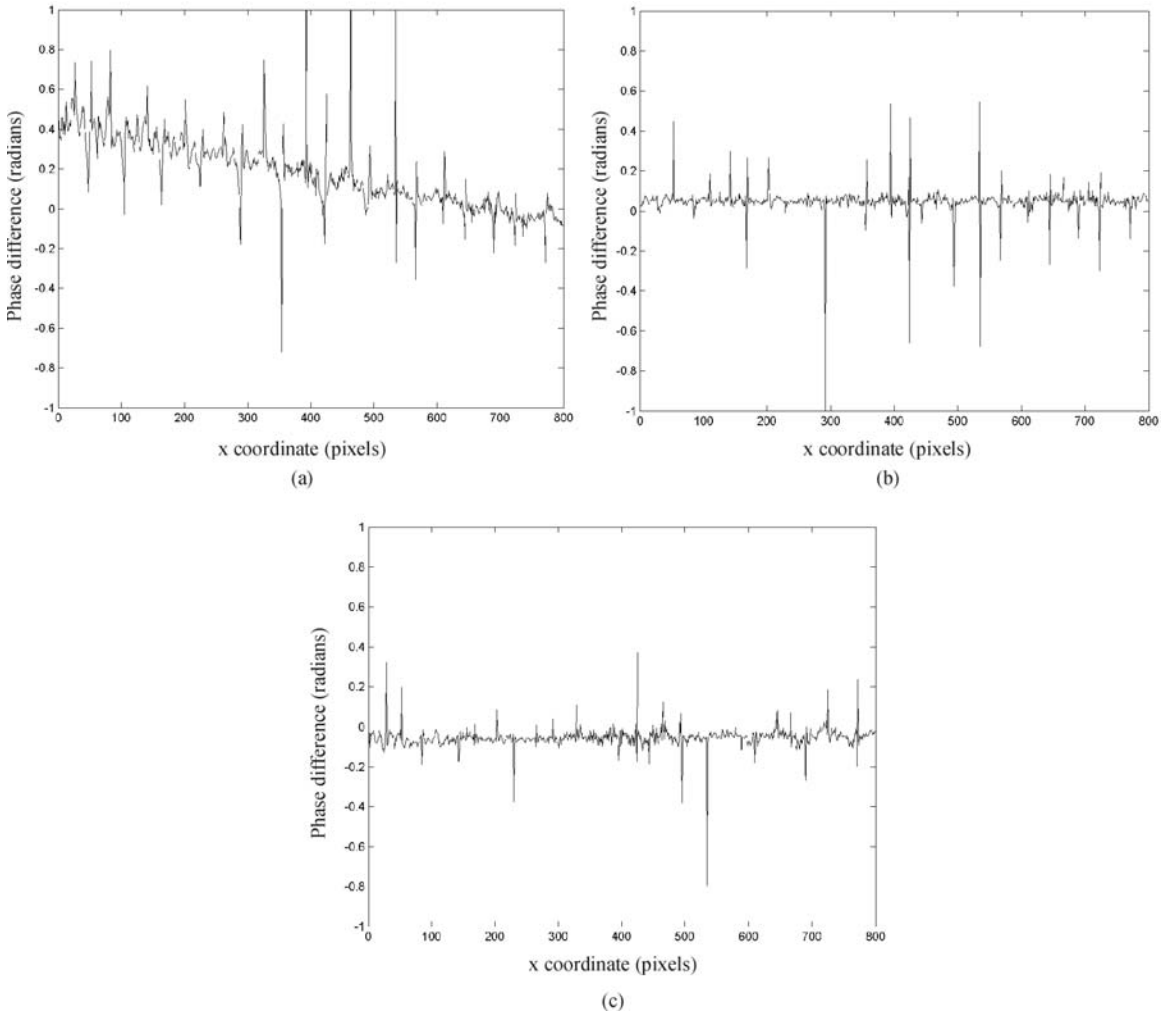

Figure 82: Difference in phase between two plane measurements where (a) planes are at different angles, (b) probe has been moved to a different angle and returned, and (c) probe has been removed from the head and replaced.

Table 14: Mean phase differences due to different actions between measurements.

Action between measurements	Mean phase difference (mrad)	Equivalent mean height difference (μm)
Plane and probe at different orientation (but same relative orientation)	183±11	204±12
Probe moved to different orientation then returned	52±4	58±4
Probe removed from head and replaced	57±22	64±24

The results above clearly show that phase measurement is not repeatable, either when the probe was moved to a different angle, or returned to the original one, or when it was removed from the head and then replaced. The non-repeatability with angle was expected and is due to gravity making the projector and camera move slightly relative to each other as the head E angle* was increased. It was expected that the movement would be reversed as the E angle was decreased; however re-measurement at the original orientation showed that this was not the case. It is possible that the magnets holding the probe to the head were not strong enough, and that the probe was becoming slightly unseated at high E angles and not re-seating in a repeatable manner. A small phase measurement difference due to removing and replacing the probe was expected. Probe changes are generally repeatable if carried out automatically using a probe change rack, but not if the probe is changed by a human operator. However, the effect of this on the phase measurement was somewhat larger than expected.

The lack of repeatability points towards a requirement to carry out a different phase to height calibration each time the probe is attached to the head or moved to a new E angle. This requirement was reduced to a requirement to measure a new reference plane rather than a whole phase to height calibration. This was because relative phase measurements under the same actions were repeatable, even though the absolute phase measurements were not. To prove this, the experiment above was repeated, but each time the plane was measured from two different heights so that the phase of one height relative to the other could be calculated. Figure 83 plots the difference in relative phase measured for the repeated plane measurements, and Table 15 summarises the results from repeated experiments.

* The head's D and E angles are the azimuth and zenith angles, respectively. See Figure 17.

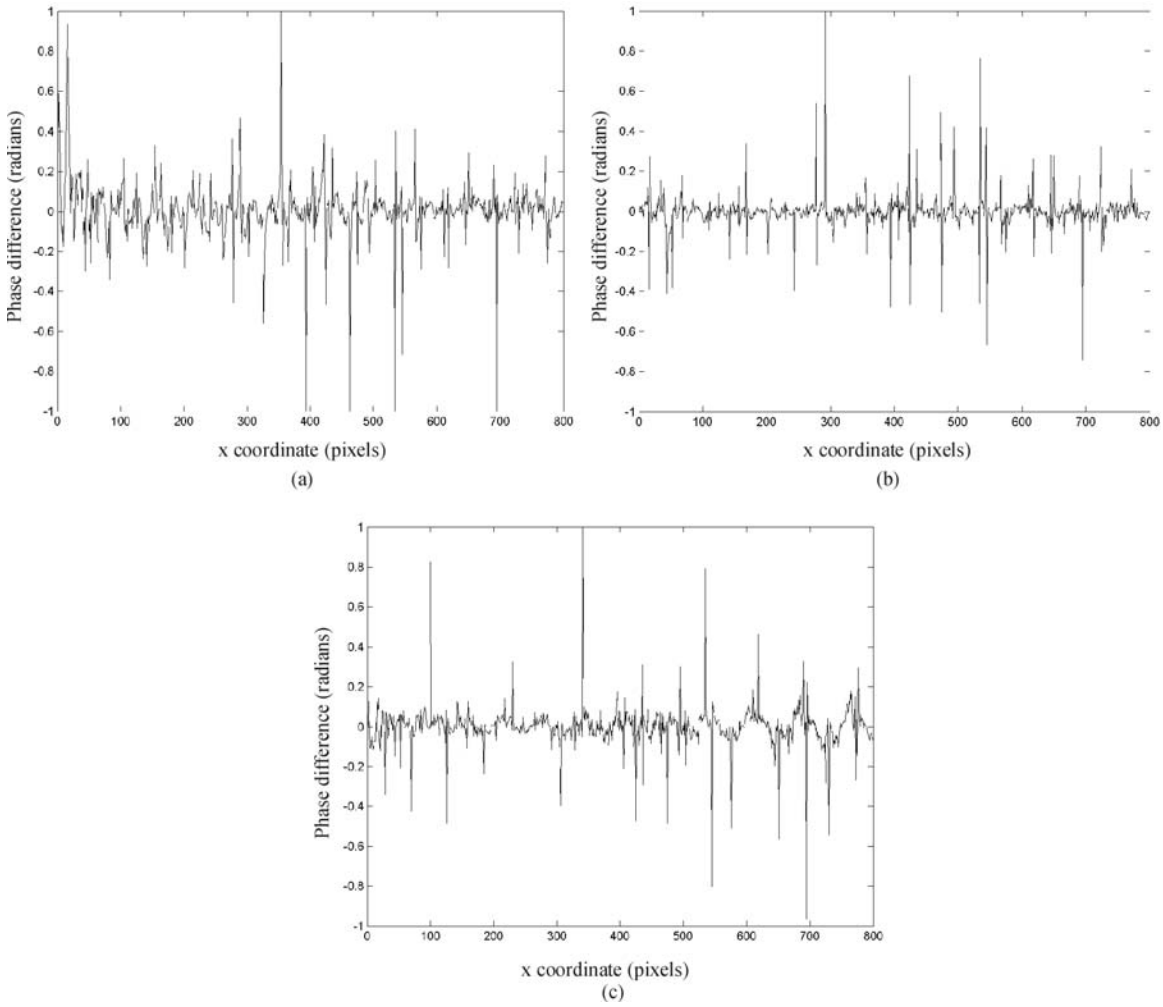

Figure 83: Difference in relative phase between two plane measurements where (a) planes are at different angles, (b) probe has been moved to a different angle and returned, and (c) probe has been removed from the head and replaced.

Table 15: Mean phase differences due to different actions between measurements.

Action between measurements	Mean phase difference (mrad)	Equivalent mean height difference (μm)
Plane and probe at different orientation (but same relative orientation)	13±7	14±8
Probe moved to different orientation then returned	3±2	4±2
Probe removed from head and replaced	5±7	5±7

The relative phase measurements show repeatability very close to the baseline level, apart from the measurement at different angles which shows repeatability approximately 3 times the baseline result. These results suggests that a different phase to height calibration should be carried out for each head E angle used for measurement, or alternatively some kind of compensation must be carried out to account for the effect of gravity on the probe. However it was decided that the time required to carry out repeated phase to height calibration was not justified by the relatively small mean error

of 14 μm recorded when using the probe at different angles. Instead a reference plane was measured each time the head was moved to a new E angle, but the full phase to height calibration was only carried out for one angle. It is possible that the effect of gravity on the probe could be modelled and compensated for, but this was not possible within the time constraints of this project. The reference plane was also re-measured each time the head was moved to a different E angle. And, because the probe mounting of the head was suspected to be a cause of instability, the position and orientation of the camera with respect to the head was re-found each time the probe was re-attached.

These requirements limited the measurements that could be made with the prototype. The need for a different reference plane for each E angle meant that the possible number of E angles was limited to the number of suitable reference planes. Two planes were available – a custom-made reference plane and an aluminium oxide plate (see section 4.3.7). If it were possible to remove the prototype and reliably replace it easily then these could have been used in more orientations, however the lack of repeatability in the probe mounting meant that a new camera to CMM calibration was taken each time the probe was removed, making measurements using more head E angles impractical. To make a measurement, the procedure was as follows:

1) Set up calibration planes with normals approximately 0° and 40° degrees to vertical.
2) Measure both calibration planes using a touch probe.
3) Replace the touch probe with the prototype.
4) Carry out a camera to CMM calibration (including internal camera parameters if they have not already been found) and use results for all the following steps.
5) Carry out a phase to height calibration with head angle E=0°.
6) Take measurement images at E=0°.
7) Re-orient the head to E=40° and record reference plane.
8) Take measurement images at E=40°.
9) If the probe is removed for any reason repeat step 4, measure a reference plane at E=0°, and proceed with steps 6, 7 and 8 as required.

All data processing was offline after data collection. The processing for the camera to CMM calibration must be carried out before data collection for phase to height calibration or data collection. This is because the position and orientation of the camera

must be accurately known for the compensation of rotation about the perspective centre used to create the phase stepped image. If the probe is removed and then replaced, the phase to height calibration remains valid but the camera to CMM calibration must be repeated and the reference plane phase must be re-measured.

7.6 Measurement results

A selection of objects was measured using the probe. The probe was created for proof-of-principle rather than to achieve high accuracy, but an idea of the accuracy achievable is useful. Two parallel planes with a known separation were measured and also a calibration sphere. The results of the measurements are given in section 7.6.1.

A chief requirement of the techniques under investigation is to enable automatic or semi-automatic measurement of complex objects. The curved object with two stepped blocks that was partially measured in Chapter 6 was re-measured using the prototype and the results are presented in section 7.6.2.

Measurements of objects with a variety of surface properties are presented in section 7.6.3. The objects used are three of the objects whose roughness and speckle contrasts were measured in section 4.3.9.

7.6.1 Measurement accuracy

A gauge block with plane parallel sides 7.0 mm apart was measured using two perspectives per side. The point density was approximately 1 point per 50 μm per viewing image. Matlab's "griddata" function was used as a spatial filter to cut the point density to 1 point per 50 μm in-plane. A plane was then fitted to each set of filtered points. The non-planar errors are summarised in Table 16. The RMS errors are approximately double the phase to height calibration errors. The surface of the block is smoother than the phase to height calibration plane and would be expected to exhibit a moderate speckle contrast greater than the 10% measured for the calibration plane. The speckle contrast is likely to be the main source of the extra phase measurement error. The angle between the plane normals was found to be 2.0°. The instability of the probe mounting and the small error from not repeating the phase to height calibration for both head E angles are thought to be the main reasons for the error.

Table 16: Errors from plane fit from two sides of gauge block.

Plane	Maximum error (μm)	RMS error (μm)	Maximum error (% of a fringe period)	RMS error (% of a fringe period)
1	838	240	12	3.4
2	828	191	12	2.7

Figure 84 shows a measurement of the top section of a calibration sphere. Only the top section could be measured because of the restriction on the usable head angles. The sphere was a 25 mm radius metal calibration sphere with a non-Lambertian surface. The sphere would be expected to cause a moderate to high speckle contrast, above the 10% found for the phase to height calibration plane. The radius of the fringe projection measurement had a mean error of 22±110μm and a maximum error of 770μm. The centre of the sphere was found to be 92±18μm from the correct value (found by a touch probe measurement). The measurement errors are dominated by noise. Figure 85 shows the radial error against the X, Y, and Z CMM coordinates (relative to the sphere centre).

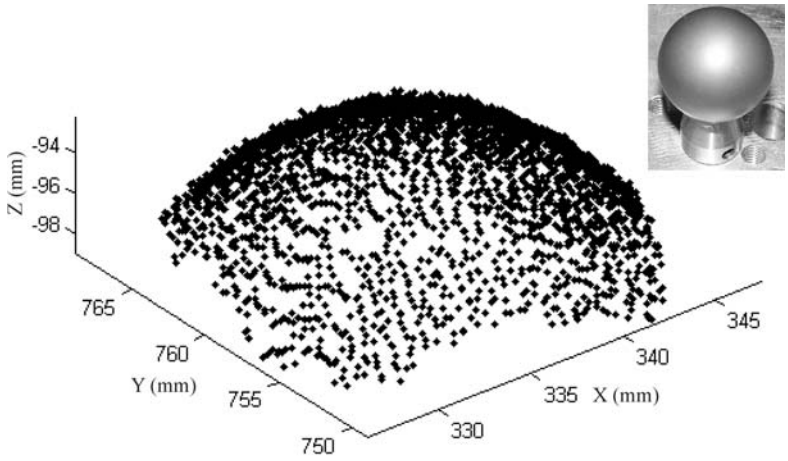

Figure 84: partial measurement of calibration sphere and (inset) photograph of sphere

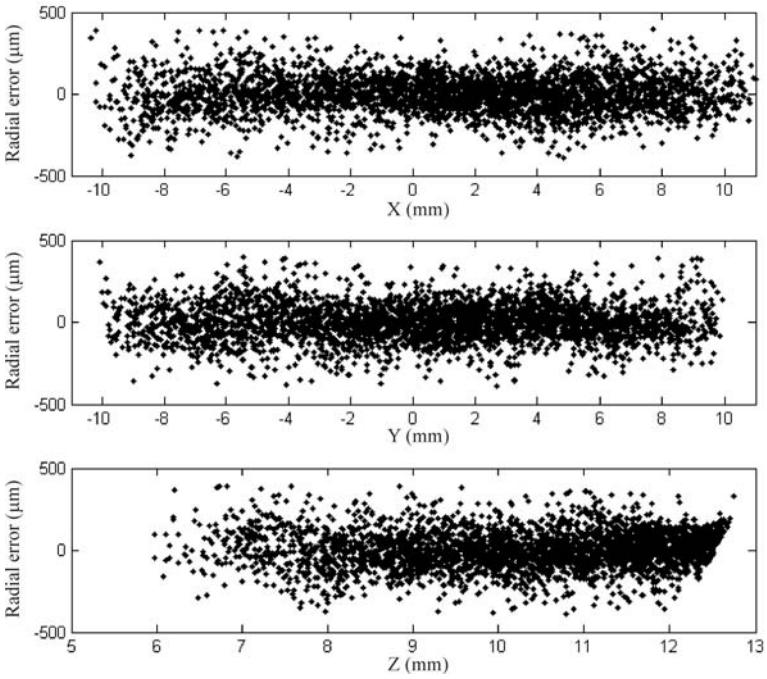

Figure 85: radial error from calibration sphere measurement

7.6.2 Automatic measurement of complex object

The object used in Chapter 6 (see Figure 86) was re-measured using the prototype to demonstrate the measurement of a fairly complex object by building it up from different surfaces. The perspectives from which the measurement was built up were chosen arbitrarily, but with the restriction of only using E angles of 0° and 40°. Figure 87 shows 3D plots of the measured points from a number of different angles.

Figure 86: Object with curved surface and steps used for measurement demonstration

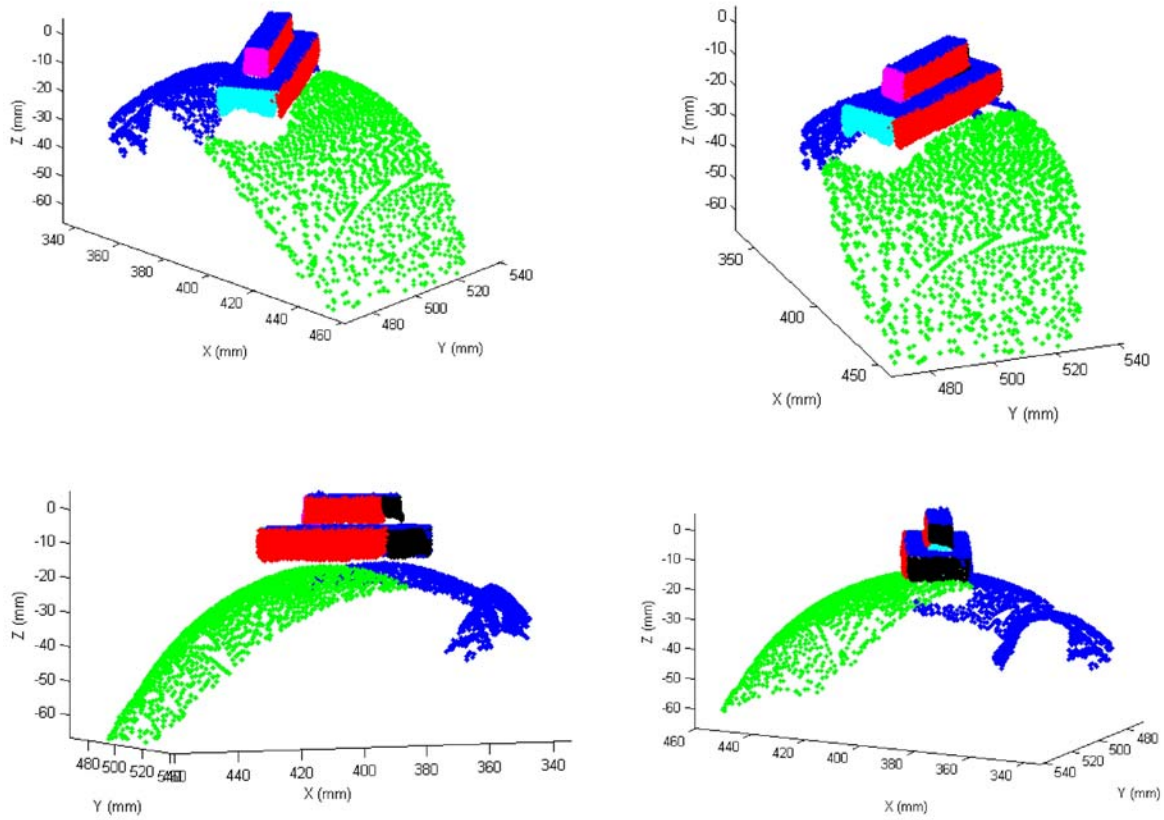

Figure 87: measured object from different perspectives. Different colours indicate different probe positions used as originating camera for 2π ambiguity resolution

In future the data collection will ideally be integrated with path-planning software, but here, the probe was moved to different perspectives by controlling the CMM using a joystick. At each of 37 different perspectives, eight phase stepped images were taken. Each set of images took approximately 5 seconds to collect, the majority of which is the image transfer time from the head to the UCC. The data were processed offline. The only user interaction required to carry out the processing is to choose segmented areas to measure. The phase calculation, image segmentation, unwrapping and 2π ambiguity resolution on each selected area is entirely automatic. The choice of segmented areas could be automated in future, resulting in an entirely automatic measurement. The data processing took approximately 90 minutes, but this is expected to decrease considerably with an optimised implementation. The potential improvements are discussed in Chapter 8.

7.6.3 Measurement of different surfaces

Figure 88(a) shows a measurement of a machined aluminium block built up from seven perspectives. The surface of this object makes it challenging to measure optically – it is shiny, has a high degree of specular reflection and a large speckle contrast. The curved

sides of the object are textured, and the top surface contains ridges and a number of scratches. In section 4.3.9 the top surface was found to have an RMS roughness of 0.4 μm and exhibited a speckle contrast of 17% of mean intensity under the prototype's light source. Inter-frame intensity variations close to the specular direction have caused obvious errors in a small area close to one of the object's edges, highlighted in the figure. Nevertheless, the figure shows that the model of the object has been built up with reasonable success.

Figure 88(b) shows partial measurement of the machined stainless steel air-bearing housing. Phase errors close to the specular direction have been reduced here by simply thresholding on the modulation amplitude of the fringes. The measurement was built from only three perspectives, and appears to be at least qualitatively successful despite the smooth, highly non-Lambertian surface with a large speckle contrast (18% of mean intensity).

Figure 88(c) shows a partial measurement of the timing belt cover also previously used. Different colours in the plot are used to indicate the separate surfaces that were automatically segmented. A large noise level is clear on the lowest surface, which was the roughest surface considered and had a speckle contrast of 16% of mean intensity. The measurement was built from five perspectives. More perspectives may be useful for averaging to reduce the noise, as well as to build up the model including the occluded surfaces.

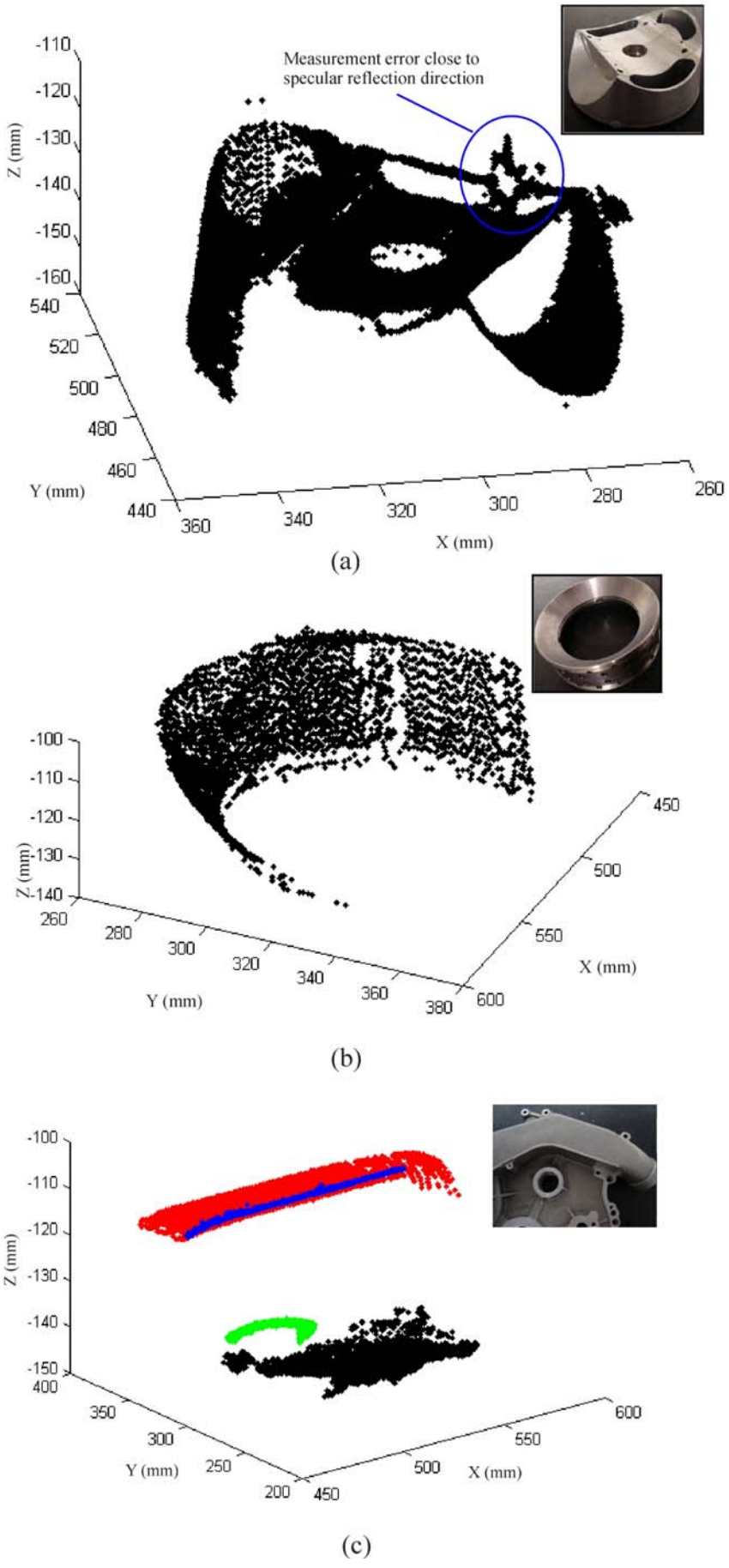

Figure 88: Measurements of objects with varying surface properties. (a) A machined aluminium block. (b) A machined stainless steel air-bearing. (c) A cast aluminium timing belt cover.

7.6.4 Discussion

All of the measurements presented above were created with very little user input beyond moving the prototype to different perspectives using the CMM. The processing took a considerable amount of time (around an hour and a half for 37 perspectives) due to the large amount of data collected, but no code optimisation has been carried out to date. The accuracy of the sphere and the calibrated gauge block showed that noise and phase calculation error are significant sources of error.

Post-processing of the data could cut down the number of rogue points by, for example, removing points that are a large distance from their neighbours and so cannot correspond to real surface points. Analysis of the surface gradient with respect to the probe positions could be used to remove points that have been viewed close to the specular direction. As more datapoints were generated than were required, averaging could be used, possibly with weights related to fringe modulation amplitude or viewing and illumination angles as appropriate. With the exception of sub-sampling for the parallel plane measurements, no post-processing has been carried out on the results reported here.

The restrictions on the head angles that could be used, and the requirement to re-measure a reference plane each time a new head E angle is moved to, are clearly unreasonable for a real product. Work to improve the mounting of the probe on the head, and to reduce the weight of the components in order to reduce the effect of gravity, is underway. Any remaining sag will be modelled and calibrated for to enable use of the probe at a large range of head angles. Smaller components must also be used so that the probe is compatible with the automatic probe change rack.

7.7 Conclusions

A prototype CMM probe was built and used to demonstrate the techniques developed in Chapters 5 and 6. Initial accuracy and repeatability tests were carried out and error sources identified. Measurements of a number of different objects were carried out to demonstrate the measurement of complex objects with a variety of surface finishes. The processing is highly automated and robust in the face of noise and phase calculation errors.

Two parallel sides of a gauge block were measured. The measured angle between the sides had an error of 2°. The distance between the two sides had an error of 250±300 µm. A calibration sphere was measured with a mean radial error of 22±110 µm and a positional error of the sphere centre of 92±18 µm.

The errors were from a variety of sources. Surfaces with a high speckle contrast and non-Lambertian reflectance properties cause phase measurement error that may be reduced by implementing a phase calculation algorithm with more phase steps [85], at the expense of data collection and processing time. Finer fringes would enable better height resolution. A white light source would reduce speckle noise. Errors due to the positioning of the device and the effect of gravity will be improved in future iterations of the probe with smaller and lighter, possibly custom-made components. These improvements are discussed in more detail in the next chapter.

Chapter 8 Conclusions and Future work

Novel techniques for automatic non-contact shape measurement have been described. The goal throughout has been the development of a simple fringe projection probe for a five axis coordinate measuring machine (CMM) for fast and accurate shape measurement in an industrial setting. A prototype probe has been developed and shape measurement successfully demonstrated with minimal user input. The probe consists of a fringe projector capable of projecting a single fringe pattern only, and a camera to record the images. Phase shifted fringe images are created by moving the probe using the CMM on which it is mounted. By rotating the probe about the camera's perspective centre, the images may be compensated for so that a given pixel in each compensated fringe image views the same point on the object. The compensated images are used to calculate the phase using a phase step algorithm. They are also used to help identify steps and edges on the object. The phase corresponding to any surface patch is only correct to some unknown integer multiple of 2π. The adjustment that must be made to the phase is found by using phase maps created from different perspectives. Different perspectives of the object are easily achieved by moving the probe using the CMM. Measurements of complex objects with different surface finishes were demonstrated using the prototype. The position of a sphere was measured correct to 100 μm with a mean radial error of 22 μm. The main reason for this error is the instability of the mounting of the probe on the head, combined with the effect of gravity on the probe affecting the phase to height conversion at different head angles.

The new phase step technique using rotation of the probe about the camera perspective centre was demonstrated to be correct to 1 part in 1250 of the field of view a single perspective. At first sight, this does not compare favourably with the other commercial fringe projection systems considered in section 2.5, for example the Breuckmann OptoTopHE, which reports accuracy of 1 part in 8000 of field of view. However, expressing the accuracy found in terms of fringe periods, the phase calculation for a single prototype perspective was accurate to be around 1.5% of a fringe period. Reducing the nominal fringe pitch at the object from 7 mm to 2 mm would result in an adequate fringe pitch at the camera image plane of around 16 pixels and would be expected to improve the accuracy to around 1 part in 4000. Phase calculations correct to 0.2% fringe periods have been reported from digital fringe projection systems using phase stepping

[144,145], although results correct to around 1% are more usual. The use of phase shift algorithms allowing an unknown phase step to calculate the phase results in slightly less accurate phase calculation results than are possible with more traditional phase shift techniques so the expectation of accuracy to 1.5% of a fringe period even with finer fringes than were used here seems realistic. Fringe contrast can be improved using non-illuminated images to remove any effect of ambient illumination. Metallic surfaces and machined parts will always reduce the accuracy achievable, but as previously mentioned, by avoiding highly specular directions the effect can be minimised.

This fringe projection technology is under active development within Renishaw. The intention is to market a fringe projection probe as a product complementing the existing range of CMM and machine tool probes. A number of ways to improve the prototype have been highlighted. These improvements may be categorised as software (section 8.1) and hardware (section 8.2) development. Alternative approaches are discussed in section 8.3. Finally, other possible applications of the new techniques are discussed briefly in section 8.4.

8.1 Software development

8.1.1 Phase step algorithm

The use of relative motion of object and projector to create the phase step means that error sources not significant for traditional temporal phase stepping must be considered. In particular, as discussed in Chapter 5, multiplicative intensity noise (speckle) and inter-frame intensity variations can have a significant effect on the results of the phase calculation. Furthermore, the phase shift created is unknown and dependent on the distance between object and probe. The algorithms used to calculate the phase when the phase shift is unknown have not received the same attention in the literature as many of the more commonly used algorithms. The algorithms used here have been modelled under conditions of additive noise and non-linear phase shift error [138,84]. It would be useful to fully model the response of the unknown phase shift algorithms in the presence of speckle noise and also for a combination of errors. This would enable the implementation of a more optimal algorithm for the system. The trade-off is likely to be between number of images taken and required accuracy, since the algorithmic response to noise generally improves with more phase steps.

8.1.2 Corresponding points

In Chapter 6 a technique was introduced to locate object edges in phase maps by processing fringe images in different orders. These edges can then be measured using photogrammetry, if either corresponding points or line segments can be matched in different perspectives. Only limited success of measurement of corresponding feature points was achieved in section 6.3, partly due to the limitations of the experimental setup being used, and partly because only a simplistic algorithm was used. It would be preferable to use more sophisticated matching algorithms. As discussed in 3.3.4 there are a number of these, such as least squares techniques, correlation techniques, RANSAC algorithms, relaxation labelling and many others. The alternative approach presented in section 6.4 enables surfaces to be measured without identifying individual corresponding features. If required, edges and corners could be identified once the surfaces have been measured, either by calculating the intersections of different surfaces, or by analysing surface gradient and curvature to identify edges and corners. Product requirements will determine the most appropriate algorithm or combination of algorithms to use.

8.1.3 Parallelisation

At present, the software to process the phase stepped images and construct a measurement is implemented in Matlab. Each image is undistorted and the phase step motion compensated for, then the phase is calculated from a set of images. The phase maps from each perspective are processed to get 3D measurements of the viewed object surfaces. All this processing takes time. Much of the processing is repetitive – the same operations are carried out on every pixel in an image with little or no interaction between individual pixels. Hence much of the processing is inherently parallelisable and could be carried out on simultaneously on multiple pixels. The computer games industry has driven the development of massively parallel processors at low prices affordable to the consumer in the form of graphics cards. These can provide speedup factors of up to around 1000 [146]. By implementing much of the processing of the images and phase maps it is hoped that real time processing can be achieved. An NVIDIA GeForce GTX 260 has been purchased to develop parallelised data processing algorithms.

The process to remove lens distortion from images is one sub-process that would benefit from parallelisation. In section 4.3.3 an iterative algorithm was shown to be more accurate than the more direct distortion removal technique used throughout the thesis, but

it was too slow to be used for entire images. By implementing the iterative technique to simultaneously run on each pixel or a selection of pixels within the image it is likely to be usable for real time measurement.

The processing to resolve the 2π ambiguity (section 6.4) can also be improved by parallelisation. There are a number of different ways in which this could be done. Firstly the processing of groups of pixels to find 3D points, and the inverse to find the image coordinates of groups of 3D points is clearly parallelisable. Secondly, processing of different point sets from the same image area corresponding to different 2π multiples could be carried out simultaneously. Similarly, the processing to find the match to an area from one perspective in the other perspectives could be parallelised on a perspective basis. Finally multiple areas from a single image provide another way to break the processing into independent, parallelisable blocks.

The best way to parallelise the processing has not yet been settled, but it is clear that there a number of different areas that could be sped up by an optimised implementation.

8.1.4 Integration with other software modules

The measurement data are currently collected manually. Users must joystick or programme a series of moves ensuring that the whole object is measured. Once the software has been parallelised and sped up to operate in real-time it should be easier to see which areas have been measured. However, path planning software should be incorporated to enable more automatic usage. Another step will be to convert the point clouds produced to describe the measurement object into more useful entities such as planes, conic sections or NURBS surfaces, depending on the object being measured and the requirements of the task. At the very least some averaging of the point clouds is likely to be desirable. Work is underway to incorporate the measurement software with a set of in-house geometry libraries, the output from which can then be integrated into industry standard CAD software.

8.2 Hardware improvements

8.2.1 Light source

The light source used in the prototype is a high-power red LED. This is permanently on when the probe is in use and is powered by a bench-top power supply. The leads connecting the probe to the power supply restrict the motion of the CMM and head and therefore the positioning of the probe. In a future version of the probe the light source will be replaced by a white light source such as a xenon flash lamp. The light source will be powered through the head. The camera shutter and the light source will be synchronised within the UCC controller software. A white light has the advantage of reducing speckle noise compared to the LED and therefore increasing the measurement accuracy. A xenon flash tube also produces a much greater light output than the current LED, which should mean less camera gain is required and fewer exposures are needed to get low noise images.

8.2.2 Grating

The grating used for the prototype is a 3 fringe/mm sinusoidal amplitude grating, resulting in around 15 fringes across the field of view with nominal period 7 mm. The phase calculation achieved had an RMS of around 1.4% of the fringe period resulting in a height error RMS of 96 μm (from the phase to height calibration). By projecting finer fringes an improvement in the height measurement should be possible. However there is a trade-off between height accuracy and measurement time. The resolution of 2π ambiguity is harder with finer fringes as the effective signal to noise ratio increases with decreasing fringe pitch. More perspectives may be required to confidently resolve the absolute measurement, which would result in both a longer data collection time and more data processing time. The limit to the fringe pitch depends on the camera resolution. Optimisation of the data collection and processing elements of the system will almost certainly justify a considerably finer fringe pitch however, with commensurate improvements in measurement accuracy.

8.2.3 Miniaturisation

The prototype was largely constructed using off-the-shelf components. The size and weight of the probe and the fact that the LED was externally powered all contribute to problems with sag and repeatability. The effect of gravity on the probe was shown in

section 7.5. It may be possible to calibrate for the effect of gravity on the probe but it is preferable to design the probe so that its effect is minimised. The lack of repeatability is believed to be largely because the probe is too heavy for the magnets holding it to the head. There are two sets of magnets involved. One set holds a kinematic mount between the camera lens/projector module and the camera together. The second set holds a kinematic mount between the probe (camera lens, projector and camera) and the head together. In the prototype, the first set was not strong enough to hold the lens and projector to the camera, so this joint was glued. The second set were strong enough to keep the probe attached up to an angle of approximately 50°, but repeated measurements separated by reorientation of the probe were not consistent, and the seating of the probe was suspected to be changing slightly (see section 7.5). Stronger magnets have been sourced, but it is likely that space requirements will result in them not being usable in the long term. Furthermore, it must be possible to store and automatically change the probe in a probe change rack – the probe is currently too large to allow this to happen. The probe will be miniaturised by a combination of sourcing different off-the-shelf components and by designing custom-made key components if necessary. An obvious place to start is the projection and imaging lenses. For flexibility during development these were variable focus lenses. In the next generation of the prototype these will be replaced by lenses with a fixed focus and a fixed aperture, chosen to be suitable values. Long-term, different interchangeable lens modules may be produced allowing varying stand-off distances, the required module chosen for the task at hand. Other parts of the probe may also be miniaturised, for example the condensing lens in the projector. The clamp holding the projector and camera together can be made fixed rather than hinged and the whole assembly will be optimised for minimum weight and maximum stiffness once the projector and camera lenses are lighter.

8.3 Alternative approaches

8.3.1 Stripe or spot projection

A probe projecting a single line or a point rather than a set of fringes enables considerably simpler processing. Only the location of the line or point within the images must be calculated and converted to distance from the camera and therefore 3D measurement. The drawback is the increased data collection time. To collect the equivalent of one image-worth of data requires 1000 images of a stripe to be taken or 1 million spot images (assuming an image is 1000 by 1000 pixels). With the prototype probe the same surface

patch could be measured with sixteen images (assuming eight phase steps at each of two perspectives). The more complex processing required for the fringe projection data is expected to be outweighed by the longer data collection time required for a stripe or spot projection, but it does remain a valid alternative approach.

8.3.2 Pattern projection

A pattern of lines or spots could provide a compromise between data collection time and data processing time. As an example, consider a probe projecting 10 parallel lines. The multiple perspective technique developed here could enable unambiguous measurement. An image-worth of data could be collected in 200 images (again assuming an image of 1000 by 1000 pixels and two perspectives). Alternatively an encoded pattern could be projected to remove the need for 2π ambiguity resolution, perhaps using colour or by marking a zero order stripe in some way. Successful use of colour tends to be object-dependent, and requires a colour rather than a simple monochrome camera. The increased complexity of pattern projection compared to projection of a single stripe, and the increased data collection time compared to fringe projection make it less likely to be a competitive approach, however it may be worth some consideration.

8.3.3 Multiple cameras

A probe consisting of two cameras and a single fringe projector could enable unambiguous measurement of a surface patch from a single perspective. Viewing the same fringe pattern simultaneously using two cameras allows corresponding points to be identified and then measured using photogrammetric techniques. The measured points can be used to resolve 2π ambiguity over the remainder of the surface which can therefore be measured from the fringe data. This has not been considered in detail here because of the size and weight limits on the probe, but it may provide a useful alternative implementation.

8.3.4 Programmable projector

A mini-projector has been considered as an alternative to a fixed-grating fringe projector. This removes the requirement to create phase stepped images by moving the probe, and therefore simplifies the data processing. There are a number of disadvantages associated with a programmable projector. The currently-available mini-projections do not have the

required resolution or luminosity, although this is likely to change in the near- to mid-term future. The lack of stability and long warm-up time demonstrated in section 4.3.5 are drawbacks, although not insurmountable. It is uncertain that a mini-projector would withstand the accelerations exerted on the probe, particularly when being automatically changed in a probe change rack. The extra cost associated with a mini-projector compared with the simpler fixed pattern projector provides an important commercial driver for the fixed pattern projector used here.

8.4 Further applications

The use of the algorithms and techniques developed here go beyond the specific application of a CMM-mounted probe.

A system consisting of a simple projector and a camera mounted on a simple mechanical structure could be used to create phase shifted images if the structure constrains the camera and projector to rotate about the camera's perspective centre. An amplitude grating with one of the fringes marked as the zero order fringe should be straightforward to manufacture. This setup could enable quick and easy measurement using cheap, robust equipment, possibly for the consumer market or for other applications where only moderate accuracy is required.

The technique of 2π ambiguity resolution is equally applicable to other structured light projection techniques as to fringe projection, for example grid or line projection. It can also be used for fringe projection systems in which phase shifting is possible internally to the projector, or for situations where a Fourier Transform or other single frame technique can be used to calculate phase. In any of these cases, only one camera and projector is required for a full measurement. Either the object or the camera and projector can be moved, providing the effective camera motion (relative to the object) is well known. A simple example is of production line measurement of objects on a conveyor belt moving at a constant speed. If an object being measured has trackable features, then the relative position and orientation of the camera can be found from the images, eliminating the need for a robot or CMM to move the camera and projector (or object) to different perspectives.

Leitz PMM-G

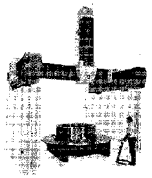

Leitz PMM-G - Worlds largest high precision CMM & gear inspection system

The Leitz PMM-G provides highest accuracy and a highly enhanced throughput for large-size XXL workpieces. These workpieces are used for example in aircraft and aerospace industries or in ship engine constructions. Also the measurement of large gears used in wind turbines is possible. Despite such large measuring strokes, the Leitz PMM-G reaches a precision and performance level, which is usually common with much smaller 3D measuring machines.

Leitz PMM-G

Description Features & Benefits Technical Data Related Information Applications Downloads

CMM Specifications and Gear Inspection

CMM Specifications

Model	X stroke [mm]	Y stroke [mm]	Z stroke [mm]	Accuracy [µm]
XX.20.12	3000/4000/5000/6000/7000	2000	1200	$MPE_E = 2.4 + L/400$
XX.30.12	3000/4000/5000/6000/7000	3000	1200	$MPE_E = 2.4 + L/400$
XX.40.12	5000/6000/7000	4000	1200	$MPE_E = 2.8 + L/400$
XX.20.16	3000/4000/5000/6000/7000	2000	1600	$MPE_E = 2.6 + L/400$
XX.30.16	3000/4000/5000/6000/7000	3000	1600	$MPE_E = 2.8 + L/400$
XX.40.16	5000/6000/7000	4000	1600	$MPE_E = 3.0 + L/400$
XX.20.20	3000/4000/5000/6000/7000	2000	2000	$MPE_E = 2.8 + L/400$
XX.30.20	3000/4000/5000/6000/7000	3000	2000	$MPE_E = 3.0 + L/400$
XX.40.20	5000/6000/7000	4000	2000	$MPE_E = 3.3 + L/400$
XX.30.25	3000/4000/5000/6000/7000	3000	2500	$MPE_E = 3.5 + L/400$
XX.40.25	5000/6000/7000	4000	2500	$MPE_E = 3.9 + L/400$
XX.30.30	3000/4000/5000/6000/7000	3000	3000	$MPE_E = 3.9 + L/400$
XX.40.30	5000/6000/7000	4000	3000	$MPE_E = 4.5 + L/400$

Gear Inspection

Cylindrical gears:

- Spur, helical, double helical, spines (internal and external)

- Clutch gears (internal and external)
- Gear segments (minimum No. of teeth: 1)
- Gear racks

Bevel gears:

- Straight bevel, spiral bevel, hypoid bevel, crown gears

Available interfaces:

- Gleason GAGE 4/WIN; Klingelnberg KIMOS; bevel-gear-chain from University of Aachen

Gear cutting tools:

- Hob cutter, broach, shaper cutter, shaving gears, form cutter

Evaluation standards:

- DIN, ISO, AGMA, ANSI, JIS, CNOMO, CAT

Leitz PMM-G gear inspection systems - Related specifications	PMM-G XX.20.ZZ	PMM-G XX.30.ZZ	PMM-G XX.40.ZZ
Modul range [mm]	0.5 - 100	0.5 - 100	0.5 - 100
Max. gear dia. - spur [mm]	1950	2950	3950
Max. gear dia. - helical* [mm]	1600	2500	3500
Max. shaft length [mm]	up to 7000	up to 7000	up to 7000

*The max. gear diameter depends on modul and shaft configuration. Even bigger diameters can be measured, if related area for x/y during the measurement.

F25
Measuring Nanometers

- Ultra-precise kinematics
- Miniature touch stylus
- Multi-sensor system

ZEISS

We make it visible.

Smallest Parts – Maximum Precision

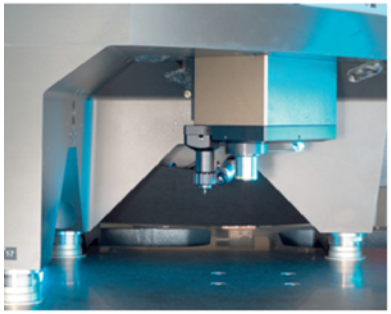

Micro-motors, micro-switches and precision components are showing up in more and more areas of our lives. Their reliability depends on their quality which is defined by measuring. With its intricate parts, micro-system technology is the challenge facing touch or optical measuring. Extremely small dimensions and different forces exist here; other principles apply.
With the F25, Carl Zeiss has developed a coordinate measuring machine capable of measuring micro-system components.

Overview

3D coordinate measuring machines supported on air bearings with a measuring volume of one cubic decimeter. The ultra-precise kinematics combined with the highly accurate measuring system enable measuring uncertainty of 250 nanometers at a resolution of 7.5 nanometers. Using minimal probe forces, this resolution, along with optimum control of the linear drives, enables touch measurements even in bores less than one millimeter in diameter.

Touch scanning sensor

A touch, passive measuring stylus was developed based on a 6.5 x 6.5 mm silicon chip membrane and integrated piezo-resistive elements. The stylus permits measurements in both single point and scanning mode.
The 3D micro-stylus is designed for stylus diameters of 50 – 500 micrometers and stylus tip diameters of 100 – 700 micrometers. With a free shaft length of up to 4 mm, it is possible to measure in small, deep-lying structures with probe forces of less than 0.5 mN/µm.

Optical sensor

The ViScan camera sensor from the standard program, combined with an objective lens based on those used in Zeiss microscopy, is used as an optical sensor for 2D measurements. These optics, which are optimized for depth of field and have minimized distortion, ensure accurate measuring results with maximum resolution in reflected and transmitted light.

Multi-sensor system

The combination of touch and optical sensors enables measurements of 2D and 3D structures in the same coordinate system. An additional camera aids visualization when probing the miniaturized features, thus simplifying part programming.

Software

Time-tested CALYPSO from Carl Zeiss enables you to evaluate captured data using standard measuring software with an intelligent user interface that can also be used on all other coordinate measuring machines.

Range of applications

- Rotation symmetrical parts with freeform surfaces, small radii, undercuts
- Prismatic parts with small and deep bores
- Flat metal parts with low form stability
- 2D parts with bores and cut-outs

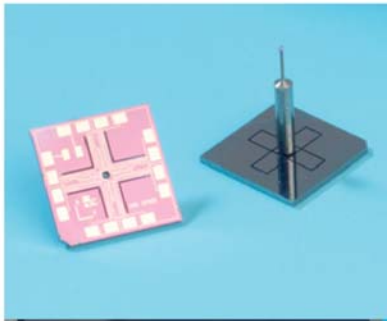

F25 description			
Kinematics	Highly accurate, air-bearing kinematics with linear drives and base with active air damping		
Measuring systems	Ultra-precise, incremental length measuring systems with glass-ceramic scales in all machine axes with a resolution of 0.0078 µm		
Touch sensor system	Highly accurate silicon stylus kinematics with integrated sensor system and resolution of 0.001 µm including flexible changer		
Optical sensor system			
Camera system for image analysis	S/W CCD camera (based on ViSCAN)		
Illumination	Reflected light LED ring (orange 605 nm) Transmitted light Light table white		
Optical system	Highly accurate lens with 13x magnification, 17 mm working distance		
Observation camera	Single lens with focus on the touch sensor system S/W CCD camera		
F25 measuring ranges, dimensions, weight			
Measuring range	Touch	Optical	Touch and optical
X [mm]	135	135	100
Y [mm]	135	135	100
Z [mm]	100	100	100
Dimensions (W x H x D)	approx. 1650 x 1450 x 2000		
Max. workpiece weight	up to 5 kg		
F25 weight	600 kg		
Weight of base	150 kg		
F25 accuracy			
Solid state joint probe Linear measuring tolerance MPE complies with DIN EN ISO 10360-2 L* = measuring length in mm	for E (µm) at 19.5 – 20.5 °C (67.7 – 68.9°F) 0.25 + L*/666		
Probing tolerance MPE complies with DIN EN ISO 10360-2	for P (µm) 0.25		
ViScan (Optical image analysis) Probing tolerance Complies with VDI 2617-6	R2 (µm) 0.4		
Acceleration	300 mm/s² per axis		
Travel speed	20 mm/s per axis		
F25 Ambient conditions			
Humidity	40% (+59°F) to 60% (86°F)		
Ambient temperature for operational readiness	+15 °C (+59°F) to +30 °C (86°F)		
Temperature conditions to guarantee specifications	Complies with measuring lab class 1 in accordance with VDI/VDE 2627		
Ambient temperature	20 °C (68°F) ± 0.5 K		
Temperature gradient	0.2 K/h 0.4 K/d 0.1 K/m		

Carl Zeiss
Industrial Metrology GmbH
73446 Oberkochen/Germany
Contact: Karl Seitz
Tel.: ++49 (0)73 64/20-4326
Email: seitz@zeiss.de
Internet: www.zeiss.com/imt

For further details, please contact:

Dynamic Laser Interferometer

Quality Without Correction

The FizCam 3000 interferometer is an entirely new on-axis dynamic Fizeau design, providing highly accurate measurement of optical grade surfaces even in the presence of vibration and air turbulence.

The FizCam 3000 incorporates patented technology using a single camera, high-speed optical phase sensor that makes a wavefront measurement in less than 1 millisecond. Because acquisition time is so short, the FizCam 3000 can be used under almost any conditions, even for measuring moving parts, without additional vibration isolation.

With a completely on-axis design, the dynamic FizCam 3000 interferometer eliminates the inherent aberrations, software corrections and painstaking calibrations and alignments typical of tilted beam Fizeau systems. The result is remarkable measurement quality and ease of setup.

Complete Measurement System

The FizCam 3000 is a turnkey instrument that includes the interferometer, 4Sight™ advanced wavefront analysis software, and complete high-speed computer system. In addition, the FizCam 3000 offers true 4X motorized optical zoom imaging, and a hand controller for remote control of Focus and Zoom.

Accessory Optics

With the FizCam 3000, it is not necessary to replace expensive accessories. 100 millimeter Fizeau accessories from a wide variety of manufacturers are compatible. When you need additional components, 4D Technology offers precision components to cover almost any need.

Industry Leading Analysis, Standard

4Sight wavefront analysis software features a user-friendly interface with unmatched simplicity, analysis features and graphical displays. The Measurement Console display aids alignment and execution of single, averaged, burst or continuous data acquisition. The Measurement Flow interface lets you visualize the entire measurement data flow, from raw acquisition through masking, reference subtraction, terms removal, etc. The unique Measurement Stack enables complex data manipulation and comparison. Zernike, Seidel, geometric and diffraction analyses are easy to perform. Comprehensive data sharing capabilities let you read, write, save and print from most file types, including MetroPro IDL®, MatLab®, Opticode®, Vision®, HDF5 and CodeV®. Generating phase movies to characterize deforming surfaces and moving parts is simple and straightforward.

FizCam 3000

FEATURES

- Vibration Insensitive Dynamic Operation
- Motorized Remote Operation Hand Controller
- 4X Optical Zoom Imaging
- Bayonet Mount Optics
- 1000 x 1000 Pixel Camera

APPLICATIONS

- Long Cavity Measurements
- Optical Testing of Moving Parts
- Production Environment Ready
- Environmental Chamber Testing

3280 E Hemisphere Loop, Ste 146, Tucson, AZ 85706 • Tel: +1 (520) 294-5600 • Fax: +1 (520) 294-5601 • www.4DTechnology.com

Specifications

Configuration	Model 3000
Description	Turnkey vibration insensitive dynamic Fizeau interferometer system
Acquisition Mode	Instantaneous Phase Shifting with pixelated phase sensor or Temporal PSI
Laser Source	632.8 nm HeNe, 100 m coherence
Output Beam	100 mm collimated, standard; 150 mm optional
Reference Optics	Bayonet mounted
	100 mm model: 10.8 cm (4.25 in) optical axis, horizontal or side
	150 mm model: 13.3 cm (5.25 in) optical axis, horizontal or side
Optical System	Fizeau with coherent imaging, test and reference beams fully on-axis
Zoom	4X, optional zoom encoder
Pupil Focus Range	Motorized, ±2 m, at all zoom settings
Alignment	Twin spot
Camera	1K x 1K pixels standard, 10-bit progressive scan with CameraLink™
Hand Controller	Remote control of focus and zoom
Data Array	Selectable: full, half, quarter resolution
Exposure	< 1 ms typical
Computer System	Minimum Dual Core 2 GHz processor
	1 GB RAM, 160 GB hard drive, CDRW and DVDRW
	19 in LCD monitor, keyboard and mouse
Operating System	Windows XP®
System Software	4Sight™ Version 1.7 or later, with User Manual
	Instantaneous Phase Shifting data acquisition
	Reference generation, subtraction, data averaging, masking
	2D and 3D surface maps
	Zernike / Seidel / Slope / Geometric / Fourier Analysis
	Fiducial aided data set mapping
	HDF4 / HDF5 data format standard, others supported
	Upgrades free during warranty period
Physical Envelope	100 mm model: 72.4 x 42.0 x 22.9 cm (28.5 x 16.5 x 9 in)
	150 mm model: 98.0 x 44.5 x 25.4 cm (38.6 x 17.5 x 10 in)
Weight	100 mm model <45 kg (100 lbs); 150 mm model < 56.5 kg (124.5 lbs)
Power consumption	< 750 Watts
Temperature Range	Operational: 60–80° F, non-condensing
	Storage: 30–100° F, non-condensing
Warranty	One Year, limited, on-site system installation and operator training
System Performance	
Acquisition Rate	> 14 frames/sec display
	> 14 frames/sec burst acquisition
Sample Reflectivity	1 to 100%
RMS Repeatability	< 0.0002 waves*
Uncalibrated Accuracy	< λ/20 transmission flats (typical with reference subtract)

*One sigma for RMS of 10 data sets of calibration mirror, each data set being an average of 128 measurements.

100 mm model dimensions

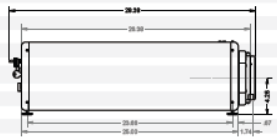

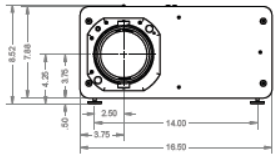

3280 E Hemisphere Loop, Ste 146, Tucson, AZ 85706 • Tel: +1 (520) 294-5600 • Fax: +1 (520) 294-5601 • www.4DTechnology.com

NewView™ 7300 Specifications

System	
Measurement Technique	Non-contact, three-dimensional, scanning white light interferometry
Scanner	Closed-loop piezo-based, with highly linear capacitive sensors
Objectives	1X, 2X, 2.5X, 5X, 10X, 20X, 50X, 100X; objectives available in standard and long working distances Refer to the NewView Objective Chart for objective specifications
Objective Mounting Options	• Single objective dovetail • Manual 6-position turret • Motorized 6-position turret
Field Zoom Lenses	High-quality discrete zoom lenses; 0.5X, 0.75X, 1.0X, 1.5X, 2.0X
Image Zoom	Motorized 3-position system zoom
Field of View	From 0.03 to 14 mm; larger area imaged with field stitching; objective and zoom dependent
Illuminator	Unique single white-light LED design with superior life, uniform imaging and high efficiency
Controls	Filter Tray, Aperture Stop, and Field Stop (Focus-aid)
Measurement Array	Selectable, includes standard- 640x480, 320x240, 160x120; optional- 992 x 992 (1K)
Part Viewing	Secondary LCD monitor
Focus	Motorized manual and auto focus
Z-Drive (Focus) Stage	DC brushless microstepper motor with ballscrew drive, 4 in. range, and 0.1 µm resolution
Part Stage Options	• Manual Tip/Tilt/X/Y with ±6° tip/tilt, ±2 in. x/y • Motorized Tip/Tilt/X/Y with ±4° tip/tilt, ±3 in. x/y • Motorized Tip/Tilt/X-Theta (or Y-Theta) with ±4° tip/tilt, ±3 in. linear travel
Computer	High-performance Dell PC with LCD monitor
Software	ZYGO MetroPro software running under Microsoft Windows XP
Physical	
Dimensions (H x W x D)	Overall System: 62 x 52 x 35 in. (157 x 132 x 89 cm) NewView: 32 x 23 x 16 in. (81 x 58 x 41 cm) Vibration Isolation Table: 30 x 24 x 24 in. (76 x 61 x 61 cm) Workstation Table: 33.5 x 52 x 35 in. (85 x 132 x 89 cm)
Weight	System: ≈ 950 lb (430 kg) NewView: ≈ 200 lb (90 kg) Vibration Isolation Table: ≈ 600 lb (272 kg)

Performance	
Vertical Scan Range	150 µm (5906 µin); Extended scan range to 20 mm (0.79 in.)
Vertical Res.	< 0.1 nm (0.004 µin)
Lateral Res.	0.36 to 9.5 µm; objective dependent
Data Scan Rate	≤135 µm/sec, user-selectable; camera and scan mode dependent
Maximum Data Points	307,200; 984,064 (optional); camera dependent
RMS Repeatability	< 0.01 nm (0.0004 µin) RMSσ
Step Height	Accuracy < 0.75% Repeatability ≤ 0.1% @ 1σ
Test Part Characteristics	
Material	Various surfaces: opaque, transparent, coated, uncoated, specular, and nonspecular
Maximum Size (H x W x D)	3.5 x 8 x 8 in. (89 x 203 x 203 mm); larger sample sizes possible
Reflectivity	1-100%
Environmental Requirements	
Temperature	15 to 30°C (59 to 86°F)
Rate of Temp. Change	<1.0°C per 15 min
Humidity	5 to 95% relative, noncondensing
Vibration Isolation	Required for vibration frequencies in the range of 1 Hz to 120 Hz
Utility Requirements	
Input Voltage	100 to 240 VAC, 50/60 Hz
Compressed Air	60 to 80 psi (4.1 to 5.5 bar); dry and filtered source; 1/4 in. input

zygo®

ZYGO CORPORATION
LAUREL BROOK ROAD • MIDDLEFIELD, CT 06455
VOICE: 860 347-8506 • FAX: 860 346-4188
WWW.ZYGO.COM • EMAIL: inquire@zygo.com

A1.5 3DShape Gmbh Cam3d

Home
Company
Products
Metrology services
3D Gallery
News
For the press
Downloads
Contact
Masthead

KORAD3D
µKORAD3D
KorMASTER3D
FaceSCAN3D
BodySCAN3D
CAM3D
SCAN3D
SpecGAGE3D
SLIM3D
3DViewer

Deutsche Version

print version

Products > CAM3D

Introduction
Measurement Principle
Measurement Examples

Flexible shape measuring system for mid-sized objects

Many applications, such as medical engineering, demand the fast scanning of an object's shape. The CAM3D optical sensor enables complete surface measurement of an object in under a second. The generated point clouds are available immediately after measurement and can be computer processed to create a triangle mesh within a few minutes.

Fast evaluation and 3D display of data with easy-to-use software open up numerous opportunities for the user.

CAM3D is used for:
- Non-contact measurement of works of art
- Reverse engineering
- Industrial shape and positioning inspection

CAM3D

top

3D-Shape GmbH
Henkestraße 91
D-91052 Erlangen
Germany

Phone: +49-9131-977 959-0
Fax: +49-9131-977 959-11
E-mail: info@3d-shape.com

Measurement Examples

The following objects were first digitized using CAM3D, then the SLIM3D reverse engineering software was used to process and display the data as triangle meshes

Mesh of a human head, reconstructed from 45 measurements (from the real-life subject) with a measurement accuracy of 130 µm.

top

Mesh of a bronze sculpture by Franz Marc (Moritzburg National Gallery, Halle / Saxony-Anhalt Regional Studies Museum), reconstructed from 32 measurements with a measurement accuracy of 120 µm.

top

Mesh of the "Trumpet Angel" at the Bamberg cathedral, reconstructed from 200 measurements with a measurement accuracy of 140 µm

Textued 3D mesh of a potato chip bag, aquired with CAM3D.

Click the image to the right to start an Flash animation.

3D-Shape GmbH also provides 3D measurement services using the CAM3D measuring system.

top

Measurement Principle

CAM3D is an optical sensor based on coded illumination. Measurement is based on a patented process that involves illuminating the surface of the measured object with a fringe pattern. A camera observes the illuminated object from the side. The surface shape of the object is calculated according to the resulting displacement of the fringes.

Fringe pattern projected onto the object surface, seen from the camera's perspective.

Field (mm²)	Depth measurement range	Resolution	Measurement error	Measurement time
100 x 100	60 mm	100 µm	30 µm	< 1s
200 x 200	120 mm	200 µm	60 µm	< 1s
300 x 300	180 mm	300 µm	90 µm	< 1s

400 x 400	240 mm	400 µm	120 µm	< 1s
600 x 600	360 mm	600 µm	180 µm	< 1s
800 x 800	480 mm	800 µm	240 µm	< 1s
1000 x 1000	600 mm	1000 µm	300 µm	< 1s

top

A1.6 GOM Tritop

gom Optical Measuring Techniques

Workflow
Datasheet
Add-ons
Software
Download

Measuring Systems | TRITOP | System | Datasheet

TRITOP

Using TRITOP, objects of up to some 20 m can be measured. Depending on the measuring task, different camera systems are available.

All TRITOP systems are self-calibrating and self-checking.

System Configurations	HR / Std
Camera Resolution	up to 21 million pixels
Data Transfer	wireless or flash card
Measuring Area	0.1 x 0.1 to >> 10 x 10 m² 4 x 4 to >> 400 x 400 inch²
Calibration	self-calibrating
Certification	according to VDI 2634/1
Operating Temperature	-40 to 120°C -40 to 250 °F

GOM mbH
Mittelweg 7-8
38106 Braunschweig
Germany

Tel.: +49 531 390 29 0
Fax.: +49 531 390 29 15
info@gom.com
www.gom.com

Contact|Imprint

A1.7 Geodetic V-Stars

Geodetic Systems, Inc.
3D Industrial Measurement Systems

Picture Perfect Measurements™

Why V-STA
Benefits
What is Photogrammetry?
Papers
FAQ
Glossary
Download Papers
Why V-STARS?
Prod
Applicat
Sup
Part
F
About
Contac

Latest News
Click here to see how V-STARS can quickly and accurately build even in unstable environments

Benefits

Photogrammetry offers users a number of attractive and **unique advantages** over conventional measurement techniques.

High accuracy	The single camera **E3** system is capable of producing accuracies of the order of **1:60,000** of the object size. The single camera **V-STARS/S** system is capable of producing accuracies of the order of **1:120,000** of the object size. (0.08mm on a 10m object). The dual camera **V-STARS/M** system is capable of producing accuracies of the order of **1:60,000** of the object size. (0.17mm on a 10m object)
Non-contact	The measurement process is totally non-contact. This makes it ideal to measure delicate items that deform when touched.
Fast results	Results are typically available within minutes of completing the object photography with single camera (**V-STARS/S**). In the two camera on-line system (**V-STARS/M**) results are available instantly.
Flexibility	The system is routinely used in a wide range of applications. It is suited to part inspection, deformation measurement or even part adjustment.
Portable	The entire system is battery operated and hence is highly portable. The system can be taken to even the remotest places. One "size-wise" carry on case and a laptop computer is all the equipment needed to complete a measurement. This makes it ideal to complete measurements at the supplier or customer site. 

Picture Perfect Measurements

Picture Perfect Measurements

Click here to view a short video about VSTARS

Minimal temperature effect	As the photography is completed in less than 10-15 minutes the effect of temperature differential between the start and end of measurement is greatly minimized.
Immune to vibration	**V-STARS** works in unstable environments. This includes vibrating or unstable floors, man lifts, cranes and ladders. Additionally the object itself can be vibrating or moving during the measurement without affecting the results.
Versatile in confined spaces	The system is small enough to operate in even the most challenging line of sight environments.
High data rates	The system lends itself well to high point data requirements. It is capable of measuring thousands of points in the same amount of time it would take to measure ten.
Thermal vacuum chamber	With **I-CAN**, **GSI's** state-of-the art **INCA** cameras can now operate in thermal vacuum environments while maintaining the high accuracy of the **INCA** digital camera and **V-STARS** system.
Target projection operation	**GSI** has developed a target projection system that can be used to measure thousands of points on a surface without applying a single target. The system is suited to rapid surface measurement for inspection or adjustment purposes. Refer to **PRO-SPOT** in the product section for more information. 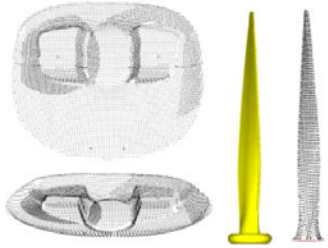
Proven track record	**GSI** has established itself as the premier manufacturer of measurement systems for aerospace, automotive, and antenna manufacturing.

Wolf&Beck
SENSORIK

OTM Series
Data Sheet

Dr. Wolf&Beck GmbH • Daimlerstr. 19 • 73117 Wangen / Germany • Tel.: +49/7161/1585-0 • Fax: -200 • www.wolfbeck.com

Wolf&Beck
SENSORIK

Technical data

- **General technical data:**

Working temperature range	+18°C to +22°C
Operating temperature range	+10°C to +40°C
Storage temperature range	-10°C to +70°C
Air humidity	max. 80% (non-condensing)
Warm-up time	generally: 30 min, OTM3M with temp.compensat.: 0 min
Threshold frequency of measuring system	200 Hz, with option /F 2 kHz
Threshold angle for detection of inclined surfaces[1]	80°
Threshold angle for precision specifications[1]	60°
Maximum wire length, measuring head-controller	50 m

[1] dependent on measured surface, figures for reference surface

- **Technical data measuring head:**

	OTM3-03	OTM3-10	OTM3-20	OTM3A-20	OTMA-35	OTM3A-50
Measurement range	3 mm	10 mm	20 mm	20 mm	35 mm	50 mm
Mean stand-off	20 mm	44 mm	59 mm	85 mm	110 mm	140 mm
Triangulation angle	26°	14°	10°	15°	10°	9°

- **Accuracy:**
  The definition of the terms used and the implementation of the corresponding measurements are done on the basis of DIN 32877 (Opto-electronic distance, profile and shape measurement).

	OTM3-03	OTM3-10	OTM3-20	OTM3A-20	OTMA-35	OTM3A-50
Resolution	0.3 µm	1 µm	2 µm	2 µm	3.5 µm	5 µm
Repeatability[1]	1.5 µm	5 µm	10 µm	10 µm	18 µm	25 µm
Local meas. uncertainty[2]	7.5 µm	25 µm	50 µm	20 µm	35 µm	50 µm
Linearity	6 µm	20 µm	40 µm	40 µm	70 µm	100 µm

[1] multiple distance measurement in fixed position on a measured surface (electric noise), with option /F 3 times the value
[2] multiple distance measurement at various positions within three times the laser beam diameter on a level measured surface (optical noise), figures dependent upon surface

- **Safety distance, laser:**

	OTM3-03	OTM3-10	OTM3-20	OTM3A-20	OTMA-35	OTM3A-50
NOHD[1] with Option /L:	0.3 m	0.3 m	0.4 m	0.6 m	0.8 m	0.9 m
NOHD[1] with Option /H:	0.5 m	0.5 m	0.7 m	1.1 m	1.4 m	1.6 m
NOHD[1] with Option /H[2]:	0.7 m	0.7 m	1.0 m	1.5 m	1.9 m	2.2 m

[1] NOHD = Nominal Ocular Hazard Distance = distance at which the radiation strength equals the threshold value of the maximum admissible radiation for the eyes. Figures stated apply taking the lid-closing reflex into account (0.25 s).

- **Laser beam geometry:**

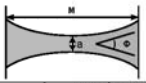

	OTM3-03	OTM3-10	OTM3-20	OTM3A-20	OTM3A-35	OTM3A-50
∅ middle of meas.range (a)[1]	40 µm	60 µm	90 µm	100 µm	120 µm	140 µm
Beam divergence Φ	1.7°	1.7°	1.2°	0.8°	0.6°	0.5°

[1] Measuring uncertainty approx. ± 5%

Dr. Wolf&Beck GmbH • Daimlerstr. 19 • 73117 Wangen / Germany • Tel.: +49/7161/1585-0 • Fax: -200 • www.wolfbeck.com

Wolf&Beck
SENSORIK

- **Dimensions and weights:**

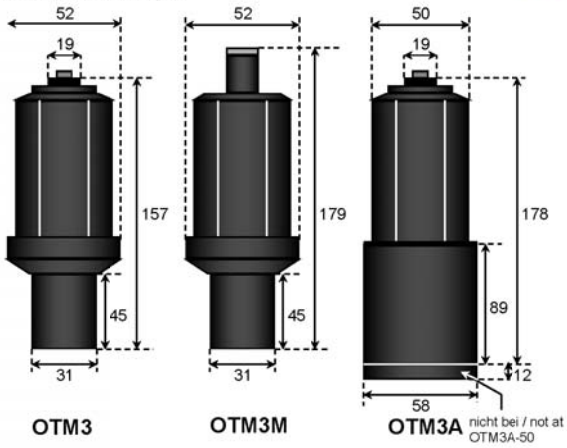

(all figures in mm)

Standard fitting elements of the measuring head are M8 screw threads (except for OTM3M with auto joint adapter). However, customer-specific special adapters are also possible.

Type of head:	OTM3	OTM3M	OTM3A
Weight:	350 g	350 g	750 g

Dr. Wolf&Beck GmbH • Daimlerstr. 19 • 73117 Wangen / Germany • Tel.: +49/7161/1565-0 • Fax: -200 • www.wolfbeck.com

A1.9 Nikon ModelMaker

Groundbreaking performance

The digital scanner

The unmatched accuracy, usability and performance of the digital ModelMaker scanner make it the perfect tool for all inspection, reverse engineering, and other 3D data capture applications. The top model ModelMaker MMDx is again a leap forward in 3D digitizing, as it introduces Enhanced Sensor Performance of the 3rd generation (ESP3) making it suitable to scan any material.

Scan any material

Through Enhanced Scanning Performance (ESP3), the ModelMaker MMDx scanner adapts its laser power to suit the surface characteristics of the object.
During scanning, it automatically tracks changes in surface conditions – both color and reflectivity – and adapts laser power and sensor settings accordingly in real-time. As a result, ModelMaker is able to accurately and efficiently handle parts with any surface color and texture, without requiring re-scanning or spraying.

MMDx with ESP3 good optical signal on both rubber and metallic paint at same time

Standard laser scanner good signal on metallic paint or rubber only

MMDx also features an intelligent anti-reflection filter to provide accurate measurements when scanning very shiny or polished materials. The functionality filters out all reflective laser light that is scattered in many directions.

MMDx ESP3

Thanks to ESP3, ModelMaker is able to scan the steep sides of convex surfaces, often a challenge due to poor light reflection.

Best-in-class productivity

Featuring high frame rates and laser stripes up to 200mm, the digital ModelMakers provide the ultimate in scanning productivity. The scanners' digital cameras benefit from a true (non-interpolated) resolution of over 1,000 points per stripe, providing optimum resolution for scanning freeform surfaces and features efficiently.

Easy to use

One single cable between the arm with scanner and the PC, is sufficient to start scanning.
Weighing only 395 grams and featuring a comfortable stand-off distance, ModelMaker scanners are optimized for ergonomic use.

Localizer compatibility

Nikon Metrology ModelMaker laser scanners are compatible with all major brands of portable CMM equipment:
- Nikon Metrology MCA / MCAii articulated arms
- Nikon Metrology K-Scan Optical CMMs
- Faro articulated arms
- Hexagon (Romer/Omicron) articulated arms

The right tool for the right job

The ModelMaker is available in 2 performance variants and 3 stripe widths to match your specific productivity and resolution needs.

	Scan rate	Productivity	Accuracy
MMDx50	•••••	••	•••••
MMDx100	•••••	•••	•••
MMDx200	•••••	•••••	••
MMC80	••	•	•••
MMC80	••	••	••
MMC160	••	•••	•

A1.10

A1.11

Intuitive scanning - one click analysis

Total solution

ModelMaker scanners are supplied with Focus Scan Handheld data acquisition and optionally with Focus Inspection processing software for inspection and reverse engineering. ModelMaker laser stripe scanning solutions tightly integrate hardware and software, guaranteeing smooth and error-free operation.

Scanning and application software

The Focus Handheld software enables operators to intuitively complete handheld scanning using articulated arms or optical CMMs for both inspection and reverse engineering projects. Focus Handheld is specifically designed to easily control data flows with minimum user interaction. The point cloud mesh is built up in real-time with immediate inspection of the specimen geometry against CAD or another scan.

For acvanced inspection functionality including feature inspection and gap & step analysis, Focus Inspection is seamlessly integrated with Focus Scan Handheld software.

Alternatively, the Focus Handheld API integrates Nikon Metrology handheld scanning with other 3rd party inspection software, such as PolyWorks, PowerInspect, Rapidform, Spatial Analyzer, etc.

For reverse engineering applications, users can select from a broad offering of applications including Focus Reverse Engineering or 3rd party packages software, all tightly integrated with the scanning application.

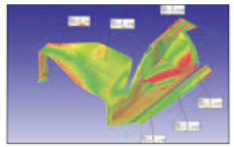

The operator navigates the left software menu using the localizer arm

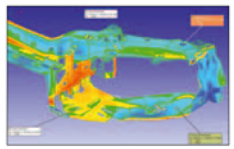

Focus Scan Handheld's scan data for part-to-CAD inspection analysis

Focus Handheld software features

- Patented real-time rendering and instant surface inspection
- Point cloud filtering, and (polygon) meshing tools
- Advanced datuming, coordinate system creation
- Remote menu navigation using articulated arm and K-Scan probe
- Automatic sensor intensity adaptation to scan surfaces with varying color or high reflectivity
- Uses sound as standoff indicator
- Support leapfrogging for scanning large objects
- Import/export of all standard CAD formats (IGES, STL, CATIA, UG, Pro-E, STEP, VDA)
- Macro support for scanning automation

Applications

- Fast & accurate 3D scanning
- Part-to-CAD inspection: First article inspection against CAD model
- Inspection of geometric features
- Gap-and-flush inspection
- Reverse engineering: from concept studio clay to class A surfaces
- Input for rapid prototyping

Specifications

ModelMaker benefits

- Faster and more accurate scanning saves time and money
- Ergonomic scanner that is compact and lightweight
- Optimized for hard-to-scan surfaces
- Designed for use under all shop floor or field conditions
- Extremely temperature stable
- Quick and easy plug-and-play setup
- Calibration files stored on on-board memory
- One-stop-shop for a total scanning solution
- Compatible with all major brands of portable localizers/pointcloud software

Technical specifications

	MMDx50	MMDx100	MMDx200	MMC40	MMC80	MMC160
Stripe width (Y) (mm)	50	100	200	40	80	160
Start measuring range (mm)	95	100	120	100	100	55
Measuring range (Z) (mm)	50	100	150	50	100	150
Accuracy (1σ) (µm)	10	15	30	12	17	34
Data rate at full FOV (Hz)	45	50	60	30		
Enhanced Sensor Performance	ESP3			ESP2		
Points per stripe[1]	1.000			800		
Temperature compensation	Yes			No		
Sensor weight (g)	395					
Laser power	Class 2M					
Localiser compatiblity	Nikon Metrology MCA / MCAII Nikon Metrology K-Scan Romer / Cimcore Infinite Faro Platinum / Titanium / Fusion / Quantum (pending)					

All specifications are subject to change without notification

NIKON METROLOGY NV
Geldenaaksebaan 329
B-3001 Leuven, Belgium
phone: +32 16 74 01 00 fax: +32 16 74 01 03
info@nikonmetrology.com

NIKON CORPORATION
Shin-Yurakucho Bldg., 12-1, Yurakucho 1-chome
Chiyoda-ku, Tokyo 100-8331 Japan
phone: +81 3 3773 9026 fax: +81 3 3773 9062
www.nikon-instruments.jp/eng/

NIKON METROLOGY EUROPE NV
tel. +32 16 74 01 01
sales_europe@nikonmetrology.com

NIKON METROLOGY GMBH
tel. +49 6023 91733-0
sales_germany@nikonmetrology.com

NIKON METROLOGY SARL
tel. +33 1 60 86 09 76
sales_france@nikonmetrology.com

NIKON METROLOGY, INC.
tel. +1 810 2204360
sales_us@nikonmetrology.com
us.nikonmetrology.com
www.nikoninstruments.com

NIKON METROLOGY UK LTD.
tel. +44 1332 811349
sales_uk@nikonmetrology.com

NIKON INSTRUMENTS (SHANGHAI) CO. LTD.
tel. +86 21 5836 0050
tel. +86 10 5869 2255 (Beijing office)
tel. +86 20 3882 0550 (Guangzhou office)

NIKON SINGAPORE PTE. LTD.
tel. +65 6559 3618

NIKON MALAYSIA SDN. BHD.
tel. +60 3 7809 3609

NIKON INSTRUMENTS KOREA CO. LTD.
tel. +82 2 2186 8400

More offices and resellers at **www.nikonmetrology.com**

A1.14 Nikon XC65

A1.15 GOM Atos (excerpt from brochure)

Technical Data

	ATOS II	ATOS IIe	ATOS III
System Configurations			
Measured Points	1 400 000 in 1s	1 400 000 in 1s	4 000 000 in 2s
Measurement Time	1 second	1 second	2 seconds
Measuring Area (min.)	175 x 140 mm²	175 x 140 mm²	150 x 150 mm²
Measuring Area (max.)	2000 x 1600 mm²	2000 x 1600 mm²	2000 x 2000 mm²
Point Spacing	0.12 - 1.4 mm	0.12 - 1.4 mm	0.07 - 1.0 mm
Stand-Off	730 - 2000 mm	730 - 2000 mm	760 - 2800 mm
Brightness	400 ANSI-Lumen	4500 ANSI-Lumen	4500 ANSI-Lumen
Camera Pixels	2 x 1 400 000	2 x 1 400 000	2 x 4 000 000
Sensor Dimensions	490 x 260 x 170 mm³	490 x 300 x 170 mm³	490 x 300 x 170 mm³
Sensor Weight	5.2 kg	7.0 kg	7.4 kg
Positioning Pointers	•	•	•
High-End PC		•	•
Notebook	•	•	•
Sensor Controller	external	integrated	integrated
Automation	•	•	•
Variable Workstation	•	•	•
Cable Length		up to 30m	
Transport Case		550 x 800 x 300 mm³, 32kg	
Operating Temperature		0° - 40°C	
Humidity		non-condensing	
Power Supply		90 - 230V AC	

breuckmann

opto TOP-HE THE MEASURING RANGES

For the opto TOP-HE system we offer a large number of measuring ranges:

- standard FOV's
- extended FOV's
- customised FOV's

All fields of view (FOV) can be realised with the same basic components, camera and projector, just by changing the lenses of camera / projector and - if necessary - the sensor base.

The measuring ranges are identified by their base length L and the FOV, e.g.

L100-100 base length 100 mm, FOV 100 mm, standard lenses
L300-425 base length 300 mm, FOV 425 mm, wide angle lenses

(the identifier of the FOV is an approxmated value for the image diagonal)

To simplify the setup and calibration of the standard measuring ranges, they will be offered only with a special set of lenses for each FOV. The lenses will be delivered with a factory setting for the aperture and focal depth, which is optimised for the corresponding FOV and which must not be changed by the user.

To use the whole flexibility of our opto TOP system, including the extended FOV's, we strongly recommend special training and certification.

standard fields of view with triangulation angle of 30 degrees				
base length L	operating distance	image diagonal [mm]		
100 mm	320 mm	50	100	200
300 mm	700 mm	200	325	425
600 mm	1250 mm	375	600	775
focal length identifier		Tele	Standard	Wide angle
Recommended combinations of standard measuring ranges				
Small FOV's:	L100-50	L100-200	L300-325	
Medium FOV's:	L300-200	L300-425	L600-775	

extended fields of view with triangulation angle of 30 degrees			
base length L	operating distance	image diagonal [mm]	
50 mm	250 mm	30	200
300 mm	700 mm	125	600
600 mm	1250 mm	250	1050
focal length identifier		eXtreme Tele (XT)	eXtreme Wide angle (XW)

extended fields of view for large objects (triangulation angle 20 degrees)						
base length L	operating distance	image diagonal [mm]				
600 mm	2000 mm	400	600	900	1200	1700
focal length identifier		XT	T	S	W	XW

opto TOP-HE-sensors with customised FOV's (3 x 2 mm² up to 2500 x 1800 mm²) on inquiry.

breuckmann

opto TOP-HE SPECIFICATIONS

light source	100 W halogen lamp
number of projected fringes	128
min. measuring time	980 ms
sensor weight	2 - 3 kg
digitisation (x,y)	1388 x 1036 pixel
size of measuring range	about 0.8 x 0.6 of image diagonal
depth of measuring volume	typically 1 / 2 of image diagonal
X,Y resolution	typically 1 / 1.500 of image diagonal
feature accuracy	typically 1 / 15.000 of image diagonal
noise (Z)	typically 1 / 20.000 of image diagonal

specifications of typical fields of view						
image diagonal*	[mm]	50	100	200	400	800
X,Y resolution*	[µm]	30	60	120	240	480
resolution limit (Z)*	[µm]	1	2	4	8	16
noise (Z)*	[µm]	± 5	± 7	± 10	± 20	± 40
feature accuracy*	[µm]	± 7	± 10	± 15	± 30	± 60

* The measurement specifications given above are average values for the central field of view, which are achieved under defined measurement conditions and after precise calibration of the sensor. All details concerning accuracy and resolution are possibly dependent on the surface of the object and the environment.

The resolution limit is defined as the theoretical limit using a phase evaluation of 10 bit.
The feature accuracy is defined as the difference of the measured positions of index marks towards the target-values (2σ value).
The noise is measured as deviation of the measured points towards a best-fit curve.

The data given above are valid for a single view only.

The accuracy of a complete measurement cycle depends strongly on the measuring strategy. In combination with photogrammetry or CMM, the overall accuracy is given by those systems. The gap between two adjacent images is minimised approx. to the noise level of the sensor by using advanced 3D-alignment and merging techniques.

Technical data are subject to change without notice dated January 2005

A1.17 Steinbichler Comet V (excerpt from brochure)

COMET 5 is designed for applications in the most diverse areas of industry. Variable fields of view and a modular sensor concept allow for digitizing objects of a vast variety of sizes with highest precision.

- Quality Control / Inspection
  - Comparison of actual data with nominal data (part to CAD)
  - Boundary/edge extraction (measurement of sheetmetal parts)
  - Serial inspection in production (manual/automated)
- Mold and Toolmaking
  - Tool reconstruction
  - Scan data for generation of milling tool paths
  - Documentation of actual 3D data at tool release
- Design
  - Scanning of design models for for further processing of CAD data, documentation
- Rapid Manufacturing
  - Acquisition of 3D data for Rapid Prototyping
- Reverse Engineering
- 3D Scanning
  - Scanning of art/historical objects, archaeology
  - Medical technical applications, etc.

steinbichler

COMET® 5 SENSOR SERIES: TECHNICAL DATA

	COMET 5 1.4 M	COMET 5 2 M
Camera Resolution	1360 x 1024	1600 x 1200
Measuring Volume in mm³ 50 100 200 400 800	65 x 50 x 55 100 x 75 x 60 210 x 160 x 140 410 x 310 x 250 900 x 660 x 500	85 x 65 x 60 130 x 135 x 140 400 x 300 x 250 800 x 600 x 500
3D Point Distance in µm 50 / 100 / 200 / 400 / 800	40 / 75 / 150 / 350 / 650	- / 55 / 115 / 240 / 500
Measuring Time in Seconds HighSpeed / High Quality	2.0 / 3.5	1.5 / 2.5
PC	1 x Intel Core2Duo, 8 GB	1 x Intel Core2Duo, 8 GB
Sensor Positioning	tripod or sensor stand with manual turn and tilt axis, robot	tripod or sensor stand with manual turn and tilt axis, robot
Automated Object Positioning	rotation table, robot	rotation table, robot

	COMET 5 4 M	COMET 5 11 M
Camera Resolution	2048 x 2048	4008 x 2672
Measuring Volume in mm³ 50 100 200 400 800	55 x 55 x 50 80 x 80 x 60 190 x 190 x 140 380 x 380 x 250 760 x 760 x 500	Measuring Volume 150 in mm³: 140 x 95 x 70 Measuring Volume 350 in mm³: 330 x 220 x 200 Measuring Volume 700 in mm³: 700 x 460 x 400
3D Point Distance in µm 50 / 100 / 200 / 400 / 800	25 / 40 / 95 / 190 / 380	3D Point Distance 150 35 µm / 350 85 µm / 700 180 µm
Measuring Time in Seconds HighSpeed / High Quality	2.5 / 5.0	5.0 / 10.0
PC	HighEnd Workstation 2 x Intel XEON Multicore CPU's, 32 GB	HighEnd Workstation 2 x Intel XEON Multicore CPU's, 72 GB
Sensor Positioning	tripod or sensor stand with motorized turn and tilt axis, robot	tripod or sensor stand with motorized turn and tilt axis, robot
Automated Object Positioning	rotation table, robot	rotation table, robot

COMET 5 with its exceptionally innovative sensor concept offers high flexibility and precision for demanding measuring applications.

The modular design allows for quick and easy adaptation of the system to the measurement volume required by the application.

In combination with camera resolutions from 1.4 up to 11 megapixel, COMET 5 allows an individual configuration for customer-specific measuring tasks.

7

A.2 Experimental equipment

A2.1 3M MPro110 Micro projector

3M™ Micro Professional Projector MPro110

Operator's Guide

Specifications

Projector

Description		Specification
Imager	Technology	LCOS
	Size	11.9 mm (0.47")
	Image Resolution	640 x 480 Pixels
	Image Aspect Ratio	4:3
Projection Distance		305–1800 mm (12"–70")
Image Size		163–975 mm (6.4"–38.4")
Throw Ratio (Width/Distance)		0.53
Lens Offset		1:1 (none)
Inputs		VGA, Composite Video, DC Power
Compatible Resolution		VGA, SVGA, XGA
Refresh Rates		60 Hz
Video Compatibility		NTSC, PAL, NTSC (M), PAL (BGHI)
Dimensions		115 mm (L) x 50 mm (W) x 22 mm (H) (4 1/2" x 1 31/32" x 7/8")
Weight		160 g (5.6 oz.)
Tripod Socket		¼"-20
Operating Temperature		10°–27°C (50°–80°F)
Attitude		Sea Level to 1,829 m (6000')

14

Flea® Specifications

Specification	640x480	1024x768
Overview	Boxed IEEE-1394 camera	
Imaging Sensor	Sony® ICX424AQ/AL 1/3" CCD sensor Progressive scan, global shutter	Sony® ICX204AQ/AL 1/3" CCD sensor Progressive scan, global shutter
Resolution	640x480 B/W or Color	1024x768 B/W or Color
Format	8-bit or 16-bit, 12-bit AtoD	
Pixel Size	7.4µm x 7.4µm	4.65µm x 4.65µm
Frame Rates	640x480 at 60FPS	1024x768 at 30FPS
Partial Image Modes	Format 7_Mode_0 (ROI), Format 7 Mode_1 and _2 pixel binning	
Voltage Requirements	8-32V	
Power Consumption	< 3W	
Gain	Automatic / Manual modes at 0.035dB -5.45 to 30.75dB	Automatic / Manual modes at 0.035dB -6.8 to 29.4dB
Shutter	Automatic / Manual modes 0.04ms to 66.66 ms at 15FPS	Automatic / Manual modes 0.03ms to 66.6 ms at 15FPS
Trigger Modes	DCAM v.1.31 Trigger_Mode (0,1,3)	
Signal To Noise Ratio	> 59dB	
Dimensions	30x31x29mm w/o optics	
Mass	60g without optics	
Camera Specification	IIDC 1394-based Digital Camera Specification v1.31	
Emissions Compliance	Complies with CE rules and Part 15 Class B of FCC Rules	
Operating Temperature	Commercial grade electronics rated from 0° to 45°C	
Storage Temperature	-30° to 60°C	

Flea® Camera Dimensional Drawings

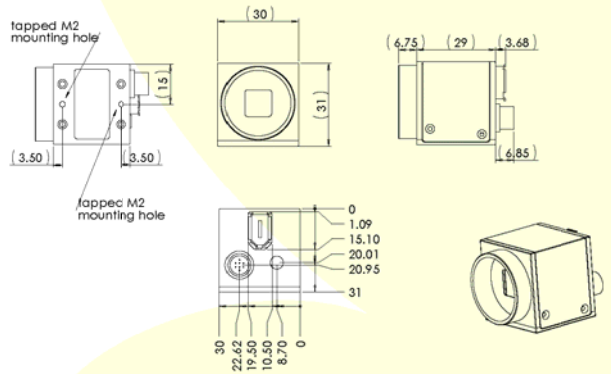

Measurements in mm. CAD drawings available online at www.ptgrey.com/support

November 2006

North America T +604.730.9937 E sales@ptgrey.com Europe T + 49 89 454 63224 E eu-sales@ptgrey.com **www.ptgrey.com**

Flea® Specifications

Specification	640x480	1024x768
Overview	Boxed IEEE-1394 camera	
Imaging Sensor	Sony® ICX424AQ/AL 1/3" CCD sensor Progressive scan, global shutter	Sony® ICX204AQ/AL 1/3" CCD sensor Progressive scan, global shutter
Resolution	640x480 B/W or Color	1024x768 B/W or Color
Format	8-bit or 16-bit, 12-bit AtoD	
Pixel Size	7.4µm x 7.4µm	4.65µm x 4.65µm
Frame Rates	640x480 at 60FPS	1024x768 at 30FPS
Partial Image Modes	Format 7_Mode_0 (ROI), Format 7 Mode_1 and _2 pixel binning	
Voltage Requirements	8-32V	
Power Consumption	< 3W	
Gain	Automatic / Manual modes at 0.035dB -5.45 to 30.75dB	Automatic / Manual modes at 0.035dB -6.8 to 29.4dB
Shutter	Automatic / Manual modes 0.04ms to 66.66 ms at 15FPS	Automatic / Manual modes 0.03ms to 66.6 ms at 15FPS
Trigger Modes	DCAM v.1.31 Trigger_Mode (0,1,3)	
Signal To Noise Ratio	> 59dB	
Dimensions	30x31x29mm w/o optics	
Mass	60g without optics	
Camera Specification	IIDC 1394-based Digital Camera Specification v1.31	
Emissions Compliance	Complies with CE rules and Part 15 Class B of FCC Rules	
Operating Temperature	Commercial grade electronics rated from 0° to 45°C	
Storage Temperature	-30° to 60°C	

Flea® Camera Dimensional Drawings

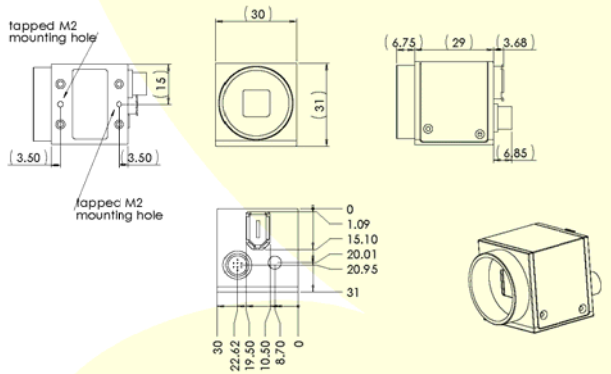

Measurements in mm. CAD drawings available online at www.ptgrey.com/support

November 2006

North America T +604.730.9937 E sales@ptgrey.com Europe T + 49 89 454 63224 E eu-sales@ptgrey.com **www.ptgrey.com**

A2.3 Edmund Optics fixed focal length megapixel lenses (excerpt from online catalogue)

Megapixel Fixed Focal Length Lenses - Edmund Optics

products : imaging : imaging lenses : : fixed focal length lenses

Megapixel Fixed Focal Length Lenses

- Lockable, Manual Focus and Aperture Control
- Working Distance from 100mm to Infinity
- Compact Size

Designed for high resolution, industrial C-Mount cameras, our Megapixel Fixed Focal Length Lenses are ideal for machine vision applications with demanding space constraints. These lenses complement the resolution of many megapixel cameras with 2/3" and smaller formats. Low distortion and high resolution enable these economically priced lenses to produce sharp, high contrast images compared to standard CCTV and compact lenses. Locking screws for the manual iris and focus allow these lenses to be used in high vibration environments. Typical applications include factory automation, inspection, and macro work. Lenses accept M30.5 filters. Maximum rear protrusion beyond the C-Mount is 1.1mm.

http://www.edmundoptics.com/onlinecatalog/displayproduct.cfm?productID=2511 (1 of 6)06/05/2010 11:39:52

Megapixel Fixed Focal Length Lenses - Edmund Optics

Description	Stock No.	Price	In Stock	
Showing **1-8** of **8** Items | Sort by Spec				
5mm Megapixel Fixed Focal Length Lens	NT64-867	£161.25	✓	BUY
Focal Length FL (mm)	5.00			
Maximum Sensor Format	1/2"			
Aperture (f/#)	F1.4-16C			
Field of View, 1/2" Sensor (°)	65.50			
Field of View @ Min Working Distance (mm)	150.00			
Working Distance (mm)	300 - ∞			
Maximum Diameter (mm)	44.50			
Length (mm)	45.50			
Maximum Rear Protrusion Beyond C-Mount (mm)	3.00			
Weight (g)	102.00			
Filter Thread	43.0 x 0.75mm			
RoHS	Compliant			
8mm Megapixel Fixed Focal Length Lens	NT56-786	£146.25	✓	BUY
Focal Length FL (mm)	8.00			
Maximum Sensor Format	2/3"			
Aperture (f/#)	F1.4-16C			
Field of View, 1/2" Sensor (°)	42.50			
Field of View @ Min Working Distance (mm)	87.00			
Working Distance (mm)	100 - ∞			
Maximum Diameter (mm)	33.50			
Length (mm)	28.20			
Maximum Rear Protrusion Beyond C-Mount (mm)	0.60			

http://www.edmundoptics.com/onlinecatalog/displayproduct.cfm?productID=2511 (2 of 6)06/05/2010 11:39:52

A2.4 Edmund Optics multi-frequency camera calibration target (excerpt from online catalogue)

Multi-Frequency Grid Distortion Targets - Edmund Optics

products : testing and targets : test targets : distortion test targets

Multi-Frequency Grid Distortion Targets

- For Calibration of Imaging Systems
- Varying Spatial Frequency for Different Fields of View
- N.I.S.T. Certificate of Accuracy Included

Although distortion can often be troublesome in measurement applications, it is important to note that no information about the object is actually lost, but merely misplaced in the image. Using these targets, one can easily determine the precise amount of distortion present and back it out of measurements. The dot center can be located using blob (or centroid) analysis in measurement software. The grid pattern scales down so that one target can be used for a variety of lenses and fields of view. Included in the packaging is a serialized N.I.S.T. Traceable Certificate of Accuracy per MIL-STD-45662A.

View to reference MIL SPEC MIL-STD-45662A (PDF 419kb)

http://www.edmundoptics.com/onlinecatalog/displayproduct.cfm?productID=1548 (1 of 4)06/05/2010 11:44:46

Multi-Frequency Grid Distortion Targets - Edmund Optics

Description	Stock No.	Price	In Stock

Showing **1-5** of **5** Items | Sort by Spec

3 Frequency Grid Distortion Target, Chrome on Glass NT46-250 £288.75 EMAIL BUY

Type	3 Frequency
Substrate	Soda Lime
Dimensions (mm)	75 x 75
Thickness (mm)	1.5
Surface Accuracy (λ)	4-6 per 25.4 mm Area
Surface Quality	40-10 (within 51mm Square Area)
Coating	Vacuum Deposited Chromium Oxide (Specular Reflectivity <5% @ 550nm)
RoHS	Compliant

3 Frequency Grid Distortion Target, Chrome on Opal NT58-774 £371.25 EMAIL BUY

Type	3 Frequency
Substrate	Opal Glass
Dimensions (mm)	75 x 75
Thickness (mm)	1.5
Surface Accuracy (λ)	4-6 per 25.4 mm Area
Surface Quality	40-10 (within 51mm Square Area)
Coating	Vacuum Deposited Chromium Oxide (Specular Reflectivity <5% @ 550nm)
RoHS	Compliant

3 Frequency Grid Distortion Target, Mylar NT46-249 £224.25 EMAIL BUY

http://www.edmundoptics.com/onlinecatalog/displayproduct.cfm?productID=1548 (2 of 4)06/05/2010 11:44:46

A2.5 BenQ MP720 digital projector

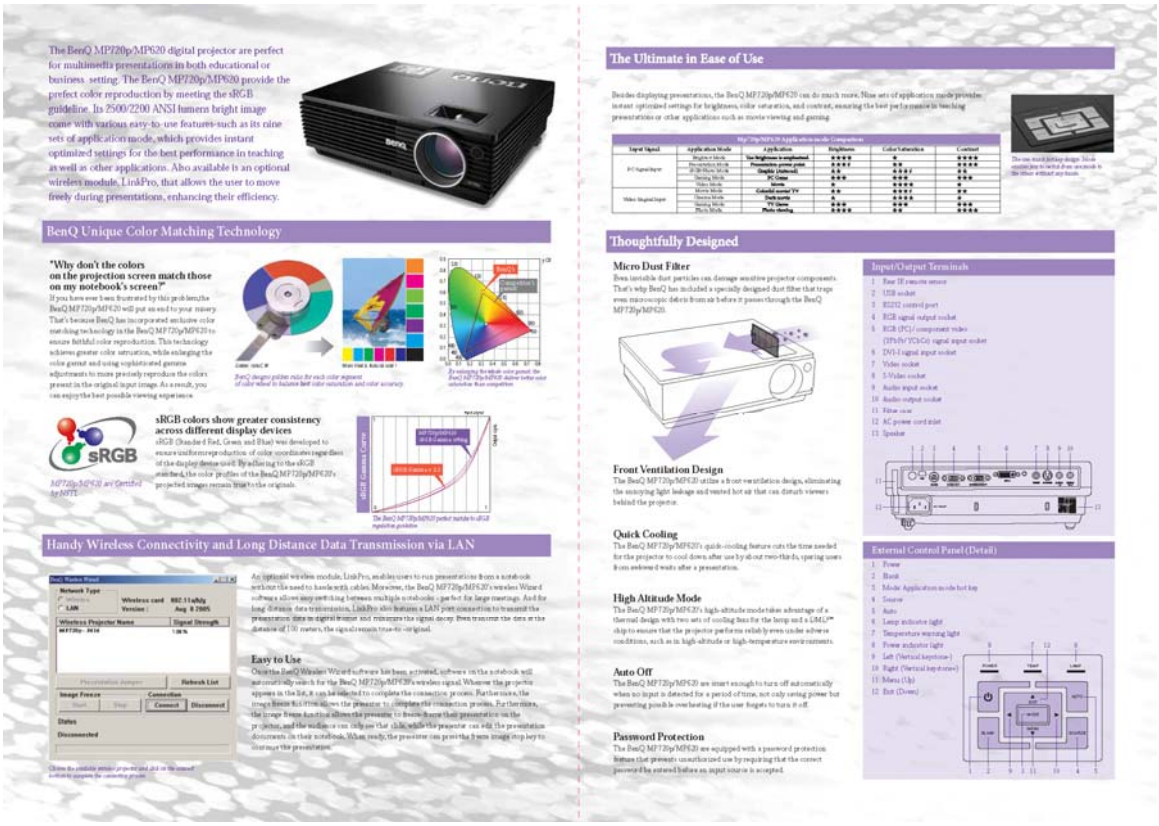

The BenQ MP720p/MP620 digital projector are perfect for multimedia presentations in both educational or business setting. The BenQ MP720p/MP620 provide the prefect color reproduction by meeting the sRGB guideline. Its 2500/2200 ANSI lumens bright image come with various easy-to-use features such as its nine sets of application mode, which provides instant optimized settings for the best performance in teaching as well as other applications. Also available is an optional wireless module, LinkPro, that allows the user to move freely during presentations, enhancing their efficiency.

BenQ Unique Color Matching Technology

"Why don't the colors on the projection screen match those on my notebook's screen?"

If you have ever been frustrated by this problem,the BenQ MP720p/MP620 will put an end to your misery. That's because BenQ has incorporated exclusive color matching technology in the BenQ MP720p/MP620 to ensure faithful color reproduction. This technology achieves greater color saturation, while enlarging the color gamut and using sophisticated gamma adjustments to more precisely reproduce the colors present in the original input image. As a result, you can enjoy the best possible viewing experience.

sRGB colors show greater consistency across different display devices

sRGB (Standard Red, Green and Blue) was developed to ensure uniform reproduction of color coordinates in image files of the display device used. By adhering to the sRGB standard, the color profiles of the BenQ MP720p/MP620's projected images remain true to the originals.

MP720p/MP620 are Certified by NTU.

Handy Wireless Connectivity and Long Distance Data Transmission via LAN

An optional wireless module, LinkPro, enables users to run presentations from a notebook without the need to hassle with cables. Moreover, the BenQ MP720p/MP620's wireless Wizard software allows easy switching between multiple notebooks - perfect for large meetings. And for long distance data transmission, LinkPro also features a LAN port connection to transmit the presentation data in digital format and minimize the signal decay. Even transmit the data at the distance of 100 meters, the signal remain true-to-original.

Easy to Use

Once the BenQ Wireless Wizard software has been activated, software in the notebook will automatically search for the BenQ MP720p/MP620's wireless signal. Whenever the projector appears in the list, it can be selected to complete the connection process. Furthermore, the image freeze function allows the presenter to freeze frame their presentation on the projector, and the audience can only see the slide, while the presenter can edit the presentation documents in their notebook. When ready, the presenter can press the Esc image stop key to continue the presentation.

The Ultimate in Ease of Use

Besides displaying presentations, the BenQ MP720p/MP620 can do much more. Nine sets of application mode provides instant optimized settings for brightness, color saturation, and contrast, ensuring the best performance in teaching presentations or other applications such as movie viewing and gaming.

Thoughtfully Designed

Micro Dust Filter

Even invisible dust particles can damage sensitive projector components. That's why BenQ has included a specially designed dust filter that traps even microscopic debris from air before it passes through the BenQ MP720p/MP620.

Front Ventilation Design

The BenQ MP720p/MP620 utilize a front-ventilation design, eliminating the annoying light leakage and vented hot air that can disturb viewers behind the projector.

Quick Cooling

The BenQ MP720p/MP620's quick-cooling feature cuts the time needed for the projector to cool down after use by about two-thirds, sparing users from awkward waits after a presentation.

High Altitude Mode

The BenQ MP720p/MP620's high-altitude mode takes advantage of a thermal design with two sets of cooling fans for the lamp and a LIMLP™ chip to ensure that the projector performs reliably even under adverse conditions, such as in high-altitude or high-temperature environments.

Auto Off

The BenQ MP720p/MP620 are smart enough to turn off automatically when no input is detected for a period of time, not only saving power but preventing possible overheating if the user forgets to turn it off.

Password Protection

The BenQ MP720p/MP620 are equipped with a password protection feature that prevents unauthorized use by requiring that the correct password be entered before an input source is accepted.

Input/Output Terminals

External Control Panel (Detail)

7 Reference

This chapter lists the specifications, safety information, and regulatory information for the projector.

Specifications

Because HP continually improves its products, the following specifications are subject to change. For the latest specifications, visit the HP website at http://www.hp.com.

Projector Specifications

Size	280 × 255 × 102 mm (11.0 × 10.1 × 4.0 in.)
Weight	3.5 kg (7.7 lb)
Resolution	vp6310 series: SVGA (800 × 600) vp6320 series: XGA (1024 × 768)
Technology	DLP
Video connectors	VGA-in (D-sub) with optional cable for component-video input VGA-out (D-sub) S-video (mini-DIN) Composite video (RCA) DVI-D (vp6320 series)
Audio connectors	Stereo-in (2 RCA and mini-phone)
Other connectors	USB 1.1 type B RS-232 control (vp6320 series) 12-Vdc trigger output (vp6320 series)
Video compatibility	NTSC 3.58 MHz and 4.43 MHz PAL B, D, G, H, I, M, N SECAM B, D, G, K, K1, L HDTV (480i/p, 575i/p, 720p, 1080i) DVI with HDCP (vp6320 series) PC video up to SXGA

Projector Specifications (continued)

IR receivers	Front and back of projector
Lamp	210-watt lamp 4000-hour average lamp life (to half of original brightness) Lamp saver mode reduces lamp power to 168 watts Replacement lamp: L1695A
Optics	1 to 10 m (3 to 33 ft) focus range 1.16:1 optical zoom vp6310 series: 1.7 to 2.0 throw ratio (distance/width) 128% offset (relative to half-height) vp6320 series: 1.8 to 2.1 throw ratio (distance/width) 125% offset (relative to half-height)
Light engine	vp6310 series: 0.55-in. 12° DDR DMD vp6320 series: 0.7-in. 12° DDR DMD
Audio	Monaural speaker, 6-watt peak output
Noise level	less than 36 dBA
Vertical tilt	0° to 9°
Vertical keystone correction	±20%
Remote control	USB mouse
Mounting options	Ceiling and tabletop, front and rear projection
Security	Kensington lock compatible Unlock sequence protects against unauthorized use
Power	100 to 240 V at 50 to 60 Hz

Projector Specifications (continued)

Environment	Operating: Temperature: 10 to 35 °C (50 to 95 °F) Humidity: 80% RH max, non-condensing Altitude: up to 3,000 m (10,000 ft), up to 25 °C (77 °F) Storage: Temperature: –20 to 55 °C (–4 to 131 °F) Humidity: 80% RH max, non-condensing Altitude: up to 12,000 m (40,000 ft)

Video mode compatibility

Compatibility	Resolution	Refresh rates (Hz)
Analog		
VGA	640 × 350	70, 85
	640 × 400	85
	640 × 480	60, 66.66, 66.68, 72, 75, 85
	720 × 400	70, 85
SVGA	800 × 600	56, 60, 72, 75, 85
	832 × 624	74.55
XGA	1024 × 768	60, 70, 75, 85
	1152 × 870	75, 75.06
	1280 × 960	75
SXGA	1280 × 1024	60, 75
SXGA+	1400 × 1050	60
Digital (vp6320 series)		
VGA	640 × 350	70, 85
	640 × 400	85

Video mode compatibility (continued)

Compatibility	Resolution	Refresh rates (Hz)
	640 × 480	60, 72, 75, 85
	720 × 400	70, 85
SVGA	800 × 600	56, 60, 72, 75, 85
XGA	1024 × 768	60, 70, 75
SXGA	1280 × 1024	60, 75
SXGA+	1400 × 1050	60

Safety information

LED safety

The infrared ports located on the digital projector and remote control are classified as Class 1 LED devices according to International Standard IEC 825-1 (EN60825-1). This device is not considered harmful, but the following precautions are recommended:

- If the unit requires service, contact an authorized HP service center.
- Do not attempt to make any adjustment to the unit.
- Avoid direct eye exposure to the infrared LED beam. Be aware that the beam is invisible light and cannot be seen.
- Do not attempt to view the infrared LED beam with any type of optical device.

Mercury safety

⚠ **WARNING!** This digital projector lamp contains a small amount of mercury. If the lamp breaks, adequately ventilate the area where the breakage occurred. Disposal of the lamp might be regulated due to environmental considerations. For disposal or recycling information, contact your local authorities or the Electronic Industries Alliance at http://www.eiae.org.

A2.7 Renishaw PH10 motorised head (excerpt from web page)

PH10M

Top

The PH10M can carry long extension bars and complex probes such as SP25M or TP7M. The highly repeatable autojoint allows rapid probe or extension bar changing without the need for re-qualification.

PH10M specification

Top

Length	117 mm
Width	62 mm
Weight	645 g
Probe mounting	Autojoint (multiwire)
Head mounting	PH10M shank to suit CMM
Suitable controller	PHC10-2
Repeatability of position	0.4 µm (0.00002 in) specified at a distance of 62 mm
Total no. of positions	720
Max recommended drive torque	0.45 Nm
Maximum extension bar	300 mm (11.8 in) using PAA3 extension

References

1 K. Harding, "Engineering precision," Nature Photonics, 2, 667-669, (2008).

2 EPSRC, “EPSRC – Engineering Doctorate”, http://www.epsrc.ac.uk/funding/students/coll/Pages/engdoctorate.aspx (accessed 16 March 2010)

3 Renishaw Plc, “Renishaw: touch probes, rotary encoders, linear encoders, angle encoders, laser calibration, dental CAD/CAM, raman spectroscopy and surgical robots”, www.renishaw.com (accessed 16 March 2010).

4 N. J. Weston, Y. R. Huddart, A. J. Moore, T. C. Featherstone, “Phase analysis measurement apparatus and method”, International Patent Application, Publication number WO2009024757 (2009).

5 N. J. Weston, Y. R. Huddart, “Non-contact object inspection”, International Patent Application, Application number 0915904. (Not yet published).

6 N. J. Weston, Y. R. Huddart, A. J. Moore, “Non-contact measurement apparatus and method”, International Patent Application, Publication number WO2009024756 (2009).

7 N. J. Weston, Y. R. Huddart, “Non-contact probe”, International Patent Application, Publication number WO2009024758 (2009).

8 Committee SS/6, “Accuracy (trueness and precision) of measurement methods and results. General principles and definitions”, BS ISO 5725-1 (1994).

9 Committee SS/6, “Guidance for the use of repeatibility, reproducibility and trueness estimates in measurement uncertainty estimation”, DD ISO/TS 21748 (2004).

10 Committee JCGM/WG 1, “Evaluation of measurement data – Guide to the expression of uncertainty in measurement”, JCGM 100:2008 (2008).

11 Committee TDW/4, “Geometrical Product Specifications (GPS). Acceptance and reverification tests for coordinate measuring machines (CMM)”, BS EN ISO 10360 (2001).

12 Committee TDW/4, “Assessment of surface texture. Guidance and general information”, BS 1134-2 (1990).

13 NPL, “Freeform surfaces: Products and surfaces: Dimensional measurements: Dimensional: Engineering”, http://www.npl.co.uk/freeform (accessed 24 January 2010).

14 E. R. Davies, “Machine Vision. Theories, algorithms, practicalities”, Elsevier (2005).

15 Committee TDW/4, “Geometrical product specifications (GPS). General concepts. Model for geometrical specification and verification”, DD CEN ISO/TS 17450-1 (2007).
16 P. J. Besl, “Geometric modeling and computer vision”, Proceedings of the IEEE 76(8), 936-958 (1988).
17 D. R. McMurtry, “Measuring apparatus”, United States patent, publication number US4084323 (1978).
18 Hexagon Metrology GmbH, WLeitz PMM-G 3D coordinate measuring machines and gear inspection systems”, http://www.leitz-metrology.com/3D_measuring_machines_gear_inspection_systems_Leitz_PMM-G.shtml (accessed 24 January 2010). See Appendix A1.1.
19 Carl Zeiss IMT Corporation, “Welcome to Carl Zeiss Industrial Metrology”, http://www.zeiss.com/imt (accessed 24 January 2010). See Appendix A1.2.
20 M.-C. Amann, et. al., “Laser ranging: a critical review of usual techniques for distance measurement“, Optical Engineering 40(1), 10-19 (2001).
21 G. S. Buller and A. M. Wallace, “Time-correlated single-photon counting and point-by-point acquistiion”, IEEE Journal of Selected Topics in Quantum Electronics, 13(4), 1006-1015 (2007).
22 4D Technology, “4D Technology:: FizCam Fizeau interferometers”, http://www.4dtechnology.com/products/fizcamfamily.php (accessed 24 January 2010). See Appendix A1.3.
23 Zygo, “3D optical surface profilers (profilometers)”, http://www.zygo.com/?/met/profilers/ (accessed 24 January 2010). See Appendix A1.4.
24 J. Salvi, "Pattern codification strategies in structured light systems," Pattern Recognition, 37, 827-849 (2004).
25 R.A. Jarvis, "A perspective on range finding techniques for computer vision," IEEE Transactions on Pattern Analysis and Machine Intelligence, 52, 122-139 (1983).
26 M. Takeda and K. Mutoh, “Fourier transform profilometry for the automatic measurement of 3-D object shapes”, Applied Optics 22(24), 3977-3981 (1983).
27 K. Creath, “Temporal phase measurement methods” in D.W. Robinson and G.T. Reid (eds.), “Interferogram Analysis”, 94–140, Institute of Physics (1993).
28 B. V. Dorrio and J. L. Fernandez, “Phase-evaluation methods in whole-field optical measurement techniques”, Measurement Science and Technology 10, R33-R55 (1999).

29 J. Li, X.-Y. Su and L.-R. Guo, “Improved Fourier transform profilometry for the automatic measurement of three-dimensional object shapes”, Optical Engineering, 29(12), 1439-1444 (1990).

30 S. Zhang and S.-T. Yau, “Generic nonsinusoidal phase error correction for three-dimensional shape measurement using a digital video projector”, Applied Optics 46(1), 36-43 (2007).

31 J. D. R. Valera, Y. R. Huddart, N. J. Weston and A. J. Moore, “Measurement of object shape and surface slope with combined fringe projection and photometric stereo techniques”, in preparation for submission (2010).

32 J. M. Huntley and H. O. Saldner, “Temporal phase-unwrapping algorithm for automated interferogram analysis”, Applied Optics 32(17), 3047-3052 (1993).

33 3D shape GmbH, “3D shape GmbH – flexibile shape measuring system”, http://www.3d-shape.de/produkte/cam_e.php (accessed 24 January 2010). See Appendix A1.5.

34 K. Creath and J.C. Wyant, "Moiré and Fringe Projection Techniques," in D. Malcara, “Optical Shop Testing”, 653-685, John Wiley & Sons, inc. (1992).

35 M. Takasaki, "Moiré Topography," Appl. Opt, vol. 9, 1970, pp. 1467-1472.

36 J. A. N. Buytaert, J. E. F. Aernouts, J. J. J. Dirckx, “Indentation measurements on the eardrum with automated projection Moiré profilometry”, Optics and Lasers in Engineering 47, 301-309 (2009).

37 M.A.R Cooper with S. Robson, “Theory of close-range photogrammetry” in K. B. Atkinson (ed.), “Close range photogrammetry and machine vision”, 9-51, Whittles Publishing (2001).

38 GOM, “GOM – Measuring systems – TRITOP – Datasheet”, http://www.gom.com/EN/measuring.systems/tritop/system/datasheet/datasheet.html (accessed 24 January 2010). See Appendix A1.6.

39 Geodetic Systems, Inc, “Geodetic products”, http://www.geodetic.com/products/products.asp?vstars-m.htm (accessed 5 March 2010). See Appendix A1.7.

40 T. A. Clarke, “An analysis of the properties of targets used in digital close range photogrammetric measurement”, Videometrics III. SPIE Vol 2350 pp251-262 (1994).

41 R. Campbell and P. Flynn, "A survey of free-form object representation and recognition techniques," Computer Vision and Image Understanding, vol. 81, 2001, p. 166–210.

42 H. Heier, K.-P. Koch, and K.-H. Breyer, "Method and apparatus for non-contact measurement of object surfaces", United States Patent, Publication number US5251165.

43 Carl Zeiss, "WOLF&Beck Gmbh", http://www.wolfbeck.com/e/p_dist-otm.htm (accessed 5 March 2010). See Appendix A1.8.

44 Nikon Metrology NV, "Nikon Metrology – 3D scanning: ModelMaker D – The digital scanner for articulated arm scanning",
http://www.nikonmetrology.com/handheld_scanners/modelmaker_d/ (accessed 5 March 2010). See Appendix A1.9.

45 Nikon Metrology NV, "Nikon Metrology – XC65D(-LS) digital cross scanner – The ultimate scanner for feature inspection",
http://us.nikonmetrology.com/products/cmm_scanners/xc65d/ (accessed 5 March 2010). See Appendix A1.10.

46 GOM, "GOM – Measuring systems – ATOS III",
http://www.gom.com/En/Products/atos3.html (accessed 5 March 2010). See Appendix A1.11.

47 Breuckmann, "optoTOP-HE",
http://www.breuckmann.com/index.php?id=optotop-he&L=2 (accessed 5 March 2010). See Appendix A1.12.

48 Steinbichler, "Steinbichler Optotechnik – Competence in optical measuring and sensor technology", http://www.steinbichler.de/en/main/comet_5.htm (accessed 5 March 2010). See Appendix A1.13.

49 R. Y. Tsai and R. K. Lenz, "A new technique for fully autonomous and efficient 3D robotics hand eye calibration", IEEE Transactions on Robotics and Automation, 5(3), 345-358 (1989).

50 G. Puskorius and I. Feldkamp, "Global Calibration of a robot/vision system", IEEE International Conference on Robotics and Automation, 4, 190-195 (1987).

51 R. Horaud and F. Dornaika, "Hand-Eye Calibration", International Journal of Robotics Research, 14(3), 195-210, (1995).

52 H. O. Saldner and J. M. Huntley "Temporal phase unwrapping: application to surface profiling of discontinuous objects", Applied Optics 36(13), 2770-2775 (1997).

53 G. Sansoni, M. Carocci, R. Rodella, “Three-dimensional vision based on a combination of gray-code and phase-shift light projection: analysis and compensation of the systematic errors”, Applied Optics 38(31):6565-6573 (1999).

54 3M, “3M MPro 110 Micro projector”, http://www.3mselect.co.uk/p-1783-3m-mpro-110-micro-projector-uk-model.aspx (accessed 5 February 2010). See Appendix A2.1.

55 D. C. Brown, “Close-range camera calibration”, Photogrammetric Engineering, 37(8):855-866, (1971).

56 R. G. Willson, S. A. Schafer, “What is the centre of the image?”, JOSA A 11(11), 2946-2955 (1994).

57 J.G Fryer, “Camera Calibration” in K. B. Atkinson (ed.) “Close range photogrammetry and machine vision”, 156-179, Whittles publishing (1996).

58 C. Bräuer-Burchardt, M. Heinze, C. Munkelt, P. Kuhmstedt and G. Notni, “Distance dependent lens distortion variation in 3D measuring systems using fringe projection”, BMVC 2006, 327-336, BMVA (2006).

59 B. Triggs, P. McLauchlan, R. Hartley, A. Fitzgibbon, “Bundle adjustment – a modern synthesis”, ICCV ’99: Proceedings of the International Workshop on Vision Algorithms, 298-372 (1999).

60 N. Ayache, F.Lustman, “Trinocular stereo vision for robotics”, IEEE Transactions on Pattern Analysis and Machine Intelligence 13, 73-85 (1991).

61 A. Grün, “Least squares matching: a fundamental measurement algorithm” in K. B. Atkinson (ed.), “Close range photogrammetry and machine vision”, 217-255, Whittles Publishing (2001).

62 M. Fischer and R. Bolles, “Random sample consensus: a paradigm for model fitting with applications to image analysis and automated cartography”, Communications of the ACM, 24(6), 381-395 (1981).

63 J. P. P. Starink and E. Backer, “Finding point correspondences using simulated annealing”, Pattern Recognition 28(2), 231-240 (1995).

64 A. Bishnu, S Das, S. C. Nandy and B. B. Battacharya, “Simple algorithms for partial point set pattern matching under rigid motion”, Pattern Recognition 39(9), 1662-1671 (2006).

65 Z. Zhang, “Iterative point matching for registration of free-form curves”, Rapports de Recherche, No. 1658, March 1992.

66 C. Schmid and A. Zisserman, “The geometry and matching of lines and curves over multiple views”, International Journal of Computer Vision 40(3), 199-233 (2000).
67 Y. J. Xiao and Y. F. Li, “Optimized stereo reconstruction of free-form space curves based on a nonuniform rational B-spline model”, JOSA A 22(9), 1746-1762 (2005).
68 B. A. Rajoub, D. R. Burton, M. J. Lalor, S. A. Karout, “A new model for measuring object shape using non-collimated fringe-pattern projections”, Journal of Optics A: Pure and Applied Optics 9, S66-S75 (2007).
69 H. Guo, H. He, Y. Yu, M. Chen, “Least-squares calibration method for fringe projection profilometry”, Optical Engineering 44(3), 033603 (2005).
70 M. Reeves, A. J. Moore, D. P. Hand, J. D. C. Jones, “Dynamic shape measurement system for laser materials processing”, Optical Engineering 42(10), 2923-2929 (2003).
71 C. R. Coggrave, “Wholefield optical metrology: surface profile measurement”, Phase Vision Ltd. (2002-2004).
72 P. Brakhage, G. Notni, R. Kowarschik, “Image aberrations in optical three-dimensional measurement systems with fringe projection”, Applied Optics 43(16): 3217-3223, (2004).
73 L.-C. Chen and C.-C. Liao, “Calibration of 3D surface profilometry using digital fringe projection”, Measurement Science and Technology 16, 1554-1566 (2005).
74 M. Takeda, H. Ina, S. Kobayashi “Fourier-transform method of fringe-pattern analysis for computer-based topography and interferometry”, Journal of the Optical Society of America 72(1):156-160 (1982).
75 L. R. Watkins, S. M. Tan, T. H. Barnes, “Determination of interferometer phase distributions by use of wavelets”, Optics Letters 24(13), 905-907 (1999).
76 M. A. Sutton, W. Zhao, S. R. McNeill, H. W. Schreier, Y. J. Chao, “Development and assessment of a single-image fringe projection method for dynamic applications”, Experimental Mechanics 41(3):205-217, (2001).
77 T. Peng, S. Gupta, K. Lau, “Algorithms for constructing 3D point clouds using multiple digital fringe projection patterns”, Computer-Aided Design and Applications 2(6):737-746 (2005).
78 A. Patil, P. Rastogi, “Guest editorial. Moving ahead with phase”, Optics and Lasers in Engineering 45, 253-257 (2007).

79 M. J. Baker, J. Xi and J. F. Chicharo, “Elimination of gamma non-linear luminance effects for digital video projection phase measuring profilometers”, 4th IEEE International Symposium on Electronic Design, Test and Applications, 496-501 (2008).

80 J. H. Bruning, D. R. Herriott, J. E. Gallagher, D. P. Rosenfeld, A. D. White, D. J. Brangaccio, “Digital wavefront measuring interferometer for testing optical surfaces and lenses”, Applied Optics 13(11), 2693-2703 (1974).

81 J. Schwider, R. Burow, K.-E. Elssner, J. Grzanna, R. SPolaczyk, K. Merkel, “Digital wave-front measuring interferometry: some systematic error sources“, Applied Optics 22(21), 3412-3432 (1983).

82 K. Hibino, B. F. Oreb, D. I. Farrant, “Phase shifting for nonsinusoidal waveforms with phase-shift errors”, JOSA 12(4) 761-768 /(1995).

83 P. Carré, “Installation et utilisation du comparateur photoelectrique et interferential du Bureau International des Poids et Mesures”, Metrologia 2, 13-23 (1966).

84 J. Novak, P. Novak, A. Miks, “Multi-step phase-shifting algorithms insensitive to linear phase shift errors”, Optics Communications 281(21), 5302-5309 (2008).

85 P. A. A. Magalhaes, Jr., P. S. Neto, C. S. de Barcellos, “Phase shifting technique using generalization of Carré algorithm with many images“, Optical Review 16(4), 432-441 (2009).

86 X. Su, W. Chen, “Reliability-guided phase unwrapping algorithm: a review”, Optics and Lasers in Engineering 42, 245-261 (2004).

87 J. Huntley, “Noise-immune phase unwrapping algorithm”, Applied Optics, 28(16), 3268-3270 (1989).

88 D. C. Ghiglia, L. A. Romero, “Minimum LP-norm two-dimensional phase unwrapping”, JOSA A 13(10), 1999-2013 (1999).

89 G. Fornaro, G. Franceschetti, R. Lanari, E. Sansosti, M. Tesauro, “Global and local phase-unwrapping techniques: a comparison”, Journal of the Optical Society of America 14(10), 2702-2708 (1996).

90 J. M. Huntley and H. O. Saldner, “Shape measurement by temporal phase unwrapping: comparison of unwrapping algorithms”, Measurement Science and Technology 8, 966-992 (1997).

91 C. Reich, R. Ritter and J. Thesing, “3-D shape measurement of complex objects by combining photogrammetry and fringe projection”, Optical Engineering 39(1): 224-231, (2000).

92 J. M. Fitts, “Hidden change distribution grating and use in 3D Moiré measurement sensors and CMM applications”, US Patent 5319445 (1994).

93 D. Scharstein and R. Szeliski, “High-accuracy stereo depth maps using structured light”, Proceedings of the 2003 IEEE Computer Society Conference on Computer Vision and Pattern Recognition (CVPR’03).

94 C. Bräuer-Burchardt, C. Munkelt, M. Heinze, P. Kunmstedt, G. Notni, “Phase unwrapping in fringe projection systems using epipolar geometry”, LNCS 5259, 422-432 (2008).

95 R. Ishiyama, S. Sakamoto, J. Tajima, T. Okatani, K. Deguchi, “Absolute phase measurements using geometric constraints between multiple cameras and projectors”, Applied Optics 46(17) 3528-3538 (2007).

96 R. Sitnik, M. Kujawinska, J. Woznicki, “Digital fringe projection system for large volume 360-degree shape measurement”, Optical Engineering 41(2):443-449 (2002).

97 W. Li, X. Su and Z. Liu, “Large-scale three-dimensional object measurement: a practical coordinate mapping and image data-patching technique”, Applied Optics 40(20) 3326-3333 (2001).

98 W. Schreiber and G. Notni, “Theory and arrangements of self-calibrating whole-body three-dimensional measurement systems using fringe projection technique”, Optical Engineering 39(1): 159-169 (2000).

99 R. Ishiyama, T. Okatani, K. Deguchi, “Precise 3D measurement using uncalibrated pattern projection”, IEEE International Conference on Image Processing (ICIP), 225-228 (2007).

100 R. Kowarschik, P. Kuhmstedt, J. Gerber, W. Schreiber, G. Notni, “Adaptive optical three-dimensional measurement with structured light” Optical Engineering 39(1) 150-158 (2000).

101 R. G. Dorsch, G. Häusler, J. M. Herrmann, “Laser triangulation: fundamental uncertainty in distance measurement”, Applied Optics, 33(7):1306-1314, (1994).

102 J. W. Goodman, “Some fundamental properties of speckle”, JOSA 66(11) 1145-1150 (1976).

103 R. A. Sprague, “Surface roughness measurement using white light speckle”, Applied Optics 11(12) 2811-2816 (1972).

104 H. M. Pederson, “On the contrast of polychromatic speckle patterns and its dependence on surface roughness”, Journal of Modern Optics 22(1) 15-24 (1975).

105 K. Nakagawa, T. Asakura, “Contrast dependence of white light image speckles on surface roughness”, Optics Communications 27(2), 207-213 (1978).
106 K. Nakagawa, T. Asakura, “Average contrast of white-light image speckle patterns”, Journal of Modern Optics (Optica Acta), 16(8) 951-960 (1979).
107 J. C. Dainty, “Detection of images immersed in speckle noise”, Journal of Modern Optics 18(5), 327-339 (1971).
108 K. Nakagawa, N. Nagamatsu, T. Asakura, Y. Shindo, “An effect of the extended detecting aperture on the contrast of monochromatic and white-light speckles”, Journal of Optics 13(3), 147-153 (1982).
109 N. George, A. Jain, “Speckle reduction using multiple tones of illumination”, Applied Optics 12(6), 1202-1212 (1973).
110 T. S. McKechnie, “Speckle reduction” in J. C. Dainty (ed.), “Laser speckle and related phenomena”, 123-170, Springer (1984).
111 J. I. Trisnadi, “Speckle contrast reduction in laser projection displays”, in M. H. Wu, “Projection Displays VIII”, Proceedings of the SPIE 4567, 131-137 (2002).
112 Y-Q. Hu, “Dependence of polychromatic-speckle-pattern contrast on imaging and illumination directions”, Applied Optics 33(13) 2707-2714 (1994).
113 J. M. Huntley, “Simple model for image-plane polychromatic speckle contrast”, Applied Optics, 38(11) 2212-2215 (1999).
114 H. Lui, G. Lu, S. Wu, S. Yin, F. Yu, “Speckle-induced phase error in laser-based phase-shifting projected fringe profilometry”, JOSA 16(6) 1484-1495 (1999).
115 Point Grey Research Inc. “Imaging products – Flea”, http://www.ptgrey.com/products/flea/index.asp (accessed 5 February 2010). See Appendix A2.2.
116 Edmund Optics, “Megapixel fixed focal length lenses”, http://www.edmundoptics.com/onlinecatalog/displayproduct.cfm?productID=2411 (accessed 5 February 2010). See Appendix A2.3.
117 Edmund Optics, “Multi-frequency grid distortion targets”, http://www.edmundoptics.com/onlinecatalog/displayproduct.cfm?productID=1948 (accessed 5 February 2010). See Appendix A2.4.
118 BenQ “BenQ United Kingdom – Service and Support”, http://benq.co.uk/support/downloads/downloads.cfm/dtype/S/page/downloads/product/834 (accessed 5 February 2010). See Appendix A2.5.
119 HP “HP vp6311 Digital Projector – HP technical support”,

http://h10025.www1.hp.com/ewfrf/wc/product?product=454051&lc=en&cc=uk&dlc=en&lang=en&cc=uk (accessed 5 February 2010). See Appendix A2.6.

120 Renishaw Plc, "PH10 motorised indexing heads", http://www.renishaw.com/en/ph10-motorised-indexing-heads—6684 (accessed 7 March 2010). See Appendix A2.7.

121 J-Y. Bouguet, "Camera calibration toolbox for Matlab", http://www.vision.caltech.edu/bouguetj/calib_doc/index.html (accessed 5 February 2010).

122 J. Heikkilä and O. Silven, "A four-step camera calibration procedure with implicit image correction", Proceedings of the 1997 Conference in Computer Vision and Pattern Recognition, 1106-1112 (CVPR '97).

123 I. D. Wallace, N. J. Lawson, A. R. Harvey, J. D. C. Jones, A. J. Moore, "High-speed photogrammetry system for measuring the kinematics of insect wings", Applied Optics 45(17), 4165-4173 (2006).

124 N. Guilbert, "Projective and Euclidean bundle adjustment", http://www.maths.lth.se/matematiklth/personal/nicolas/software/pedagogical_bundle.zip (accessed 5 February 2010).

125 S. G. Gaffney, "Unmarked wing tracking of the Eristalis hoverfly", MSc Dissertation, Heriot-Watt University, (2006).

126 R. Wang and A. J. Moore, "Theoretical and experimental analysis of wavelength-multiplexed PTV", Photon 06, Institute of Physics (2006).

127 P. K. Roy, "Aerodynamic and wing shape measurements of the flow over a flapping wing using advanced laser methods", MSc Dissertation, Cranfield University (2008).

128 A. J. Moore, R. McBride, J. S. Barton, J. D. C. Jones, "Closed-loop phase stepping in a calibrated fiber-optic fringe projector for shape measurement", Applied Optics 41(16) 3348-3354 (2002).

129 J. Heikkilä, "Geometric camera calibration using circular control points", IEEE Transactions on Pattern Analysis and Machine Intelligence 22(10), 1066-1077 (2000).

130 M. De Santo, C. Liguori, A. Paolillo, A. Pientrosanto, "Standard uncertainty evaluation in image-based measurements", Measurement 36, 347-358 (2004).

131 C. S. Fraser, "On the use of non-metric cameras in analytical non-metric photogrammetry", International Archives of Photogrammetry and Remote Sensing 24(5), 156-166 (1982).

132 A. Grün, “Accuracy, reliability and statistics in close-range photogrammetry”, Proceedings of the Symposium of Comm. V of the ISP, Stockholm, August 14-17, 117-133 (1978).

133 J. Novak, P. Novak, A. Miks, “Multi-step phase-shifting algorithms insensitive to linear phase shift errors”, Optics Communications 281(21), 5302-5309 (2008).

134 C. P. Brophy, “Effect of intensity error correlation on the computed phase of phase-shifting interferometry”, JOSA A 7(4), 537-541 (1990).

135 D. M. Kranz, E. P. Rudd, D. Fishbaine, C. E.Haugan, “Phase profilometry system with telecentric projector”, International Patent, Publication Number WO01/51887 (2001).

136 Q. Kemao, S. Fangjun, W. Xiaoping, “Determination of the best phase step of the Carré algorithm in phase shifting interferometry”, Measurement Science and Technology 11(8), 1220-1223 (2000).

137 Y. Hu and S. Chen, “The noise sensitivity of the Carré fringe-analysis technique”, Measurement Science and Technology 8(8) 871-874 (1997).

138 J. Novak, “Five-step phase-shifting algorithms with unknown values of phase shift”, Optik 114(2), 63-68 (2003).

139 H. Ragheb, E. R. Hancock, “Surface radiance: empirical data against model predictions”, International Conference on Image Processing (ICIP) 2689-2692, IEEE (2004).

140 K. E. Torrance, E. M. Sparrow, “Theory of off-specular reflection from roughened surfaces”, Journal of the Optical Society of America 57(9), 1105-1114 (1967).

141 W. Nadeborn, P. Andra, W. Osten, “A robust procedure for absolute phase measurement”, Optics and Lasers in Engineering 24, 245-260 (1996).

142 J. R. Parker, “Algorithms for image processing and computer vision”, Wiley Computer Publishing, 1-67 (1997).

143 M. G. L. Somerville, “Viewer-centred geometric feature recognition”, PhD thesis, Heriot-Watt University (1996).

144 S. Zhang and S.-T. Yau, “Generic nonsinusoidal phase error correction for three-dimensional shape measurement using a digital video projector”, Applied Optics 46(1), 36-43 (2007).

145 J. D. R. Valera, Y. R. Huddart, N. J. Weston and A. J. Moore, “Measurement of object shape and surface slope with combined fringe projection and photometric stereo techniques”, in preparation for submission (2010).
146 NVIDIA Corporation, “CUDA Zone”, http://www.nvidia.co.uk/object/cuda_home_new_uk.html, (accessed 28 February 2010).